Subcritical and supercritical dynamics of incompressible flow over miniaturized roughness elements

Michele Alessandro Bucci

To cite this version:

Michele Alessandro Bucci. Subcritical and supercritical dynamics of incompressible flow over miniaturized roughness elements. Fluids mechanics [physics.class-ph]. Ecole nationale supérieure d'arts et métiers - ENSAM, 2017. English. NNT : 2017ENAM0053 . tel-01881371

HAL Id: tel-01881371

https://pastel.hal.science/tel-01881371

Submitted on 25 Sep 2018

2017-ENAM-0053

École doctorale n° 432 : Sciences des Métiers de l'ingénieur

Doctorat ParisTech
THÈSE

pour obtenir le grade de docteur délivré par

l'École Nationale Supérieure d'Arts et Métiers

Spécialité " Mécanique des fluides "

présentée et soutenue publiquement par

Michele Alessandro BUCCI

04/12/2017

Subcritical and supercritical dynamics of incompressible flow over miniaturized roughness elements

Directeurs de thèse :	**Pr. Jean-Christophe ROBINET**
Co-encadrement de la thèse :	**Pr. Stefania CHERUBINI**

Jury

M Jose-Eduardo WESFREID, Professeur, PMMH, ESPCI, Paris	President
M. Dan HENNINGSON, Professeur, Linné Flow Center, KTH, Stockholm	Rapporteur
M. Denis SIPP, Directeur de recherche, DAAA, ONERA, Meudon	Rapporteur
M. Ulrich RIST, Professeur, IAG, Universität Stuttgart, Stuttgart	Examinateur
Mme. Estelle PIOT, Chargé de recherche, ONERA, Toulouse	Examinateur
M. Jean-Christophe LOISEAU, MdC, DynFLuid, Arts et Métiers ParisTech, Paris	Examinateur
M. Jean-Christophe ROBINET, Professeur, DynFLuid, Arts et Métiers ParisTech, Paris	Directeur
Mme Stefania CHERUBINI, Professeur associé, DMMM, Politecnico di Bari, Bari	Co-directeur

THÈSE

Arts et Métiers ParisTech - ENSAM
Laboratoire DynFluid

Mémoire de thèse

pour obtenir le grade de

DOCTEUR

de

L'ÉCOLE NATIONALE SUPÉRIEURE
D'ARTS ET MÉTIERS

Spécialité : Mécanique

présenté et soutenu

par

Michele Alessandro BUCCI

en Décembre 2017

Subcritical and supercritical dynamics of incompressible flow over miniaturized roughness elements

Directeur de thèse : **Pr. Jean-Christophe Robinet**
Co-directeur de thèse : **Pr. Stefania Cherubini**

devant le jury composé de :

M. Dan Henningson	Professeur, Linné FLOW Centre and SeRC, KTH, Stockholm	Rapporteur
M. Denis Sipp	Directeur de recherche, DAAA, ONERA, Meudon	Rapporteur
M. Jose-Eduardo Wesfreid	Professeur, Pmmh, ESPCI, Paris	President
M. Ulrich Rist	Professeur, IAG, Universität Stuttgart, Stuttgart	Examinateur
Mme. Estelle Piot	Chargé de recherche , ONERA, Toulouse	Examinateur
M. Jean-Christophe Loiseau	Maître de Conférences, DynFluid, Arts et Métiers ParisTech, Paris	Examinateur
M. Jean-Christophe Robinet	Professeur, DynFluid, Arts et Métiers ParisTech, Paris	Examinateur
Mme. Stefania Cherubini	Professeur associé, DMMM, Politecnico di Bari, Bari	Examinateur

DynFluid - Laboratoire de Dynamique des Fluides

Arts et Métiers ParisTech, centre de Paris

« A Ph.D thesis is: a period of life in which a guy is thrown in a sea of shit and his ability to getting out is evaluated»
J-C. Robinet

Acknowledgements

I would have never obtained the results presented in thesis without the help of those many people I had the pleasure of discussing them with. Like any respected explicit time integration of a PDEs, the result relies on the boundary condition and sometime also on the initial condition. Therefore, it is mandatory for me to thank few people.

I would like to thank Jean-Christophe Robinet and Stefania Cherubini for giving me the opportunity of carrying out this thesis. They believed in me and gave me complete freedom in the different choices I have made. They supported me and made me feel part of the group since the first day, even if at the beginning my role was not clear for me. Every discussion with them (around a coffee) was a good opportunity to grow up and understand that Krylov was not a friend but a method. I have to thank Jean-Christophe Loiseau, who is like a big brother for me in the field of research. He spent a lot of time to explain me in a simple way all his PhD work. I thank also Franco Auteri for having welcomed in Politecnico di Milano for six months.

I also must thank my colleagues in the DynFluid laboratory for the fun time together and for the never enough beers on Friday nights. In particular, I thank Mirko for the fruitful discussions and his point of view, always orthogonal with respect to mine. I thank Andrea Sansica for being a great food pusher, Luca for sharing good “amari”, Elio for the amazing dinners, Ciccio, Cosimo, JC poussin, Lucien, Davide and all the guys I had the pleasure of meeting in this laboratory. I also want to thank all the people that were not in the laboratory but that had a role in fixing the NaN generation. I thank Onofrio for having provided effective memes, Dario, Cesare, Nicolò and the residents of the MEASE.

I thank my father, my mother, my brothers and my sister for teaching me the perseverance and encouraging me in this adventure. Thanks to them, Puglia was not so far.

I thank my girlfriend because she supported my choices, she followed me in Paris, she motivates me to pursue my dreams and makes me a stable fix point far away from the chaos.

Contents

List of Figures

List of Tables

Chapter I

Introduction

I.1 Motivation: drag reduction

Drag reduction in fluid flows is today an hard challenge. From an engineering point of view decreasing the drag means decreasing the fuel needed to supply a car, increasing the payload of an airplane, or also decreasing the power needed to move a fluid in a pipeline. The drag comes from the viscous stress that, by first and reasonable approximation, can be considered linearly proportional to the strain rate. Locally, this means that those forces are proportional to the rate of change of the fluid velocity vector as one moves away from the considered point in every directions. The fluids characterised by a constant viscosity tensor that links the viscous stress to the strain rate are known as Newtonian fluid. In this framework, for an incompressible and isotropic Newtonian fluid, the viscous stress is given by a simple relation

$$\tau = \mu \frac{du}{dy}$$

where τ is the shear stress, μ is the dynamic viscosity of the considered flow and du/dy is the variation of the velocity component parallel to the shear in the wall-normal direction. The integral of the shear stress over the wall surface gives the force required to counterbalance the fluid resistance. Without taking into account the cases in which the pressure forces play an important role (presence of a separation zone or shock wave) and considering a constant viscosity (setting the fluid and the temperature at which it operates) the shear stress strictly depends on the streamwise velocity gradient. The flow behaviour close to the wall also depends on the flow state in which it is moving: laminar, turbulent, or transitional, as sketched in fig. I.1. The laminar flow is organised by layers (latin *lamina*: sheet) and it is characterized by low velocity gradients and low skin friction drag. On the other hand, the turbulent state is characterized by a chaotic motion. Strong velocity gradients are present at the wall due to the presence of the *viscous sublayer* and the presence of strong velocity fluctuations. The presence of laminar or turbulent state is somehow linked to the value of the Reynolds number, that is a dimensionless number representing the ratio between the inertial forces and the viscous forces. Starting from a laminar state and increasing the Reynolds number the flow becomes turbulent. The critical Reynolds number is the number at which the flow becomes unstable.

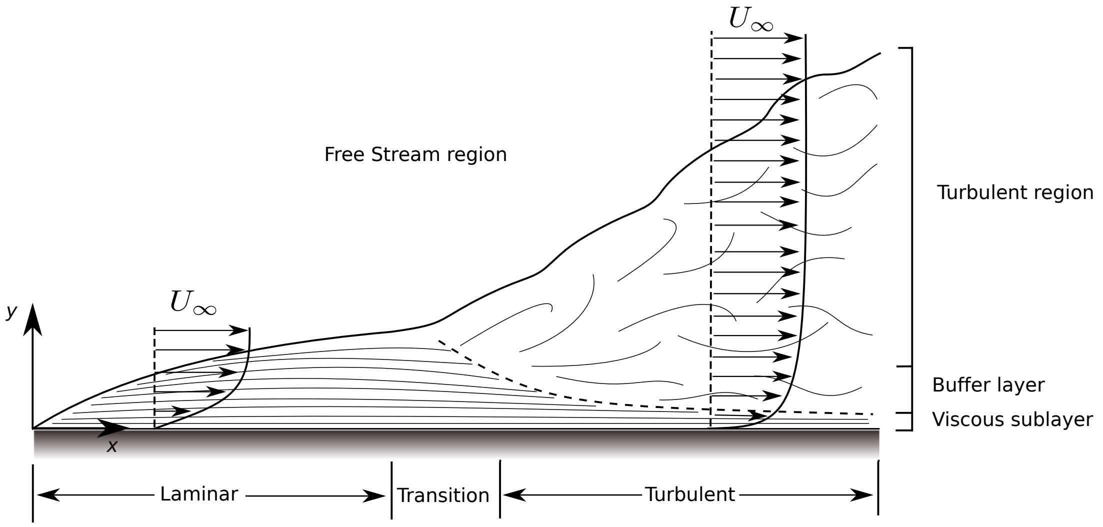

Figure I.1: Sketch of the flow over a flat plate. Firstly the flow state is laminar and the wall normal gradient decrease in the stramwise direction. Afterwards the flow becomes turbulent with high wall normal velocity gradients due to the presence of the viscous sublayer and high velocity fluctuations.

I.1.1 Historical overview

Many solutions have been proposed and tested experimentally and numerically in the last half-century to decrease the drag. In order to achieve this objective one can think to modify the wall properties or shape to change the mean velocity profile or to reduce the velocity fluctuations killing the structures like the streaks that selfsustain the turbulence (Waleffe, 1995) or delaying transition in order to increase the laminar region. Walsh (1982) showed experimentally how introducing longitudinal V-groove riblet surfaces it was possible to produce consistent net drag reductions for a boundary layer flow. The reduction was as large as 8 percent respect to the unmodified flat plane. The main idea is to create an higher viscous sublayer in the transverse direction able to alter the formation and the growth of the streaks. Babenko and Kozlov (1972) investigated experimentally the use of an elastic surface to increase the critical Reynolds number and decrease the amplification rate of unstable disturbances. A more recent solution is the use of super-hydrophobic surfaces as suggested by Daniello et al. (2009). A pattern of micro- or nano features on hydrophobic wall surface are applied in order to support a shear-free air-water interface between wall peaks in the surface. The consequent drag reduction approaches 50% of the drag of the uncontrolled case. This kind of solution can be applied only for some fluids. With the same philosophy McCORMICK and Bhattacharyya (1973) proposed to produce a near wall air film by electrolysis to eliminate the water-solid contact. Unfortunately, the air film is highly unstable and the energy required for the electrolysis was not negligible at all. A wall modification by using porous surfaces is useful to control separated flow but it increases the skin friction (Kong and Schetz, 1982; Kong et al., 1982). An other interesting solution proposed at the beginning of the 1960 is the use of additives like polymers in the flow. Large length-to-diameter particle can provide considerable drag reduction from 20 to 50% (Lumley, 1969). It has also been shown how

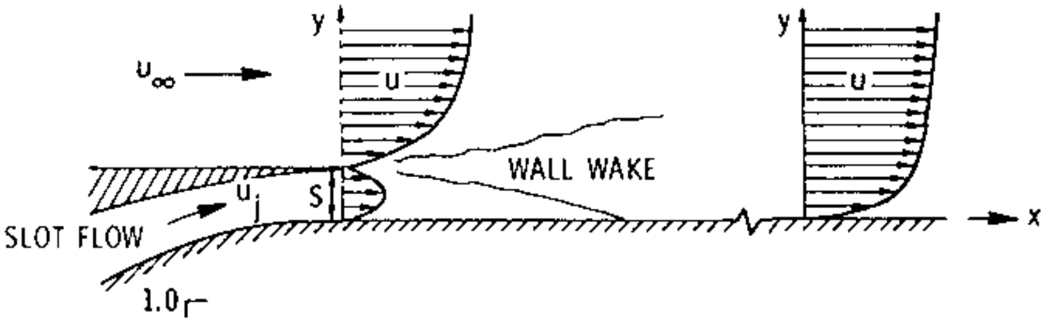

Figure I.2: Sketch of Carry's solution to drag reduction (Cary Jr et al., 1977). A controlled wake allows to get separation. Keeping the the velocity profile close to the separation is possible to drastically reduce the drag.

spherical particles can not yield the same effect. The explanation for the fibrous drag reduction is that the fibres provide a distributed anisotropic body force since the fibers in the flow are aligned with the streamwise direction. For this reason features like flexibility or extensibility of the fibres can impact on the drag reduction. The anisotropy of this body force allows longitudinal velocity fluctuations but those in the cross-stream direction are much more constrained. The "mono-dimensionalizing" effect alter the turbulent production and reduce the drag. Of course this kind of solution cannot be used in an open flow, even if different solutions have been tested. For example one could inject particles near the leading edge and attempt to recover them at the trailing edge. The fibers capture is not straightforward and even if it was possible, there is an additional cost for the recirculation of the particles. Another approach is to generate the fiber by combustion, but this solution is not viable for environmental problems. By using the same principle of the fiber to introduce anisotropy, another proposed body force is the magnetic field (Anderson and Wu, 1971; Fraim and Heiser, 1968). A magnetic field aligned with the mean flow only affect radials and tangential velocity fields that for a pipe flow represent fluctuations. This allows to have the same effect as the fibers. The MHD (Magneto Hydro Dynamics) limitation is that it can be applied only for magnetic fluids. To reduce the wall normal velocity gradient it is possible to induce a controlled separation because in the limit of attached flow the wall normal gradient of the streamwise velocity is equal to zero. Cary Jr et al. (1977) proposed to use a parallel wall jet to produce a wake close to the wall as in fig. I.2. The interaction between the wake and the wall induces a separation. Trying to keep the velocity profile over a long distance in the limit of the separation it is possible to get a drastic reduction of the drag. The same effect can be achieved by using controlled adverse pressure gradient (Spangenberg et al., 1967; Stratford, 1959). Finally, there are two recent solutions that it is worth mentioning. The first one is proposed by Quadrio and Ricco (2004). It consists in the use of spanwise wall oscillation that are able to inhibit the formation of elongated wall structures. The research is very active in this topic as the drag reduction achieved in turbulent flows is around 40%. There are many variants of this method, for example introducing a moving wall or a body forcing or, as recently proposed, wall travelling waves (Viotti et al., 2009). Another solution for drag reduction is to delay transition killing Tollmien-Schlichting waves which represent the unsteady perturbations that grow spatially up to get transition. Cossu and Brandt (2004) demonstrated how streaks optimally distributed are able to damp and (in some cases) annihilate these unsteady perturbations and consequently delay transition. This stabilization effect has also been demonstrated experimentally using a distributed array of cylindrical roughness elements to generate streaks (Fransson et al., 2004). This is just a small list of the possible solutions adopted or studied in the last half-century. Many other possibilities could be mentioned like distributed suction or distributed blowing in the boundary layer, use of localized jets up to the most recent studies on the use of plasma actuators to generate localized forcing. Some of these solutions come from theoretical investigations, some others from an heuristic procedure. Some of these cannot be adopted because the energy economized by drag reduction is lower than the energy used to supply the control. In some cases, the control is effective only for specific kinds of fluids or flows. An unique and general solution does not exist and this is the reason why the interest in this field is so high.

I.2 Origin of the present work

The importance of drag reduction is clear but which kind of solution is worthy of being studied? In this Ph.D work we were interested in using roughness to generate stable steady streaks to delay transition. The reason of this choice comes from a natural succession of researches carried out in the DynFluid laboratory in the last ten years. The main *fil rouge* pursued is the study of the numerous issues involved in the transition problem. More precisely, the transition could be divided in three frameworks: how external perturbations excite disturbances in the laminar state (receptivity), how the latter grow (instability), and when and where the flow becomes turbulent (breakdown). These three topics are proper of the hydrodynamic instability framework.

The three topics are depicted in figure I.3. Focusing on open flows, the first work carried out at the DynFluid laboratory that is worth to cite is Alizard's study on the spatially convective global mode in a boundary layer (Alizard and Robinet, 2007). In this work, the boundary layer flow was studied by using the global stability theory without any simplifying hypothesis on the parallelisms of the flow like in the local stability theory. The convective character of the Tollmien-Schlichting waves appears in the global analysis as a discretized branch of stable global modes. Local properties as the position of the neutral curve are also recovered. This work refers to the **A**-way toward transition as depicted in fig. I.3. The second step was to investigate on the transient growth due to the non-orthogonality of the global modes in the boundary layer flow (Alizard and Robinet, 2011). The results show that to lead optimal transient growth many global modes have to be considered. This two works brought the foundations for other two research fields. The first one is the study of more complex flow configuration like separated flows (Alizard et al., 2009). The second one is a fully 3D transient growth analysis (Cherubini et al., 2010b) since further investigation on non-modal behaviour was necessary to understand the role in the transient of non zero streamwise wave number perturbations. In this case the TS waves are not present in the dynamics towards turbulence and the transition is triggered by secondary instability of the elongated vortex structures. These two works were a necessary step to understand how the boundary layer receptivity changes in presence of a

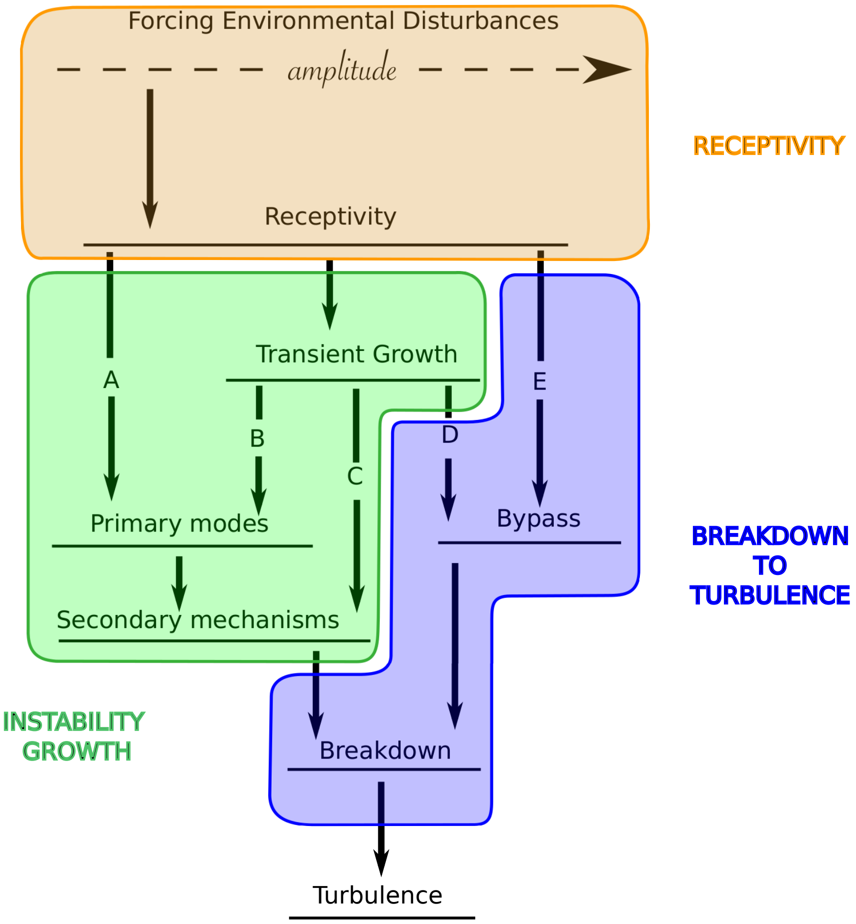

Figure I.3: Illustration of the different mechanisms involved in the transition scenario. Depending on the amplitude of the external disturbance, it is possible to get transition via different ways. Picture from (Morkovin et al., 1994).

geometrical disturbance and also to understand why the TS waves are not the most common route towards transition observed in the experiments. The last two works refer to the **B**- and **C**-way in figure I.3. In 2010, thanks to Cherubini's work (Cherubini et al., 2010a), it was possible to demonstrate that a non-linear optimal perturbation can efficiently induce transition. The effect of the non-linear terms in the optimization loop is a spatial localization of the optimal initial perturbation and an inclination of the elongated wall vortices. The non linear evolution of the initial perturbation shows the generation of hairpin vortices that cause the breakdown towards turbulence. The transition due to a non-linear optimal perturbation refers to the **D**- and **E**-way in figure I.3. Introducing a local geometrical perturbation (smooth roughness) it is possible to get transition in the boundary layer due to transient growth mechanisms (Cherubini et al., 2013). A varicose perturbation that wraps the low streaks behind the roughness induces a breakdown between the laminar streaked boundary layer and the turbulent state due to the generation of a wave packet advected downstream which gives rise to hairpin structures. The capability of the roughness element to stabilize the TS waves was then questioned. The roughness is able to generate stable steady streaks but at the same time it increases the non-normalities of the system. Loiseau during his Ph.D work (Loiseau, 2014) investigated on stability of the boundary layer straked due to the presence of a cylindrical roughness (Loiseau et al., 2014). The main result was that the presence of the roughness not only increases the non-normalitiy of the system but it could also induce a self-sustained oscillation owing to the presence of an unsteady global mode. The source of the unsteady global mode was linked to the shear generated by the separation zone behind the roughness when the global mode is varicose and it is linked to the Von Karman instability when the global mode is sinuous. A parametric analysis on the aspect ratio of the roughness showed that it is possible to switch from a sinuous to a varicose global mode increasing the size of the diameter related to the height of the cylindrical roughness.

I.3 Objective of this thesis

In the light of the results achieved in the Loiseau's Ph.D work many questions could be posed:

- What is the upper limit of the use of the roughness to delay transition?
- If the roughness affects the transient growth of the energy and the stability of the system, does it change also its receptivity?
- If the receptivity changes, how the eigenmodes interact between each other when they are forced?
- Is the receptivity analysis predictive of the dynamics when a broad band external perturbation acts on the streaky boundary layer?
- Are experimental observations coherent with the linear global analyses?
- When the global mode is triggered, is it the cause of the transition or it forces other secondary unstable mechanisms that evolve towards transition?

- By using a roughness that does not allow a separation zone is it possible to annihilate the unstable global mode?

Under the supervision of Jean-Christophe Robinet and Stefania Cherubini, in this Ph.D. work we tried to give an answer at all this questions.

I.3.1 Approach

Thanks to the collaboration with the *IAG* laboratory in the Stuttgart university, namely thanks to Prof. Ulrich Rist and Mr. Dominik Puckert, a numerical-experimental comparison has been possible. The experiment is performed in a water channel in which a boundary layer flow is reproduced. At the wall a cylindrical roughness is installed to modulate the boundary layer and to check critical Reynolds number after which the flow becomes unsteady. The first step was to perform a Direct Numerical Simulation (**DNS**) corresponds to the experimental setup to compare the statistical quantities. Under the assumption of parallel flow the neutral curve has been found by a Bi-Local Stability Analysis (**Bi-LSA**). A Global Stability Analysis (**GSA**) has been performed to check the existence of an unsteady or steady global mode linked to the presence of roughness. The sensitivity of the eigenspectra has been evaluated looking at the **Pseudospectra**. For steady state configurations the optimal response to a periodic forcing has been evaluated solving an Optimal Forcing (**OF**) problem. A synthetic Free Stream Turbulence (**FST**) has been put in place to verify that the response of the system to an external broad band uncontrolled perturbation was coherent with the resolvent curve. Finally the dynamics resulting from the receptivity of the boundary layer has been decomposed by a Dynamical Mode Decomposition (**DMD**) to check a posteriori how much the global modes take part into transition behind the cylindrical roughness. Changing the roughness shape and using the Miniaturized Vortex Generators the separation zone disappears and an Optimal initial Perturbation (**OP**) analysis has been carried out to check the non-normalities introduced by the boundary layer deformation.

The implementation of the algorithms necessary to perform some of the previously cited analyses took a great part of this Ph.D work. For this reason a detailed description will be provided to the reader in the next chapters.

I.4 Organization of the manuscript

First of all (**Chapter II**)fundamental mathematical notions about stability analysis are provided. Local and global analysis, transient energy growth and receptivity of the system are then explained and discussed. The CFD code and the implemented algorithms are then discussed (**Chapter III**). The implementation of each algorithm is explained and a validation test case to each implementation is also provided to the reader. The stability analysis is then performed onto the cylindrical roughness experimental case (**Chapter IV**). The predictability of the linear stability analysis is then verified by perturbed DNS (**Chapter V**). Flow parameters are then changed to study their influences on the flow dynamics (**Chapter VI**). The cylindrical roughness shape is then substituted by miniaturized vortex generators (**Chapter VII**) to evaluate the difference between roughness shapes with and without induced separation zone. Finally, general conclusions and perspectives are provided (**Chapter VIII**).

Chapter II

Mathematical and theoretical basic notions

Contents

II.1 Equation of Fluid Dynamics

The mathematical formulation of the flow dynamics is represented by the well know Navier-Stokes equations. For the cases of interest we refer to the incompressible dimensionless Navier-Stokes (NS) equations:

$$\begin{cases} \nabla \cdot \mathbf{U} = 0 \\ \dfrac{\partial \mathbf{U}}{\partial t} + (\mathbf{U} \cdot \nabla)\mathbf{U} = -\nabla P + \dfrac{1}{Re}\Delta \mathbf{U} \end{cases} \tag{II.1}$$

where $\mathbf{U}(\mathbf{x}, t)$ is the velocity field, $P(\mathbf{x}, y)$ the pressure and Re is the dimensionless number characterising the flow. The first equation in the system II.1 represents the incompressibility constrain and it comes from the mass conservation. The second equation is the momentum conservation. The presence of the non linear term $(\mathbf{U} \cdot \nabla)\mathbf{U}$ in the momentum conservation implies that the solution of the PDE system is highly dependent from the initial condition for a fixed Re number. The analytical solution of the NS equations is even today an open problem. The only way to solve this equation is to discretize it in time and in space. The temporal feature of the solution (e.g. steady, periodic or chaotic) depends on the Re number that is then the *critical parameter.* The Re value at which a steady solution becomes unsteady is the *critical value* (i.e. Re_c).

II.2 Instability framework

The stability or instability definition pertains to the tendency of a physical system to move away or not from its initial condition when this is perturbed. More properly, if at an infinitesimal perturbation of a physical system corresponds a small variation of the present state which does not grow in time then the system is said to be stable. On the other hand, if the infinitesimal perturbation is amplified in time, then the system is said to be unstable. The notion of instability is not related only to fluid mechanics but is a general concept that can be applied to every physical system or mathematical model.
From a general point of view, a system of equations like (II.1) can be written in a contract form as

$$\frac{\partial \mathbf{Q}}{\partial t} = \boldsymbol{\mathcal{F}}(\mathbf{Q}) \tag{II.2}$$

where $\mathbf{Q} = (\mathbf{u}, p)^T$ and $\boldsymbol{\mathcal{F}}$ is the non linear operator of the considered problem. The previous definition of instability could be translated mathematically defining all physical quantities as the sum of a base state and a fluctuation:

$$\mathbf{Q}(\mathbf{x}, t) = \mathbf{Q}_b(\mathbf{x}) + \mathbf{q}(\mathbf{x},\mathbf{t}) \tag{II.3}$$

The base state $\mathbf{Q}_b(\mathbf{x})$ is the time-independent part of the solution. On the other hand, $\mathbf{q}(\mathbf{x}, t)$ is the fluctuating component of the solution $\mathbf{Q}(\mathbf{x}, t)$ and represents the unknown of the problem. Substituting eq. (II.3) in eq. (II.2) one has

$$\begin{cases} \dfrac{\partial \mathbf{Q}_b}{\partial t} = \boldsymbol{\mathcal{F}}(\mathbf{Q}_b) = 0 & \text{(II.4a)} \\ \dfrac{\partial (\mathbf{Q}_b + \mathbf{q})}{\partial t} = \boldsymbol{\mathcal{F}}(\mathbf{Q}_b + \mathbf{q}) & \text{(II.4b)} \end{cases}$$

Hence, the same problem defined by eq. (II.2) has two solutions: $\mathbf{Q}_b$ and $\mathbf{Q}_b + \mathbf{q}$.

On the basis of this mathematical formulation, different definitions of instability can be given. Let us assume that the time evolution of a physical problem (such as fluid mechanics, electromagnetism, particles, etc.) in a domain $\mathcal{V}$ is governed by a set of partial differential equations (PDE), closed with a convenient set of initial conditions at $t = 0$, and a set of boundary conditions on $\partial\mathcal{V}$. We note $\|\mathbf{Q} - \mathbf{Q}_b\|$ the amplitude of the perturbation such that:

$$\|\mathbf{Q} - \mathbf{Q}_b\|(t) = \left[\iiint_{\mathcal{V}} (\mathbf{Q} - \mathbf{Q}_b)^2 \, d\mathcal{V}\right]^{\frac{1}{2}}$$

Definition II.1. *Stability (according to Lyapunov).*
The basis field $\boldsymbol{Q}_b(\boldsymbol{x}, t)$ *is said stable if* $\forall\epsilon > 0$, $\exists\delta(\epsilon) > 0$ *such that if* $\|\boldsymbol{Q}(\boldsymbol{x}, 0) - \boldsymbol{Q}_b(\boldsymbol{x}, 0)\| < \delta$ *then* $\|\boldsymbol{Q}(\boldsymbol{x}, t) - \boldsymbol{Q}_b(\boldsymbol{x}, t)\| < \epsilon$, $\forall t \geq 0$.

The base state is stable if, for a given norm, it exists a limit for which the perturbations are small compared to the initial perturbation, $\forall t$. A more restrictive definition of stability is that given below:

Definition II.2. *Asymptotic stability.*
The base state $\boldsymbol{Q}_b(\boldsymbol{x}, t)$ *is said asymptotic stable if is stable according to Lyapunov and also* $\lim_{t\to\infty} \| \boldsymbol{Q}(\boldsymbol{x}, t) - \boldsymbol{Q}_b(\boldsymbol{x}, t)\| = 0$.

An even more restrictive definition of stability is that of global, or unconditional stability

Definition II.3. *Global stability or unconditional.*
The base state $\boldsymbol{Q}_b(\boldsymbol{x}, t)$ *is unconditionally stable if it is stable and* $\forall \| \boldsymbol{Q}(\boldsymbol{x}, 0) - \boldsymbol{Q}_b(\boldsymbol{x}, 0)\| \Rightarrow \lim_{t\to\infty} \| \boldsymbol{Q}(\boldsymbol{x}, t) - \boldsymbol{Q}_b(\boldsymbol{x}, t)\| = 0$.

A base state which is stable but not unconditionally stable is called *conditionally stable*, i.e. there are finite amplitude perturbations that can grow asymptotically.

When the equation of evolution is non-linear, there is not a general theory to determine the non-linear stability. However, **if the disturbance is small** for a given base state, the equation of evolution can be linearised. In this context, there is a complete stability theory of the linearised operators.

Definition II.4. *Linear stability.*
The base state $\boldsymbol{Q}_b(\boldsymbol{x}, t)$ *is said to be stable if all infinitesimal perturbation evolving onto* $\boldsymbol{Q}_b(\boldsymbol{x}, t)$ *decrease asymptotically.*

A state that is not linearly stable, is linearly unstable. Therefore, the definitions of linear stability derive from general definition within the limits $\delta, \epsilon \to 0$. If the flow is linearly asymptotically unstable, it is consequently also asymptotically unstable (linear instability can be a sufficient condition for instability). In this work we will carry out a linear instability analysis, thus from now we will consider the hypothesis that the fluctuation is small compared to the value of the base state.

II.2.1 Linear analysis

As said before, both $\mathbf{Q}_b$ and $\mathbf{Q}_b + \mathbf{q}$ are solutions of the problem (II.2). If the assumption of small fluctuations is true, then the governing equations of the system may be linearised around the base state as follows. Let us consider the non-linear operator $\boldsymbol{\mathcal{F}}$

$$\boldsymbol{\mathcal{F}}(\mathbf{Q}) = \boldsymbol{\mathcal{F}}(\mathbf{Q}_b) + \nabla\boldsymbol{\mathcal{F}}(\mathbf{Q}_b) \cdot \mathbf{q} + \mathcal{O}(\|\mathbf{q}\|^2) \tag{II.5}$$

with $\nabla\boldsymbol{\mathcal{F}}(\mathbf{Q}_b)$ being a differential operator, depending on the base state. As the base state is the stationary solution of equations (II.2), and neglecting the second order terms, the previous relation becomes

$$\boldsymbol{\mathcal{F}}(\mathbf{Q}) = \nabla\boldsymbol{\mathcal{F}}(\mathbf{Q}_b) \cdot \mathbf{q} \tag{II.6}$$

Finally, considering that in a linear context the principle of superposition of the effects holds

$$\frac{\partial \mathbf{Q}}{\partial t} = \frac{\partial(\mathbf{Q}_b + \mathbf{q})}{\partial t} = \cancel{\frac{\partial \mathbf{Q}_b}{\partial t}} + \frac{\partial \mathbf{q}}{\partial t} = \frac{\partial \mathbf{q}}{\partial t} \tag{II.7}$$

equation (II.2) can be rewritten as

$$\frac{\partial \mathbf{q}}{\partial t} = \nabla\boldsymbol{\mathcal{F}}(\mathbf{Q}_b) \cdot \mathbf{q} \tag{II.8}$$

or, similarly

$$\begin{cases} \mathbf{B}\dfrac{\partial \mathbf{q}}{\partial t} = \mathbf{J}\mathbf{q} \\ \mathbf{q}(\mathbf{x}, t = 0) = \mathbf{q}_0 \\ \mathcal{L}\mathbf{q}(\mathbf{x}_0, t) = 0 \in \partial\mathcal{D} \end{cases} \tag{II.9}$$

This is the general form of the equations used for a linear stability analysis of fluctuations, where

- $\mathbf{B}$ is a mass matrix;
- $\mathbf{J}$ is the Jacobian operator;
- $\mathbf{q}_0$ is the initial condition of the problem;
- $\mathcal{L}\mathbf{q}(\mathbf{x}_0, t)$ are the boundary conditions of the problem.

At this point, a more rigorous definition of the base state must be given.

Definition II.5. *Base state.*
The base state is an equilibrium or periodic solution of the system under consideration: in the context of linear stability theory, this solution has to be time-independent, hence stationary. Moreover, it is the solution that maximises the possible symmetries of the problem under consideration.

Therefore, since the base state is stationary, the system under analysis is stable if the solution tends asymptotically to $\mathbf{Q}_b$. Being the linearised system of equation autonomous, its solution could be written as

$$\mathbf{q}(\mathbf{x}, t) = \frac{1}{2\pi}\int_{F_\omega} \hat{\mathbf{q}}(\mathbf{x}; \omega)e^{-i\omega t}d\omega + c.c. \tag{II.10}$$

where $\hat{\mathbf{q}}$ is the Fourier-Laplace transform of $\mathbf{q}$ and *c.c.* is its complex conjugate. This is a function of complex amplitude and ω is the complex pulsation wave. F_ω is a path in the complex plane ω, which must be compatible with the convergence of the integral. Replacing (II.10) in (II.9), an eigenvalue and eigenvector problem is obtained:

$$\omega\mathbf{B}\hat{\mathbf{q}}(\mathbf{x}, \omega) = \mathbf{J}(\mathbf{Q}_b)\hat{\mathbf{q}}(\mathbf{x}, \omega) \quad \Rightarrow \quad [\mathbf{J}(\mathbf{Q}_b) - \omega\mathbf{B}]\,\hat{\mathbf{q}}(\mathbf{x}, \omega) = 0 \tag{II.11}$$

where ω is the eigenvalue and $\hat{\mathbf{q}}$ is the associated eigenvector. If the imaginary part of ω is greater than zero ($\Im(\omega) > 0$) there is no growth in time of the fluctuation. The eigenvalues are the global modes of the base state, conversely, the eigenvectors represent the fluctuation shape associated with the different modes.

The physical space is three-dimensional and the most general framework in which a linear stability analysis can be performed is that all these three spatial directions are resolved and small time-periodic disturbances (inhomogeneous in all three directions) are superimposed upon a steady base state (itself inhomogeneous in space). This is consistent with the separability of the governing equations of time, on the one hand, and the three spatial directions, on the other. The relevant decomposition in this context is

$$\mathbf{Q}(x, y, z, t) = \mathbf{Q}_b(x, y, z) + \varepsilon\mathbf{q}(x, y, z, t) \tag{II.12}$$

with $\varepsilon \ll 1$.

A problem treated according to the decomposition (II.12) can be solved in general only numerically. In the past, without the computational tools that we have today, linear stability analysis had to neglect the dependence of the base state on one or two spatial directions, i.e. a *parallel-flow* assumption was made. With this assumption, an analytical base state can be used and the stability analysis can be carried out analytically. In the case just mentioned of parallel-flow, for example, the general form of the base flow is $\mathbf{U}_b = (U_b(y), 0, 0)^T$. Therefore the Navier-Stokes equations are homogeneous in the x and z directions, and in time t, so these can be solved using *normal modes expansion* of perturbation. In this case the solution can be found:

$$\mathbf{q}(\mathbf{x}, t) = \frac{1}{(2\pi)^3} \int_{F_\omega} \left[\int_{L_\beta} \left(\int_{L_\alpha} \hat{\mathbf{q}}(y; \alpha, \beta, \omega) e^{i(\alpha x + \beta z - \omega t)} d\alpha \right) d\beta \right] d\omega + c.c. \tag{II.13}$$

where β is the wave number in the z direction and α is the wave number in the longitudinal direction of the fluctuations. α, $\beta \in \mathbb{C}$ and similarly to the path F_ω, path L_β is a path in the complex plane β while path L_α is a path in the complex plane α.

Thanks to the homogeneity assumption in two directions of space and the normal modes expansion, the result of the substitution of (II.13) in the linearised equations of the problem under consideration falls into the framework of *local stability theory*. The modal solution in both streamwise and spanwise direction is common in a great number of parallel baseflows (e.g. Blasius, Poiseuille, shear flow) but in the case of a boundary layer modulated by the presence of the streaks at the wall, the base flow cannot be considered homogeneous in the spanwise direction. In this case, only in the stremwise direction one can make the homogeneous solution ansatz since the the base flow changes slightly in the x-direction (*quasi-parallel assumption*). In this case the solution will be:

$$\mathbf{q}(\mathbf{x}, t) = \frac{1}{(2\pi)^3} \int_{F_\omega} \left(\int_{L_\alpha} \hat{\mathbf{q}}(y, z; \alpha, \omega) e^{i(\alpha x - \omega t)} d\alpha \right) d\omega + c.c. \tag{II.14}$$

where just the streamwise wave number α is taken into account. This decomposition is part of *local stability* framework but with two inhomogeneous direction. For this reason this kind of analysis can be called *bi-local stability analysis*[1] also because the base flow turns out to be a 2-D field $\mathbf{Q}_b(y, z)$.

With a local stability analysis the system of differential equations is written formally as

$$\boldsymbol{\mathcal{N}}(\alpha, \beta, \omega, \mathbf{Q}_b)\hat{\mathbf{q}}(\mathbf{x}; \alpha, \beta, \omega) = 0 \tag{II.15}$$

where $\boldsymbol{\mathcal{N}}$ is the operator of the eigenvalue problem that has to be solved. For a local stability analysis and according to eq. (II.13) and (II.14), two approaches can be chosen:

- **Temporal approach**.
  Investigation of the asymptotic time behaviour of perturbations having real spatial

---

[1] According to Theofilis (2011) this case should be called *BiGlobal* since two inhomogeneous direction are taken into account in the base flow. Nevertheless we prefer to call it *bi-local* because the homogeneous hypothesis is made on the streamwise direction. The latter consideration is consistent with respect to the absolute instability (Huerre and Monkewitz, 1985) in a local framework. Moreover, the *bi-local* terminology is also accepted by other authors.

wavenumbers (Michalke, 1964)

$$[\boldsymbol{\mathcal{N}}_1 - \omega \boldsymbol{\mathcal{N}}_2]\, \hat{\mathbf{q}}(\mathbf{x}; \alpha, \beta, \omega) = 0 \tag{II.16}$$

where α and β are frozen. The asymptotic time evolution of an infinitesimal perturbation is then solely governed by the sign of $\Im(\omega)$ (i.e. the real part of the complex frequency ω). If $\Im(\omega) < 0$, the perturbation decays exponentially in time and the base flow U_b is then denoted as linearly temporally stable and vice-versa.

- **Spatial approach** (also know as Signaling problem).
  Investigation of the base state response to time-harmonic localised forcing. In such analysis, the prescribed frequency of the forcing is real whereas the wavenumbers characterising the perturbation can be complex (Michalke, 1965)

  $$\left[\boldsymbol{\mathcal{C}}_2 \alpha^2 + \boldsymbol{\mathcal{C}}_1 \alpha + \boldsymbol{\mathcal{C}}_0\right] \hat{\mathbf{q}}(\mathbf{x}; \alpha, \beta, \omega) = 0 \tag{II.17}$$

  where β and ω are frozen. If the imaginary part of α is greater than 0 then the base state is spatially stable ($\Im(\alpha) > 0$), and vice-versa.

Another distinction is worth being noticed. The physics literature (Huerre et al., 2000; Schmid and Henningson, 2012) distinguishes between two different kinds of instability, namely *absolute* and *convective* instabilities. This distinction is necessary because an infinitesimal perturbation can grow in time and in space. The *absolute-convective stability analysis* is pertinent for open shear flows, i.e. situations where fluid particles enter and leave the domain of interest in finite time without being recycled, in contrast to closed flows in a finite box such as the lid-driven cavity flow. Investigating the absolute-convective instability of such a flow allows to determine whether the considered flow behave as a noise amplifier, sensitive to external noise (*convectively unstable*) or as a flow oscillator with a well-defined frequency relatively insensitive to external noise (*absolutely unstable*).

Following Huerre et al. (2000) we can introduce the stream function ψ of the infinitesimal perturbation $\mathbf{q}(x,t)$ (for simplicity only one spatial direction has been considered):

$$D\left(-\frac{\partial}{\partial x}, i\frac{\partial}{\partial t}, Re\right) \psi(x,t) = S(x,t) \tag{II.18}$$

where $D(\cdot)$ is the dispersion relation of the equations and $S(x,t)$ a source term specifying the forcing imposed on the system in some localised interval both in time and space. If $S(x,t)$ is put equal to zero then the temporal or spatial analysis would have been sufficient. Introducing the Green function $G(x,t)$, i.e. the impulse response of the system, one can then write:

$$D\left(-\frac{\partial}{\partial x}, i\frac{\partial}{\partial t}, Re\right) G(x,t) = \delta(x)\delta(t) \tag{II.19}$$

where δ is the Dirac impulse. The $G(x,t)$ provides all the necessary information, so the concept of the temporal and spatial instability could be redefined as follows:

- if the flow is linearly stable then:

  $$\lim_{t\to\infty} G(x,t) = 0 \quad \text{along all rays} \quad x/t = const$$

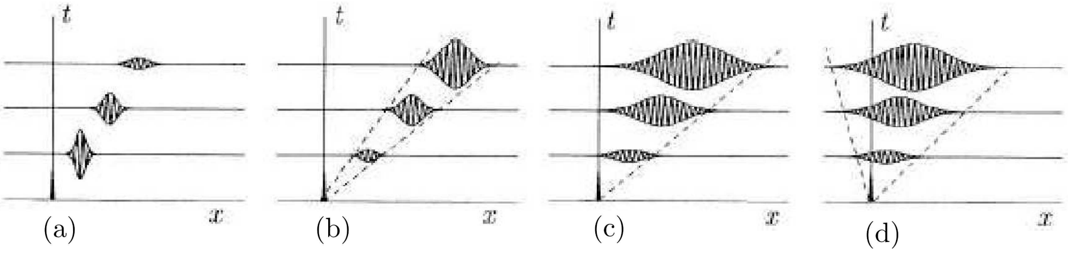

Figure II.1: Linear impulse response $G(x, t)$. (a) Linearly stable flow; (b) linearly convectively unstable flow; (c) marginally convectively/absolutely unstable flow; (d) absolutely unstable flow. Figure from (Huerre et al., 2000).

- if the flow is linearly unstable (temporal or spatial instability) then:

$$\lim_{t\to\infty} G(x,t) = 0 \quad \text{along at least one ray} \quad x/t = const$$

If linearly unstable, the impulse response of the flow then consists of an unstable wavepacket confined in a wedge in the (x, t) plane growing either in time or space. Among linearly unstable flows, one can then make the distinction between absolute and convective instability:

- An unstable flow is said to be convectively unstable if:

$$\lim_{t\to\infty} G(x,t) = 0 \quad \text{along the rays} \quad x/t = 0$$

- It said to be absolutely unstable if:

$$\lim_{t\to\infty} G(x,t) = \infty \quad \text{along the rays} \quad x/t = 0$$

The different impulse responses are summarized in fig. II.1.

II.2.2 Linearised Navier-Stokes equations

In the previous subsection the general mathematical tools for the instability investigation have been given. The decomposition (II.3) can now be applied to the dimensionless Navier-Stokes equations (II.1). The resulting perturbative equations are represented in the system (II.20):

$$\begin{cases} \nabla \cdot \mathbf{u} = 0 \\ \dfrac{\partial \mathbf{u}}{\partial t} + (\mathbf{u} \cdot \nabla)\mathbf{U}_b + (\mathbf{U}_b \cdot \nabla)\mathbf{u} = -\nabla p + \dfrac{1}{Re}\Delta \mathbf{u} \end{cases} \tag{II.20}$$

in which $\mathbf{U}_b$ is the base flow, $\mathbf{u} = (u(\mathbf{x}, t), v(\mathbf{x}, t), w(\mathbf{x}, t))^T$ and $p(\mathbf{x}, t)$ are respectively the fluctuation of the velocity field and pressure field.

As said before, depending on the nature of the base flow, it may make sense to perform a local, a bi-local or a global stability analysis.

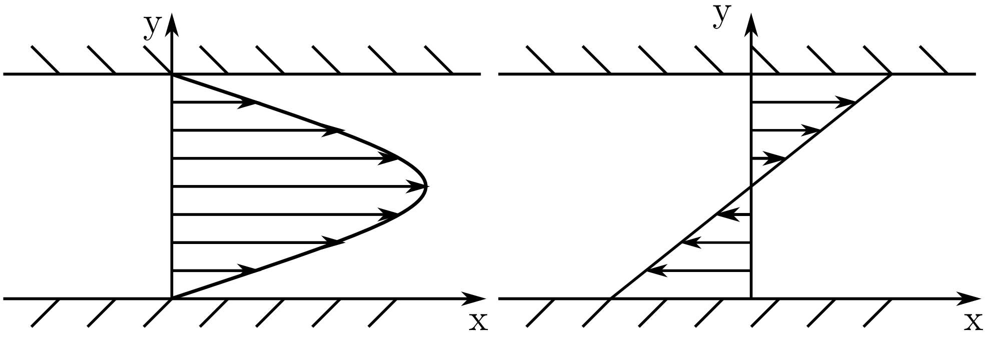

(a) Poiseuille (b) Couette

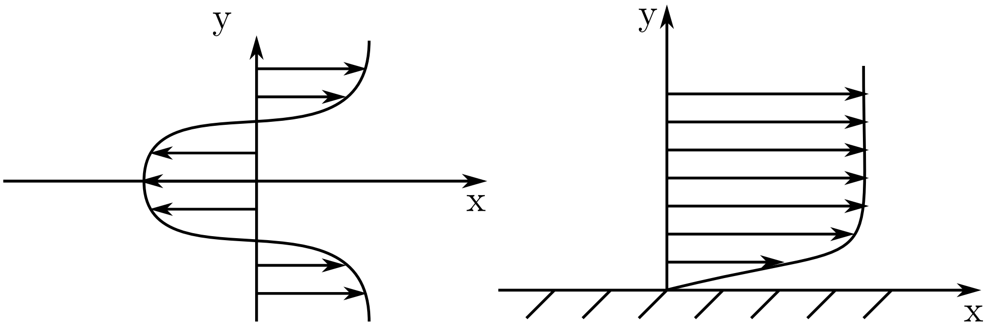

(c) Wake (d) Blasius

Figure II.2: (a) and (b): Examples of parallel flows. (c) and (d): Examples of quasi-parallel flows.

II.2.2.1 Local approach to the NS equations.

In nature, there are many cases in which the base flow is homogeneous in one or two directions or in which its variation is slow in one or two direction. Some examples of such flow are represented in fig. II.2.

With this kind of base flow the vector $\mathbf{U}_b$ is reduced at just one component, $\mathbf{U}_b = (U(y), 0, 0)$. The choice of the parallel flow approximation has also an historical explanation. The solution of the eigenvalue problem for a solution vector as (u, v, w, p) requires a large memory. Thanks to this approximation the perturbation can be expanded into normal modes not only in time (λt) but also in the streamwise direction (αx) and in spanwise direction (βz).

Substituting this new base flow in (II.20) and making some mathematical manipulation, it is possible to recast the linearised Navier-Stokes equations in just two scalar equations:

$$\left[\left(\frac{\partial}{\partial t} + U_b \frac{\partial}{\partial x}\right) \nabla^2 - U_b'' \frac{\partial}{\partial x} - \frac{1}{Re} \nabla^4\right] v = 0 \tag{II.21}$$

$$\left[\frac{\partial}{\partial t} + U_b \frac{\partial}{\partial x} - \frac{1}{Re} \nabla^2\right] \eta = -U_b' \frac{\partial v}{\partial z} \tag{II.22}$$

where U_b'' is the second derivative of the base flow in the y-direction and η satisfies the condition $\eta = \frac{\partial u}{\partial z} - \frac{\partial w}{\partial x}$. Eq. (II.21) and (II.22) are called the *Orr-Sommerfeld* and the *Squire* equation, respectively.

This pair of equations together with boundary conditions

$$v = \frac{\partial v}{\partial y} = \eta = 0 \quad \text{at a solid wall and in the far field}$$

and the initial conditions

$$v(x, y, z, t = 0) = v_0(x, y, z)$$

$$\eta(x, y, z, t = 0) = \eta_0(x, y, z)$$

provide a complete description of the evolution of an arbitrary disturbance in both space and time. Using the equation (II.22) and the null divergence condition the fluctuation components u and w can also be obtained. It is possible also to rewrite the system composed by eq. (II.21) and (II.22) in a matrix form like

$$\frac{\partial}{\partial t}\begin{pmatrix} v \\ \eta \end{pmatrix} = \begin{pmatrix} \boldsymbol{\mathcal{L}}_{Orr,Somm} & 0 \\ \boldsymbol{\mathcal{C}} & \boldsymbol{\mathcal{L}}_{Sq} \end{pmatrix}\begin{pmatrix} v \\ \eta \end{pmatrix} \tag{II.23}$$

where $\boldsymbol{\mathcal{L}}_{Orr,Somm}$ and $\boldsymbol{\mathcal{L}}_{Sq}$ are the Orr-Sommerfeld and Squire operator, and $\boldsymbol{\mathcal{C}}$ is a coupling term. Taking a look to (II.23), some interesting informations could be deduced. The dynamics of the cross-stream velocity v are decoupled from the dynamics of the normal vorticity η. In this sense the linear (in)stability of the Squire equation is dictated by the linear (in)stability of the Orr-Sommerfeld one. The vorticity η cannot extract energy from the base flow. As a consequence, to determine the asymptotic time-evolution ($t \to \infty$) of an infinitesimal perturbation, it is sufficient to consider the Orr-Sommerfeld equation only. Finally the first equation of (II.23) is autonomous in time t, and in the space coordinates x and z, so its solutions can be sought in the form of normal modes.

Following the mathematical procedure explained in §II.2.1 and considering eq. (II.21) and (II.22) together with the parallel assumption of the baseflow, one can introduce wavelike solutions of the form

$$\{v, \eta\}(x, y, z, t) = \{\hat{v}, \hat{\eta}\}(y)e^{i(\alpha x + \beta z - \omega t)}$$

Substituting these two solutions in (II.21) and (II.22) it is possible to obtain:

$$\left[(-i\omega + i\alpha)(D^2 - k^2) - i\alpha U_b'' - \frac{1}{Re}(D^2 - k^2)^2\right]\hat{v} = 0 \tag{II.24}$$

$$\left[(-i\omega + i\alpha)(D^2 - k^2) - \frac{1}{Re}(D^2 - k^2)\right]\hat{\eta} = -i\beta U_b'\hat{v} \tag{II.25}$$

where $k^2 = \alpha^2 + \beta^2$ and D is the derivative operator. To equations (II.24) and (II.25) are associated the relative boundary conditions $\hat{v} = D\hat{v} = \hat{\eta} = 0$ at the solid wall and in the free stream.

Equations (II.24) and (II.25) are another well known form of the *Orr-Sommerfeld equation* and *Squire equation*, respectively. Due to computational reasons many years these two equations have been the only way to study the asymptotic behaviour of a flow in space ($\omega, \beta \in \mathbb{R}$ and $\alpha \in \mathbb{C}$) and in time ($\alpha, \beta \in \mathbb{R}$ and $\omega \in \mathbb{C}$).

Accomplishing this stability analysis means that an eigenvalue problem for eq. (II.24) must be solved. In order to simplify this task, a two-dimensional perturbation instead

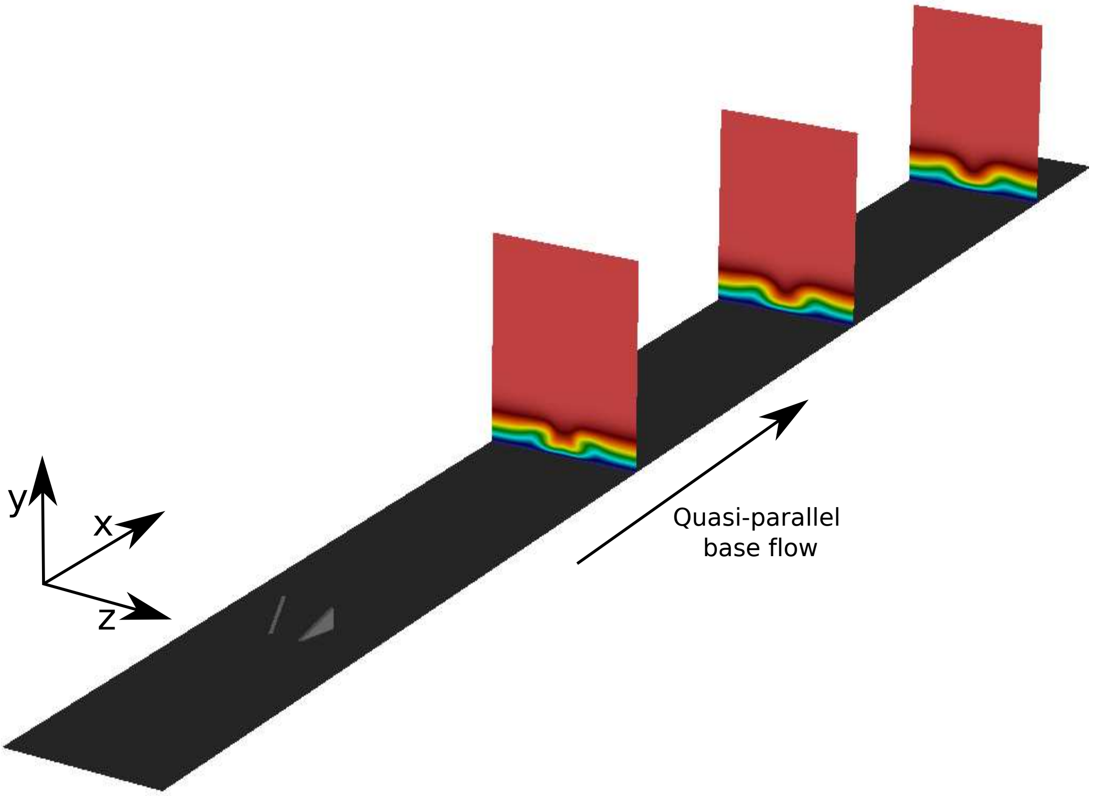

Figure II.3: Weakly parallel base flow generated by the presence of MVG at the wall. Behind the roughness the velocity field can be considered homogeneous in the x-direction.

of a three-dimensional one could be considered (for example imposing that the spanwise component of the perturbation is equal to zero). It could be said that disturbances superimposed on a two-dimensional base flow are not necessarily two-dimensional if the purpose is to perform a stability analysis as general as possible. However, this issue was dispelled by Squire (1933), who in 1933 proved, by assuming periodic disturbances also in the spanwise direction, that a two dimensional infinitesimal perturbation becomes unstable at lower Reynolds numbers if the perturbation is two-dimensional (i.e. when it has $\beta = 0$), with respect to the case in which three-dimensional disturbances are considered. For this reason in simple parallel flows, the destabilizing effect of two-dimensional perturbations is greater than their respective three-dimensional counterparts, so the lowest limit of stability is reached with respect to the first and not to these latter.

II.2.2.2 Bi-local approach to the NS equations.

As suggested before, the baseflow could be non homogeneous in the spanwise direction. In this case the modal solution can be accomplished only in the streamwise direction. An example of baseflow that is homogeneous only in the x-direction is shown in figure II.3.

Tatsumi and Yoshimura (1990) proposed an extended version of the Orr-Sommerfeld equation for a base flow $U(y,z)$ where U is the streamwise component of the base flow. However in this 2-D formulation of the Orr-Sommerfeld equation the wall-normal velocity component $V(y,z)$ and the spanwise velocity component $W(y,z)$ of the base flow are equal to zero. This hypothesis is not always true and especially in the case depicted in fig. II.3 the $V(y,z)$ and $W(y,z)$ velocity component have an important role in the lift-up mechanism so they cannot be neglected. For the sake of generality the primitive variables are considered with no reduction in the order of the NS equations. Performing the following decomposition:

$$\{u,v,w,p\}(x,y,z,t) = \{\hat{u},\hat{v},\hat{w},\hat{p}\}(y,z)e^{i(\alpha x-\omega t)} \tag{II.26}$$

and substituting the modal ansatz (eq. II.26) into the linearised NS equations (II.20) we obtain the following stability problem for each generic section in the streamwise direction:

$$i\alpha\hat{u} + \frac{\partial\hat{v}}{\partial\hat{y}} + \frac{\partial\hat{w}}{\partial\hat{z}} =0 \tag{II.27a}$$

$$-U_b\alpha\hat{u} + \xi\hat{u} + i\hat{v}\frac{\partial U_b}{\partial y} + i\hat{w}\frac{\partial U_b}{\partial z} - \alpha\hat{p} + \alpha^2\frac{i}{Re}\hat{u} = -\,\omega\hat{u} \tag{II.27b}$$

$$-U_b\alpha\hat{v} + \xi\hat{v} + i\hat{v}\frac{\partial V_b}{\partial y} + i\hat{w}\frac{\partial V_b}{\partial z} - \frac{\partial\hat{p}}{\partial y} + \alpha^2\frac{i}{Re}\hat{v} = -\,\omega\hat{v} \tag{II.27c}$$

$$-U_b\alpha\hat{w} + \xi\hat{w} + i\hat{v}\frac{\partial W_b}{\partial y} + i\hat{w}\frac{\partial W_b}{\partial z} - \frac{\partial\hat{p}}{\partial z} + \alpha^2\frac{i}{Re}\hat{w} = -\,\omega\hat{w} \tag{II.27d}$$

where:

$$\xi = \left[iV_b\frac{\partial}{\partial y} + iW_b\frac{\partial}{\partial z} - \frac{i}{Re}\left(\frac{\partial^2}{\partial y^2} + \frac{\partial^2}{\partial z^2}\right)\right]$$

The stability problem is completed by the boundary conditions. If Ny is the number of points that discretize the y-direction, the Orr- Sommerfeld Squire operator in a temporal approach turn out to have a dimension equal to $(Ny \times 2)^2$. In the case of a bi-local analysis, if Nz is the dimension of the vector that discretize the z-direction, the linearised NS operator will have a dimension equal to $(Ny \times Nz \times 4)^2$. It is clear how decreasing the number of the homogeneous directions, the computational cost increases.

II.2.2.3 Global approach to the NS equations

In the global stability framework no spatial assumptions are made, the base flow is three-dimensional and defined in a finite domain. Whereas, in the local approach the homogeneous directions are infinitely extended. On the contrary in the global approach the x, y and z-direction are delimited by the chosen numerical domain. For this reason an initial perturbation on the base flow could grow up and exit the domain if there are not self sustained mechanisms that regenerate the instabilities. For this reason, convective modes appear to be stable in a global eigenspectrum. This is the first main difference between global and local analysis. There is another difference that comes from the latter. In the local analysis we can distinguish between temporal analysis (i.e. we fix a real α and/or

β and we seek for the most unsteady complex temporal wave ω) and spatial analysis (i.e. we fix the real ω and one of the two real spatial wave lengths α or β and we seek for the most complex unsteady β or α). On the contrary, the global analysis is a spatio-temporal analysis because we ask for the most unsteady ω, and linked to this eigenmode there is an eigenvector that contains all the spatial information. The eigenvector could also take into account differents mechanisms involved in the growth of the instability. Referring always to the example of the MVG in fig. II.3, if slightly far to the MVG the parallel hypothesis is almost acceptable, close to the cylinder this is not, since the presence of the recirculation bubble makes the base flow highly non-parallel. A modal streamwise decomposition in this zone is unacceptable. A bi-local analysis could be done anyway imposing a complex ω (i.e. spatial analysis) or a complex α (i.e. temporal analysis) in order to fix the causality of the events and establishing if there exists or not an absolute instability (Huerre et al., 2000). For the sake of clarity we will not explain more on the absolute instability and we will focus on the global approach. We impose a modal solution in time:

$$\{u, v, w, p\}(x, y, z, t) = \{\hat{u}, \hat{v}, \hat{w}, \hat{p}\}(x, y, z)e^{\lambda t} \tag{II.28}$$

Imposing the decomposition II.28 into the linearised NS equation II.20, we obtain:

$$\begin{cases} \nabla \cdot \hat{\mathbf{u}} = 0 \\ \lambda \hat{\mathbf{u}} = (\hat{\mathbf{u}} \cdot \nabla)\mathbf{U}_b + (\mathbf{U}_b \cdot \nabla)\hat{\mathbf{u}} + \nabla \hat{p} - \dfrac{1}{Re}\Delta \hat{\mathbf{u}} \end{cases} \tag{II.29}$$

Introducing the Jacobian matrix $\mathbf{J}$, the mass matrix $\mathbf{B}$ and the state vector $\hat{\mathbf{q}} = (\hat{\mathbf{u}}, \hat{p})^T$, one can recast system (II.29) into the following linear system form

$$\lambda \mathbf{B}\hat{\mathbf{q}} = \mathbf{J}\hat{\mathbf{q}} \tag{II.30}$$

where $\lambda = \sigma + i\omega$ is the eigenvalue and $\hat{\mathbf{q}}$ is the eigenvector associated to the eigenproblem II.30. The sign of the real part of the leading eigenvalue σ then determines whether the fixed point $\mathbf{Q}_b$ is linearly stable or unstable, whereas its imaginary part ω characterises the stationary or oscillatory nature of the associated eigenvector. Moreover, the imaginary part of the first eigenvalue to step within the upper-half $\sigma - \omega$ plane also determines whether the fixed point experiences a pitchfork ($\omega = 0$) or a Hopf bifurcation ($\omega \neq 0$).

The dimension of the linear operator acting on $(\hat{\mathbf{u}}, \hat{p})^T$ is $(Nx \times Ny \times Nz \times 4)^2$, where Nx, Ny and Nz are the dimension of the vector that discretizes the numerical domain in the streamwise, wall-normal and spanwise direction respectively. Today is **impossible** to perform a global stability analysis because the memory required to stock such operator is inaccessible. Table II.1 provides some estimates of the memory requirements if one would typically need to explicitly construct the generalised eigenvalue problem (II.30) depending on the spatial dimension of the initial problem under investigation.

Though the actual memory footprint highly depends on the size of the problem and the choice of dicretization used, these rough estimates clearly highlight how costly and impractical it would be for one to explicitly construct these matrices in the fully three-dimensional global stability framework. To overcome this problem time-stepping algorithms are used to have a great approximation of the Jacobian operator with a dimension affordable for all computers.

Base Flow	Inhom. direction(s)	Size of $u(t)$	Storage of $\mathbf{J}$
$\mathbf{U}_b(y)$	1D	10^2	~ 1 Mb
$\mathbf{U}_b(x, y)$	2D	10^5	~ 4.3 Gb
$\mathbf{U}_b(x, y, z)$	3D	10^7	~ 17.6 Tb

Table II.1: Estimation of the memory footprint required for explicit construction of the matrices involved in generalised eigenvalue problems. Data from (Theofilis, 2003) for a boundary layer problem.

II.3 Non-normal operator

For many years because of the Squire's theorem only 2-D flows was studied since the lower critical Reynolds number was provided by a $\beta = 0$ perturbation. But it was unclear why for a Poiseuille flow transition was observed for Reynolds number lower than the critical one. If the linear stability analysis predicts unstable behaviour at $Re_c = 5772$ (Orszag, 1971), transition to turbulence was observed already at $Re \approx 1000$ (Patel and Head, 1969). Couette flow is unconditionally stable (Romanov, 1973) according to linear stability but transition was observed already at $Re \approx 350$ (Lundbladh and Johansson, 1991). The explanation was given only in the early 90's (Reddy et al., 1993) through the use of the pseudospectrum to analyse non-normal operators. An operator $\mathbf{A} \in \mathbb{C}$ is said to be normal if its eigenvectors are orthogonal between each other (Kato, 2013). If it is so the eigenvectors of the operator $\mathbf{A}$ are sufficient to explain the whole dynamics. In other case, the non orthogonality of the eigenvectors could cause a transient amplification of the initial disturbance even if all the eigenvalues are in the stable part of the eigenspectra. This is not the only effect of a non-normal operator. Also the receptivity of the system changes. In many cases a simple study of the eigenspectra may be not sufficient.

II.3.1 Short time dynamics

The geometrical explanation of the transient behaviour is given in figure II.4. In both cases the axes represent the eigenvectors that are independently damped in time. The thick line represents the initial condition that is a combination of the two eigenvectors. In the normal case if both eigenvectors decay, the length of the initial condition decreases monotonically. This is not true in the non-normal case. This is the reason why it is possible to get a transient growth of the energy even for Reynolds numbers lower than the critical one (Reddy and Henningson, 1993). If in the linear framework for $t \to \infty$ the energy of the initial disturbance must go to zero when the system is stable, this could not be the case in the non-linear framework. The initial linear transient growth can trigger non-linear mechanisms that evolve towards transition. The aim of the optimal perturbation analysis is to find the initial condition that maximises this growth at a fixed *target time*. Also the optimal perturbation analysis can be carried out in local or global ansatz but for the purpose of this thesis only the global optimal perturbation will be presented. Let consider the $\mathbf{A}$ operator that is the Jacobian operator in a divergence-free space then

$$\frac{\partial \mathbf{u}}{\partial t} = \mathbf{A}\mathbf{u} \tag{II.31}$$

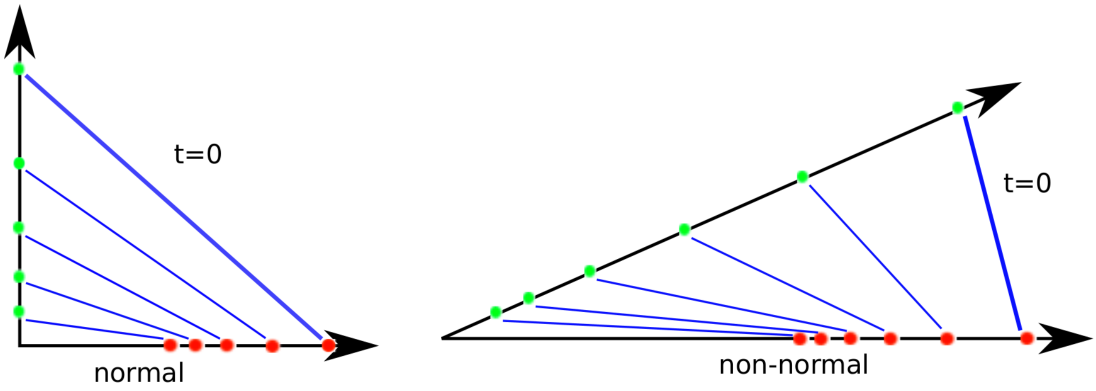

Figure II.4: Geometrical interpretation of the transient growth. Example from (Schmid and Brandt, 2014).

is the linearized NS equation. The velocity field at the target time will be given by:

$$\mathbf{u}_T = \mathbf{M}\mathbf{u}_0 \tag{II.32}$$

$\mathbf{u}_0$ being the initial condition at t_0, $\mathbf{u}_T$ the solution at the target time $t = T$ and $\mathbf{M}$ the propagation matrix $e^{\mathbf{A}T}$. We are interested to find the perturbation $\mathbf{u}_0$ that maximize the ratio

$$\mathit{\Lambda} = \frac{E_T}{E_0} \tag{II.33}$$

where E_T is the final perturbation energy at the target time T defined as the inner product $\langle \mathbf{u}_T, \mathbf{u}_T \rangle$ and $\mathit{\Lambda}$ is the energy gain. The ratio (II.33) can be recast in:

$$\mathit{\Lambda} = \frac{E_T}{E_0} = \frac{\langle \mathbf{u}_T, \mathbf{u}_T \rangle}{\langle \mathbf{u}_0, \mathbf{u}_0 \rangle} = \frac{\langle \mathbf{M}\mathbf{u}_0, \mathbf{u}_0 \rangle}{\langle \mathbf{u_0}, \mathbf{u_0} \rangle} = \frac{\langle \mathbf{u_0}, \mathbf{M}^{+}\mathbf{M}\mathbf{u_0} \rangle}{\langle \mathbf{u}_0, \mathbf{u}_0 \rangle} \tag{II.34}$$

where $\mathbf{M}^{+}$ is the adjoint operator of $\mathbf{M}$ and it is equal to its conjugate transposed[2]. The optimal perturbation problem II.34 turns out to be an eigenvalue problem

$$(\mathbf{M}^{+}\mathbf{M} - \Lambda)\mathbf{u}_0 = 0 \tag{II.35}$$

The matrix $\mathbf{M}^{+}\mathbf{M}$ is defined positive and the optimal perturbation $\mathbf{u}_0$ turn out to be the eigenvector associated to the greatest eigenvalue Λ. Using the eq. (II.32) it is possible to recover the velocity field $\mathbf{u}_T$ at the target time.

II.3.2 Response to harmonic forcing

The dynamics of harmonically forced problem does not depend only on the homogeneous solution of the problem (II.31). How and how much the eigenvalues interact between each other when the system is forced depends on the non-normalities of the considered system. Let consider the system (II.31) with harmonic forcing

$$\frac{\partial \mathbf{u}}{\partial t} = \mathbf{A}\mathbf{u} + \Re(\hat{\mathbf{f}} exp(i\omega t)) \quad \text{with} \quad \hat{\mathbf{f}}(\mathbf{x}) \in \mathbb{C} \text{ and } \omega \in \mathbb{R}. \tag{II.36}$$

---

[2] The continuous adjoint NS equation can also be defined by means of the integration by parts as shown by Luchini and Bottaro (2014). The adjoint NS equation for the non-linear optimal perturbation are reported in appendix VIII.2.

If the eigenspectrum of $\mathbf{A}$ shows only stable modes, this means that the homogeneous solution of the system (II.36) goes to zero and only the particular solution exists. For this reason the solution of the velocity field will be on the form

$$\mathbf{u} = \hat{\mathbf{u}} exp(i\omega t). \tag{II.37}$$

Substituting the solution (II.37) in (II.36), the system that links the harmonic forcing to the harmonic response at fixed ω is

$$\hat{\mathbf{u}} = (i\omega\mathbf{I} - \mathbf{A})^{-1}\hat{\mathbf{f}} \tag{II.38}$$

the operator $\mathbf{R} = (i\omega\mathbf{I} - \mathbf{A})^{-1}$ is known as resolvent matrix. Following the mathematical steps like in the optimal perturbation procedure, it is possible to find the shape of the forcing that maximises the dimensional ratio $\Lambda = \|\hat{\mathbf{u}}\|/\|\hat{\mathbf{f}}\|$ solving the following eigenvalue problem

$$(\mathbf{R}^{+}\mathbf{R} - \Lambda)\hat{\mathbf{f}} = 0 \tag{II.39}$$

The optimal forcing procedure helps us to characterize the *receptivity* of the system to an external forcing looking at the curve $\Lambda(\omega)$. Note that the harmonic forcing does not change the spectrum of the operator $\mathbf{A}$. Therefore, the eigenvectors form a complete basis and it is possible to project the particular solution onto this basis. Invoking the adjoint eigenfunction and taking advantage of the bi-orthogonality[3] condition, for a globally stable case we get

$$\mathbf{u} = \sum_{j=1}^{N} \left\langle \hat{\mathbf{u}}_j^{+}, \frac{\hat{\mathbf{f}}}{i\omega_f - \lambda_j} \right\rangle \frac{\hat{\mathbf{u}}_j}{\langle \hat{\mathbf{u}}_j^{+}, \hat{\mathbf{u}}_j \rangle} exp(i\omega_f t) \tag{II.43}$$

where $\hat{\mathbf{u}}^{+}$ is the adjoint eigenmode, $\hat{\mathbf{u}}$ the direct one, λ is the eigenvalue and ω_f is the pulsation of the forcing. From eq. (II.43) some important considerations can be extracted. If the operator $\mathbf{A}$ is normal, using any adjoint eigenmode $\hat{\mathbf{u}}_i^{+}$ as forcing, only the associated direct mode will constitute the response due to the non-null first inner product. This is not true for a non-normal operator.

II.3.3 Pseudospectrum

Another way to quantify the non-normalities in the $\mathbf{A}$ operator is the evaluation of the pseudospectrum (TREFETHEN et al., 1993). It is clear that the information provided by the eigenmodes are not sufficient and to complete this information one could refer to

---

[3] Consider the eigenvalue problem for the direct and the adjoint system

$$\lambda\hat{\mathbf{u}} - \mathbf{A}\hat{\mathbf{u}} = 0 \tag{II.40}$$

$$\lambda^{+}\hat{\mathbf{u}}^{+} - \mathbf{A}^{+}\hat{\mathbf{u}}^{+} = 0 \tag{II.41}$$

where $\hat{\mathbf{u}}^{+}$ and $\hat{\mathbf{u}}$ are the eigenvectors and λ and λ^{+} are the eigenvalue. The bi-orthogonality condition refers to the propriety between the direct $\{\lambda_i, \hat{\mathbf{u}}\}$ and adjoint $\{\lambda_i^{+}, \hat{\mathbf{u}}^{+}\}$ eigenpair for which it is true:

$$(\lambda_i - \lambda_j^{+*})\langle \hat{\mathbf{u}}_j^{+}, \hat{\mathbf{u}}_i \rangle = 0 \tag{II.42}$$

This means that the inner product $\langle \hat{\mathbf{u}}_j^{+}, \hat{\mathbf{u}}_i \rangle$ is zero for every pair of eigenfunctions except when $i = j$, as long as $\lambda_j^{+} = \lambda_j^{*}$ (Salwen and Grosch, 1981).

the resolvent matrix $(z\mathbf{I} - \mathbf{A})^{-1}$ where $z \in \mathbb{C}$. In other words it is not only important to know for which z the resolvent matrix norm is singular but it is interesting to know for which z the resolvent norm is large. For each $\epsilon > 0$ it is possible to define a new subset of the complex plane, namely the ϵ-pseudospectrum of $\mathbf{A}$, as follows:

$$\Lambda_\epsilon(\mathbf{A}) = \{z \in \mathbb{C} : \|(z\mathbf{I} - \mathbf{A})^{-1}\| \geq \epsilon^{-1}\}. \tag{II.44}$$

$\Lambda_0(\mathbf{A})$ denotes the eigenvalue points where $\|(z\mathbf{I} - \mathbf{A})^{-1}\| = \infty$ (*resonance* condition). $\Lambda_\epsilon(\mathbf{A})$ denotes the complex plane where $\|(z\mathbf{I} - \mathbf{A})^{-1}\| \geq \epsilon^{-1}$ and ϵ^{-1} is a measure of the amplitude response of the system when it is "perturbed".

Chapter III

Numerical methods for instability analysis

Contents

III.1 Nek5000

The linear stability analysis refers to the capacity or not of an initial disturbance to extract energy from the base flow. The base flow is a steady solution of the Navier-Stokes equation. Hence, the first step is to find the steady (laminar) solution for which $\partial \mathbf{U}/\partial t = 0$. For some flow set-ups on the analytical solution exists (e.g. Poiseuille, Couette) or it can be approximated (e.g. Blasius) but in most cases the use of computational fluid dynamics (CFD) is mandatory. In this Ph.D work the Nek5000 (Fischer et al., 2008) spectral element code has been used to solve numerically the linear, non-linear and adjoint Navier Stokes equations.

III.1.1 Spatial discretisation: spectral elements

Concerning the spatial discretization, Nek5000 is based on the spectral element methods (SEM). This method was first introduced by Patera (1984) and it combines finite elements and spectral methods. The combination of these two methods allows to have high geometrical flexibility and high-order resolution. For this reason this method is widely used to study stability and transition. Finite element methods are based on the Galerkin approximation for this reason the NS equations are solved in the weak formulation. Introducing a set of test functions the variational formulation of the NS equations reads:

Find $(\mathbf{u}, p) \in H_b^1(\Omega)^d \times L_0^2(\Omega)$ *such that*

$$\frac{\partial}{\partial t}\langle \mathbf{w}, \mathbf{u}\rangle + \langle \mathbf{w}, \mathbf{u}\cdot\nabla\mathbf{u}\rangle = \langle \nabla\cdot\mathbf{w}, p\rangle - \frac{1}{Re}\langle \nabla\mathbf{w}, \nabla\mathbf{u}\rangle + \langle \mathbf{w}, \mathbf{f}\rangle \quad \forall \mathbf{w} \in H_0^1(\Omega)^d \tag{III.1a}$$

$$-\langle q, \nabla\cdot\mathbf{u}\rangle = 0 \quad \forall q \in L_0^2(\Omega) \tag{III.1b}$$

where $L_0^2(\omega)$ is a space of functions that are L^2-integrable on the domain Ω with zero average value, and $H_b^1(\Omega)^d$ and $H_0^1(\Omega)^d$ are Sobolev spaces of vector functions having d components and satisfying inhomogeneous and homogeneous boundary conditions. The determination of the particular numerical approximation depends on the choice of the test function. In the Nek5000, these functions have been chosen to be based on the Legendre polynomials. The Legendre polynomials provide the best approximation in the H^1 norm (see (Deville et al., 2002) and (Karniadakis and Sherwin, 2013)).

The domain Ω is discretized and divided into E quadrilateral elements. Each element is defined as $\Omega^e := \{\mathbf{x}\ ;\ \mathbf{x}_{e-1} < \mathbf{x} < \mathbf{x}_e\}$, $1 \le e \le E$, and let $\hat{\Omega} := \{\xi\ ;\ -1 \le \xi \le 1\}$ be the reference (or parent) element onto which each element Ω^e will be mapped using an affine transformation. Assuming a three-dimensional flow case ($d = 3$), the discrete velocity in element Ω^e mapped onto the three-dimensional reference element $\hat{\Omega}^3$ can be written as

$$\mathbf{u}(\mathbf{x}(\xi,\zeta,\eta))|_{\omega^e} = \sum_{i=0}^{N}\sum_{j=0}^{N}\sum_{k=0}^{N} \mathbf{u}_{i,j,k}^e h_{N,i}(\xi) h_{N,j}(\zeta) h_{N,k}(\eta) \quad (\xi,\zeta,\eta) \in \hat{\Omega} \tag{III.2}$$

where $h_{N,i}$, $h_{N,j}$ and $h_{N,k}$ are one-dimensional Nth-order Lagrange interpolants based on the Legendre polynomials, $\mathbf{x}$ is a mapping function of the local geometry and $\mathbf{u}_{i,j,k}^e$ are the unknown nodal values in Ω^e (Deville et al., 2002). Two different quadrature rules are used for the velocity field and pressure field to avoid spurious pressure modes. The $\mathbb{P}_N - \mathbb{P}_{N-2}$ formulation refers to a staggered SEM where the velocity is represented on $N+1$ Gauss-Lobatto-Legendre (GLL) quadrature points and the pressure on the $N-1$ Gaus-Legendre (GL). Taking advantage of the GLL- and GL- quadrature rules the discretized Navier-Stokes equations turn out to be:

$$\begin{cases} \mathbf{M}\dfrac{d}{dt}\mathbf{u} = -\mathbf{C}(\mathbf{u})\mathbf{u} - \dfrac{1}{Re}\mathbf{K}\mathbf{u} + \mathbf{D}^T p + \mathbf{M}\mathbf{f} \\ -\mathbf{D}\mathbf{u} = 0 \end{cases} \tag{III.3}$$

In III.3 **M** is the mass matrix containing the integration weights, **K** is the stiffness matrix and represent the discrete Laplacian, **D** and $\mathbf{D^T}$ are the divergence and gradient operators and $\mathbf{C}(\mathbf{u})\mathbf{u}$ is the advection operator evaluated using the convective form. Furthermore, **D** and $\mathbf{D^T}$ are transposed matrices, as they are adjoint operators in the continuous formulation, a property that is preserved in the discrete level. Figure III.1 displays the structure

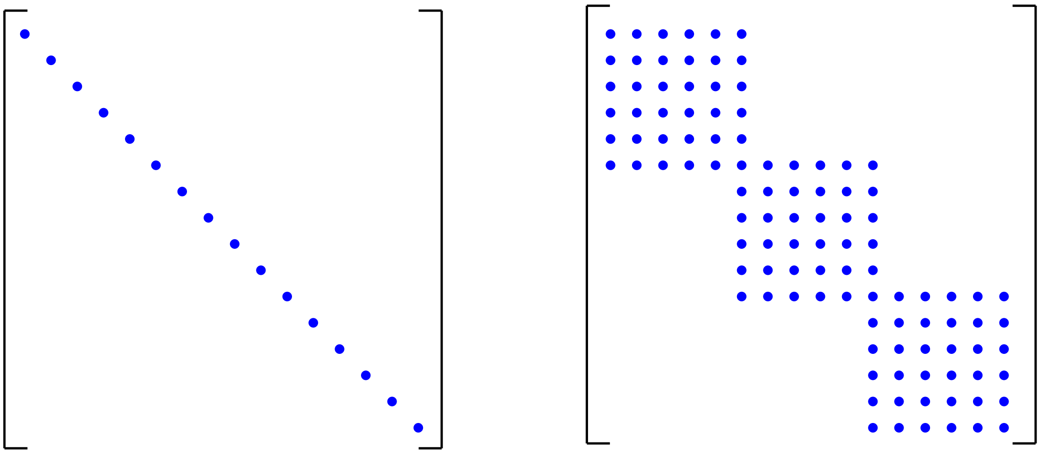

(a) Global mass matrix **M**

(b) Global stiffness matrix **K**

Figure III.1: Structure of the global mass and stiffness matrices for $E = 3$ and $N = 5$.

of the global stiffness **K** and mass **M** matrices resulting from the direct stiffness summation. As one can see, the mass matrix **M** exhibits a diagonal structure (it usually is tri- or penta-diagonal in the FEM), whereas the stiffness matrix **K** exhibits a block-diagonal structure, another major difference with the finite element method where the matrices are sparse. The stiffness matrix is moreover symmetric and positive-definite.

Once the pressure field has been evaluated onto GL- collocation points, its gradient need to be interpolated in the GLL- collocation points in eq III.3. For further details see Deville et al. (2002).

Meshing process

The mesh generation for the discretization of the numerical domain is divided in two step. The first one is the definition of the elements grid. The numerical domain is discretized by three dimensional quadrilaterals. The only constrain is that there must not be overlapping between the elements, on the other hand this discretization benefits from all advantage of the FEM discretization (i.e. high geometrical flexibility). The seconds step is the spectral discretization within each elements by the chosen polynomial order. The first step is done by commercial grid generators, on the contrary the second one is automatically achieved by the Nek5000 taking also into account the elements deformation (Deville et al., 2002). In order to refine the mesh, two different types of refinements can be used:

- One can add more spectral elements to the spectral elements distribution, a refinement known as h-type.
- Or keeping the spectral elements distribution unchanged and increases the polynamial order within each of the spectral element. This is known as p-type refinement.

The choice of the balance between the number of elements and the polynomial order is not trivial. A high number of elements with a low polynomial order turns out in a low spatial order resolution losing the power of the SEM. Contrariwise, few elements with a high polynomial order could be dangerous because if some spurious oscillation is generated between the elements or close to the boundary condition, these are not dissipated due to the high spatial order discretization and the non dissipative scheme. In this case a further stabilizing filter is necessary (Deville et al., 2002). As a general guideline we try to get an element grid that provides results in agreement with experiments with a spectral order equal to 8. Subsequently we increase the spectral order to reach convergence in the results.

III.1.1.1 Boundary conditions

The spatial discretization should take into account the boundary condition to complete the PDEs system (II.1) and (II.20). The variational formulation of the Navier-Stokes equations (III.1) is completed by the surface integrals on the edge of the numerical domain. The only terms affected in this integral are the pressure and the diffusive terms

$$\oint_{\mathrm{T}} (\mathbf{w} \cdot \mathbf{n}) p dS + \frac{1}{Re} \oint_{\mathrm{T}} \mathbf{w} \cdot \frac{\partial \mathbf{u}}{\partial \mathbf{n}} dS = \oint_{\mathrm{T}} \mathbf{w} \cdot \mathbf{n} \cdot \left(\frac{1}{Re} \nabla \mathbf{u} - p \mathbf{I} \right) dS, \tag{III.4}$$

with $\mathrm{T} = \partial \Omega$. The Dirichlet boundary conditions is imposed by the choice of the test function. In other cases we need to annihilate $\mathbf{n} \cdot (Re^{-1} \nabla \mathbf{u} - p\mathbf{I}) = 0$.

Fringe method

For both linearized and adjoint Navier-Stokes equation the boundary condition are reported in the table III.1. Unfortunately the outflow condition for the adjoint system is not allowed in the Nek5000 and its implementation is not straightforward. To overcome this problem two choices are possible. The first one is the *far field* ansatz. The second one is to force the solution to go towards the Dirichlet boundary condition $\mathbf{u}^+ = 0$. In the first case the inflow boundary condition is simply substituted by $\mathbf{u}^+ = 0$ supposing that the perturbation goes naturally towards zero. This solution could be true in the case of a roughness installed at the wall. The adjoint system represents the sensitivity of the base flow and then it is indirectly linked to the gradients of the base flow itself. For the 2D cylinder the sensitivity region is located behind it and on both sides of the cylinder (Giannetti and Luchini, 2007) and this allows the far field hypothesis if the numerical domain is large enough. If the adjoint perturbation does not go naturally to zero the far field hypothesis is not permitted. For this reason, a sponge zone is adopted at the beginning and in the ending of the domain for the linear numerical simulations to avoid any

Table III.1: Boundary conditions for the adjoint and direct solver

	Direct	Adjoint
Inflow	$\mathbf{u} = 0$	$P^+\mathbf{n} + Re^{-1}(\nabla \mathbf{U}^+) \cdot \mathbf{n} = -(\mathbf{U} \cdot \mathbf{n})\mathbf{U}^+ + (\mathbf{U} \cdot \mathbf{n})\mathbf{u}^+$
Outflow	$p\mathbf{n} - Re^{-1}(\nabla \mathbf{u}) \cdot \mathbf{n} = 0$	$\mathbf{u}^+ = 0$
Wall	$\mathbf{u} = 0$	$\mathbf{u}^+ = 0$

influence of the boundary condition on the solution. The *damping method* was introduced as solution to all CFD codes that implement periodic inflow-outflow boundary condition for a non-periodic flow. The main idea is to add a volumetric forcing term on the right end side of (II.20) that forces the solution to go towards a target solution that in our case is $\mathbf{u}^+ = 0$. The general form of the fringe forcing is given by:

$$G_i = \lambda(x)(\mathcal{U}_i - u_i) \tag{III.5}$$

where $\lambda(x)$ represents the shape of the forcing and it is non-null only close to a boundary where the condition $\mathbf{u}^+ = 0$ has to be ensured. In (III.5) $\mathcal{U}_i$ is the target solution and u_i is the instantaneous velocity component. The form of the fringe λ introduced in (Lundbladh et al., 1999) is:

$$\lambda(x) = \lambda_{max}\left[S\left(\frac{x - x_{start}}{\Delta_{rise}}\right) - S\left(\frac{x - x_{end}}{\Delta_{fall}} + 1\right)\right]$$

x_{start} and x_{end} being the position in which the forcing term is active. λ_{max} identifying the maximum strength of the forcing and its shape being driven by the function $S(x)$ and the parameters Δ_{rise} and Δ_{fall}. $S(x)$ is a C^∞ smooth step function:

$$S(x) = \begin{cases} 0 & x \leq 0, \\ 1/[1 + \exp(\frac{1}{x-1}) + \frac{1}{x}] & 0 < x < 1, \\ 1 & x \geq 0 \end{cases} \tag{III.6}$$

The function $\lambda(x)$ for the cylinder case studied in this thesis is reported in figure III.2.

The application of the fringe method imposes an additional restriction on the maximum possible time step of the integration scheme (Schlatter et al., 2005).

III.1.2 Time discretisation

The presence of $\mathbf{C}(\mathbf{u})\mathbf{u}$ term makes the NS equations (III.3) non-linear and non-symmetric. If the non-linear term was not, it would have been possible to solve eq. (III.3) by using stable implicit methods. The advection operator can be treated in three different ways. In the Nek5000 the advection operator is evaluated using convective form. In order to avoid the algorithmic difficulties resulting from an implicit treatment of the non-symmetric non-linear terms $\mathbf{C}(\mathbf{u})\mathbf{u}$, the remaining possibility is to treat them explicitly. The temporal discretization scheme used in Nek5000 is the semi-implicit scheme BDF_k/EXT_k: the viscous terms are discretized implicitly using a backward differentiation scheme of order k whereas the non-linear terms are treated explicitly by an extrapolation of order k, with $k = 1, 2$ or 3. For $k = 3$, the fully discretized Navier-Stokes problem then reads:

$$\left(\frac{11}{6\Delta t}\mathbf{M} + Re^{-1}\mathbf{K}\right)\underline{u}_i^{n+1} - \mathbf{D}_i^T\underline{p}^{n+1} = \frac{\mathbf{M}}{\Delta t}\left(3\underline{u}_i^n - \frac{3}{2}\underline{u}_i^{n-1} + \frac{1}{3}\underline{u}_i^{n-2}\right) - \left(3\mathbf{C}\underline{u}_i^n - 3\mathbf{C}\underline{u}_i^{n-1} + \mathbf{C}\underline{u}_i^{n-2}\right) + \mathbf{M}\mathbf{f}^n \tag{III.7}$$

$$-\mathbf{D}^T\mathbf{u}^{n+1} = 0 \tag{III.8}$$

This numerical scheme produce a residual $\mathbf{r}^{n+1}$ that depends on $\underline{p}^{n+1}$. To avoid non-vanishing error for steady-state solution it is necessary to add $\mathbf{D}_i^T\underline{p}^n$ to both sides. In

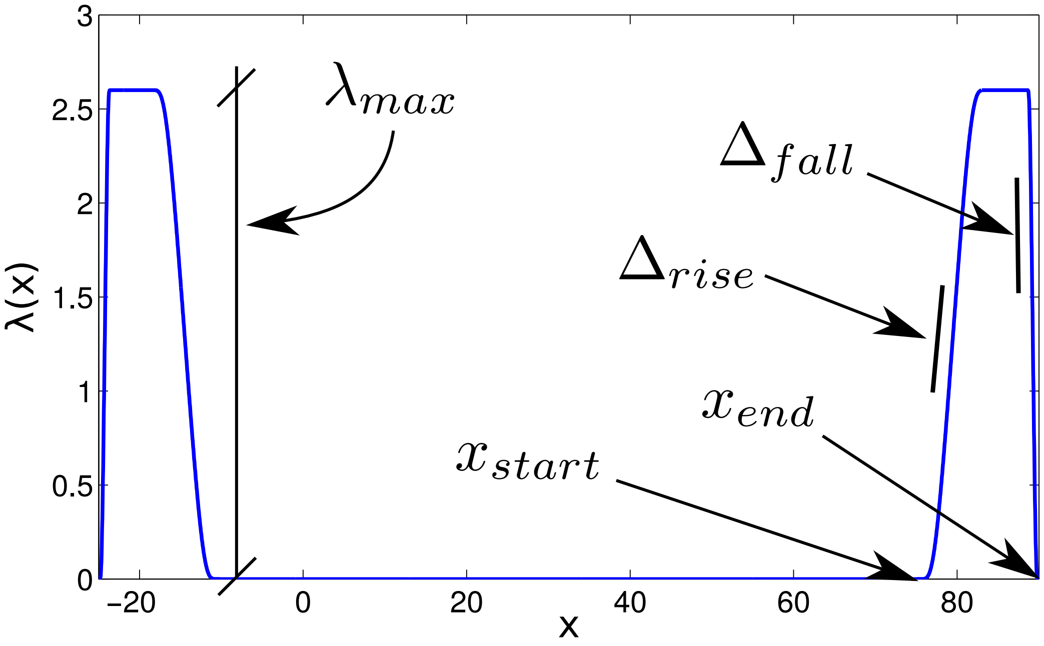

Figure III.2: $\lambda(x)$ function applied to the cylinder case in the linear simulation. $x_{start} = [-25, 75]$, $x_{end} = [-10, 90]$, $\Delta_{rise} = 60\%$ of $x_{end} - x_{start}$ and $\Delta_{fall} = 10\%$. λ_{max} is keep constant for all numerical simulations and it is equal to 2.6.

this way the error will be function of $\underline{\delta p}^{n+1} = \underline{p}^{n+1} - \underline{p}^{n}$ and it goes to zero for a steady solution (Deville et al., 2002). Reshuffling the terms on the right-hand side as a simple forcing vector $\mathbf{M}\underline{\mathbf{F}}_i^n$, and collecting the left-hand side in one operator, the system of equations (III.7 III.8) can be recast into the following matrix form of the unsteady forced Stokes problem:

$$\begin{pmatrix} \mathbf{H} & -\mathbf{D}^T \\ -\mathbf{D} & 0 \end{pmatrix} \begin{pmatrix} \underline{\mathbf{u}}^{n+1} \\ \underline{\delta p}^{n+1} \end{pmatrix} = \begin{pmatrix} \mathbf{M}\underline{\mathbf{F}}^n + \mathbf{D}^T \underline{p}^n \\ 0 \end{pmatrix} \tag{III.9}$$

where $\mathbf{H}$ is known as the Helmholtz operator. This matrix problem can be solved using a LU decomposition. Taking advantage of an arbitrary $\mathbf{Q}$ matrix for the sake of projection purpose, the solution to such LU decomposition is a two-step procedure:

$$\begin{pmatrix} \mathbf{H} & 0 \\ -\mathbf{D} & -\mathbf{D}\mathbf{Q}\mathbf{D}^T \end{pmatrix} \begin{pmatrix} \underline{\mathbf{u}}^{*} \\ \underline{\delta p}^{n+1} \end{pmatrix} = \begin{pmatrix} \mathbf{M}\underline{\mathbf{F}}_i^n + \mathbf{D}^T \underline{p}^n \\ 0 \end{pmatrix} \tag{III.10}$$

and

$$\begin{pmatrix} \mathbf{I} & -\mathbf{Q}\mathbf{D}^T \\ 0 & \mathbf{I} \end{pmatrix} \begin{pmatrix} \underline{\mathbf{u}}^{n+1} \\ \underline{\delta p}^{n+1} \end{pmatrix} = \begin{pmatrix} \underline{\mathbf{u}}^{*} \\ \underline{\delta p}^{n+1} \end{pmatrix} \tag{III.11}$$

in the first step the velocity field $\underline{\mathbf{u}}^{*}$ unprojected in the divergence-free space is evaluated and in the second step the divergence correction is applied to obtain the $\underline{\mathbf{u}}^{n+1}$ velocity field. The choice of the matrix $\mathbf{Q}$ determines which projection method is used. If the matrix $\mathbf{Q}$ is set to be:

$$\mathbf{Q} = \mathbf{H}^{-1} \tag{III.12}$$

no decupling error is introduced, resulting in the Uzawa algorithm. Unfortunately evaluations of the inverse of the Helmholtz operator might be computationally costly and not well preconditioned due to the presence of the laplacian operator. In order to overcome this problem, instead of the Uzawa algorithm, the Blair-Perot algorithm is implemented within Nek5000. The projection matrix then is $\mathbf{Q} = \gamma \mathbf{M}^{-1}/\Delta t$ (with $\gamma = 11\Delta t/6$ for the BDF3/EXT3 scheme). Since the mass matrix $\mathbf{M}$ is diagonal, the computation of its inverse is a straightforward task. Using the Blair-Perot algorithm a non-zero splitting error is introduced and it is proportional to $\delta \underline{p}^{n+1}$. This need to be taken into account for the choice of the time step Δt of the time marching.

III.2 Steady solution of Navier-Stokes equation.

The steady state computation is not a straightforward task for a 3D computation due to the large degrees of freedom of the problem. A general procedure is to use the Newton algorithm. Unfortunately this technique can not be used in the way it is because the inverse of the Jacobian matrix is required. Many variants exist such as the use of a properly preconditioned Krylov-subspace to project the Jacobian in a smaller subspace where the inversion can be done with a reasonable computational cost (Edwards et al., 1994). The preconditioning is done by increasing the Δt in the time step to increase the weight of the diffusive operator in the semi-implicit scheme. Such method can not be used in Nek5000 due to the splitting error introduced by the Blair-Perot algorithm. Another recent proposed solution is to use the adjoint equations whose trajectories converge asymptotically to the equilibrium solution (Farazmand, 2016). The convergence of this method is slow and a coupling with a Newton method is mandatory. Today two possibilities exist to search fix points: the selective frequency damping (Åkervik et al., 2006) and the more recent BoostConv algorithm (Citro et al., 2017).

III.2.0.1 Selective frequency damping

The main idea of the method introduced by Åkervik et al. (2006) is to add a low-pass time filter that consists in an ad hoc dissipative term proportional to the high-frequency velocity fluctuations. This procedure is common in the control theory and consists in an additional volumetric forcing term on the right-hand side of the Navier-Stokes equation (II.1). The forcing term has to drive the instantaneous solution $\mathbf{U}$ towards a filtered target solution $\bar{\mathbf{U}}$. A supplementary equation is then necessary for the target solution. The extended Navier-Stokes system is then composed by the following set of equations:

$$\begin{cases} \dot{\mathbf{U}} + (\mathbf{U}\cdot\nabla)\mathbf{U} = -\nabla P + \dfrac{1}{Re}\Delta\mathbf{U} - \chi(\mathbf{U}-\bar{\mathbf{U}}) \\ \dot{\bar{\mathbf{U}}} = \omega_c(\mathbf{U}-\bar{\mathbf{U}}) \\ \nabla\cdot\mathbf{U} = 0 \end{cases} \tag{III.13}$$

with χ being the strength of the filter and ω_c the cutting circular frequency. The choice of these two parameters is crucial for the computation: χ has to be positive and larger than the growth rate of the instability that one would like to kill, whereas ω_c has to be lower than the eigenfrequency ω_I of the instability (usually $\omega_c = \omega_I/2$). The effect of the filter is to lead the unsteady mode in the steady part of the eigenspectrum (Åkervik et al., 2006). Despite the knowledge a priori of the bifurcation is necessary for the filter setup, no particular initial conditions are required for the initialization of the method. The equation on the target solution evolution ($\dot{\bar{\mathbf{U}}}$) needs to be discretized in time. For the sake of simplicity a first order explicit Euler scheme has been used

$$\bar{\mathbf{U}}^{n+1} = \bar{\mathbf{U}}^n + \Delta t \left(\omega_c \left(\mathbf{U}^n - \bar{\mathbf{U}}^n \right) \right)$$

equally for the forcing term, which has been treated explicitly

$$-\chi(\mathbf{U}^n - \bar{\mathbf{U}}^n). \tag{III.14}$$

The numerical implementation is straightforward in any existing code and few code lines are required.

III.2.0.2 BoostConv

The BoostConv algorithm is a recent method proposed by Citro et al. (2017) that acts as convergence accelerator for an existing algorithm (e.g. GMRS, BiCGStab, PGM). In this framework, we refer to all iterative algorithms that produce at each iteration a residual and successively the last residual is used to start a new iteration up to convergence. By means of a Krylov method it is possible to boost the convergence of the iterative method towards a null residual. Considering the residual vector $r_n \in \mathbb{R}^m$ at the iteration n, the effect of a common iterative algorithm can be taken into account by the operator $\mathbf{A} \in \mathbb{R}^{m \times m}$. In this way the residual r_{n+1} is equal to:

$$r_{n+1} = r_n - \mathbf{A} r_n \tag{III.15}$$

or equivalent

$$r_n - r_{n+1} = \mathbf{A} r_n. \tag{III.16}$$

The goal of the BoostConv algorithm is to modify the equation (III.16) by correcting r_n:

$$r_n - r_{n+1} = \mathbf{A} \xi_n \tag{III.17}$$

where ξ_n is such that $\mathbf{A}\xi_n = r_n$. If it is so, r_{n+1} turns out to be equal to zero from eq. (III.15). The challenge is then to find the best approximation of ξ_n to annihilate r_{n+1}. Following Citro's work it is possible to build up two Krylov subspaces one spanning r_n and the other spanning $r_n - r_{n+1}$. Let be $\mathbf{X}$ and $\mathbf{Y} \in \mathbb{R}^{m \times N}$ two operators with $N \ll m$, N being the Krylov-space dimension

$$\begin{aligned} \mathbf{X} &= \{r_1, r_2, \dots, r_N\} \\ \mathbf{Y} &= \{r_1 - r_2, r_2 - r_3, \dots, r_N - r_{N+1}\} \end{aligned} \tag{III.18}$$

then from eq. (III.16) $\mathbf{Y} = \mathbf{AX}$. It is possible to define ξ_n as a linear combination of the previous residuals r_i

$$\xi_n = \mathbf{X} c \tag{III.19}$$

where c is the $(N \times 1)$ vector that contains the weight associated to each previous residual. The purpose is to find c that minimizes $|r_n - \mathbf{A}\xi_n|^2$. This is achieved by a standard least-square procedure

$$\begin{aligned} \mathbf{A}\xi_n &= r_n \\ \mathbf{AX}c &= r_n \\ \mathbf{Y}c &= r_n \\ c &= (\mathbf{Y}^T\mathbf{Y})^{-1}\mathbf{Y}^T r_n. \end{aligned} \tag{III.20}$$

The vector c is obtained invoking the pseudo-inverse matrix of $\mathbf{Y}$ where $\mathbf{Y}^T\mathbf{Y}$ is a small $(N \times N)$ matrix easy to invert. By using this correction the new residual vector will be:

$$\begin{aligned} r_{n+1} &= r_n - \mathbf{A}\xi_n \\ &= r_n - \mathbf{AX}c \\ &= r_n - \mathbf{AX}(\mathbf{Y}^T\mathbf{Y})^{-1}\mathbf{Y}^T r_n \\ &= (\mathbf{I} - \mathbf{Y}(\mathbf{Y}^T\mathbf{Y})^{-1}\mathbf{Y}^T) r_n. \end{aligned} \tag{III.21}$$

The $\mathbf{Y}(\mathbf{Y}^T\mathbf{Y})^{-1}\mathbf{Y}^T$ is an idempotent operator and then act as a projector. This means that the residual is annihilated just in a small subspace keeping unchanged the residual in the subspace orthonormal to the first one $(\mathbf{I} - \mathbf{Y}(\mathbf{Y}^T\mathbf{Y})^{-1}\mathbf{Y}^T)$. This procedure will never converge if we do not take into account in the correction ξ_n the residual marching to the iteration $n+1$ of the uncontrolled part of the residual

$$\begin{aligned} \xi_n &= \mathbf{X}c + (\mathbf{I} - \mathbf{Y}(\mathbf{Y}^T\mathbf{Y})^{-1}\mathbf{Y}^T) r_n \\ &= \mathbf{X}c + r_n - \mathbf{Y}c \\ &= r_n + (\mathbf{X} - \mathbf{Y})c. \end{aligned} \tag{III.22}$$

The equation (III.22) provides on estimation sof the correction as suggested in Citro's work and the final residual step is now

$$r_{n+1} = (\mathbf{I} - \mathbf{A})(\mathbf{I} - \mathbf{Y}(\mathbf{Y}^T\mathbf{Y})^{-1}\mathbf{Y}^T) r_n, \tag{III.23}$$

meaning that if the Krylov subspace has dimension equal to zero the original residual iteration III.15 is recovered.

The correlation matrix $(\mathbf{Y}^T\mathbf{Y})$ turns out to be ill conditioned. If the residual decay is slow, the norm of $\mathbf{Y}_n$ vector is close to zero and all the vectors in the $\mathbf{Y}$ operator could be highly correlated between each other. In other words it is not sure that span$\{\mathbf{Y}\}$ has the same dimension of $\mathbf{Y}$. To overcome this problem a *QR* decomposition $[\mathbf{Q}, \mathbf{R}] = qr(\mathbf{Y})$ can be used to evaluate the pseudoinverse of $\mathbf{Y}$

$$(\mathbf{Y}^T\mathbf{Y})^{-1}\mathbf{Y}^T = \mathbf{R}^{-1}\mathbf{Q}^T \tag{III.24}$$

$\mathbf{R}$ being a $(N \times N)$ upper triangular matrix and $\mathbf{Q}$ the subset of N orthonormal vectors $\mathbf{q} \in \mathbb{R}^m$. From an implementation point of view the *QR* decomposition can be carried out by a *modified Gram-Schmidt* iteration. Moreover the system $\mathbf{R}^{-1}$ can be easily solved by *successive substitution* for triangular matrices; thus, no additional libraries are required into the existing code.

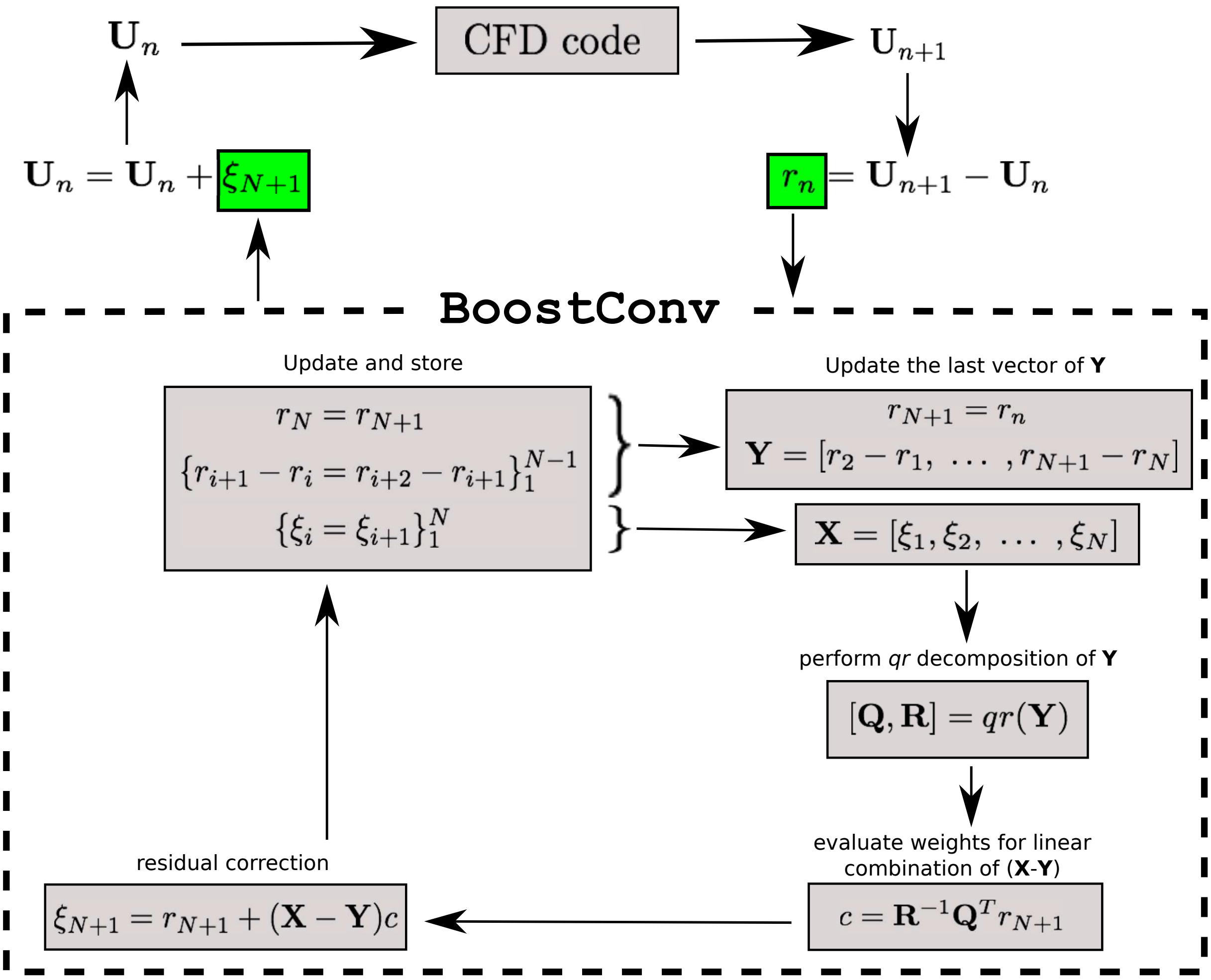

Figure III.3: Boostconv algorithm implementation in an exiting CFD code. The Boostconv procedure is a black-box with just one input and one output.

Application to the Navier-Stokes equation The time step iteration in a generic CFD code can be considered as an iterative procedure that produces a residual

$$r_n = \mathbf{U}_{n+1} - \mathbf{U}_n \tag{III.25}$$

this residual can be handled by the BoostConv algorithm that returns a correction ξ_n that will be used to update the $\mathbf{U}_n = \mathbf{U}_n + \xi_n$ solution for the new time step iteration. A sketch of the Boostconv numerical implementation is depicted in fig. III.3.

Even if the implementation is not straightforward, such as, for instance the SFD, the Boostconv procedure requires just one variable as input and provides to the CFD code just one as output. This allows the use of the BoostConv algorithm as a black-box.

III.2.0.3 SFD vs BoostConv

Concerning the benefits of the choice of the SFD algorithm to find the base state, we have already discussed its easy implementation. The SFD acts as low pass filter cutting of the frequencies components above a given cut-off frequency. Thus a steady mode ($\Im(\lambda) = 0$),

	Sfd 1	Sfd 2	Sfd 3	Sfd 4	Sfd 5
χ	0.5	0.25	0.125	0.125	0.125
ω_c	0.05	0.05	0.05	0.1	0.2
Number of iterations	379'861	232'315	152'428	94'046	64'533

Table III.2: Values of the different couples (χ, ω_c) for selective frequency damping as well as the number of iterations needed to reach a steady state converge down to $\|\mathbf{u}^{n+1} - \mathbf{u}^n\|_{L_2}/\mathrm{dt} \leq 10^{-8}$ for all the cases considered. A two-dimensional cylinder flow at $Re = 60$ has been considered.

such as that recovered in a supercritical pitchfork bifurcation[1], cannot be handled by this kind of approach. To shed light on the effect of the choice of χ and ω in the Selective Frequency Damping algorithm the 2D cylinder case has been taken as test case. The flow around a 2D cylinder becomes globally unsteady at $Re_c = 48$. Therefore, starting from a steady solution at $Re = 45$, the SFD has been used to find the base state at $Re = 60$. In order to set the SFD procedure it is mandatory to know a priori the main features of the unsteadiness. In this case, previous global stability analyses showed that the leading eigenvalue for this Reynolds number is $\lambda \simeq 0.02 + i0.8$. Thus, one must have $\chi \geq 0.02$ and $\omega_c \leq 0.4$.

A parametric investigation has been carried out to understand the influence on the residual convergence of the choice of the χ and ω_c parameters. In table III.2 the number of iteration necessary to converge towards the fixed point are reported. The steady state is considered well converged when a residual level $\|\mathbf{U}^{n+1} - \mathbf{U}^n\| < 10^{-8}$ is reached.

In figure III.4 the residual time history is depicted for the different analysed cases. Changing the parameters (χ, ω) the residual evolution can drastically change. In any case, the convergence is ensured for the conditions $\chi \geq 0.02$ and $\omega_c \leq 0.4$. Mathematical details about the dependence of the convergence slope curve on χ and ω, are provided in Åkervik et al. (2006).

Regarding the BoostConv performance something more has to be said about its implementation for a nonlinear system. As already said, successive residual fields could provide a highly ill conditioned $(\mathbf{Y}^T\mathbf{Y})$ matrix. Calling fs the number of Navier-Stokes iteration between two successive residual snapshots to build the Krylov space, it is necessary to appropriately choosing the value of fs, avoiding too small or too high values. The BoostConv procedure is based on a linear residual prediction, thus a high value of fs can give a residual correction in disagreement with the nonlinear evolution. In table III.3 the number of iterations required to reach the convergence is reported in function of the krylov space dimension and the number of Navier-Stokes iteration between two successive residual snapshots.

The time evolution of the residual norm is reported in figure III.5 for the parameters in table III.3.

No particular dependencies with respect to the Krylov space dimension can be noticed. Decreasing the fs value some slight differences could be noticed due to the conditioning of $(\mathbf{Y}^T\mathbf{Y})$. In any case, the BoosConv procedure seems to be today a valid alternative to the selective frequency damping algorithm especially because even a steady bifurcation

---

[1] The pitchfork bifurcation is a particular bifurcation in which the steady state get transition from one fix point to another fix point.

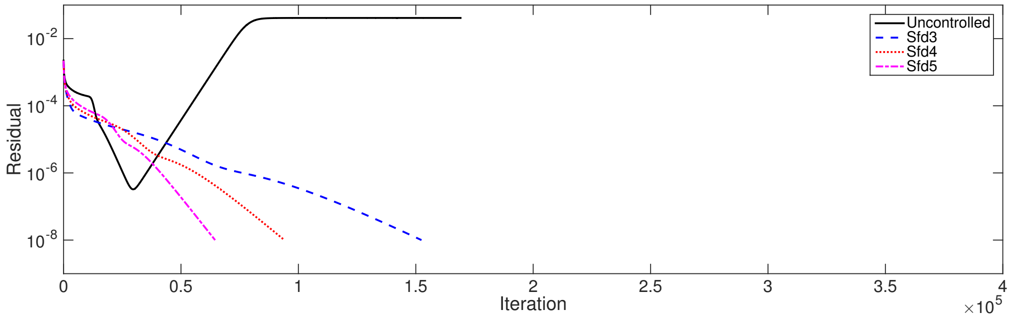

(a) Fixed $\omega_c = 0.05$

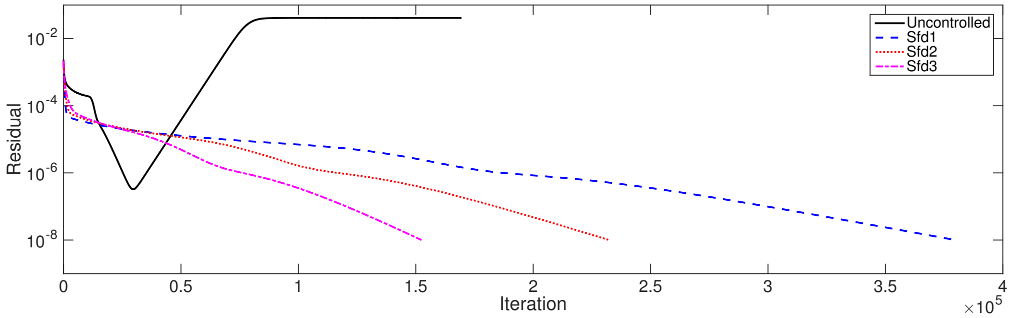

(b) Fixed $\chi = 0.125$

Figure III.4: Time-evolution of the residual for the different set of parameters (χ, ω_c) considered in table III.2. Convergence threshold is set to 10^{-8}.

	Boost 1	Boost 2	Boost 3	Boost 4	Boost 5
N	5	5	5	10	15
fs	25	50	100	100	100
Number of iterations	32'252	41'502	28'640	26'854	30'439

Table III.3: Values of the different couples (N, fs) for BoostConv procedure as well as the number of iterations needed to reach a steady state converge down to $\|\mathbf{u}^{n+1} - \mathbf{u}^n\|_{L_2}/\mathrm{dt} \leq 10^{-8}$ for all the cases considered. A two-dimensional cylinder flow at $Re = 60$ has been considered.

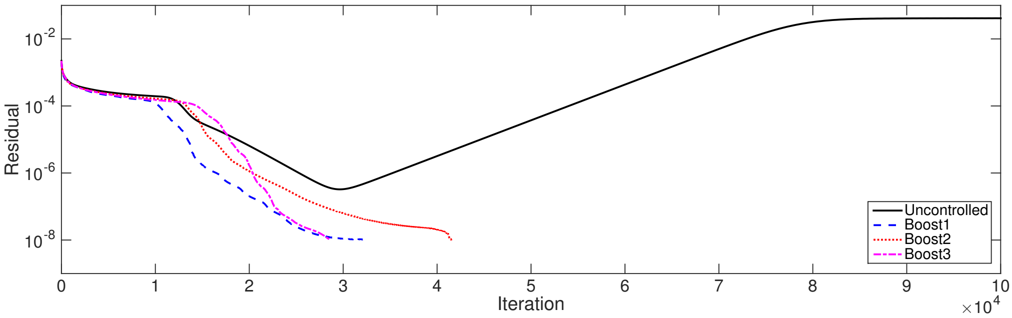

(a) Fixed $N = 5$

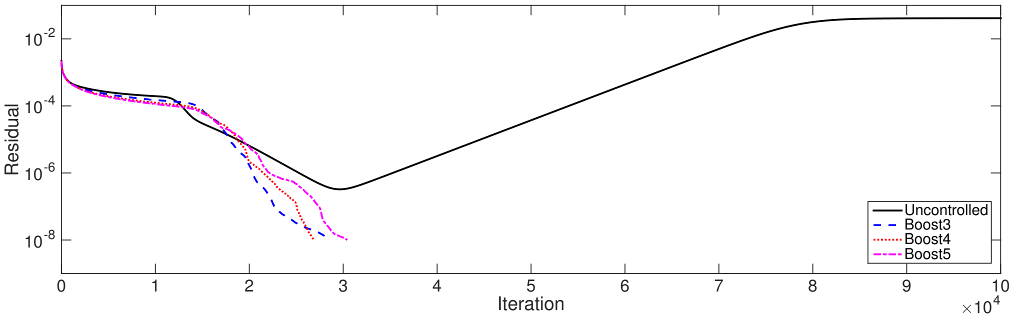

(b) Fixed $fs = 0.100$

Figure III.5: Time-evolution of the residual for the different set of parameters (N, fs) considered in table III.3. Convergence threshold is set to 10^{-8}.

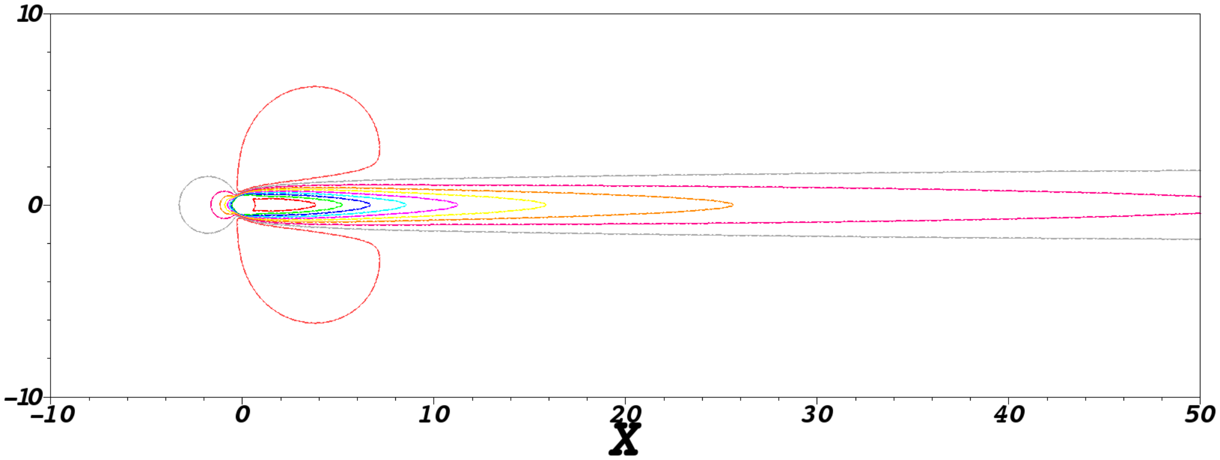

Figure III.6: Base flow for 2D cylinder case at $Re = 60$. Base flow obtained with Boostconv algorithm $(N, fs) = (15, 100)$ (dashed line) and selective frequency damping $(\chi, \omega_c) = (0.2, 0.125)$ (continuous line).

can be treated with this method. Finally, a comparison between the base flow obtained with the two methods is depicted in figure III.6.

III.3 Modal decomposition

The theoretical basis for the linear stability analysis has been given in the previous chapter §II. Because of the memory issues the Bi-local and the Global stability analysis need to be treated in a different way. An explanation of the used algorithm and adopted strategy to handle the memory required to store the Jacobian will be now given in this section.

III.3.1 Bi-Local stability analysis: numerical approach

Using a Bi-local stability analysis is possible to store the whole matrix in sparse fashion. Depending on the numerical scheme used to discretize the derivative operator the Jacobian matrix can have many null values. A sparse matrix allows to store just the non-null elements, economising the memory. The Bi-local analysis has been carried out by a home-made code written in MATLAB®. For both stability analyses we need to discretize the Jacobian of the linearised system II.27. To discretize the derivative operator in both directions y and z a spectral collocation method has been used as those implemented in the Nek5000. More extensive details will be now provided. The fundamental idea behind this approach is to interpolate a function by a polynomial that is a uniform and accurate representation of that function over a certain interval and evaluates the derivative of the interpolant polynomial on the grid. In comparison to spatial methods such as finite differences, the polynomial is constructed by a sum of basis functions that are evaluated at the entire set of grid data points of the considered domain:

$$f(x) = p_N(x) = \sum_{i=0}^{N} \phi_i(x) a_i \qquad \text{(III.26)}$$

where ϕ_i is an expansion function and a_i is a weight function. Increasing the number of grid points leads to an exponential convergence, which provides this method higher accuracy than spatial methods. Moreover, spectral methods are memory-minimizing as they require less degrees of freedom in each dimension to achieve the same accuracy compared to spatial methods (Boyd, 2001). Among different types of spectral methods, this study exclusively makes use of the collocation approach, in which the polynomial takes the value of the differential equation at the grid points or rather collocation points. This means that the weight function a_i is the unknown function $f(x)$ itself and only the expansion function ϕ_i determines the accordance between the function and the polynomial.

$$f(x) \approx p_N(x) = \sum_{i=0}^{N} \phi_i(x) f(x_i) \tag{III.27}$$

The choice of the expansion functions is restricted to the physics of the flow. For a periodic problem, we use trigonometric basis functions on an equispaced grid, which are normally Fourier series. For a non-periodic problem, we normally use algebraic polynomials on an unevenly, asymptotically spaced grid. A good choice here are Chebyshev polynomials, which by simple trigonometric identity can be transformed to trigonometric functions as well.

III.3.1.1 Chebyshev Gauss-Lobatto collocation method

The flow domain in the wall normal direction is discretized into $n_y + 1$ collocation points. We use a n_y^{th}-order Chebyshev polynomial T_{n_y}, defined in the interval $(\zeta_i) \in [-1; +1]$ where the collocation points ζ_i are the extrema of T_{n_y} plus the endpoints of the interval and are given by

$$\zeta_i = cos\left(\frac{\pi i}{n_y}\right), \quad i = 0, \ldots, n_y$$

and represented in fig. III.7

In order to apply the spectral collocation method, an interpolant polynomial is constructed for the dependent variables in terms of their values at the collocation points.

$$\hat{\mathbf{z}}(\zeta, \xi) = \sum_{k=0}^{n_y} \sum_{l=0}^{n_z} h_k(\zeta) h_l(\xi) \hat{\mathbf{z}}(\zeta, \xi_l),$$

where ξ denotes the array of collocation points in spanwise direction. In order to express $\hat{\mathbf{z}}$ only in wall-normal direction we fix $\xi = \xi_j$. The above expression can then be written as

$$\hat{\mathbf{z}}(\zeta_k, \xi) = \sum_{k=0}^{n_y} h_k(\zeta) \hat{\mathbf{z}}(\zeta, \xi_l),$$

where $h_k(\zeta)$ is the Lagrange interpolant, which for a Gauss-Lobatto grid becomes

$$h_k(\zeta) = \left(\frac{1-\zeta_k^2}{\zeta - \zeta_k}\right) \frac{T'_{n_y}(\zeta)}{n_y^2 c_k} (-1)^{k+1}$$

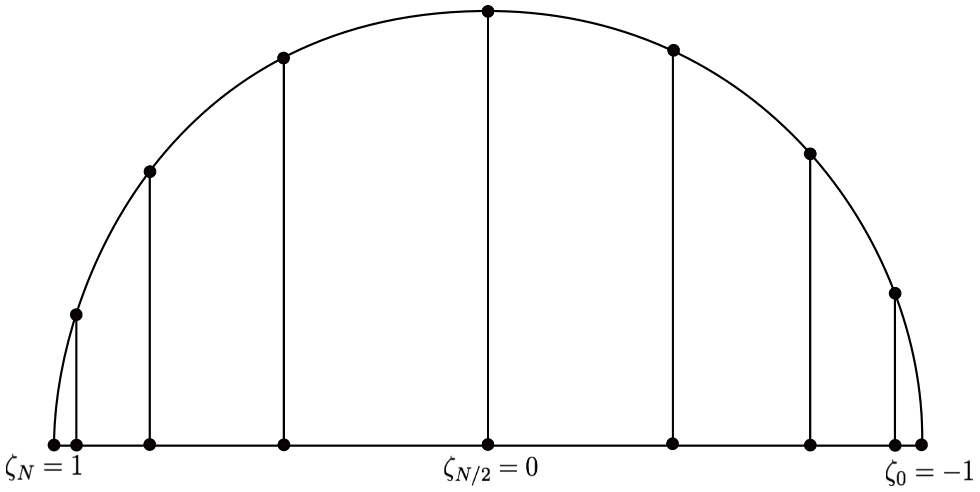

Figure III.7: Chebyshev collocation points are the projections onto the x-axis of equally spaced points on the unit circle.

with

$$c_0 = c_{n_y} = 2, c_k = 1, \quad for \quad k \in \{1, \dots, n_y - 1\}$$

(Gottlieb and Hirsh, 1989). The first derivative of $\hat{\mathbf{z}}(\zeta, \xi)$ with respect to ζ may be written as

$$\frac{d\hat{\mathbf{z}}}{d\zeta}(\zeta_i, \xi_j) = \sum_{k=0}^{n_y} D_{ik} \hat{\mathbf{z}}(\zeta_k, \xi_j)$$

where $D_{ik}^{(1)}$ are the elements of the derivative matrix given by

$$D_{ik}^{(1)} = \frac{c_i}{c_k} \frac{(-1)^{i+k}}{\zeta_i - \zeta_k}, \quad i \neq k, \quad D_{ii}^{(1)} = -\frac{\zeta_i}{2(1-\zeta_i^2)}, \quad D_{00}^{(1)} = \frac{2n_y^2 + 1}{6} = -D_{n_y n_y}^{(1)}.$$

The Chebyshev interval $(\zeta_i) \in [-1; +1]$ is transformed to the computational domain $[0; y_m]$ by the use of the conformal mapping:

$$y(\zeta_i) = \frac{a_0(1-\zeta_i)}{a_1 + \zeta_i} \quad \text{with} \quad a_0 = \frac{y_a y_m}{(y_m - 2y_a)} \quad \text{and} \quad a_1 = 1 + \frac{2a_0}{y_m}$$

where y_a correspond to the distance from the wall where 50% of the points are located. Applying the chain rule, the scaling factor for the transformation between physical and computational domain is then given as $S_i = (d\zeta/dy)i, \quad i = 0, \dots, n_y$ and the first derivative matrix $\mathbf{D}^{(1)}$ in the physical domain may be written as

$$\mathbf{D}_{ik}^{(1)} = S_i D_{ik}^{(1)}$$

The second derivative matrix $\mathbf{D}^{(2)}$ is simply $\mathbf{D}_{ik}^{(2)} = \mathbf{D}_{im}^{(1)} \mathbf{D}_{mk}^{(1)}$.

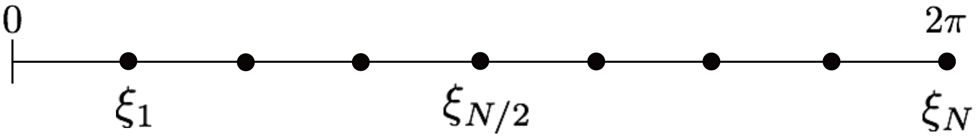

Figure III.8: Basic periodic grid is a subset of the interval $[0; 2\pi]$.

III.3.1.2 Fourier Collocation Method

Fourier approximation is performed over the interval $\xi \in [0, 2\pi]$ on equally spaced grid points

$$\xi_i = (j-1)h \quad \text{with} \quad h = \frac{2\pi}{n_z}, \quad j = 1, \ldots, n_z - 1$$

and represented in fig. III.8

Again we construct an interpolant polynomial to approximate the dependent variables, this time in spanwise direction with fixed $\zeta = \zeta_i$.

$$\hat{\mathbf{z}}(\zeta_i, \xi) = \sum_{l=1}^{n_z} h_l(\xi) \hat{\mathbf{z}}(\zeta_i, \xi_l)$$

where $\hat{\mathbf{z}}(\zeta_i, \bullet)$ represents the n_z function values of $\hat{\mathbf{z}}$ at the collocation points. The interpolation polynomial h_l is defined, depending on whether n_z is even or odd, as follow:

$$h_l(\xi) = \frac{1}{n_z} sin\left[\frac{n_z}{2}(\xi - \xi_l)\right] cot\left[\frac{1}{2}(\xi - \xi_l)\right], \quad \text{for } n_z \text{ even}$$

$$h_l(\xi) = \frac{1}{n_z} sin\left[\frac{n_z}{2}(\xi - \xi_l)\right] csc\left[\frac{1}{2}(\xi - \xi_l)\right], \quad \text{for } n_z \text{ odd}$$

The derivative of $\hat{\mathbf{z}}$ with respect to ξ in according to the above expression may be written as

$$\frac{d\hat{\mathbf{z}}}{d\zeta}(\zeta_i, \xi_j) = \sum_{k=0}^{n_y} D_{jl} \hat{\mathbf{z}}(\zeta_i, \xi_l),$$

with $D_{jl} = \frac{dh_l}{d\xi}(\xi)$ being the derivative matrix. The coefficients of the first and second derivative, $D^{(1)}_{jl}$ and $D^{(2)}_{jl}$, respectively, are defined depending on the parity of n_z. In case n_z is even the coefficients are:

$$D^{(1)}_{jl} = \begin{cases} 0 & \text{if } j = l \\ \frac{1}{2}(-1)^{j-l} cot \frac{(j-l)h}{2} & \text{if } j \neq l \end{cases}$$

$$D^{(2)}_{jl} = \begin{cases} \frac{-\pi^2}{3h^2} - \frac{1}{6} & \text{if } j = l \\ \frac{1}{2}(-1)^{j-l} csc^2 \frac{(j-l)h}{2} & \text{if } j \neq l \end{cases}$$

For odd n_z the coefficients are then:

$$D^{(1)}_{jl} = \begin{cases} 0 & \text{if } j = l \\ \dfrac{1}{2}(-1)^{j-l} csc\dfrac{(j-l)h}{2} & \text{if } j \neq l \end{cases}$$

$$D^{(2)}_{jl} = \begin{cases} \dfrac{-\pi^2}{3h^2} + \dfrac{1}{12} & \text{if } j = l \\ \dfrac{1}{2}(-1)^{j-l} csc\dfrac{(j-l)h}{2} cot\dfrac{(j-l)h}{2} & \text{if } j \neq l \end{cases}$$

Considering that the physical domain in z-direction extends over the interval $[-\lambda, \lambda]$, we therefore have to apply the transformation $z(\xi) = -\lambda + \frac{\lambda}{\pi}\xi$. As done previously for the Chebychev collocation derivative we obtain the scaling factor from the chain rule, which is simply $S_j = (d\xi/dz)_j = \frac{\pi}{\lambda}, \quad j = 0, \ldots, n_z$ and the first and second derivatives $\mathbf{D}^{(1)}$ and $\mathbf{D}^{(2)}$ in physical space may then be written as

$$\mathbf{D}^{(1)}_{jl} = D^{(1)}_{jl}\frac{\pi}{\lambda} \quad \text{and} \quad \mathbf{D}^{(2)}_{jl} = D^{(2)}_{jl}\left(\frac{\pi}{\lambda}\right)^2$$

III.3.1.3 Boundary conditions

For the studied cases, Dirichlet boundary conditions have been imposed at the bottom and at the top of the domain in the y-direction for the velocity field. In z-direction the periodicity condition is always imposed. For a 2D problem the vector state has to be reorganized in a vector like in (III.28)

$$\mathbf{u} = \begin{bmatrix} u_{11} & \cdots & u_{1n_z} \\ \vdots & \ddots & \vdots \\ u_{n_y1} & \cdots & u_{n_yn_z} \end{bmatrix} = [u_{11}, \ldots, u_{n_y1}, \ldots, u_{1n_z}, \ldots, u_{n_yn_z}]^T \tag{III.28}$$

n_y and n_z being the number of rows and columns. The derivative operator in y-direction that acts on each column, must be repeated on the diagonal n_z times. In the same way, the derivative operator that acted on each line, now it has to be reshaped in order to handle each n_y terms of the vector as n_y is the distance in the vector between two terms of the same line in the matrix (III.28). The best way to handle this reshaping is the use of the *kronecker product.* The Kronecker product of two matrices A and B is denoted by $A \otimes B$. If A and B are of dimensions $p \times q$ and $r \times s$, respectively, then $A \otimes B$ is the matrix of dimension $pr \times qs$ with $p \times q$ block form, where the i, j block is $a_{ij}B$. As example, given the general matrix

$$D = \begin{pmatrix} \spadesuit & \heartsuit \\ \diamondsuit & \clubsuit \end{pmatrix}$$

if I denotes the (3×3) identity matrix, then the kronecker product $I \otimes D$ and $D \otimes I$ will produce

$$I \otimes D = \left(\begin{array}{cc|cc|cc} \spadesuit & \heartsuit & & & & \\ \diamondsuit & \clubsuit & & & & \\ \hline & & \spadesuit & \heartsuit & & \\ & & \diamondsuit & \clubsuit & & \\ \hline & & & & \spadesuit & \heartsuit \\ & & & & \diamondsuit & \clubsuit \end{array}\right) \quad D \otimes I = \left(\begin{array}{ccc|ccc} \spadesuit & & & \heartsuit & & \\ & \spadesuit & & & \heartsuit & \\ & & \spadesuit & & & \heartsuit \\ \hline \diamondsuit & & & \clubsuit & & \\ & \diamondsuit & & & \clubsuit & \\ & & \diamondsuit & & & \clubsuit \end{array}\right).$$

In this way, it is straightforward to handle operators that act on y- and z-directions. Loking at the last example it is clear the advantage of working with sparse matrices. The periodicity condition is ensured in z-direction by the Fourier Collocation method. On the contrary Chebyshev collocation method is used in y-direction. Dirichlet condition imposed at the top and at the bottom of the 2D domain allows us to ignore the first and the last column and row of the derivative operator in y-direction (see fig. III.9) (Trefethen, 2000).

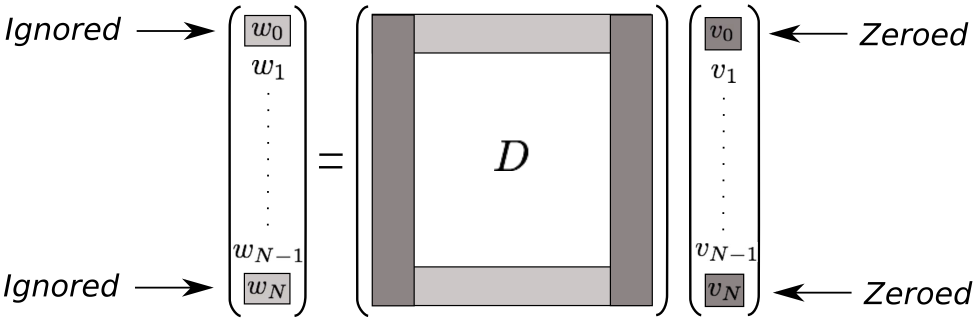

Figure III.9: Dirichlet boundary conditions imposed in the y-derivative operator. Example from Trefethen (2000).

The derivative operator will be now $n_y - 2 \times n_y - 2$ matrix. To avoid to impose any boundary condition on the pressure field, the strategy proposed by Botella (1997) as been adopted. The pressure is evaluated on a staggered grid. Practically we use only the internal point for the pressure, in this way is sufficient to generate a derivative operator of order $n_y - 2$ without removing any line or column. In summary we have to construct three operators:

- $D_z^{(1)(2)}$: $n_z \times n_z$ first and second derivative operator in z-direction.
- $D_y^{(1)(2)}$: $n_y \times n_y$ first and second derivative operator in y-direction, for which the first and last row and column will be removed to take into account the Dirichlet boundary conditions.
- $D_{yP}^{(1)}$: $n_y - 2 \times n_y - 2$ first derivative operator in y-direction that acts only on the pressure grid.

III.3.1.4 Discretized Jacobian

With the operators just defined it is possible to discretize the system (II.27). Let us define the following matrices:

- I_y the $n_y - 2 \times n_y - 2$ identity matrix
- I_z the $n_z \times n_z$ identity matrix
- I the $(n_y - 2)n_z \times (n_y - 2)n_z$ identity matrix
- Z the $(n_y - 2)n_z \times (n_y - 2)n_z$ zero matrix
- $$\Sigma = -IV_b(I_z \otimes D_y^{(1)}) - IW_b(D_z^{(1)} \otimes I_y) + \frac{1}{Re}(I_z \otimes D_y^{(2)} + D_z^{(2)} \otimes I_y)$$
- $$A_0 = \begin{pmatrix} Z & I_z \otimes D_y^{(1)} & D_z^{(1)} \otimes I_y & Z \\ \Sigma & -D_y^{(1)}U_bI & -D_z^{(1)}U_bI & Z \\ Z & \Sigma - D_y^{(1)}V_bI & -D_z^{(1)}V_bI & I_z \otimes D_{yP}^{(1)} \\ Z & -D_y^{(1)}W_bI & \Sigma - D_z^{(1)}V_bI & D_z^{(1)} \otimes I_y \end{pmatrix}$$
- $$A_1 = \begin{pmatrix} iI & Z & Z & Z \\ -iIU_b & Z & Z & -iI \\ Z & -iIU_b & Z & Z \\ Z & Z & -iIU_b & Z \end{pmatrix}$$
- $$A_2 = \begin{pmatrix} -\frac{1}{Re}I & Z & Z \\ Z & -\frac{1}{Re}I & Z \\ Z & Z & -\frac{1}{Re}I \end{pmatrix}$$
- $$B_0 = \begin{pmatrix} Z & Z & Z & i\varepsilon I \\ -iI & Z & Z & Z \\ Z & -iI & Z & Z \\ Z & Z & -iI & Z \end{pmatrix}$$

The linear stability analysis is carried out looking at the eigenmodes of the following eigenproblem:

$$(A - \lambda B)\hat{\phi} = 0$$

Depending on how the A and B matrices are built the temporal or spatial stability analysis can be provided. For the temporal stability analysis $\alpha, \beta \in \mathbb{R}$ and A and B matrices turn out to be equal to

- $$A = A_0 + \alpha A_1 + \alpha^2 A_2^* \quad \text{with} \quad A_2^* = \left(\begin{array}{ccc|c} \mathrm{Z} & \mathrm{Z} & \mathrm{Z} & \mathrm{Z} \\ \hline & & & \mathrm{Z} \\ & A_2 & & \mathrm{Z} \\ & & & \mathrm{Z} \end{array}\right)$$
- $$B = B_0 \quad \text{with} \quad \varepsilon \sim 10^{-8}$$

If ε was equal to zero, then B would have null lines. To avoid this problem a small imaginary value acting on the pressure term has to be used in B_0, as suggested by Juniper et al. (2014). In the eigenproblem λ is the complex eigenvalue (ω in the temporal stability theory) and $\hat{\phi}$ the associated complex eigenvector $\hat{\phi} = (\hat{u}, \hat{v}, \hat{w}, \hat{p})^T$. For the **spatial stability** analysis, the eigenproblem remains unchanged but $\omega, \beta \in \mathbb{R}$ and A and B are:

- $$A = \left(\begin{array}{cccc|ccc} & & & & \mathrm{Z} & \mathrm{Z} & \mathrm{Z} \\ & A_0 + \omega B_0 & & & \mathrm{Z} & \mathrm{Z} & \mathrm{Z} \\ & & & & \mathrm{Z} & \mathrm{Z} & \mathrm{Z} \\ & & & & \mathrm{Z} & \mathrm{Z} & \mathrm{Z} \\ \hline \mathrm{Z} & \mathrm{Z} & \mathrm{Z} & \mathrm{Z} & \mathrm{I} & \mathrm{Z} & \mathrm{Z} \\ \mathrm{Z} & \mathrm{Z} & \mathrm{Z} & \mathrm{Z} & \mathrm{Z} & \mathrm{I} & \mathrm{Z} \\ \mathrm{Z} & \mathrm{Z} & \mathrm{Z} & \mathrm{Z} & \mathrm{Z} & \mathrm{Z} & \mathrm{I} \end{array}\right)$$

- $$B = \left(\begin{array}{cccc|ccc} & & & & \mathrm{Z} & \mathrm{Z} & \mathrm{Z} \\ \cline{5-7} & A_1 & & & & & \\ & & & & & A_2 & \\ & & & & & & \\ \hline \mathrm{Z} & \mathrm{Z} & \mathrm{Z} & \mathrm{Z} & \mathrm{I} & \mathrm{Z} & \mathrm{Z} \\ \mathrm{Z} & \mathrm{Z} & \mathrm{Z} & \mathrm{Z} & \mathrm{Z} & \mathrm{I} & \mathrm{Z} \\ \mathrm{Z} & \mathrm{Z} & \mathrm{Z} & \mathrm{Z} & \mathrm{Z} & \mathrm{Z} & \mathrm{I} \end{array}\right)$$

with $\varepsilon = 0$. In the eigenvalue problem $\hat{\phi} = (\hat{u}, \hat{v}, \hat{w}, \hat{p}, \alpha\hat{u}, \alpha\hat{v}, \alpha\hat{w})$ is the eigenvector and the first $n_y \times n_z \times 4$ λ values are the eigenmodes of our interest (the complex α in the spatial theory).

To validate the Matlab code, the temporal stability analysis of the base flow behind a 3D roughness bump has been computed as done by Shin et al. (2015). The velocity field is taken at $2.5m$ behind the roughness, the Reynolds number based on the bump position is $Re_x = 1.88 \times 10^5$ and $\alpha = 33$. Further details on the numerical setup can be found in Shin et al. (2015). The eigenspectrum comparison is shown in figure III.10 and the leading eigenvectors are depicted in III.11.

III.3.2 Global linear stability

Once discretized, the system (II.20) can be written in a contract form

$$\mathbf{B}\frac{\partial \mathbf{q}}{\partial t} = \mathbf{J}\mathbf{q} \tag{III.29}$$

where $\mathbf{B}$ is the mass matrix and $\mathbf{J}$ the Jacobian operator defined as follows

$$\begin{aligned} \mathbf{J} &= \begin{pmatrix} -\nabla\mathbf{U}_b - \mathbf{U}_b \cdot \nabla + Re^{-1}\Delta & -\nabla \\ \nabla\cdot & 0 \end{pmatrix} \\ \mathbf{B} &= \begin{pmatrix} \mathbf{I} & 0 \\ 0 & 0 \end{pmatrix} \end{aligned} \tag{III.30}$$

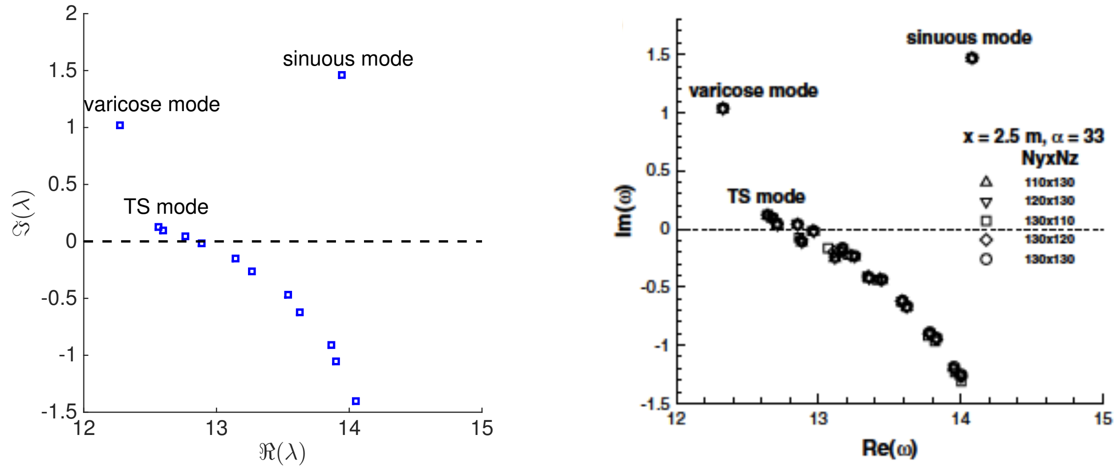

(a) Obtained eigenspectrum (b) Reference result from (Shin et al., 2015)

Figure III.10: Temporal stability analysis for a velocity field at $2.5m$ behind a bump roughness. $Re_x = 1.88 \times 10^5$, $\alpha = 33$, $n_y = 120$ and $n_z = 100$. In (a) the obtained eigenspectrum in (b) reference eigenspectrum courtesy of Shin et al. (2015).

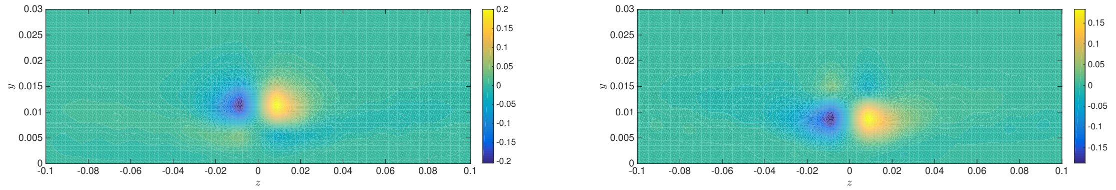

(a) $\Re(\hat{u}_s)$ (b) $\Im(\hat{u}_s)$

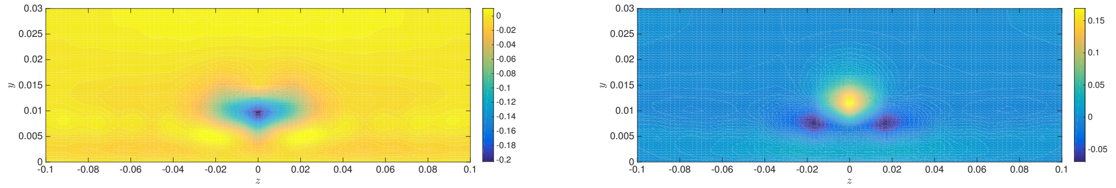

(c) $\Re(\hat{u}_v)$ (d) $\Im(\hat{u}_v)$

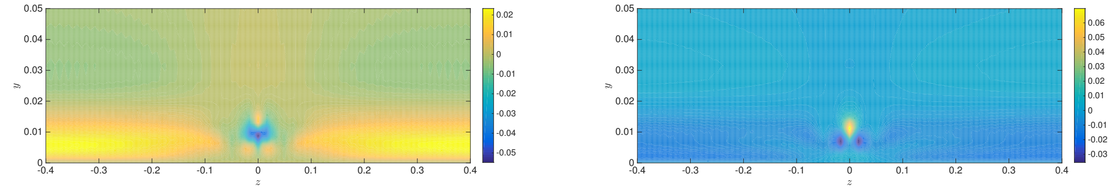

(e) $\Re(\hat{u}_{TS})$ (f) $\Im(\hat{u}_{TS})$

Figure III.11: Eigenvectors associated to the leading eigenvalue (a) real and (b) imaginary part of the sinuous eigenvector, (c) real and (d) imaginary part of the varicose eigenvector and (e) real and (f) imaginary part of the TS like eigenvector of the mode in figure III.10.

Assuming a global mode ansatz, without imposing any spatial assumption, the solution of (II.20) is in the form

$$\mathbf{q}(x, y, z, t) = \hat{\mathbf{q}}(x, y, z)e^{\lambda t} + c.c. \tag{III.31}$$

Injecting the decomposition (III.31) in the system (III.29) the following generalized eigenvalue problem is formulated:

$$\lambda \mathbf{B}\hat{\mathbf{q}} = \mathbf{J}\hat{\mathbf{q}} \tag{III.32}$$

where $\lambda = \sigma + i\omega$. The linear stability of the base flow $\mathbf{U}_b$ is then driven by the sign of the real part of the eigenvalue. If exist a global mode that has $\sigma > 0$ then the flow is linearly globally unstable otherwise if $\sigma < 0$ it is linearly stable.

III.3.2.1 Time-stepping approach

Because of the extremely large number of degrees of freedom involved in the computation, solving the generalized eigenvalue problem for a fully three-dimensional flow using standard algorithms is not possible today. As a consequence, a time-stepping approach (Bagheri et al., 2009; Edwards et al., 1994) is used. This approach relies on the fact that, once projected onto a divergence-free vector space, system III.29 reduces to:

$$\frac{\partial \mathbf{u}}{\partial t} = \mathbf{A}\mathbf{u} \tag{III.33}$$

with $\mathbf{A}$ being the projection of the Jacobian matrix $\mathbf{J}$ onto the divergence-free vector space. The time integration is then carried out involving the exponential propagator $\mathbf{M} = e^{\mathbf{A}\Delta T}$. The related eigenvalue problem becomes

$$\mu \hat{\mathbf{u}} = \mathbf{M}\hat{\mathbf{u}}. \tag{III.34}$$

The last eigenvalue problem is solved to characterize the asymptotic behaviour of the flow: if $\|\mu\| > 1$ then $\mathbf{U}_b$ is linearly unstable, otherwise, if $\|\mu\| < 1$ it is linearly stable. Though the exponential propagator $\mathbf{M}$ cannot be explicitly computed, its action onto a given vector can be easily approximated by time-marching the linearized Navier-Stokes equations from $t = 0$ to $t = \Delta T$. This property hence allows us to use Arnoldi-based iterative eigenvalue solvers. Finally, the eigenpairs $(\mu, \hat{\mathbf{u}})$ of the exponential propagator $\mathbf{M}$ are related to those of the Jacobian matrix $\mathbf{J}$ by:

$$\lambda = \frac{\log(\mu)}{\Delta T} \quad \text{and} \quad \mathbf{B}\hat{\mathbf{q}} = \hat{\mathbf{u}} \tag{III.35}$$

The main idea of the time-stepping approach is to use a subset of velocity field to build an orthonormal basis that can be used to project the whole $n \times n$ operator $\mathbf{M}$ in a smaller $m \times m$ space where $m \ll n$. Let us consider a $n \times m$ operator $\mathbf{V}_m$ composed by m orthonormalized vectors of dimension $n \times 1$ such that $\mathbf{V}\mathbf{V}^T \approx \mathbf{I}$ where $\mathbf{I}$ is the $n \times n$ identity matrix. It is possible to write the following decomposition

$$\mathbf{M} = \mathbf{V}\mathbf{V}^T\mathbf{M}\mathbf{V}\mathbf{V}^T \tag{III.36}$$

where $\mathbf{V}\mathbf{V}^T$ is the *projection operator* and $\mathbf{H} = \mathbf{V}^T\mathbf{M}\mathbf{V}$ is called Hessenberg matrix and is a $m \times m$ operator. The feasibility of the use of the projection technique is linked to the feasibility of building the $\mathbf{H}$ matrix without store the $\mathbf{M}$ operator.

Arnoldi algorithm

The projection of the propagation matrix in a smaller space is accomplished by the *Arnoldi algorithm*. Given the exponential propagator $\mathbf{M}$ and an initial vector $\mathbf{u}_0$ such that $\|\mathbf{u}_0\| = 1$, one can build-up the following Krylov sequence $\mathbf{K}_m$ of dimension m

$$\mathbf{K}_m(\mathbf{M}, \mathbf{u}_0) = \{\mathbf{u}_0, \mathbf{M}\mathbf{u}_0, \ldots, \mathbf{M}^{m-1}\mathbf{u}_0\} \tag{III.37}$$

This Krylov sequence $\mathbf{K}_m$ converges towards the eigenvector corresponding to the largest eigenvalue (in modulus) of $\mathbf{M}$. Unfortunately, as the dimension n is increased, the sequence $\mathbf{K}_m$ becomes increasingly badly conditioned. This simple iteration is known as the *power iteration*. Though such method is extremely simple to implement within a given code, it is unfortunately relatively slowly converging and only enables the recovery of the leading eigenpair discarding in the meantime all of the information contained in the $m-1$ previous vectors of the sequence. To overcome this loss of information, the Arnoldi method combines the power iteration with a Gram-Schmidt orthogonalisation process. The Gram-Schmidt procedure is used to orthogonalise the sequence $\mathbf{K}_m$ and obtain an orthonormal subset of vector $\mathbf{V}_m$. The Arnoldi factorization reads

$$\mathbf{M}\mathbf{V}_m = \mathbf{V}_m\mathbf{H}_m + \beta\mathbf{v}_{m+1}\mathbf{e}_m^T \tag{III.38}$$

with $\mathbf{V}_m$ an orthonormal set of vectors spanning a Krylov sbspace of dimension m, $\mathbf{H}_m$ a $m \times m$ upper Hessenberg matrix, and $\beta\mathbf{v}_{m+1}$ the orthogonal residual indicating how $\mathbf{V}_m$ is far from an invariant space.

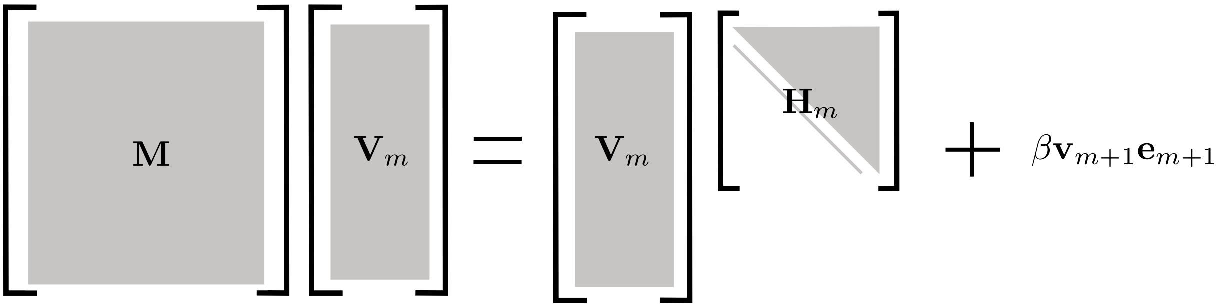

Figure III.12: Matrix representation of the Arnoldi decomposition.

Fig. III.12 depicts the structure of the matrices involved in the process. It can be shown that the Ritz pair $(\mu_H, \mathbf{V}_m\mathbf{y})$ of $\mathbf{H}_m$ provides a good approximation for the eigenpair $(\mu, \hat{\mathbf{u}})$ of the matrix $\mathbf{M}$. The Arnoldi procedure is summarized step by step in table III.4.

Table III.4: Arnoldi algorithm step-by-step

1	Set an initial arbitrary vector $\mathbf{u}_0$ and normalize it such that it has unitary norm	$\mathbf{v}_1 = \frac{\mathbf{u}_0}{\lVert\mathbf{u}_0\rVert}$
2	The successive $\mathbf{v}_k$ is recovered thanks to the propagation matrix	$\mathbf{v}_k = \mathbf{M}\mathbf{v}_{k-1}$
3	A Gram-Schmidt iteration is then used to orthonormalize the k-th with the previous. This is accomplished in two steps. $h_{j,k-1}$ are the terms in the upper diagonal Hessenberg matrix	$for \quad j = 1 \rightarrow k-1$ $h_{j,k-1} = \mathbf{v}_j\mathbf{v}_k$ $\mathbf{v}_k = \mathbf{v}_k - h_{j,k-1}\mathbf{v}_j$ *end*
4	The subdiagonal term of the Hessenberg matrix is the norm of the new orthogonal vector.	$h_{k,k-1} = \lVert\mathbf{v}_k\rVert$
5	Finally the $\mathbf{v}_k$ is normalised to 1 to get the new orthogonal direction in the krylov space.	$\mathbf{v}_k = \frac{\mathbf{v}_k}{h_{k,k-1}}$
6	Goes to the step 2 up to k equal to the chosen krylov space m.	$while \quad k \leq m$ $k = k+1$ *goto* step 2 *end*
7	Solve the eigenvalue problem using LAPACK library Andersen et al. (1999)	$[\mu_H, \mathbf{y}] = eig(H)$
8	Use the $\mathbf{V}_m$ operator to project the eigenmodes from $m \times m$ space to $n \times m$ space.	$\mu = \mu_H \quad \text{and} \quad \hat{\mathbf{u}} = \mathbf{V}_m\mathbf{y}$
9	Recover the eigenvalue of the Jacobian matrix $\mathbf{A}$ from those of the propagation matrix $\mathbf{M}$ and the relative residue r_k associated at each $\hat{\mathbf{u}}_k$.	$\lambda = \frac{\log(\mu)}{\Delta T} \quad \text{and} \quad r_k = \lvert\beta\mathbf{y}_k(m)\rvert$

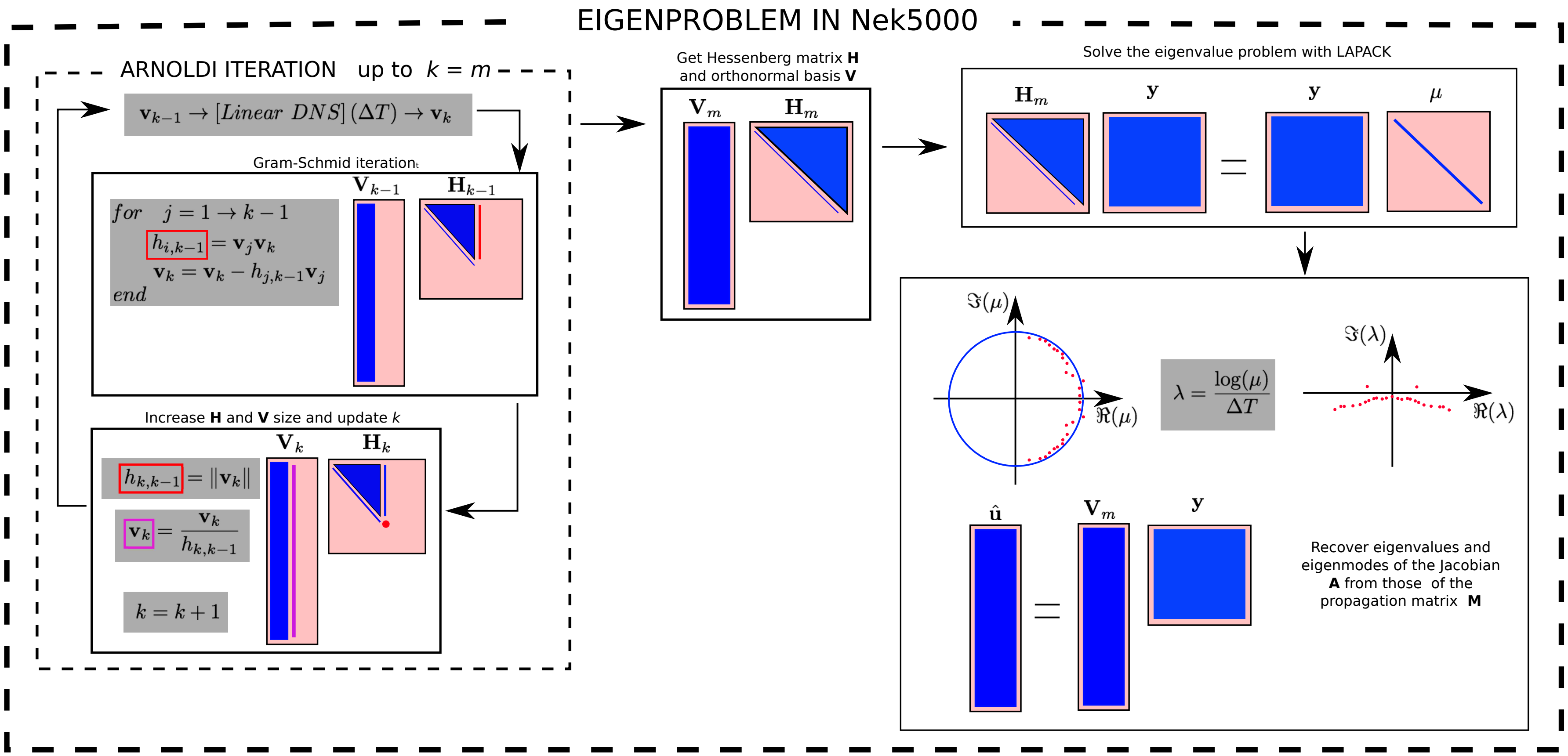

Figure III.13: Arnoldi algorithm implemented in the Nek5000 by Loiseau et al. (2014). A matrix representation of each step in table III.4 is here depicted.

Krylov-Schur decomposition

One limitation of the Arnoldi decomposition is however that the dimension m of the Krylov subspace necessary to converge the leading Ritz pairs is not known a priori. It might hence be relatively large, thus potentially causing some numerical and/or practical problems (e.g. storage of Krylov basis $\mathbf{V}_m$, forward instability of the Gram-Schmidt process involved in the Arnoldi decomposition, etc). Different approachs could be used to overcome this problem (e.g. Implicitly Restarted Arnoldi Method (Barkley et al., 2008; Sorensen, 1992)). In the present work the Krylov-Schur decomposition (Stewart, 2002) has been adopted for the sake of simplicity in its implementation. The Krylov-Schur method is based on the generalization of the m-step Arnoldi factorization (III.38) to a Krylov decomposition of order m,

$$\mathbf{M}\mathbf{V}_m = \mathbf{V}_m\mathbf{B}_m + \mathbf{v}_{m+1}\mathbf{b}_{m+1}^T \tag{III.39}$$

in which the matrix $\mathbf{B}_m$ and the vector $\mathbf{b}_{m+1}$ have no restriction. The Arnoldi decomposition then appears as a special case of Krylov decomposition when $\mathbf{B}_m$ is restricted to be in upper Hessenberg form and $\mathbf{b}_{m+1} = \mathbf{e}_m$. Another special case is the krylov-Schur decomposition in which the matrix $\mathbf{B}_m$ is in real Schur form (*i.e.* quasi-triangular form with its eigenvalues in the matrix 1×1 or 2×2 diagonal blocs). The Krylov and the Arnoldi decomposition are equivalents i.e. they have the same Ritz approximation. Moreover, by means of orthogonal similarity transformations, any Krylov decomposition can be transformed into an equivalent Krylov-Schur decomposition. The core of the Krylov-Schur method is thus based on a two-steps procedure: (i) an expansion step performed using a m-step Arnoldi factorization, and (ii) a contraction step to a Krylov-Schur decomposition of order p retaining only the most useful spectral information from the initial m-step Arnoldi decomposition. Given an initial unit-norm vector $\mathbf{v}_1$, a subroutine to compute the matrix-vector product $\mathbf{M}\mathbf{v}_i$, and the desired dimension m of the Krylov subspace, the Krylov-Schur method can be summarized as follows:

1. Construct an initial Krylov decomposition of order m using for instance the m-step Arnoldi factorization (III.38).

2. Check for the convergence of the Ritz eigenpairs. If a sufficient number has converged, then stop. Otherwise, proceed to step 3.

3. Compute the real Schur decomposition $\mathbf{B}_m = \mathbf{Q}\mathbf{S}_m\mathbf{Q}^T$ such that the matrix $\mathbf{S}_m$ is the real Shurl form and $\mathbf{Q}$ is the associated matrix of Shurl vectors. It is assumed furthermore that the Ritz values on the diagonal blocks of $\mathbf{S}_m$ have been sorted such that the p "wanted" Ritz values are in the upper-left corner of $\mathbf{S}_m$, while the $m - p$ "unwanted" ones are in the lower-right corner. At this point we have the following re-ordered Krylov-Schur decomposition as shown in figure III.14. In figure III.14 $\tilde{\mathbf{V}}_m = \mathbf{V}_m\mathbf{Q}$ is the re-ordered krylov basis, $\mathbf{S}_{11}$ the subset of the Schur matrix containing the p "wanted" Ritz values, $\mathbf{S}_{22}$ the subset containing the $m-p$ "unwanted" ones, and $[\mathbf{b}_1^T\mathbf{b}_2^T] = \mathbf{b}^T\mathbf{Q}$.

4. Truncate the Krylov-Schur decomposition (see fig. III.14) of order m to a Krylov decomposition of order p like in fig. III.15,

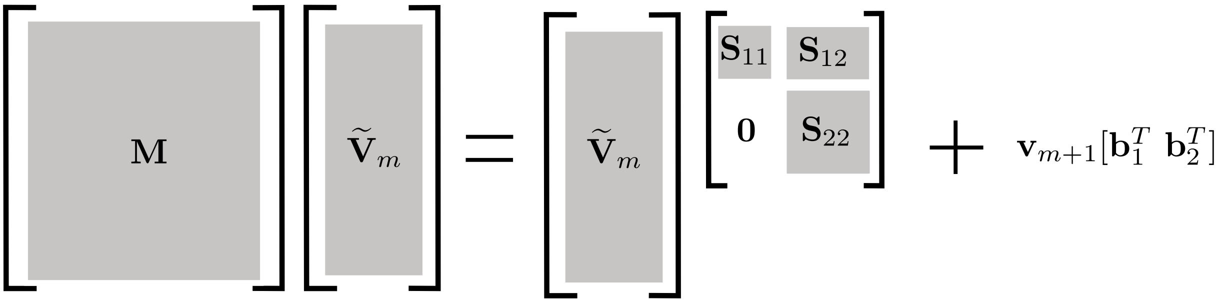

Figure III.14: matrix representation of the Shurl decomposition.

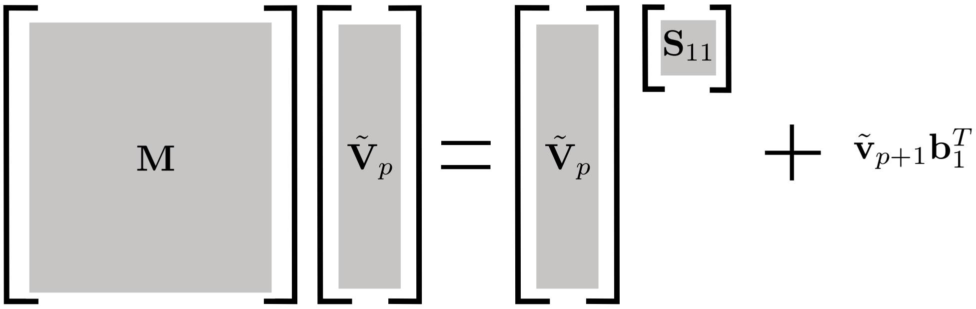

Figure III.15: Truncated krylov-Shurl decomposition.

with $\tilde{\mathbf{V}}_p$ equal to the first p columns of $\tilde{\mathbf{V}}_m$ and $\tilde{\mathbf{v}}_{p+1} = \mathbf{v}_{m+1}$.

5. Extend again to a Krylov decomposition of order m using a variation of the procedure used in the first step: the procedure is re-initialized with the starting vector $\tilde{\mathbf{v}}_{p+1}$ but all the vectors in $\tilde{\mathbf{V}}_p$ are taken into account in the orthogonalization step.

6. Check the convergence of the Ritz values. If not enough Ritz values have converged, restart from step 3.

This algorithm has two critical steps. The first one is the choice of the "wanted" Ritz values in the re-ordering of the Schur decomposition in step 2. Since we are only interested in the leading eigenvalues of the linearized Navier-Stokes operator, all the Ritz pairs being classified as "wanted" must satisfy $\|\mu_w\| \geq 1 - \delta$ (with $\delta = 0.05$ usually). In any case, other logical constrain can be added (e.g. keep the eigenmode in a range ofω). Regarding the criterion assessing the convergence of a given Ritz pair, starting from the Krylov decomposition (III.38), one can write

$$\|\mathbf{M}\mathbf{V}_m\mathbf{y} - \mathbf{V}_m\mathbf{B}_m\mathbf{y}\| = \|\mathbf{M}\mathbf{V}_m\mathbf{y} - \mu_{\mathbf{B}}\mathbf{V}_m\mathbf{y}\| = \|\beta\mathbf{e}_m^T\mathbf{y}\| \tag{III.40}$$

with $(\mu_{\mathbf{B}}, \mathbf{y})$ a given eigenpair of the matrix $\mathbf{B}_m$. A consequence of realtion (III.40) is that if its right hand side $\|\beta\mathbf{e}_m^T\mathbf{y}\|$ is smaller than a given tolerance, then the Ritz pair $(\mu_{\mathbf{B}}, \mathbf{V}_m\mathbf{y})$ provides a good approximation to the eigenpair $(\mu, \hat{\mathbf{u}})$ of the original matrix $\mathbf{M}$. Herein, a Ritz value is considered as being converged if the associated residual $\|\beta\mathbf{e}_m^T\mathbf{y}\| \leq 10^{-6}$. The numerical implementation of the Krylov-Schur decomposition used relies on the basic Arnoldi factorization presented in Loiseau's work (Loiseau et al., 2014) and on the LAPACK library (Andersen et al., 1999) for the linear algebra computations

(Schur and Eigenvalue decompositions). The matrix representation of the Krylov-Schur algorithm implemented in Nek5000 is depicted in figure III.16.

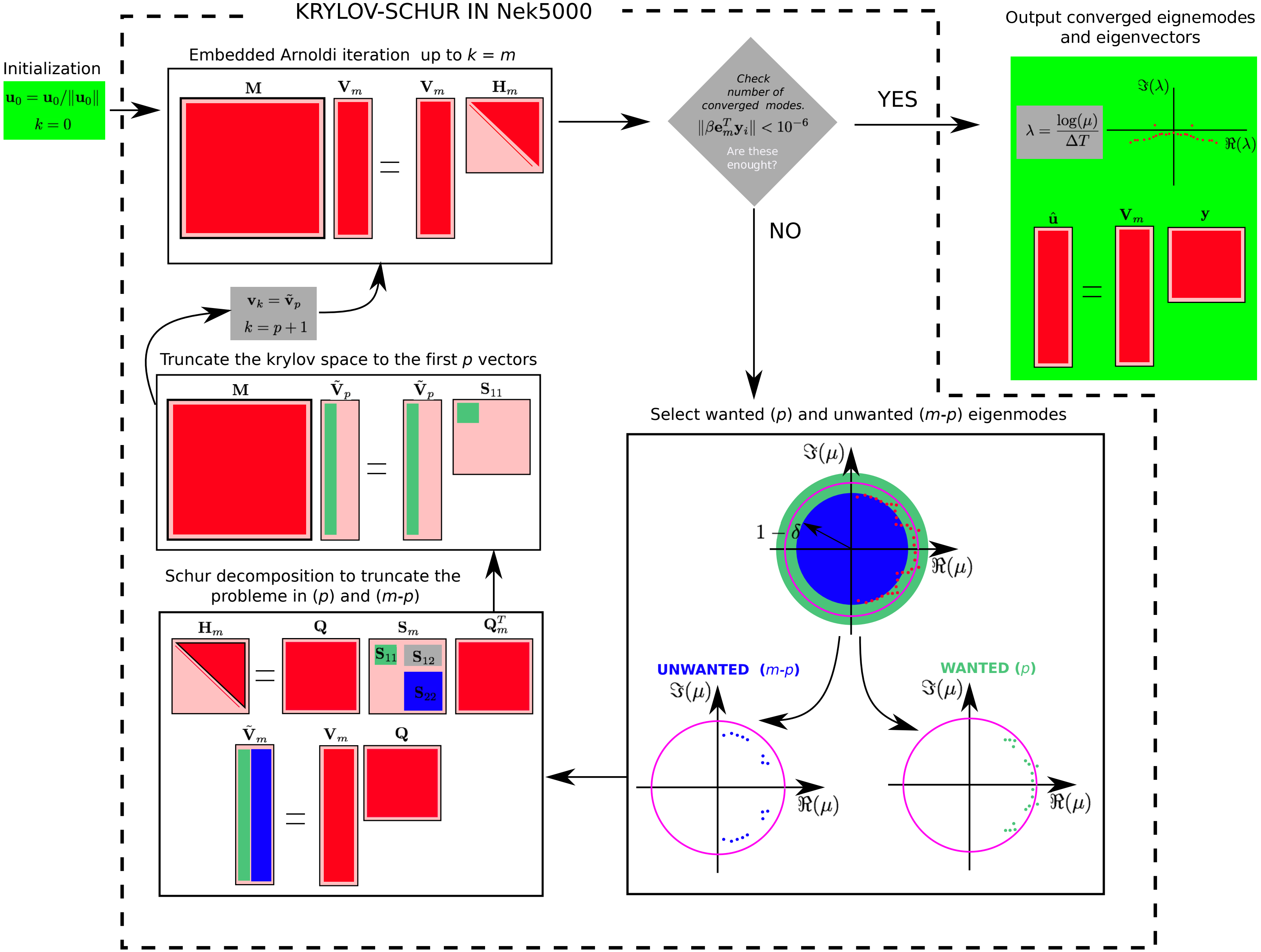

Figure III.16: Krylov-Schur decomposition algorithm implemented in the Nek5000. A matrix representation of each Krylo-Schur step is here depicted.

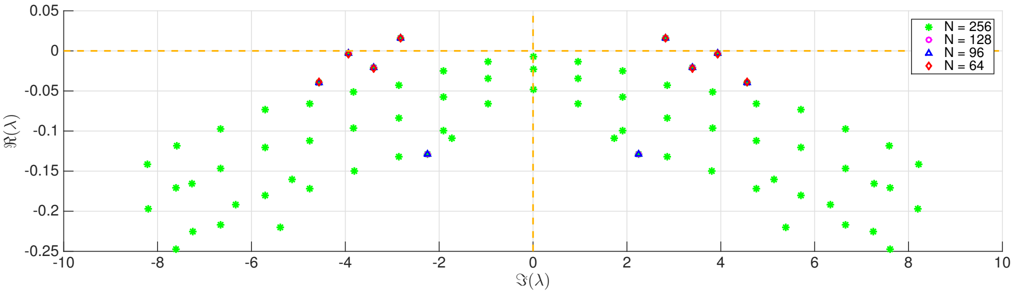

Figure III.17: Eigenspectrum for 2D lid-driven cavity case at $Re = 8500$. for the four cases $N = 256$ (green), $N = 128$ (magenta), $N = 96$ (blue) and $N = 64$ (red) the convergence of the leading eigenmode is always ensured.

Validation and performances

To understand the potential of the Krylov-Schur algorithm, the 2D lid-driven cavity has been used as test-case. The lid-driven cavity is a case highly studied in bibliography, it presents a first unstable global mode at $Re_c = 8135$ (Robinet et al., 2005). The $Re = 8500$ has been chosen for the parametric study. The element mesh is composed by 10 elements with a polynomial reconstruction of order 8 within each element. To illustrate the dependency of the Krylov space with the number of the converged eigenmodes four different Krylov dimensions have been considered, $N = 64,\ 96,\ 128,$ and 256. For the four cases the Krylov-Schur procedure stops when the required convergence 10^{-6} is reached for at least 8 eigenvectors. The obtained eigenspectrum for the four considered cases is shown in figure III.17.

It can be observed how for the four cases the convergence of the most unstable eigenmode is always ensured. The Krylov-Schur performance are summarised in table III.3.2.1.

m	converged modes	Shur iterations
256	77	0
128	10	2
96	10	3
64	8	6

Table III.5: Krylov-Schur performance

With $N = 256$ the constraint on the converged modes is satisfied already by the Arnoldi decomposition and no supplementary Schur decompositions are required. Decreasing the Krylov subspace the number of the Schur decomposition involved in the eigenvalues evaluation increases. With this method it is possible to increases drastically the number of the converged eignemodes with a fixed Krylov subspace that for a 3D problem can be a bottle neck for the memory required to store it. Unfortunately with this procedure the control on the time computation to reach convergence is lost. It is impossible to know how many Schur iteration are necessary to give to the orthonormal basis the good orientation before getting that capable of ensuring the minimum number of converged modes.

III.3.2.2 Pseudospectrum from Hessenberg matrix

The computation of the pseudospectrum is much more expensive of the eigenvalue decomposition. Following Toh and Trefethen (1996) it is possible to use the Hessenberg matrix to have an approximation of the pseudospectrum as in eq. (III.41).

$$\Lambda_\epsilon(\mathbf{A}) = \{z \in \mathbb{C} : \|(z\mathbf{I} - \mathbf{A})^{-1}\| > \epsilon^{-1}\} \approx \{z \in \mathbb{C} : \lambda_{min}(z\mathbf{I} - \log(\mathbf{H}))/\Delta T < \epsilon\}. \quad \text{(III.41)}$$

To get a good approximation of the pseudospectrum a large Krylov space has to be taken into account (Toh and Trefethen, 1996). For a non-normal operator the amplitude response ϵ^{-1} is higher than a normal case because many eigenvectors are involved. Eq. II.43 gives an idea of the contribution of each eigenmode when a generic forcing is applied. The pseudospectrum accuracy relies to the capability of the Arnoldi algorithm to take into account in the Hessenberg matrix the non normalities of Jacobian operator. Unfortunately, this task is not accomplished by the Hessenberg matrix, since a simple singular value decomposition of the Hessenberg matrix does not give an approximation of the optimal perturbation gain and a simple transconjugation of the Hessenberg matrix does not provide an approximation of the adjoint operator. For an openflow, such as a boundary layer, a huge number of eigenmodes and a large Krylov space has to be taken into account to have a basis representative of the optimal perturbation (Alizard and Robinet, 2011). Another consideration has to be done: using a the time-stepping method the Jacobian matrix is not directly handled, but instead the scalar product $\mathbf{Av}$ is achieved with a numerical simulation. For this reason, the pseudospectrum takes also into account the *numerical sensibility* of the method used for the time integration. An improvement can be achieved if an invariant subspace is considered to project the Jacobian. Let $\mathbf{U}$ be a subset of $n \times m$ selected eigenvalues of $\mathbf{M}$ and $\mathbf{QR}$ its qr decomposition then a reduced $m \times m$ matrix of $\mathbf{M}$ can be achieved by:

$$\mathbf{Q}^T\mathbf{M}\mathbf{Q} = \mathbf{U}^T\mathbf{M}\mathbf{U}\mathbf{R}^{-1} = \mathbf{U}^T\mathbf{U}\mathbf{D}\mathbf{R}^{-1} = \mathbf{R}\mathbf{D}\mathbf{R}^{-1} \quad \text{(III.42)}$$

$\mathbf{D}$ being the diagonal matrix containing the eigenvalues μ of $\mathbf{M}$. The evaluation of the pseudospectrum onto the upper-diagonal matrix $\mathbf{RDR}^{-1}$ has the same accuracy of the pseudospectrum evaluated on the Hessenberg matrix with a Krylov space twice as big (Toh and Trefethen, 1996).

III.3.2.3 Other decompositions

The global stability analysis just presented allows to decompose the linear flow dynamics around a steady state in spatial structures (eigenvectors) at which a temporal evolution (eigenvalue) is associated. If we are not interested in the characterization of the stability of the system, other decompositions can be considered and applied directly to the nonlinear system.

Proper Orthogonal Decomposition

Omitting the description of the well known *Fourier transform* to get Fourier modes, an important decomposition highly used in fluid dynamic system is the *Proper Orthogonal Decomposition* (POD) (Berkooz et al., 1993). The POD has been used in turbulent flows

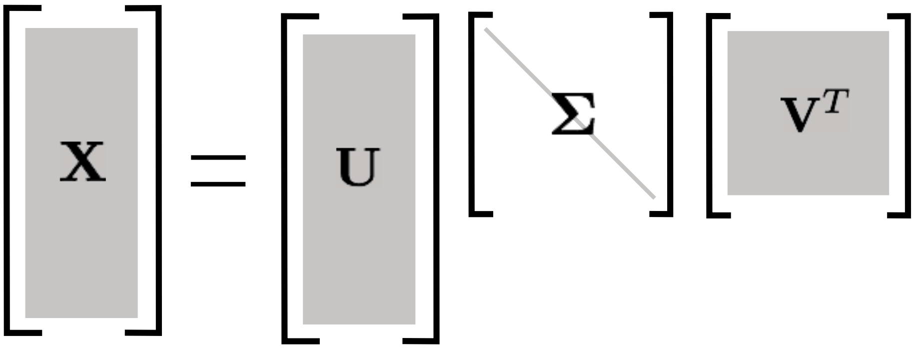

Figure III.18: Structure of the matrices resulting from singular value decomposition.

to highlight spatial uncorrelated structures that give an order to apparent complex flow. From a statistical point of view a POD base defines an orthonormal space in which at each mode is associated a variance. Giving a set of N snapshots $\mathbf{X} = \{\mathbf{x}_1, \ldots, \mathbf{x}_N\}$ representing the flow field at different times, the associated spatial POD modes can be found as the eigenvectors of the spatial correlation matrix $\mathbf{X}\mathbf{X}^T$, after removing its average

$$\mathbf{x}_i = \mathbf{x}_i - \frac{1}{N}\sum_{i=1}^{N}\mathbf{x}_i \qquad \text{(III.43)}$$

by using the definition of variance. The correlation matrix is Hermitian, then it is a positive and symmetric matrix. For this reason its eigenvectors and eigenvalues are real. The eigenvectors of the chronos correlation matrix $\mathbf{X}^T\mathbf{X}$ provide the temporal evolution of the i^{th} POD mode. More generally the POD decomposition is accomplished by a singular value decomposition (SVD) of the observable flow fields $\mathbf{x}_i$ that decomposes the $n \times N$ matrix $\mathbf{X}$ in three parts (see also figure III.18):

- **U**: a $n \times N$ matrix whose columns are orthonormal one to another. Each of these columns then contains one of the so-called POD modes.
- **Σ**: a real-valued $N \times N$ diagonal matrix containing the singular values. The i^{th} singular value indicates the importance in terms of variance of the i^{th} POD mode from **U** in the initial sequence of data.
- **V**: the $N \times N$ dynamic matrix. Its i^{th} row provides the temporal evolution of the i^{th} POD mode.

From an implementation point of view the POD decomposition is performed in two steps:

1. $[\mathbf{\Sigma}^2, \mathbf{V}] = eig(\mathbf{X}^T\mathbf{X})$,
2. $\mathbf{U} = \mathbf{X}\mathbf{V}\mathbf{\Sigma}^{-1}$.

In this way the direct SVD computation of $\mathbf{X}$ is avoided and only $\mathbf{N} \times \mathbf{N}$ matrices are handled. An example of POD decomposition for a 2D cylinder flow at $Re = 60$ is reported in figure III.19. 1000 velocity field snapshots have been used to evaluate the first 20 POD

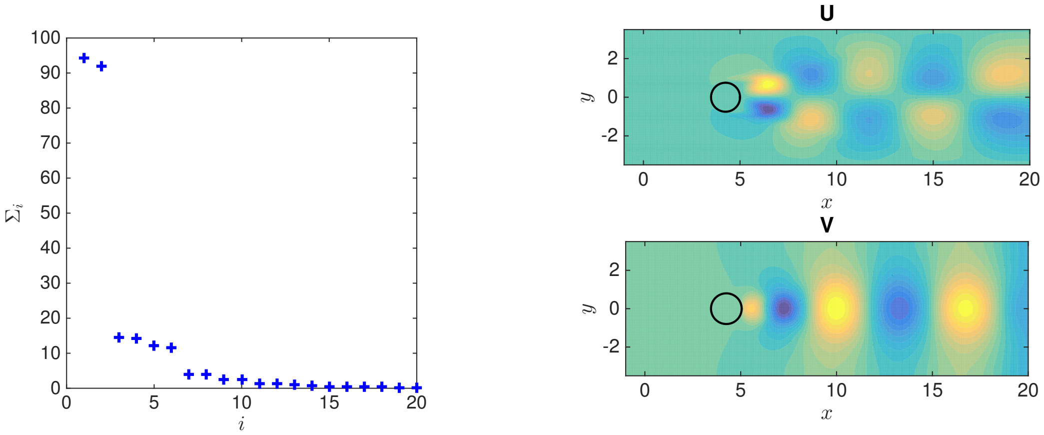

(a) POD spectre (b) First POD mode

Figure III.19: Example of POD decomposition for 2D cylinder case at $Re = 60$. The dataset is taken on the limit cycle of the Von-Karman shedding. 1000 velocity field snapshot has been used to evaluate the first 20 POD modes.

modes. Only few modes have an important role in the representation of the unsteady dynamics. To quantify the number of modes necessary to represent the unsteady behaviour, one can refers to the the Frobenius norm of **X** as

$$\|\mathbf{X}\|_F = \sqrt{\sum_{i=1}^{n}\sum_{j=1}^{N}|x_{ij}|^2} = \sqrt{\Sigma_1^2 + \Sigma_2^2 + \ldots + \Sigma_N^2}. \tag{III.44}$$

The $0.98\|\mathbf{X}\|_F$ is ensured by keeping just the first 12 POD modes.

Dynamic mode decomposition

At each POD mode many frequencies can be associated, but for a physical interpretation of the spatial structure it could be interesting to find spatial structures at which just one frequency is associated. This task is carried out by the *Koopman theory* (Koopman, 1931). Considering the non-linear dynamical system

$$\mathbf{x}_{k+1} = \mathbf{f}(\mathbf{x}_k) \tag{III.45}$$

the Koopman theory states that is always possible to define an infinite linear operator (*Koopman operator*) that captures all the main features of a nonlinear dynamical system

$$\mathbf{M}\mathbf{x}_k = \mathbf{f}(\mathbf{x}_k). \tag{III.46}$$

The eigenfunctions of **M** define a (nonlinear) change of coordinates in which the system becomes linear. This means that the solution $\mathbf{x}_{k+1}$ is a linear combination of the eigenfunction of **M**. Therefore the dynamics of a non-linear system can be investigated by studying its associated *Koopman eigenfunctions*. Starting from a discrete-time setting of data it is possible to build an approximation of the Koopman eigenvectors (Rowley et al., 2009; Schmid, 2010). The *Dynamic Mode Decomposition* (DMD) (Schmid, 2010) is an algorithm introduced by Schmid and Sesterhenn (2008) that computes an approximation of

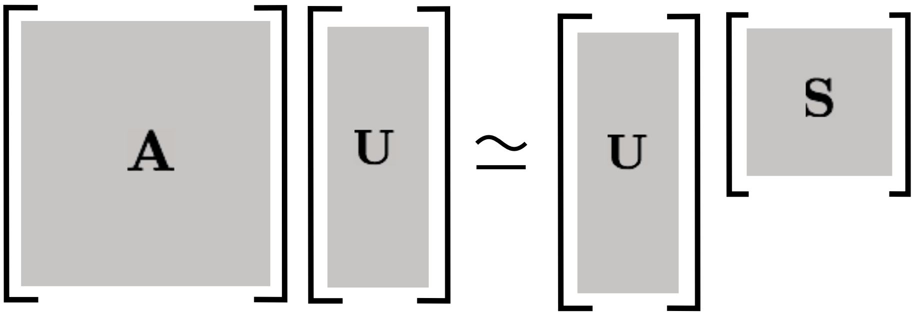

Figure III.20: Structure of the matrices resulting from DMD.

such eigenvectors starting from data acquired from numerical simulation or experiments. Given a dataset of fluid fields $\mathbf{x}_j = \mathbf{x}(j\Delta t)$ at k different time steps such that:

$$\mathbf{K} = [\mathbf{x}_0, \mathbf{x}_1, \dots, \mathbf{x}_{k-1}] \tag{III.47}$$

the DMD goal is to find an approximation of the linear operator $\mathbf{A}$ that approximates the time-discrete dynamical system and providing:

$$\mathbf{x}_{i+1} = \mathbf{A}\mathbf{x}_i. \tag{III.48}$$

The $\mathbf{A}$ matrix might not be directly accessible and if the three velocity components are considered, it may have a dimension higher than that of the Jacobian matrix. To overcome this problem let us consider the flow field sequence

$$\mathbf{X} = [\mathbf{x}_0, \mathbf{x}_1, \dots, \mathbf{x}_{k-2}] \tag{III.49}$$

and the one shifted in time

$$\mathbf{Y} = [\mathbf{x}_1, \mathbf{x}_2, \dots, \mathbf{x}_{k-1}] \tag{III.50}$$

the operator $\mathbf{A}$ has to be defined such that

$$\mathbf{A}\mathbf{X} = \mathbf{Y}. \tag{III.51}$$

At this point the singular value decomposition $svd(\mathbf{X}) = \mathbf{U}\mathbf{\Sigma}\mathbf{V}^T$ is invoked to keep just the first m "most important" modes discarding the spatial structures with low variance

$$\mathbf{A}\mathbf{U}\mathbf{\Sigma}\mathbf{V}^T = \mathbf{Y} \tag{III.52}$$

$$\mathbf{U}^T\mathbf{A}\mathbf{U} = \mathbf{U}^T\mathbf{Y}\mathbf{V}\mathbf{\Sigma}^{-1} = \mathbf{S} \tag{III.53}$$

The $\mathbf{S}$ matrix is a small $m \times m$ matrix that approximates the Koopman operator $\mathbf{A}$ see fig III.20.

As a consequence, the eigenpairs $(\mu_c, \mathbf{\Gamma})$ of the matrix $\mathbf{S}$ are a reasonably good approximation of the eigenpairs $(\mu, \mathbf{\Phi})$ of the operator $\mathbf{A}$ since:

$$\begin{cases} \mu \simeq \mu_c \\ \mathbf{\Phi} \simeq \mathbf{U}\mathbf{\Gamma} \end{cases} \tag{III.54}$$

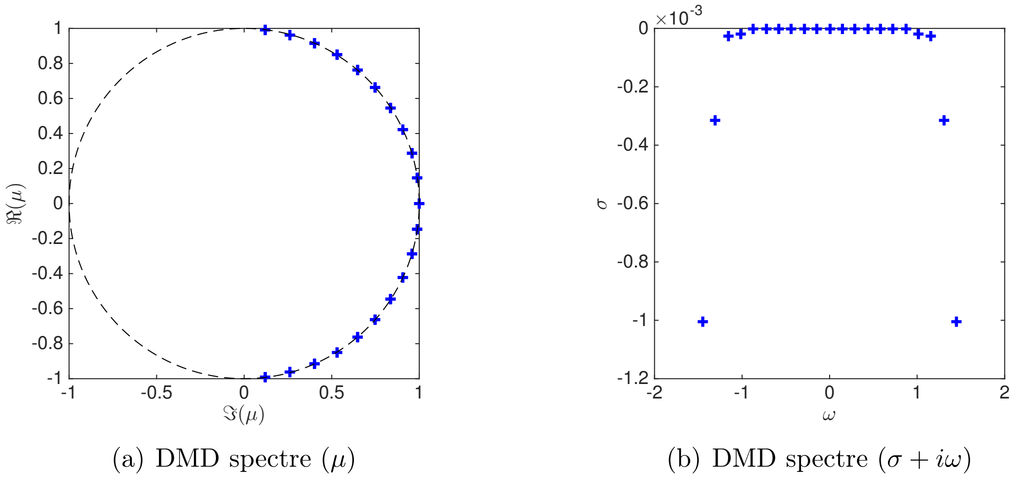

(a) DMD spectre (μ) (b) DMD spectre ($\sigma + i\omega$)

Figure III.21: Example of DMD decomposition for 2D cylinder case at $Re = 60$. The dataset is taken on the limit cycle of the Von-Karman shedding. 1000 velocity field snapshots have been used to evaluate the first 21 DMD modes.

As for global stability analysis, the growth rate and the circular frequency of the DMD modes can be recovered by:

$$\sigma + i\omega = \frac{\log(\mu)}{\Delta t} \tag{III.55}$$

Δt being the sampling period between two snapshots of the observables. In figure III.21 the DMD spectre is depicted both for μ and $\sigma + i\omega$. Since the velocity snapshots have been taken on the limit cycle of the Von-Karman shedding, all the DMD modes turn out to have $\sigma \leq 0$. If for the POD decomposition is straightforward to understand the "importance" of each spatial mode in the unsteady dynamics, this information it is not directly accessible in the DMD spectrum as it seems that all modes play the same role with the same "importance". Jovanović et al. (2014) proposed a way to assign a weight at each DMD mode. Consider the reduced system

$$\mathbf{x}_t = \mathbf{S}\mathbf{x}_0 \tag{III.56}$$

where $\mathbf{x}_0 = \mathbf{U}^T\mathbf{X}_0$ then the $\mathbf{S}$ matrix can be decomposed in a basis of its eigenvectors and eigenvalues

$$\mathbf{S} = \mathbf{\Gamma}\mathbf{D}_\mu\mathbf{Z} \tag{III.57}$$

where the $\mathbf{\Gamma}$ columns (γ_i) are the right eigenvectors of $\mathbf{S}$, $\mathbf{D}_\mu$ is the diagonal matrix containing the eigenvalues and the $\mathbf{Z}$ rows (z_i^*) [2] are the left eigenvectors of $\mathbf{S}$ or the right eigenvectors of $\mathbf{S}^T$. The solution to (III.56) can be found as

$$\mathbf{x}_t = \mathbf{\Gamma}\mathbf{D}_\mu\mathbf{Z}\mathbf{x}_0 = \sum_i^m \gamma_i\mu_i z_i^*\mathbf{x}_0 = \sum_i^m \gamma_i\mu_i\alpha_i \tag{III.58}$$

where $\alpha_i = z_i^*\mathbf{x}_0$ represent the weight associated to the mode γ_i for the evolution of the initial condition $\mathbf{x}_0$. Because of $\Phi_i = \mathbf{U}\gamma_i$ each velocity snapshot can be approximated by

---

[2] The z_i^* vector has to be normalized such that the bi-orthogonality condition $z_i^*\gamma_i = \delta_{ij}$ is respected.

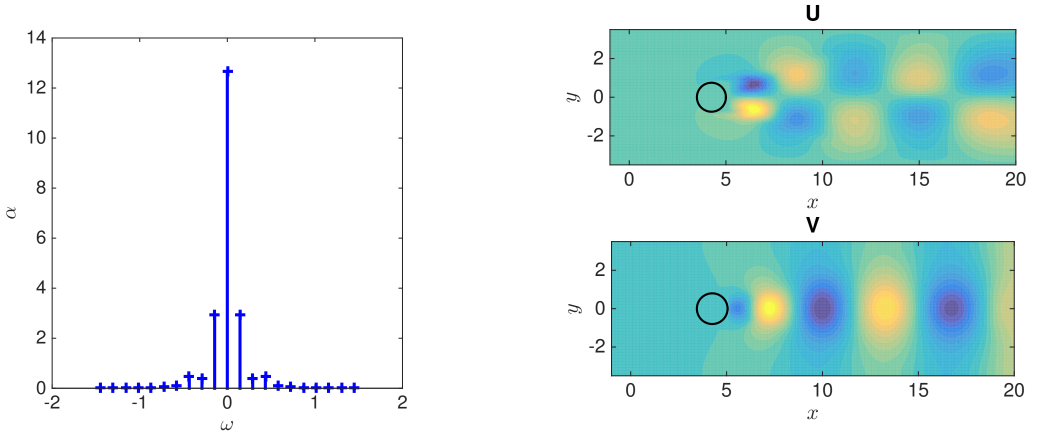

(a) DMD weight α_i (b) Real part of first DMD unsteady mode

Figure III.22: Modal contribution of DMD modes (a) for 2D cylinder case at $Re = 60$. Firt unsteady DMD mode (b).

a linear composition of the DMD mode III.22.

$$\mathbf{X}_t \approx \mathbf{U}\mathbf{x}_t = \sum_i^m \Phi_i \mu_i \alpha_i \tag{III.59}$$

The DMD spectrum of the case in figure III.21 with the relative α_i weights is shown in figure III.22.

III.4 Transient growth analysis

III.4.0.1 SVD-Arnoldi

For the optimal perturbation analysis the procedure explained in section §II.3.1 has to be followed. To solve the eigenvalue problem the propagation matrix $\mathbf{M}$ and its adjoint $\mathbf{M}^+$ need to be stored. Again, the required memory is inaccessible and the whole exponential propagation matrix cannot be computed as explained in the book Schmid and Henningson (2012). A time-stepping approach has to be used once again. The main idea is to build up a reduced order matrix of $\mathbf{M}^+\mathbf{M}$ as suggested by Barkley et al. (2008). By taking advantage of the already implemented Arnoldi and Krylov-Schur algorithm, it is possible to build an Hessenberg matrix whose eigenvalues are representative of those of $\mathbf{M}^+\mathbf{M}$ (see fig. III.23). The Arnoldi algorithm is still unchanged, the only modification to do is on the evaluation of the new vector in the Krylov space. Starting from $\mathbf{v}_{k-1}$, this is done in two steps:

1. Evaluate $\mathbf{v}_k^* = \mathbf{M}\mathbf{v}_{k-1}$ with a linear Navier-Stokes solver using $\mathbf{v}_{k-1}$ as initial condition and iterating forward in time from $t = 0$ to $t = T$. Being T the target time of interest.

2. Evaluate $\mathbf{v}_k = \mathbf{M}^+\mathbf{v}_k^*$ with an adjoint Navier-Stokes solver using $\mathbf{v}_k^*$ as initial condition and iterating backward in time from $t = T$ to $t = 0$.

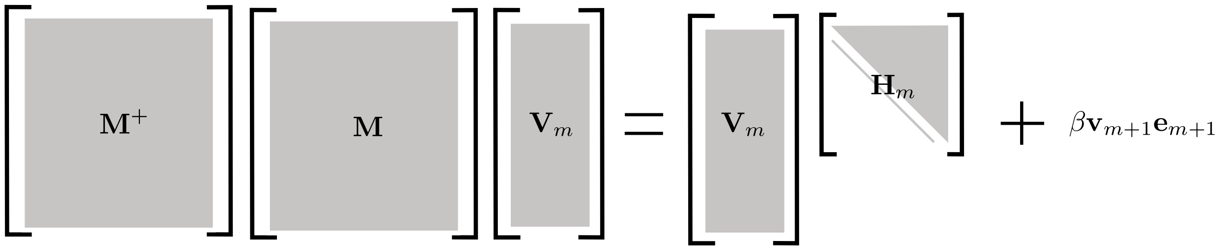

Figure III.23: Hessenberg matrix for optimal perturbation computed by SVD-Arnoldi.

The i^{th} eigenvalue of the Hessenberg matrix μ_H is the energy gain at $t = T$ associated at the eigenvector i^{th} $\mathbf{u}_0$ if it is used as initial condition at $t = 0$. The eigenvector corresponding to the $max(\mu)$ is the optimal perturbation and the others are sub-optimal. Note that the solution of the eigenvalue problem (III.60)

$$\mathbf{M}^+\mathbf{M}\mathbf{u}_0 = \Lambda \mathbf{u}_0 \tag{III.60}$$

is equivalent to the singular value decomposition

$$\mathbf{M}\mathbf{u}_0 = \Lambda \mathbf{u}_T \tag{III.61}$$

for this reason this algorithm is also known as SVD-Arnoldi. With an SVD decomposition it is possible to directly access to the perturbation at the target time $\mathbf{u}_T$. Solving the eigenvalue problem $\mathbf{u}_T$ can be recovered in a second step just using $\mathbf{u}_0$ as initial condition for a linear Navier-Stokes solver integrating forward up to $t = T$.

III.4.0.2 Optimization problem

The geometrical interpreeation of the optiaml perturbation has been given in section §II.3.1 and technical procedure to evaluate it has been explained in the previous section. Up now nothing has been said on the continuous adjoint Navier-Stokes equation. Actually, adjoint state is a concept originating from the optimisation theory. In the hydrodynamic instability framework, adjoint-bsed methods can be used to identify optimal perturbations, highlight the most receptive path to break down, select the most destabilising base flow defect in an otherwise stable configuration, and map the structural sensitivity of an oscillator. All of these uses have been reviewed by Luchini and Bottaro (2014).

Focusing on the optimization problem, an optimization loop can be setted to reach an *objective function*. In our case the objective function is still maximising the kinetic energy at the time T

$$\mathcal{L} = \langle \mathbf{u}_T, \mathbf{u}_T \rangle \tag{III.62}$$

A Lagrange function (Zuccher et al., 2004) can now be defined to take into account the objective function enforced by the *constrains*. Precisely, the optimal perturbation $\mathbf{u}_0$ need to satisfy:

- it must be solution of the linearised Navier-Stokes equation,
- it must have unit norm,

- it must be divergence-free.

The Lagrangian function then reads

$$\mathcal{L}(\mathbf{u},p,\mathbf{u}^\dagger,p^\dagger,\lambda)=\underbrace{\langle\mathbf{u}_T,\mathbf{u}_T\rangle}_{\text{objective}}\underbrace{-\int_0^T\langle\mathbf{u}^\dagger,\left(\frac{\partial\mathbf{u}}{\partial t}-\mathbf{NS}(\mathbf{U}_b,\mathbf{u},p)\right)\rangle dt-\lambda(\langle\mathbf{u}_0,\mathbf{u}_0\rangle-1)-\langle p^\dagger,\nabla\cdot\mathbf{u}_0\rangle}_{\text{constrains}} \tag{III.63}$$

$\mathbf{u}^\dagger$, $p^\dagger$ and λ being the Lagrangian multipliers (or adjoint variables) and $\mathbf{NS}$ stands for the linearised Navier-Stokes equation. Note that the quadratic objective defines a convex problem and then the existence and uniqueness of the optimal solution. To find the maximum of the functional $\mathcal{L}$ it is necessary to impose its variation equal to zero

$$\delta\mathcal{L}=\left(\frac{\partial\mathcal{L}}{\partial\mathbf{u}},\delta\mathbf{u}\right)+\left(\frac{\partial\mathcal{L}}{\partial\mathbf{u}^\dagger},\delta\mathbf{u}^\dagger\right)+\left(\frac{\partial\mathcal{L}}{\partial\lambda}\right)\delta\lambda+\left(\frac{\partial\mathcal{L}}{\partial p^\dagger}\right)\delta p^\dagger+\left(\frac{\partial\mathcal{L}}{\partial p}\right)\delta p=0. \tag{III.64}$$

This is accomplished only when each term is simultaneously equal to zero. For each variation we get the following optimization system

$$\frac{\partial\mathcal{L}}{\partial\lambda}:=\langle\mathbf{u}_0,\mathbf{u}_0\rangle=1 \tag{III.65a}$$

$$\frac{\partial\mathcal{L}}{\partial\mathbf{u}^\dagger}:=\frac{\partial\mathbf{u}}{\partial t}+(\mathbf{u}\cdot\nabla)\mathbf{U}_b+(\mathbf{U}_b\cdot\nabla)\mathbf{u}+\nabla p-\frac{1}{Re}\Delta\mathbf{u}=0 \tag{III.65b}$$

$$\frac{\partial\mathcal{L}}{\partial p^\dagger}:=\nabla\cdot\mathbf{u}=0 \tag{III.65c}$$

$$\frac{\partial\mathcal{L}}{\partial\mathbf{u}}:=\frac{\partial\mathbf{u}^\dagger}{\partial t}+(\mathbf{U}_b\cdot\nabla)\mathbf{u}^\dagger-(\nabla\mathbf{U}_b)^T\mathbf{u}^\dagger+\nabla p-\frac{1}{Re}\Delta\mathbf{u}^\dagger=0 \tag{III.65d}$$

$$\frac{\partial\mathcal{L}}{\partial p}:=\nabla\cdot\mathbf{u}^\dagger=0 \tag{III.65e}$$

$$\frac{\partial\mathcal{L}}{\partial\mathbf{u}(T)}:=\mathbf{u}(T)-\mathbf{u}^\dagger(T)=0 \tag{III.65f}$$

$$\frac{\partial\mathcal{L}}{\partial\mathbf{u}(0)}:=\mathbf{u}(0)-\lambda^{-1}\mathbf{u}^\dagger(0) \tag{III.65g}$$

Equations (III.65a), (III.65b), (III.65c) are the original constraints of the optimization problem. Equation (III.65d) and (III.65e) are the adjoint Navier-Stokes equations obtained by integration by parts of the first constraint in the functional (III.63). The last two equation represent respectively the compatibility condition (III.65f) and the solution update (III.65f). Detailed mathematical steps are reported in Appendix VIII.2 for a non-linear optimal perturbation also implemented in Nek5000 (Farano et al., 2017). In many works the optimization approach is preferred to the SVD-Arnoldi due to its flexibility for complex optimization function and for the low memory required. The optimization problem is solved iteratively as shown in the block-diagram in figure III.25.

The system solved in the way depicted in figure III.25 with a simple re-normalization to update the solution, turns out to be a power iteration method to find the higher eigenvalue of the eigenproblem (III.60). Such way is the most common and simple way to update the

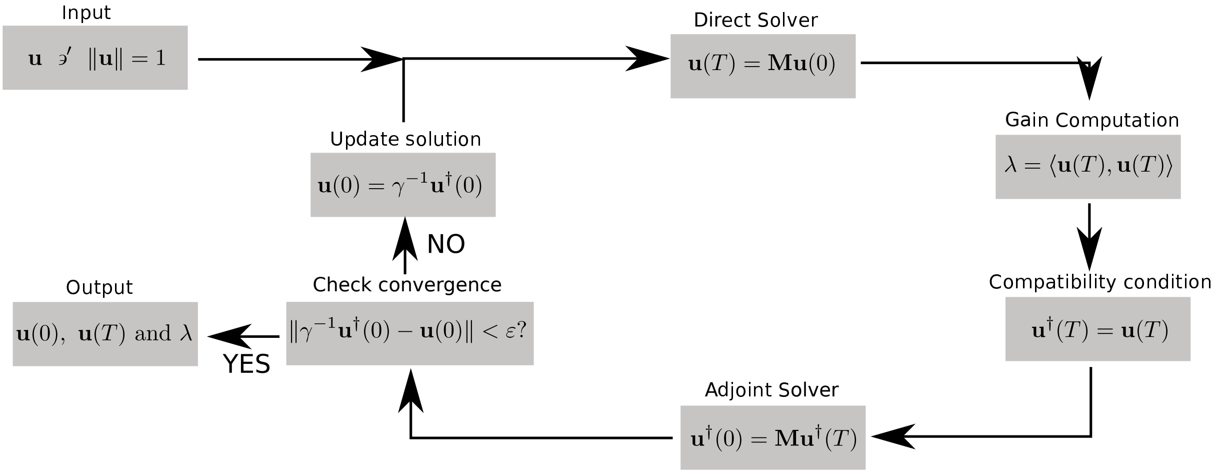

Figure III.24: Block diagram of direct-adjoint loop: power-iteration method.

solution (Cherubini et al., 2010a; Monokrousos et al., 2010; Pringle and Kerswell, 2010; Pringle et al., 2012). A gradient-based method can be used to accelerate the optimization convergence. The two most famous are the *steepest ascent* method and the *conjugate gradient* method. The algorithm used in the present work, the rotation update technique, is a modification of the steepest ascent method, based on geometric considerations, that has been used by Foures et al. (2013, 2014) and Farano et al. (2015, 2016, 2017). A schematic representation of this procedure is presented on figure III.25.

Let us consider the gradient (III.65g):

$$\frac{\partial \mathcal{L}}{\partial \mathbf{u}(0)} := \mathbf{u}(0) - \lambda^{-1}\mathbf{u}^{\dagger}(0) \tag{III.66}$$

In the following, the dependence on the time $t = 0$ will be dropped for the sake of simplicity. As can be seen, the current expression of the gradient depends on the Lagrange multiplier λ which value is unknown at the present time. One can however write down a mathematical expression of this gradient orthogonalised with respect to the input $\mathbf{u}$:

$$\frac{\partial \mathcal{L}}{\partial \mathbf{u}(0)}^{\perp} = \frac{\partial \mathcal{L}}{\partial \mathbf{u}(0)} - \frac{\langle \frac{\partial \mathcal{L}}{\partial \mathbf{u}(0)}, \mathbf{u} \rangle}{\langle \mathbf{u}, \mathbf{u} \rangle}\mathbf{u} \tag{III.67}$$

Introducing the analytical expression of the gradient (III.65g), the orthogonalised gradient can now be expressed as:

$$\frac{\partial \mathcal{L}}{\partial \mathbf{u}(0)}^{\perp} = (\mathbf{u}^{\dagger} - \lambda\mathbf{u}) - \frac{\langle (\mathbf{u}^{\dagger} - \lambda\mathbf{u}), \mathbf{u} \rangle}{\langle \mathbf{u}, \mathbf{u} \rangle}\mathbf{u} \tag{III.68}$$

$$\mathbf{u}^{\dagger} - \lambda\mathbf{u} - \frac{\langle \mathbf{u}^{\dagger}, \mathbf{u} \rangle}{\langle \mathbf{u}, \mathbf{u} \rangle}\mathbf{u} + \lambda\frac{\langle \mathbf{u}, \mathbf{u} \rangle}{\langle \mathbf{u}, \mathbf{u} \rangle}\mathbf{u} \tag{III.69}$$

After simplifications, the orthogonalised gradient finally reads:

$$\frac{\partial \mathcal{L}}{\partial \mathbf{u}(0)}^{\perp} = \mathbf{u}^{\dagger} - \frac{\langle \mathbf{u}^{\dagger}, \mathbf{u} \rangle}{\langle \mathbf{u}, \mathbf{u} \rangle}\mathbf{u} \tag{III.70}$$

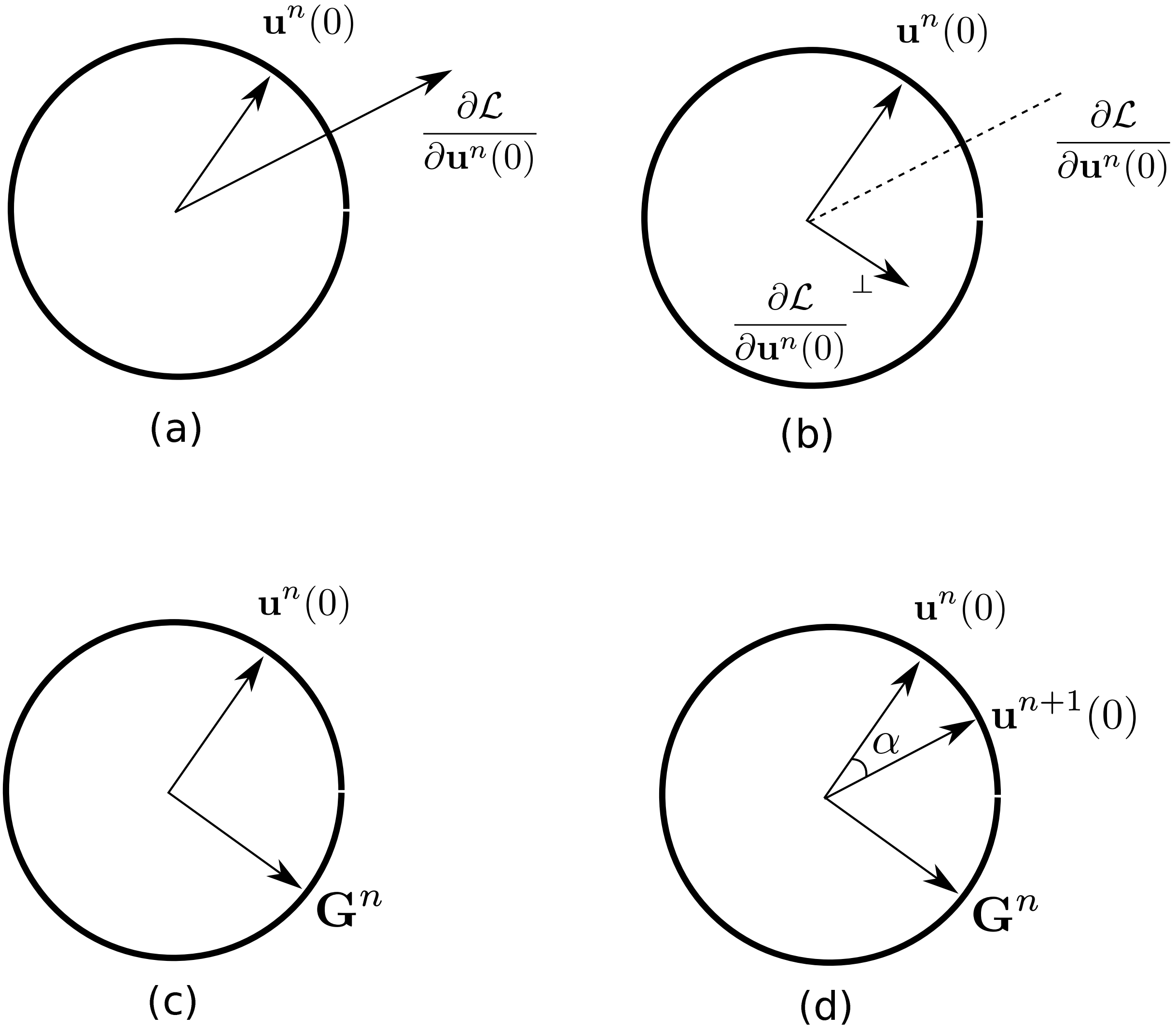

Figure III.25: Schematic representation of the rotation update method. (a) Compute the gradient $\frac{\partial \mathcal{L}}{\partial \mathbf{u}}$ of the Lagrange functional. (b) Orthogonalise the gradient with respect to $\mathbf{u}^n(0)$. (c) Compute $\mathbf{G}^n$, i.e. the orthogonalised gradient being normalised such that its energy is 1. (d) Update $\mathbf{u}^{n+1}(0)$ using a linear combination of $\mathbf{u}^n(0)$ and of the orthonormalised gradient $\mathbf{G}^n$

As one can see, the expression of the orthogonalised gradient (III.70) now solely depends on the direct variable $\mathbf{u}$ and the adjoint one $\mathbf{u}^{\dagger}$, while the dependence on the unknown Lagrange multiplier λ has been completely removed from the optimisation problem. Normalising this new gradient such that:

$$\mathbf{G}^n = \sqrt{\frac{1}{\langle \frac{\partial \mathcal{L}}{\partial \mathbf{u}(0)}^{\perp}, \frac{\partial \mathcal{L}}{\partial \mathbf{u}(0)}^{\perp} \rangle}} \frac{\partial \mathcal{L}}{\partial \mathbf{u}(0)}^{\perp} \tag{III.71}$$

now allows us to look for the update $\mathbf{u}^{n+1}$ as a simple linear combination of $\mathbf{u}^n$ and $\mathbf{G}^n$ given by:

$$\mathbf{u}^{n+1} = \cos(\alpha)\mathbf{u}^n + \sin(\alpha)\mathbf{G}^n \tag{III.72}$$

Since $\mathbf{u}^n$ and $\mathbf{G}^n$ form an orthonormal set of vectors, this update $\mathbf{u}^{n+1}$ now fulfils, directly by construction, the constraint on the initial energy (III.65a) without having a quadratic equation in λ to solve at each iteration of the optimisation loop as is the case in the classical steepest ascent method. To ensure the convergence of the method to the maximum of the functional, a check needs however to be put on the value of the angle α used for the update of the solution. Every calculation presented in this work has been started with $\alpha = \pi/4$. However, if the gain $\lambda_{n+1}(T)$ computed at the $n+1^{th}$ iteration is smaller than the gain $\lambda_n(T)$ at the previous one, then the update $\mathbf{u}^{n+1}$ is re-updated with a different value of α, typically $\alpha = \alpha/2$, until the condition $\lambda_{n+1}(T) > \lambda_n(T)$ is achieved.

III.5 Optimal forcing analysis

To study the response of the system to a time periodic forcing, the optimal forcing analysis has to be carried out. The equation that links the forcing to the response has been presented in the section §II.3.2 and here reported:

$$\hat{\mathbf{u}} = (i\omega\mathbf{I} - \mathbf{A})^{-1}\hat{\mathbf{f}} \tag{III.73}$$

where $\hat{\mathbf{u}}$ is the harmonic response, $\hat{\mathbf{f}}$ the harmonic forcing and $\mathbf{A}$ stands for the Jacobian operator in the divergence-free space. We remember that eq. III.75b lives on the hypothesis that $\mathbf{A}$ has only stable modes and thus the asymptotic solution of the forced linearised Navier-Stokes equation only depends from the particular solution. Once again, for a 3D problem the equation (III.75b) can not be treated as presented in Schmid and Henningson (2012) due to the high memory required. An Hessenberg matrix can not be built with a time-marching CFD code as the equation (III.75b) is not time-depended. The only accessible solution today is that proposed by Monokrousos et al. (2010) formulating the problem as an optimization problem. The Lagrangian function can be formulated as before:

$$\mathcal{L}(\hat{\mathbf{u}}, \hat{\mathbf{u}}^{\dagger}, \lambda, \hat{\mathbf{f}}) = \underbrace{\langle \hat{\mathbf{u}}, \hat{\mathbf{u}} \rangle}_{\text{objective}} \underbrace{- \langle \hat{\mathbf{u}}^{\dagger}, (i\omega\mathbf{I} - \mathbf{A})\hat{\mathbf{u}} - \hat{\mathbf{f}} \rangle - \lambda(\langle \hat{\mathbf{f}}, \hat{\mathbf{f}} \rangle - 1)}_{\text{constraints}}. \tag{III.74}$$

The objective function is still the kinetic energy of the response, the additional constrains are:

- The response has to be solution of the forced linearised Navier-Stokes equation

- The amplitude of the forcing is normalised to 1.

Note that no time integrals are present and that the adjoint variable $\hat{\mathbf{u}}^\dagger$ has been assumed to be harmonic. The variation of the augmented functional respect to $\hat{\mathbf{u}}$, $\hat{\mathbf{u}}^\dagger$, λ and $\hat{\mathbf{f}}$ gives:

$$\frac{\partial \mathcal{L}}{\partial \hat{\mathbf{u}}^\dagger} := (i\omega \mathbf{I} - \mathbf{A})\hat{\mathbf{u}} - \hat{\mathbf{f}} = 0 \tag{III.75a}$$

$$\frac{\partial \mathcal{L}}{\partial \lambda} := \langle \hat{\mathbf{f}}, \hat{\mathbf{f}} \rangle = 1 \tag{III.75b}$$

$$\frac{\partial \mathcal{L}}{\partial \hat{\mathbf{u}}} := (-i\omega \mathbf{I} - \mathbf{A}^\dagger)\hat{\mathbf{u}}^\dagger - \hat{\mathbf{u}} = 0 \tag{III.75c}$$

$$\frac{\partial \mathcal{L}}{\partial \hat{\mathbf{f}}} := \hat{\mathbf{f}} = \lambda^{-1}\hat{\mathbf{u}}^\dagger \tag{III.75d}$$

Equations (III.75a) and (III.75b) are the imposed constraints in the augmented Lagrangian functional (III.74). Equation (III.75c) is the adjoint resolvent and eq. (III.75d) is the update of the forcing, see Monokrousos et al. (2010) for further details. To solve the optimization problem we need to solve eq. (III.75a) and (III.75c). Unfortunately we cannot have access directly at the complex fields $\hat{\mathbf{u}}$ and $\hat{\mathbf{f}}$ as Nek5000 integrates in time the linearised and the adjoint Navier-Stokes equation. Nevertheless, we can take advantage of the fact that the Jacobian $\mathbf{A}$ is stable and for $t \to \infty$ the only possible solution is the particular one that is periodic and independent from the initial solution. Hence, initializing the numerical simulation with a zero velocity field and a random unitary forcing, it is possible to recover the complex response performing a Fourier transformation of the velocity field on one period of the forcing. The optimization loop as proposed by Monokrousos et al. (2010) is depicted in figure III.26.

Implementation details

Concerning the Fourier transformation, it should be noted that only the mode associated to the optimization pulsation is required. Therefore, a discrete Fourier transform (DFT) can be used instead of a Fast Fourier Transform (FFT). The implementation of the DFT over one pulsation ω is straightforward and it is performed with a sum over $T_p = 2\pi/\omega$:

```
if  $t < (T_{end} - T_p)$
    $\hat{\mathbf{u}}_r = 0$
    $\hat{\mathbf{u}}_i = 0$
else
    $\hat{\mathbf{u}}_r = \hat{\mathbf{u}}_r + \frac{\omega dt}{\pi}\mathbf{u}\cos(\omega t)$
    $\hat{\mathbf{u}}_i = \hat{\mathbf{u}}_i - \frac{\omega dt}{\pi}\mathbf{u}\sin(\omega t)$
end
```

To accelerate the optimization loop convergence, the gradient-rotation method can be applied also in this case instead of a simple normalization of the forcing. To reduce the

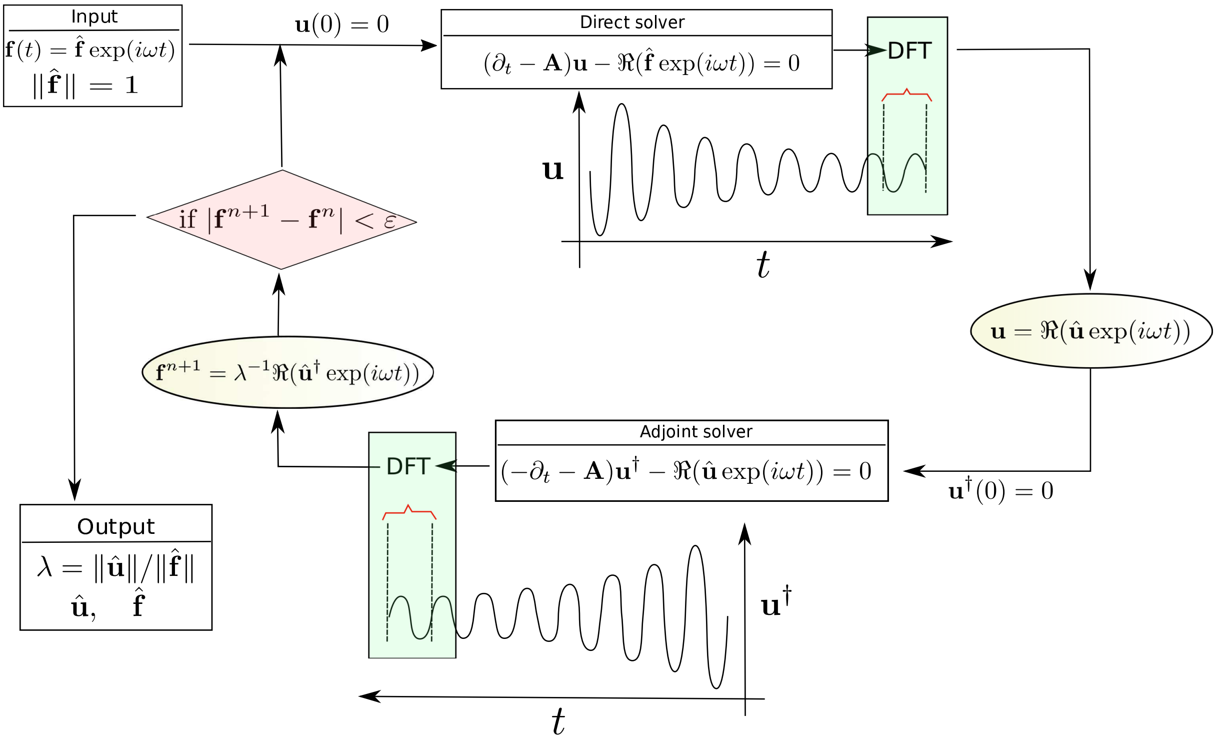

Figure III.26: Block diagram of the optimal perturbation as proposed by Monokrousos *et al.* Monokrousos et al. (2010).

time of the numerical simulation necessary to reach the time periodic behaviour before proceeding with the DFT, two solutions can be adopted. The first one is a differential form of the shift-and-relax filter proposed by Garnaud et al. (2012). It is a periodic selective frequencies damping used to converge a particular area in the complex plane of huge eigenvalue problems. In this case it can be used to damp all the frequencies different from the imposed one. A second solution is the use of BoostConv. The BoostConv algorithm can be used to find periodic base flows as shown by Carini *et al.* Carini et al. (2014) to study the flip-flop instability behind two cylinders. The main idea is to select a proper Poincaré plane in which the periodic behaviour is forced to be stationary. To achieve this goal it is sufficient to build properly the Krylov space like in eq. (III.76).

$$\mathbf{X}_k = [\mathbf{u}(t_0), \mathbf{u}(t_0 + T_p), \cdots, \mathbf{u}(t_0 + (k-1)T_p)]\,. \tag{III.76}$$

To show an application of the BoostConv to converge toward a periodic solution en example on the Rossler system (III.77) is shown.

$$\begin{cases} \frac{dx}{dt} = -y - z \\ \frac{dy}{dt} = x + ay \\ \frac{dz}{dt} = b + z(x - c) \end{cases} \tag{III.77}$$

For $a = 0.1$, $b = 0.1$ and $c = 5$ a periodic behaviour is observed over time. Keeping constant a and b values and changing c form 5 to 6 a period doubling bifurcation can be noted in the phase space. The BoostConv is then used to find the steady solution and the periodic solution. The result is shown in figure III.27.

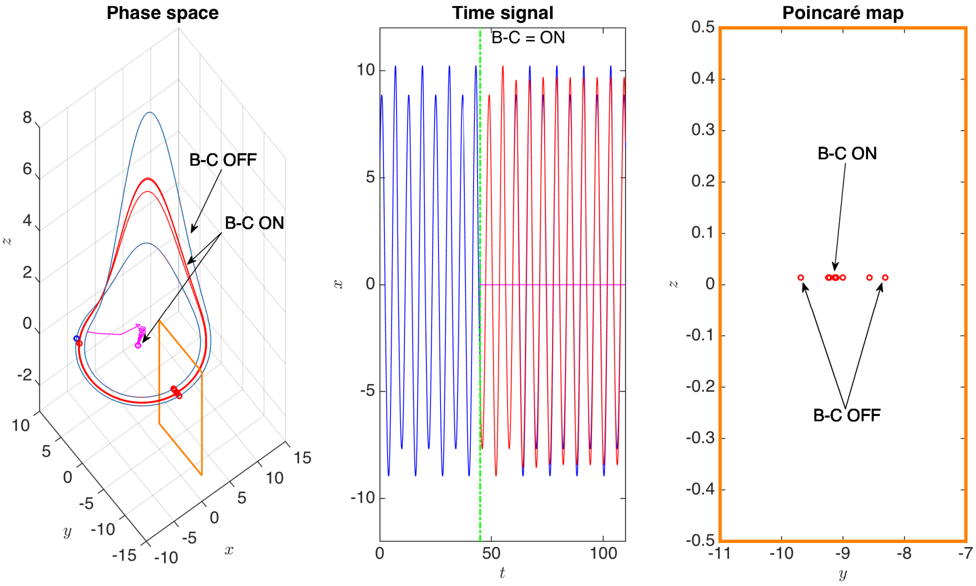

Figure III.27: Example of BoostConv application onto the Rossler system to converge towards a steady solution (magenta curve) or periodic solution (red curve). The uncontrolled solution shows a period-doubling limit cycle (blue curve) for $a = 0.1$, $b = 0.1$ and $c = 6$.

In this case the Poincaré plane is chosen looking at one spatial state variable. When the solution passes trough the $x = 0$ plane a new vector is added in the Krylov subspace. To accelerate the convergence towards the periodic solution in the optimal forcing solution, the Poincaré plane is taken looking at the time variable as it is known a priori that the period of the response must be equal to the forcing one. To validate the optimal forcing procedure two test cases has been studied. The first one is the 2D Poiseuille flow. The result at $Re = 4000$ ($Re_c = 5772$) is compared with that of the local theory. For the reference result only the Orr equation is used since when $\beta = 0$ the Sommerfeld equation is decoupled and it introduces modes that can not be taken into account in strictly 2D numerical simulation. The theoretical gain curve and the obtained one are depicted in figure III.28.

With the Lagrangian method only the optimal solution can be found. For this reason the solution obtained with Nek5000 follows the maximum gain curve. For $\omega < 0.8$ the optimal forcing has $\alpha = 1$ and for $\omega > 0.8$ the optimal forcing has $\alpha = 2$ (see fig. III.29).

In the Poiseuille case the periodic boundary condition are adopted in the streamwise direction. To test the fringe method the optimal forcing analysis on the 2D boundary layer has been also achieved. The gain curve for an inflow Blasius profile at $Re_\delta = 100$ is depicted in III.30.

The maximum gain is obtained for $\omega = 0.018$ as stated by Sipp et al. (2010)[3]. The optimal forcing and the optimal perturbation for $\omega = 0.018$ are shown in figure III.31.

---

[3] Note that in Sipp et al. (2010) different dimensionless parameters have been used.

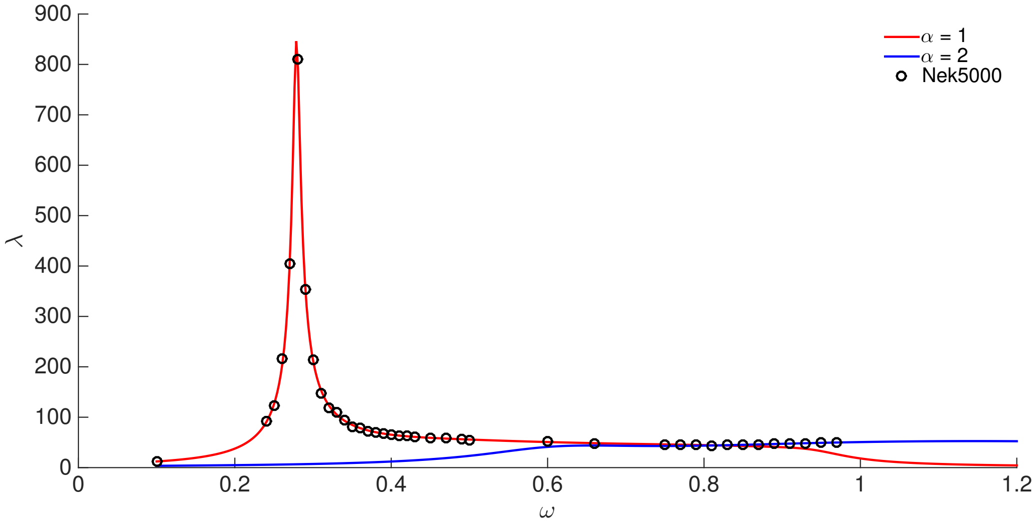

Figure III.28: Optimal forcing analysis for 2D Poiseuille flow at $Re = 4000$. The gain obtained with the optimal forcing implemented in the Nek5000 follows the curve envelope of the gain obtained with the local theory.

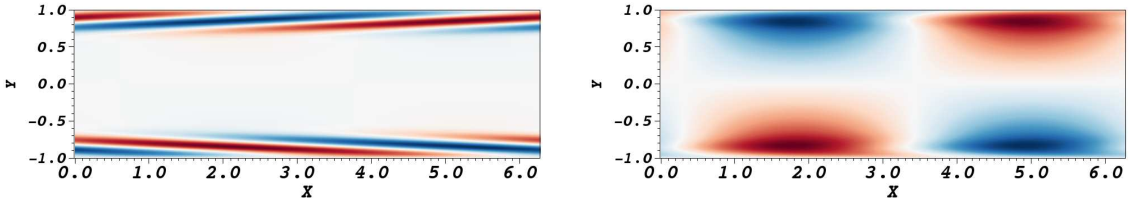

(a) Optimal forcing $\omega = 0.28$ (b) Optimal response $\omega = 0.28$

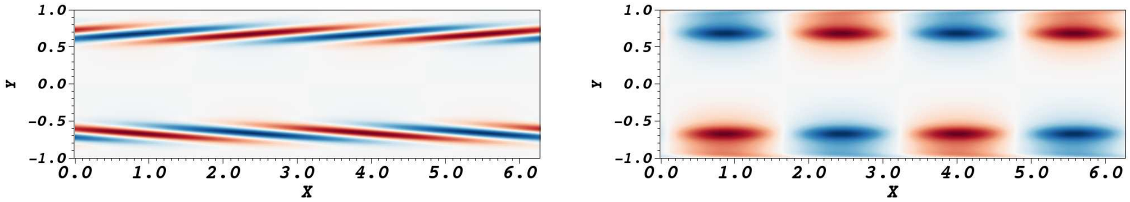

(c) Optimal forcing $\omega = 1.1$ (d) Optimal response $\omega = 1.1$

Figure III.29: Example of real part of optimal forcing (left) and real part of optimal response (right) when $\alpha = 1$ (top) and when $\alpha = 2$ (bottom).

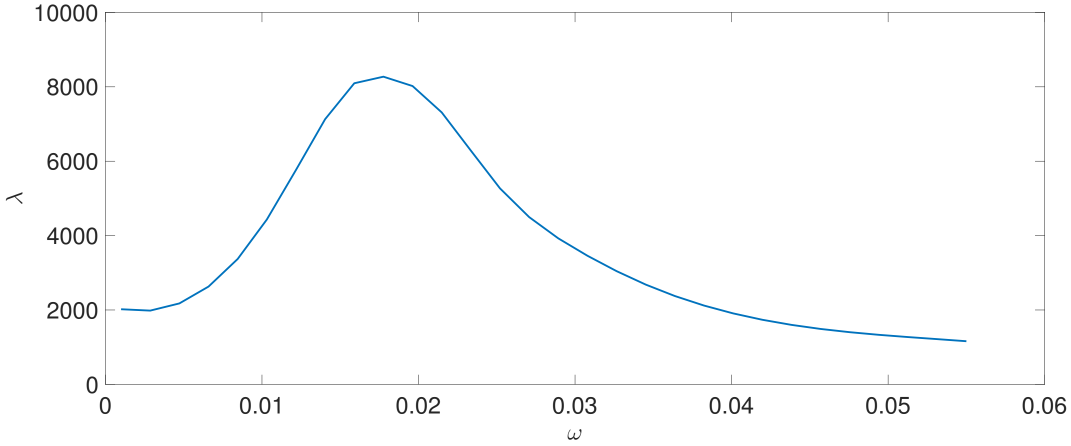

Figure III.30: Optimal forcing analysis of 2D boundary layer flow at $Re_\delta = 100$. Maximum gain at $\omega = 0.018$.

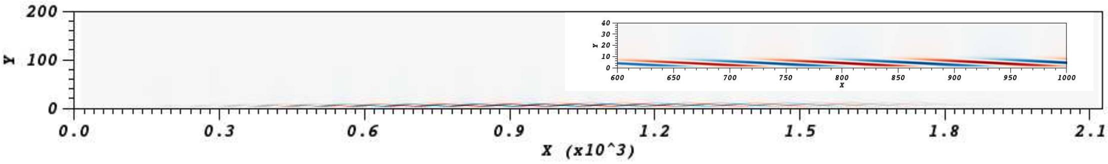

(a) Optimal forcing $\omega = 0.18$

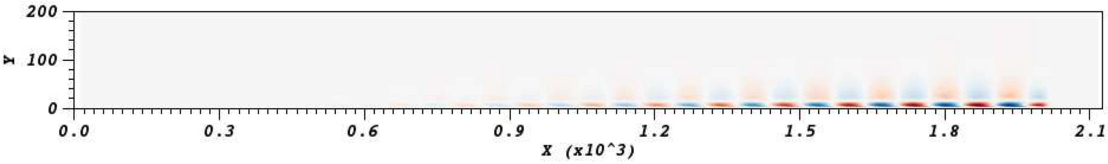

(b) Optimal response $\omega = 0.18$

Figure III.31: Example of optimal forcing (top) and response (bottom) for boundary layer case at $Re_\delta = 100$ and $\omega = 0.018$.

Chapter IV

Linear analysis of flow over cylindrical roughness

Contents

IV.1 Transition overview

IV.1.1 On the Tollmien-Schlichting wave.

The boundary layer flow is not an analytical solution of the Navier-Stokes equation like for Couette or Poiseuille solutions. As suggested by Ludwig Prandtl it is possible to neglect some terms in the Navier-Stokes equation using scaling arguments. The resulting system, know as "boundary layer equations", well represents the 2D laminar boundary layer profile. Introducing the variables η (the wall normal direction scaled by the displacement thickness δ_1) and $f(\eta)$ (the normalised stream function) the boundary layer flow is described by the self-similar Blasius solution:

$$2f''' + f''f = 0 \tag{IV.1}$$

where f''' and f'' are the third and second derivative of f. Solving the ordinary differential equation (IV.1) with $f(0) = f'(0) = 0$, $f'(\infty) = 0$ as boundary conditions, the streamwise velocity component is depicted in figure IV.1.

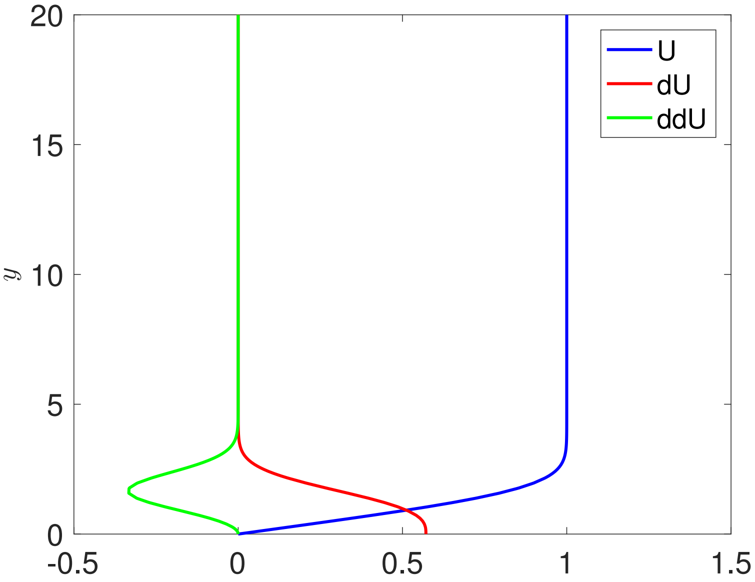

Figure IV.1: Streamwise component and its derivatives of the analytical Blasius solution.

Walter Tollmien (1935) and Hermann Schlichting (1933) showed that the Blasius profile is linearly unstable. The local stability analysis of the Orr-Sommerfend operator shows an unsteady mode for $\alpha = 0.303$ and $Re_c \geq 519.4$ at $\omega_i = 0.1202$ (see fig. IV.2).

The neutral mode that becomes unsteady for $Re > Re_c$ is known as Tollmien-Schlichting (TS) wave. It is a boundary layer perturbation with a peak in the wallnormal velocity profile around $2\delta_1$ (where δ_1 is the displacement thickness) that is convected by the flow field and grows spatially. When the amplitude of the TS perturbation grows above a threshold level (1 to 2 percent of the freestream velocity), the flow becomes susceptible to secondary instability that is three-dimensional in nature and characterized by the occurrence of λ-shaped vortices (Herbert, 1988; Kachanov, 1994). Vortices end up generating hairpin eddies, then the vortex stretching begins the breakdown cascade of these structures until reaching the turbulent state. One can observe that according to the Rayleigh's inflection point criterion, the Blasius profile should be stable even for $Re \to \infty$, because there is no change in the sign of the Blasius profile curvature, as shown in fig. IV.1. Thus, the unstable mode must be due to other physical mechanisms not accounted in Rayleigh's theory. As reported by Baines et al. (1996), the instability arises because of an interaction between two idealized modes of the system: an "inviscid" mode, which is neutral when

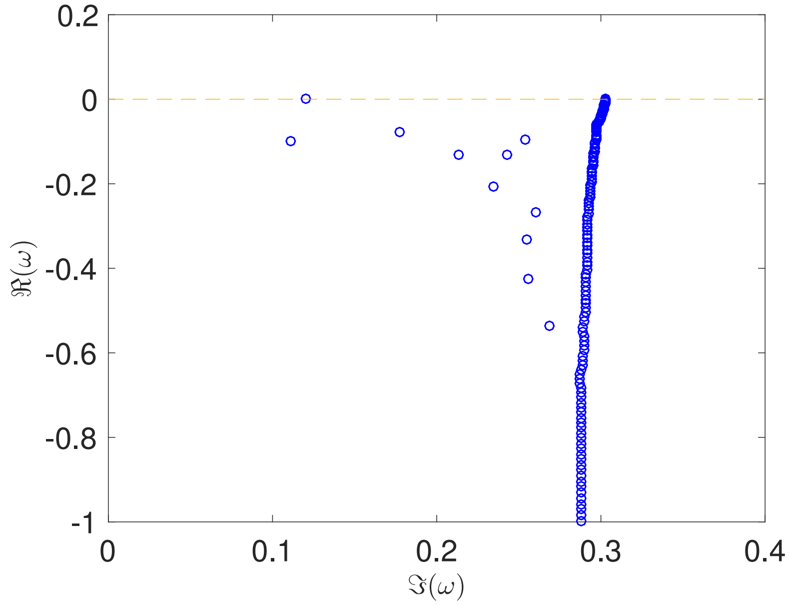

(a) Blasius eigenspectrum

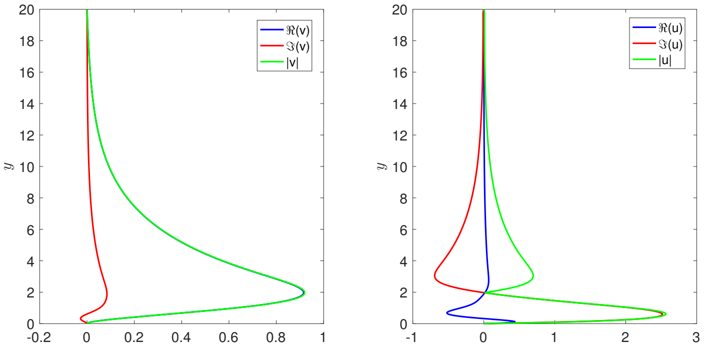

(b) Tollmien-Schlichting mode

Figure IV.2: Eigenspectra and neutral eigenmode in local ansatz associated to the Blasius velocity profile for $\alpha = 0.303$, $\beta = 0$ and $Re = Re_c = 519.4$.

viscosity is zero, and a decaying viscous mode (or modes) that exists in uniform shear. The viscous mode is forced by the inviscid one via the no-slip boundary condition at the wall. Viscous modes are concentrated only near to the wall (assuming $Re \gg 1$), where the inviscid mode fails to satisfy the no-slip boundary condition. Imagining that an inviscid “partial” mode is propagated in the fluid with a Blasius or near-Blasius profile, this motion would not respect the zero-velocity condition at the wall. But if the no-slip condition has to be satisfied by the net resulting motion, there must exist an additional viscously forced motion that brings to zero the horizontal velocity close to the wall. This viscous destabilization acting in a strong-gradients zone is responsible for the growth of unstable waves. The TS wave is a convective instability as no self-sustained mechanisms are present as shown by the global stability analysis (Alizard and Robinet, 2007; Bagheri et al., 2009) and in a 2D scenario is the most receptive mechanism as shown for leading-edge flat-plate case (Brandt et al., 2011; Sipp and Marquet, 2013). In a 3D framework the TS-wave is still the main receptive mechanism at $\beta \neq 0$ (Monokrousos et al., 2010). In the $\omega - \beta$ plane the TS-wave is not the only receptive mode. With a lower gain also the streaks can be excited by an external perturbation depending on the range of the perturbed ω.

IV.1.2 Boundary layer receptivity to the Free Stream Turbulence

In the light of the linear stability results, the boundary layer can exhibit different responses depending on the external perturbation amplitude. A natural way to excite the boundary layer is free stream turbulence (FST). A fundamental experimental work has been done by Boiko et al. (1994); Westin et al. (1994). By using an upstream grid to generate homogeneous turbulence, the transition over a flat plate has been studied for different levels of free stream turbulence. For sufficiently large values of the FST amplitude, the boundary layer transition is initiated by the growth of perturbations elongated in the streamwise direction rather than by TS waves. This perturbation induces a modulation of the base flow with high and low stremwise velocity fluctuations. This form of streaks is due to the lift-up mechanism that increases the momentum transport in the wall normal direction (Landahl, 1980, 1975). The counter rotating vortices elongated in the streamwise direction grow downstream until they trigger a secondary instability. The latter causes streak interaction and the breakdown to turbulence (Brandt et al., 2004; Schlatter et al., 2008). This kind of transition is known as “bypass transition" and it is linked to the non-normal character of the Navier-Stokes operator. A significant *transient emergy growth* of a given perturbation might occur, before the subsequent exponential behaviour (Landahl, 1980, 1975). Such an algebraic growth involves non-modal perturbations and can exist for subcritical values of the governing parameters. Andersson et al. (2001) has investigated the dynamics of the optimal streaks. He highlighted the presence of a secondary instability that has the form of sinuous modulation of the streaks when their amplitude exceeds approximately 26% of the freestream velocity. Also a varicose modulation is detected for optimal streaks having an amplitude larger than roughly 37% of the freestream velocity. Brandt (2007) demonstrates that varicose and sinuous instabilities shear the same destabilising energy production term. The low speed streak instability is associated with the work of the Reynolds stress $\tau_{xy} = -\bar{u}\bar{v}$ on the wall-normal basic shear $\partial U/\partial y$. Further information on the lift-up mechanism and its implication in the transition scenario are reported in Brandt's review paper (Brandt, 2014).

With low FST level the only possible transition scenario is the linear growth of the TS-wave. In the experiments the unsteady perturbation is triggered by a wall perturbation (Boiko et al., 1994). The experimental growth of the unstable perturbation is quite in agreement with the stability analysis prediction. In the same way the transition depending on the FST amplitude has been studied also numerically (Schlatter et al., 2007, 2010). For an intermediate level of FST it was found experimentally that the spatial amplification rate of small amplitude TS waves was lower than in the quiet FST case (Boiko et al., 1994). This was attributed at the distortion of the 2D mean profile (Andersson et al., 2001) by the presence of the non-linear saturation of the streaks. The coexistence of TS-waves, induced by the wall perturbation, and the streaks, induced by the lift-up mechanism, makes possible the transition delay.

IV.1.3 Stabilizing effect of the streaks

Starting from the last observation, Cossu and Brandt (2002) had the bright idea to induce artificially in the boundary layer optimal streaks to completely stabilise the TS waves. The stabilizing effect increases with the amplitude of the streaks A_{ST} up to the critical value for which the sinuous streak instability is triggered. The numerical observation (Cossu and Brandt, 2002) was confirmed by linear stability analysis (Cossu and Brandt, 2004). By using Floquet theory, it was demonstrated how a nonlinear periodic steady streak can stabilize the TS waves. The growth rate of the TS waves is damped increasing the streak amplitude. The 2D perturbation is modified an a 3D varicose perturbation called “streaked TS wave”. An explanation to this is provided by the kinetic energy production for the most unstable wave, showing as the work of the uw-Reynolds stresses against the spanwise shear $\partial U/\partial z$ (lift-up event) is stabilising. Hence it is the spanwise modulation of the boundary layer that allows to damp the unsteady perturbation and leads to transition delay. The numerical simulations and the theoretical analyses have been finally supported by experimental observations (Fransson et al., 2004, 2005, 2006). Fransson in its experiments used an array of roughness elements installed at the wall to modulate the boundary layer with high and low speed streaks. The pattern of periodically distributed cylindrical roughness generates the streaks that were propagated downstream. A wall perturbation is used to trigger the TS waves in the unsteady region of the boundary layer. The presence of the streaks can delay transition towards turbulence. Nevertheless, the presence of the roughness can induce a strong perturbation depending on the Re number and on the ratio between the roughness height and the boundary layer thickness. Fransson in its experiments showed that the stabilizing effect of the streaks grows with the amplitude of the streaks measured as

$$A_{ST} = \max_y \{(U(y)_{high} - U(y)_{low})/2\}/U_\infty. \tag{IV.2}$$

After an amplitude value of the streaks of about 12 % of U_∞, the presence of the cylindrical roughness induces streaks instability (Fransson et al., 2005) and turbulence is achieved by subcritical transition. Fransson's experiments open new perspectives in the passive control techniques to delay transition. For this reason, it is crucial to investigate the flow dynamics behind a roughness element to understand why the experimental limit in the streak amplitude is about 12 % of U_∞ and the theoretical one is 26 % to observe a sinuous modulation of the streak as reported by Andersson et al. (2001). Siconolfi et al. (2015a) has recently investigated numerically the possibility to use free-stream vortices to stabilize TS waves. The ideal vortices imposed at the inlet of the numerical domain in the free stream can generate stable streaks in the boundary layer by the lift-up mechanism. The provided stabilization has been verified by the local stability analysis. This is an important result because it opens new perspectives in the transition control framework. Unfortunately, this solution does not turn out to be applicable because one should generate the vortices before the leading edge of the flat plate that needs to be controlled. Thus considering the presence of roughness elements at the wall, what are the main mechanisms that make the spanwise modulated boundary layer susceptible to a critical or subcritical transition?

IV.1.4 Flow dynamics over wall roughness

Roughness elements higher than the boundary layer thickness are usually used to control separated flows (Beaudoin, 2004; Duriez, 2009). In this cases the roughness represents an obstacle for the flow. In this Ph.D work a wall roughness is a well geometrically defined object mounted at the wall that does not reach the height of the boundary layer thickness. In some conditions, by smartly modulating the flow close to the wall, such devices are able to delay transition. However, they might also induce early transition by other mechanisms that are worth investigating, with the aim of providing the limit of such passive control. The transition promoted by the presence of a roughness in the boundary layer was an active research field already in the sixties and seventies (Gregory and Walker, 1956; Sedney, 1973). As early as in those years, Braslow (1960) has reviewed all results available back then stemming from various experimental investigations into one transition diagram. This enabled them to give a first empirical criterion (fig. IV.3) for transition still widely used nowadays in industries.

The Von Doenhoff-Braslow diagram depicts a general overview for the transition due to the presence of a roughness at the wall with any form at given aspect ratio η and Re_h (the Reynolds number evaluated with the velocity value that an analytical Blasius profile would have had at the position and height of the roughness element). The presence of the roughness can delay transition but it can induce a strong perturbation depending on the Re number and the ratio between the roughness height and the boundary layer thickness. Despite the numerous parametric analysis (e.g. roughness shape, distance between two successive roughness elements, Reynolds number, Mach number, roughness aspect ratio,...), the Braslow's work (Braslow, 1960) just lists the numerical set-up at which the roughness produces an unsteady perturbation without giving an exhaustive explanation on the nature of the unsteadiness. In Klebanoff and Tidstrom (1972), for a two dimensional roughness, it is claimed that the transition behind the roughness is a stability governed phenomenon. The recovery zone makes the velocity profile much closer to a free-shear layer instead of a boundary layer. The inflection points of the velocity profile can then drive the unsteadiness. For this reason, parameters like free stream velocity and roughness shape can impact on the boundary layer destabilization (Perraud et al., 2004). A 3D extension of this experimental work for an hemispherical roughness (Klebanoff et al., 1992) shows a more complex scenario. The presence of the roughness induces the hairpin eddies that interact with the wall streaks (*inner region*) and grow in the streamwise

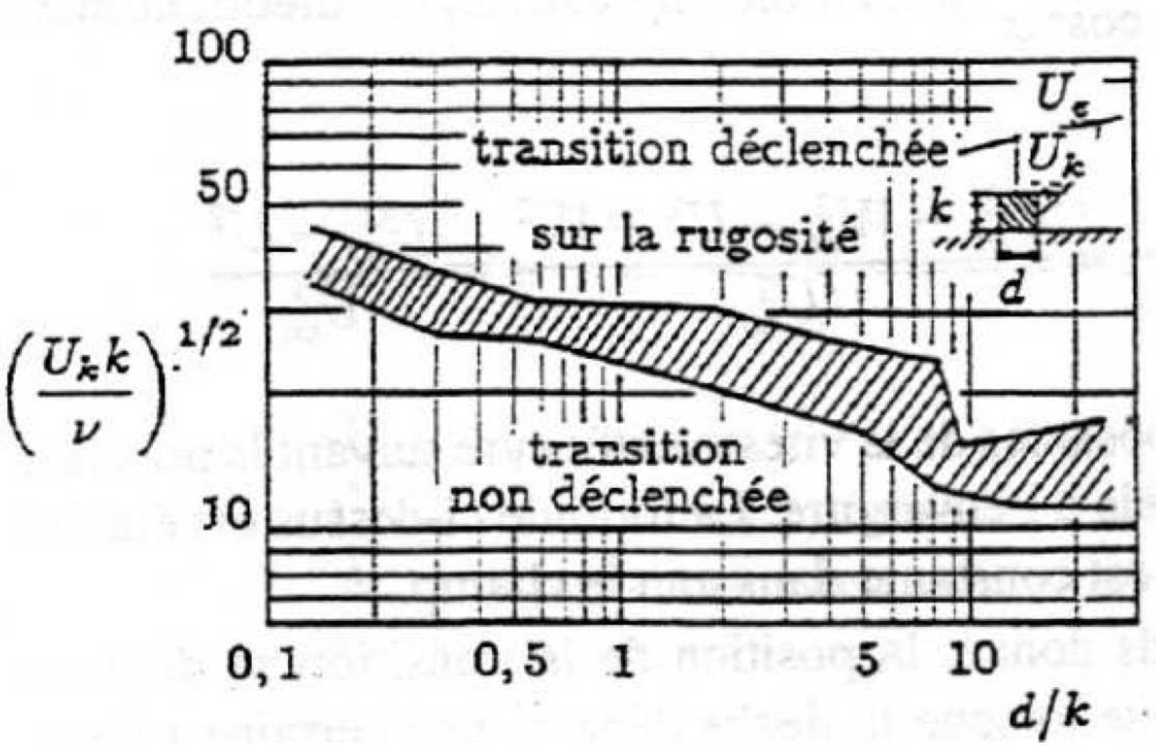

Figure IV.3: Reproduction of the transition diagram by Braslow (1960). $\eta = d/h$ is the ratio of the roughness element's diameter d over its height h and Re_h is the Reynolds number evaluated with the value of the Blasius velocity profile U_{BL} evaluated at the roughness element's position and height h.

and wall normal directions up to generate ring vortices (*outer region*). Increasing the Reynolds number transition appears earlier. Nevertheless, the roughness induced boundary layer preserves the time history for a long distance far away from the wall disturbance. The resulting turbulence was coloured by a specific frequency. This was a further indication of the presence of some instability mechanisms. A first detailed explanation on the generation of the fluid structures that give rise to the streaks was given by Baker (1979). The flow impacting onto the cylindrical roughness generates an *horseshoe vortex* that wraps the cylinder up to generate counter rotating vortices already observed by Gregory and Walker (1956). The size and the numbers of the horseshoe vortices are studied changing the dimension of the roughness. A description of the streak evolution downstream a bump roughness was highlighted by Joslin and Grosch (1995) that compared numerical and experimental results in the same work. Since the initial perturbation that provides transient growth in a boundary layer is given by elongated streamwise vortices, many authors started to investigate the transient growth on the roughness induced streaks. Experimental (Denissen and White, 2009, 2008; Ergin and White, 2006) and numerical (Choudhari, 2004; Denissen and White, 2009) works show that the streamwise transient growth of the induced streaks roughly scales with the square of the roughness Reynolds number, Re_h^2. Thanks to this results, a model taking into account the optimal perturbation has been developed to predict transition (Arnal et al., 2011). A first Bi-local stability analysis onto a boundary layer flow streaked by the presence of bump roughness has been performed by Piot et al. (2008). Behind the recovery zone of the roughness, the steady state is quasi-parallel, allowing to introduce a modal decomposition in the streamwise direction. The unsteady eigenvalue has the same wavelength of the TS wave but with a smaller growth rate. This confirms the stabilization of the TS waves. The found eigenvectors generate a good basis to project the non-linear dynamics observed in the DNS except for the streamwise position close to the roughness where the base flow is highly non-parallel. In the same way recently Siconolfi et al. (2015b) has studied the local stability behind miniature vortex generators demonstrating the stabilization effect provided by the streaks. The first three dimensional work in the instability framework onto an isolated bump roughness was performed by Cherubini et al. (2013). By using an optimization technique she demonstrated that the presence of the roughness increases the non-normalities of the system that exibiths an higher transient growth of the energy. Moreover, the presence of the roughness localises the optimal initial perturbation onto the head of the bump. The time evolution of the obtained perturbation generates a wave packet convected downstream that in the non-linear simulation gives rise to hairpin structures leading to transition far from the roughness. One year later, Loiseau et al. (2014) demonstrated how the presence of the roughness not only increases the non-normality of the system but also can make the Jacobian globally unsteady. The globally unstable mode is influenced by the Reynolds number and by the aspect ratio. A varicose or sinuous behaviour can be observed according to the aspect ratio of the cylindrical roughness. The wavemaker is located onto the separation zone that is the source of the self-sustained harmonic oscillator. Recently Siconolfi et al. (2017) demonstrates that the unsteady global mode for an hemispherical roughness (Citro et al., 2015) is related to the separation zone by the presence of an absolutely unstable zone. The research is really active in this field due to the possibility to control transition without introducing additionally energy. Other works can be cited for instance that provide detailed experimental information onto the transition scenario (Ye et al., 2016a,b) such as vortex splitting in the spanwise direction behind the unsteady streaky-induced flow. For more applicative purposes, the use of the roughness in the hypersonic setup (Bernardini et al., 2012; De Tullio et al., 2013; Ye et al., 2017) or subject to a cross-flow velocity profile (Brynjell-Rahkola et al., 2017; Kurz and Kloker, 2016) is also an active research topic.

IV.2 IAG's experiments

IV.2.1 Experimental set-up

Loiseau's work (Loiseau et al., 2014) sheds light on the origin of the modal unsteady behaviour that lead to turbulence the flow behind the roughness element. At the Institute of Aerodynamics and Gasdynamics (IAG) in the Stuttgart University the research group led by Prof. Rist tried to reproduce Loiseau's investigations fascinated by the possibility of reproducing the different symmetries recovered changing the aspect ratio of the roughness element.

The experiments are performed in the laminar water channel (Laminarwasserkanal) that is a closed circuit water channel at the Institute of Aerodynamics and Gasdynamics.

A sketch of the experimental set-up is depicted in figure IV.4.

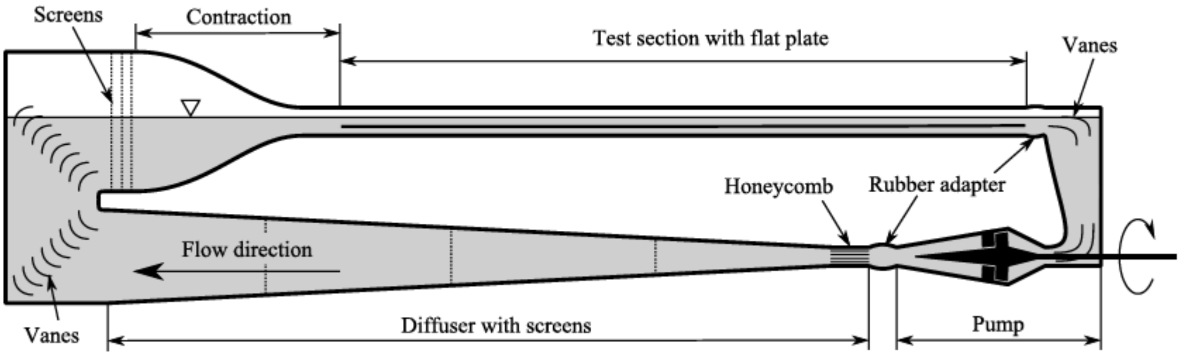

Figure IV.4: Laminarwasserkanal figure from Puckert et al. (2015)

The turbulence intensity is 0.089% of the free stream velocity in the frequency range 0.1 - 10 Hz at 0.0745 ms^{-1} and the test section is 8 x 1.2 x 0.2 m large. To maintain the turbulence intensity even at very low freestream velocities, an additional screen is installed if the freestream velocity is below 0.06 m/s as described by Puckert et al. (2017). A steady, 2D, laminar boundary layer of Blasius type is created by a flat plate with elliptical leading edge (Wiegand, 1996). The experimental set-up is sketched in figure IV.5. All length scales are non-dimensionalized by the constant roughness height h, which equals 10 mm in the physical experiment and 1 in the dimensionless domain. The roughness position is constant at $L = 57.1$ from the leading edge. The aspect ratio $\eta = d/h$ is given by the roughness diameter d and the Reynolds number $Re = hU_e/\nu$ is determined by the (variable) freestream velocity U_e and the dynamic viscosity ν of water. Due to the temperature-dependency of the dynamic viscosity, its value is determined prior to each individual experiment. The coordinate system originates from the bottom center of the roughness with non-dimensional x-, y- and z-coordinates extending in streamwise, wall-normal and spanwise directions, respectively.

Hot-film measurements have been done with a Dantec Streamline 90N10 system and two single-wire probes 55R15 which were calibrated by traversing them at increasing speeds in resting water as described in Subasi et al. (2015). The voltage signals are recorded by a 16-bit A/D-converter at 100 Hz and digitally filtered between 0.1 and 10 Hz. The voltage signal is converted into a streamwise velocity by applying King's law and decomposed into mean velocity $\overline{u}$ and disturbance signal u'. Particle image velocimetry (PIV) has been done with dual-pulse Nd:YAG Quantel Twin lasers (532 nm), seeding with $4.2\mu m$ nylon particles and image acquisition with a PCO Sensicam system.

IV.2.2 Experimental results

To check the existence of sinuous or varicose symmetries in the experimental unsteadiness, a numerical case from Loiseau et al. (2014) is taken as reference whose parameters are summarized in table IV.1.

In table IV.1 the critical Reynolds number is reported. Choosing a lower Reynold number a steady behaviour is expected. In the parametric study shown in Loiseau et al.

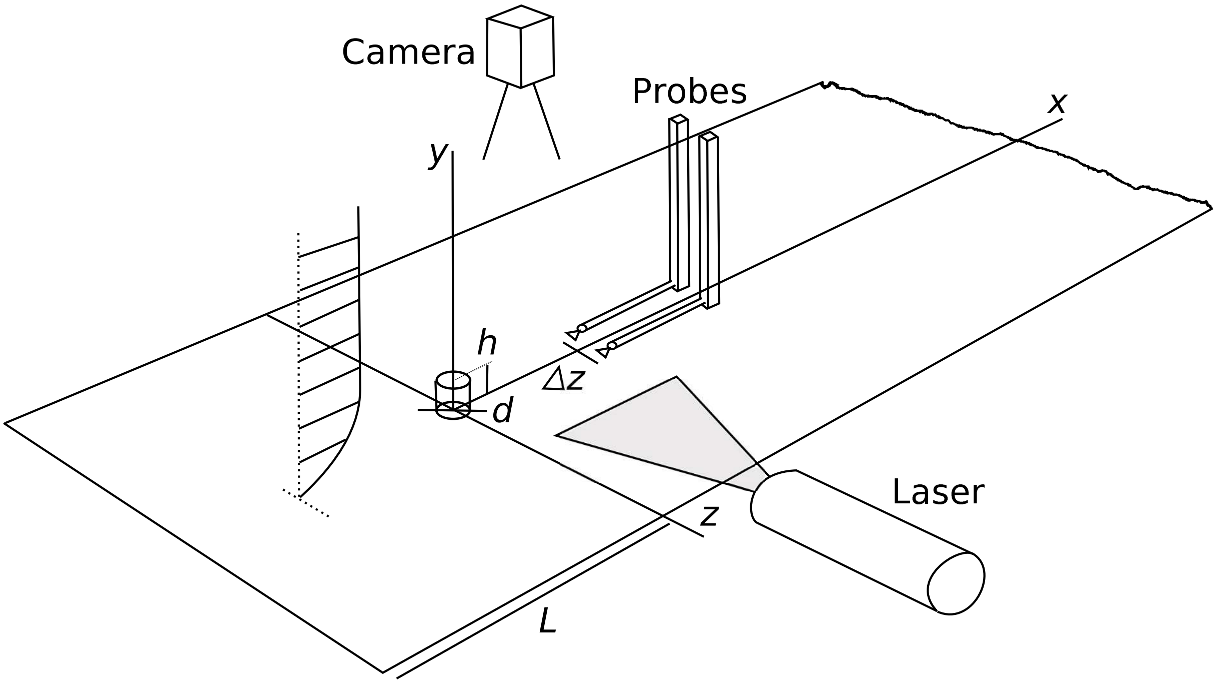

Figure IV.5: Sketch of experimental set-up. Domain size: $L = -57.1$. Δz is varied during experiments.

η	Re_c	Re_h	x_h	h/δ_1	ω	sym
1	1040	813	156.06	1.45	0.7	S

Table IV.1: Sinuous case in Loiseau et al. (2014).

(2014), the ratio between the height of the boundary layer δ_{99} at the roughness position and the height of the roughness h is kept constant and equal to 2. On the contrary, in Fransson's study and also in the IAG's experiment the distance between the leading edge and the roughness position is fixed at $x_h = 57.1$. The set-up of the studied cases is reported in table IV.2. The experimental case shows an unsteady behaviour despite the Reynolds number is lower than the critical one predicted by Loiseau. The pulsation and the spatial wavelength linked to the observed perturbation are also summarised in table IV.2.

η	$h/(mm)$	Re	Re_h	h/δ_1	ω_{exp}	$\lambda_{x,exp}$	sym
1	10	700	639	2.03	1.05 ± 0.11	4.8 ± 0.5	V

Table IV.2: Summary of the parameters, pulsation frequencies and wavelengths

The effect of the cylinder on the laminar boundary layer for the configuration $(\eta, Re) = (1, 700)$ is visualized with potassium permanganate crystals on top of and around the roughness, which dissolve in water and draw dye streaklines into the flow field. In figure IV.6 (top), crystals upstream of the roughness visualize the contour around a steady horseshoe-vortex wrapping around the roughness with nearly straight trailing legs. Sim-

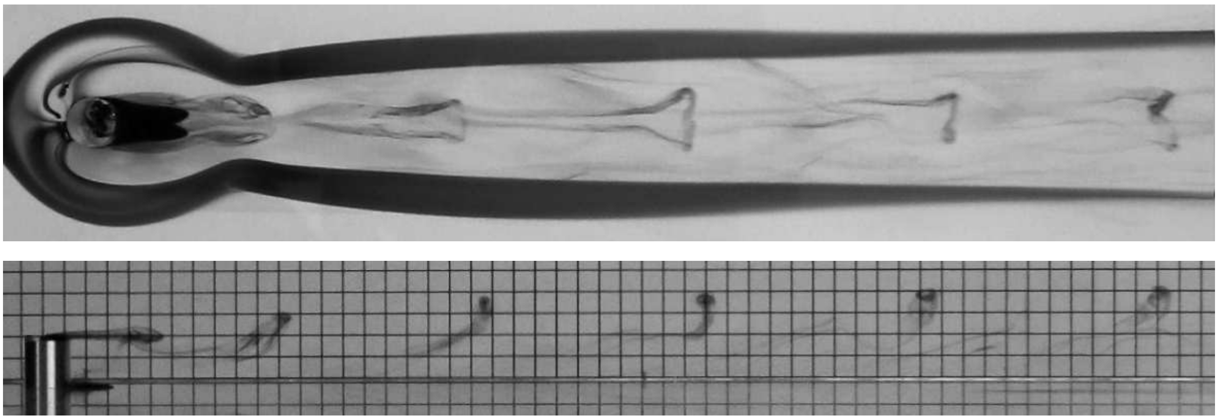

Figure IV.6: Flow visualization with potassium permanganate crystals placed upstream of roughness and in recirculation zone. (Top) Top view and (bottom) side view with 5 mm grid background.

ilarly, the recirculation zone can be seen as a dark region downstream of the roughness followed by regular ejection of hairpin vortices. These unsteady vortices consist of an omega-shaped head in the upper region of the boundary layer and legs in the lower region and have been analyzed in detail by Acarlar and Smith (1987) for instance. Figure IV.6 (bottom) shows the shedding of hairpin vortices from a side view. From this picture, the vortex wavelength can be estimated by the spacing of the heads, which is around $\lambda_x \simeq 4.8$. In both figure IV.6 (top) and (bottom), the shape of the hairpin vortices becomes less pronounced as they travel downstream, which is a manifestation of transition to turbulence. As proposed by Klebanoff et al. (1992), the lower part is more affected by turbulent mixing than the upper part, therefore the hairpin heads preserve their shape for a longer distance than the legs.

The spanwise symmetry property of the unsteady disturbances has been measured by two single-wire hot-film probes located symmetrically with respect to the $z = 0$ plane in the wake of the roughness element. Their separation Δz was increased from 0.5 to 6.5 in steps of $\Delta(\Delta z) = 0.5$ and traversed vertically in increments of $\Delta y = 0.2$ at three downstream positions $x = 10$, $x = 20$ and $x = 30$. At each position, the two disturbance signals u_1' and u_2' of the probes have been acquired for 30 s and separated into a symmetric (varicose, u_v) and antisymmetric (sinuous, u_s) component according to the following approach (Shin et al., 2015):

$$u_v = \left(\frac{u_1' + u_2'}{2}\right)_{\mathrm{rms}}, \quad u_s = \left(\frac{u_1' - u_2'}{2}\right)_{\mathrm{rms}}. \tag{IV.3}$$

The result of this decomposition is shown in figure IV.7. Here, the varicose (sinuous) component is plotted on the left (right) of the spanwise symmetry plane for $x = 10$, 20 and 30. Note that both components actually exist on both sides and that the probe spacing leads to an inevitable gap around the spanwise center. For all three downstream positions, the varicose disturbance dominates over the sinuous one. The position of maximum varicose disturbance is in agreement with the position of the heads and legs of the hairpin vortices in figure IV.6 and its amplitude grows in the downstream direction. The leading unsteadiness of the flow is therefore of varicose nature. The increasing amplitude of the

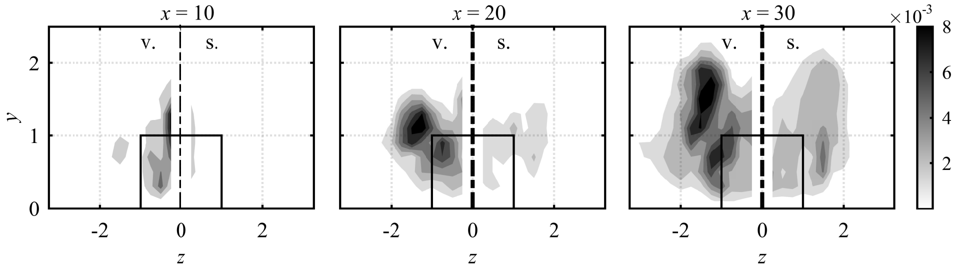

Figure IV.7: Pseudocolors showing varicose (v.) and sinuous (s.) disturbance components according to equations (IV.3) on left and right side of the spanwise symmetry plane (dash-dotted line), respectively, at three downstream positions: (left) $x = 10$, (middle) $x = 20$ and (right) $x = 30$.

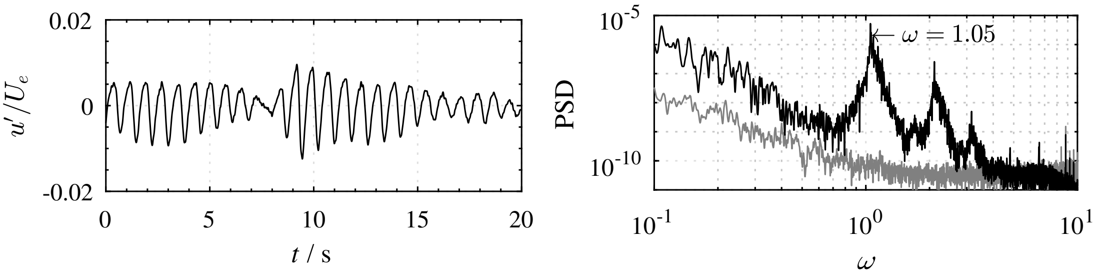

Figure IV.8: (Left) Time signals and (right) power spectrum densities (PSD) of streamwise velocity fluctuations u'/U_e for $\eta = 1$ at $(x, y, z) = (5, 1.5, 0)$ Grey lines in the spectra represent freestream turbulence spectrum at $(x, y, z) = (0, 6, 0)$

sinuous component with increasing x is probably due to nonlinear interaction of unsteady disturbances, typical for laminar-turbulent breakdown. In the limit of fully developed turbulence, the quantities in equation (IV.3) should become identical.

Figure IV.8 shows excerpts of time signals on the left hand side and spectra from Fourier-transforms of the respective signals on the right hand side. Note that the total duration was 1200 s and only 20 s are shown in the time signals whereas the full length of the signal is used for the frequency spectra. The frequency ω at the abscissa is computed with $\omega = 2\pi f h U_e^{-1}$, where f is the physical frequency in Hz. In all of the provided spectra the continuous increase of power at low frequencies is due to natural disturbances in the water channel and not related to the roughness. Both time signals and spectra show very regular oscillations at a distinct frequency with higher harmonics in the spectra. These oscillations belong to the initial stage of hairpin vortex creation visualized in figure IV.6 and the dominant ω is listed in table IV.2.

The unsteadiness is further illustrated by PIV snapshot of wall-normal planes at $y = 1$ in figure IV.9. Grey pseudocolors indicate the in-plane velocity magnitude and black vectors indicate the vector sum of streamwise and spanwise velocities. One can see the streaky wake of the roughness elements with quasi-symmetrical oscillations around the spanwise centerline. Again, this unsteadiness belongs to the observation of haipin vortices. The question to be answered by theory is how this unsteadiness can evolve despite global stability (Loiseau et al., 2014).

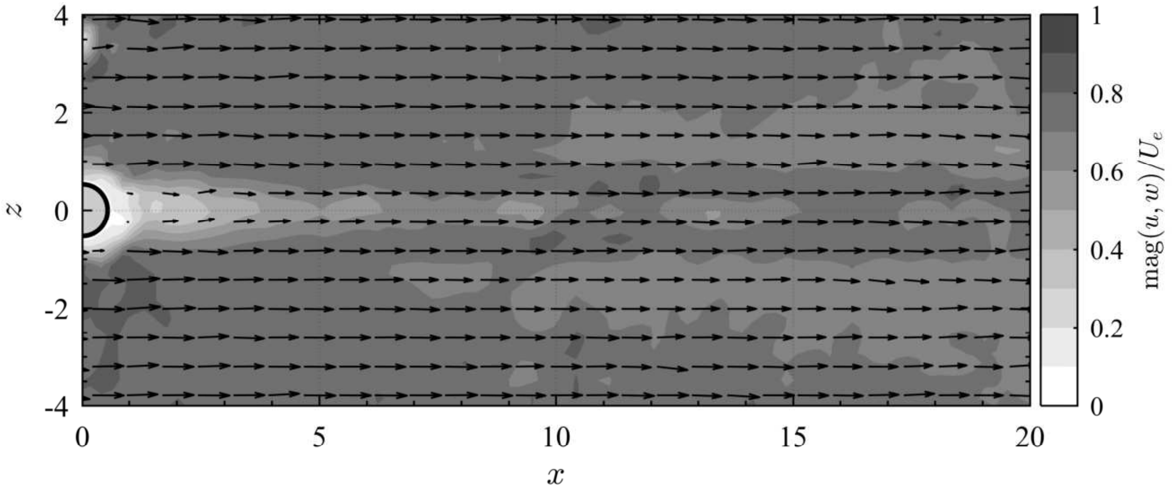

Figure IV.9: PIV snapshots at $y = 1$ for $(\eta, Re) = (1, 700)$.

IV.3 Numerical investigation

The experimental case on the cylindrical roughness at $\eta = 1$ shows an unsteady and varicose behaviour in disagreement with the previous numerical analysis that predicts a stable sinuous global mode (Loiseau et al., 2014). The main difference between experimental and numerical investigation lies in the shear ratio δ_1/h at which the roughness is subject from the incoming flow. How the stability changes in function of the shear ratio is unknown as in the Loiseau's work δ_1/h is keep constant and equal to 0.688. A further numerical investigation is then required.

IV.3.1 Numerical set-up

The parameters in table IV.2 has been used to set the numerical simulation in Nek5000. A sketch of the numerical domain over the experimental one is now depicted in figure IV.10.

The computational domain considered is given by $L_x = [-25; 90]$ (x = 0 being the cylinder position), $L_y = [0; 40]$ and $L_z = [-5; 5]$, x, y, and z being the streamwise, wall-normal and spanwise directions, respectively. The dynamics of the flow is assumed to be described by the incompressible Navier-Stokes equations

$$\begin{gathered}\frac{\partial \boldsymbol{U}}{\partial t} + (\boldsymbol{U} \cdot \nabla)\,\boldsymbol{U} = \nabla P + \frac{1}{\text{Re}} \nabla^2 \boldsymbol{U} \\ \nabla \cdot \boldsymbol{U} = 0,\end{gathered} \tag{IV.4}$$

where $\boldsymbol{U}(\boldsymbol{x}, t) = (U, V, W)^T$ is the three-dimensional velocity field and $P(\boldsymbol{x}, t)$ the pressure field. A sketch of the coarse grid distribution of the spectral elements in xz- and xy- plane is depicted in figure IV.11.

A total of 23544 elements has been used to discretise the numerical domain. Each element is then discretized in each direction by a N-Lagrange interpolant by the Nek5000. A polynomial order N equal to 8 has been used for this computation. A convergence study on the grid will be provided later on as the grid resolution is a critical point for the global

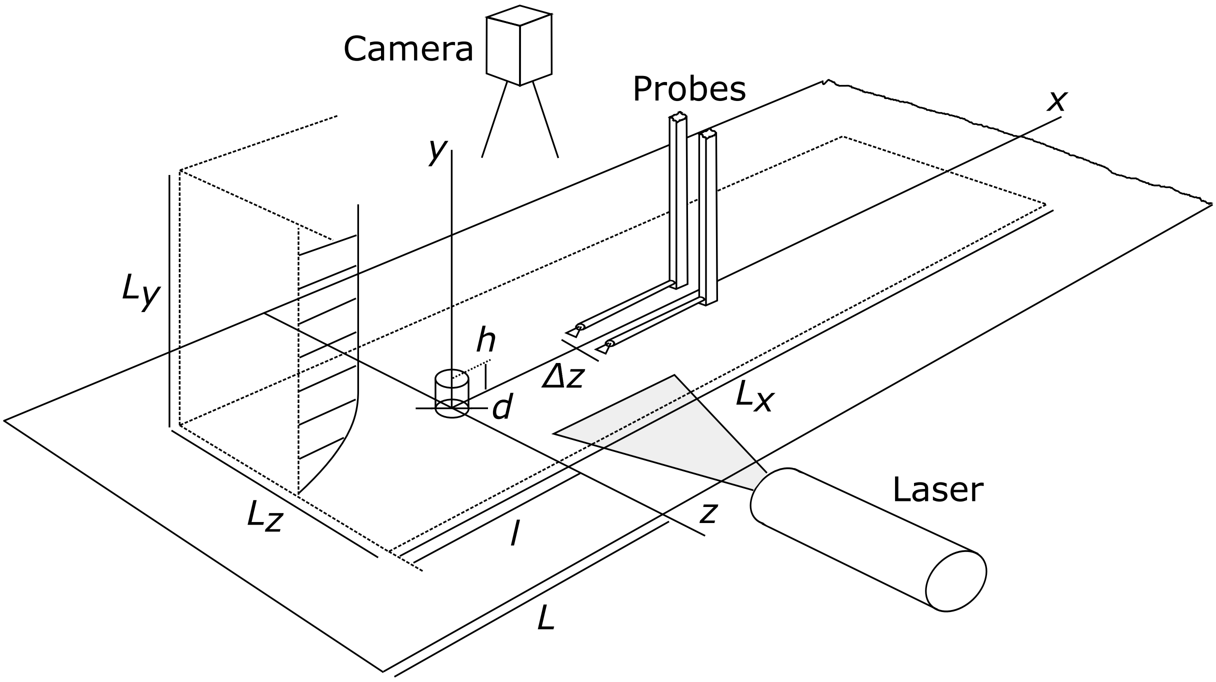

Figure IV.10: Sketch of experimental set-up and computational domain. Computational domain size: $L_x = 115$, $L_y = 40$, $L_z = 10$, $l = -25$. The cylinder position is $(x, y, z) = (0, 0, 0)$.

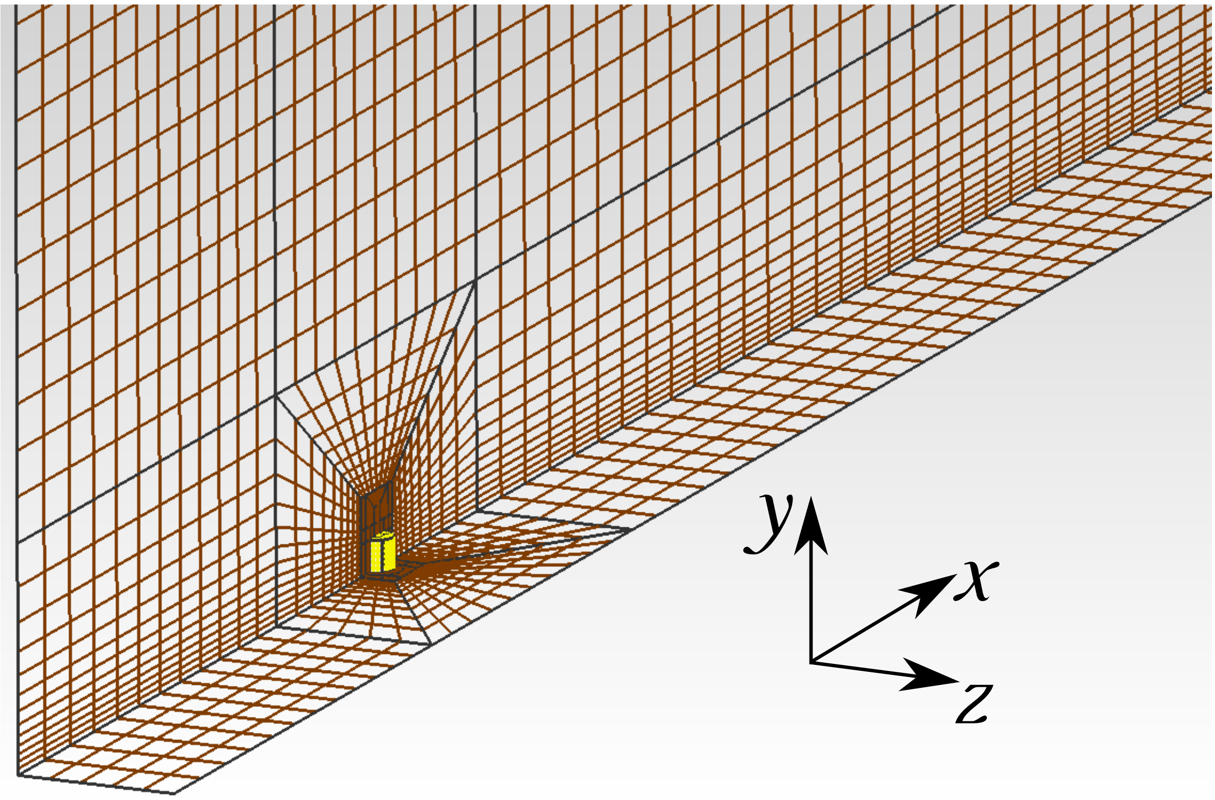

Figure IV.11: Spectral element grid. A total of 23544 elements are used to discretise the numerical domain.

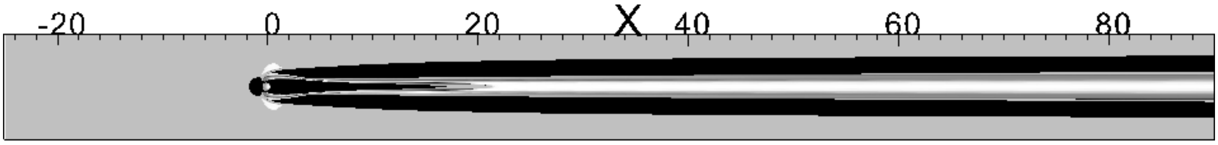

Figure IV.12: Top view of the streaks induced by the roughness elements. Low-speed (black) and high-speed streaks (white) are depicted using isosurfaces of the streamwise velocity deviation of the baseflows from the theoretical Blasius boundary layer flow, $\bar{u} = U - U_{BL}$.

stability result. The spectral grid is build with the commercial code Pointwise and then converted by an in house MATLAB code in Nek5000 format. Concerning to the adopted boundary condition, they can be summarized as follows:

- At $X_{in} = -25$. The analytical Blasius solution has been used as Inflow condition to economize memory and avoid spectral elements to discretise the whole flat plane. This is in good agreement with the boundary layer velocity profile in the experiments (Puckert et al., 2015).
- At $X_{out} = 90$. Outflow boundary condition $p\mathbf{n} - Re^{-1}(\nabla\mathbf{U}) \cdot \mathbf{n} = 0$.
- On the spanwise end planes $z_{side} = \pm L_z/2$ periodic boundary conditions are imposed for the three components of the velocity vector.
- At the upper boundary $Y_{top} = 40$ the slip condition $U = 1$ and $\partial V/\partial y = \partial W/\partial y = 0$ is applied.
- At the wall and on the roughness surface the no-slip boundary condition is imposed.

Regarding the velocity profile imposed at the inlet, the Blasius solution has been imposed in order to get $\delta_1/h = 0.49$ at the roughness position. Despite the periodic boundary condition, the spanwise dimension of the numerical domain is large enough to not affect the unsteadiness generation, and the roughness element can be considered as isolated (Braslow, 1960). The convective terms are advanced in time using an extrapolation of order 3 for the non-linear simulation and order 2 for the linear one, whereas for viscous terms a backward differentiation of order 3 for the non-linear simulation and order 2 for the linear one is used.

IV.3.2 Steady state

The direct numerical simulation of the experimental case converges towards a steady solution without any supplementary algorithm (e.g. SFD, Boostconf or Newthon). The streaked boundary layer is depicted in figure IV.12.

To highlight the low and high speed region the analytical Blasius solution is subtracted to the obtained steady solution. As one can observe, just behind the roughness five streaks are present; three of them being low-speed and two high-speed streaks. In this scenario, two mechanisms are involved in the streaks generation. The first one is the lift-up mechanism that is triggered by the counter rotating vortices generated by horseshoe

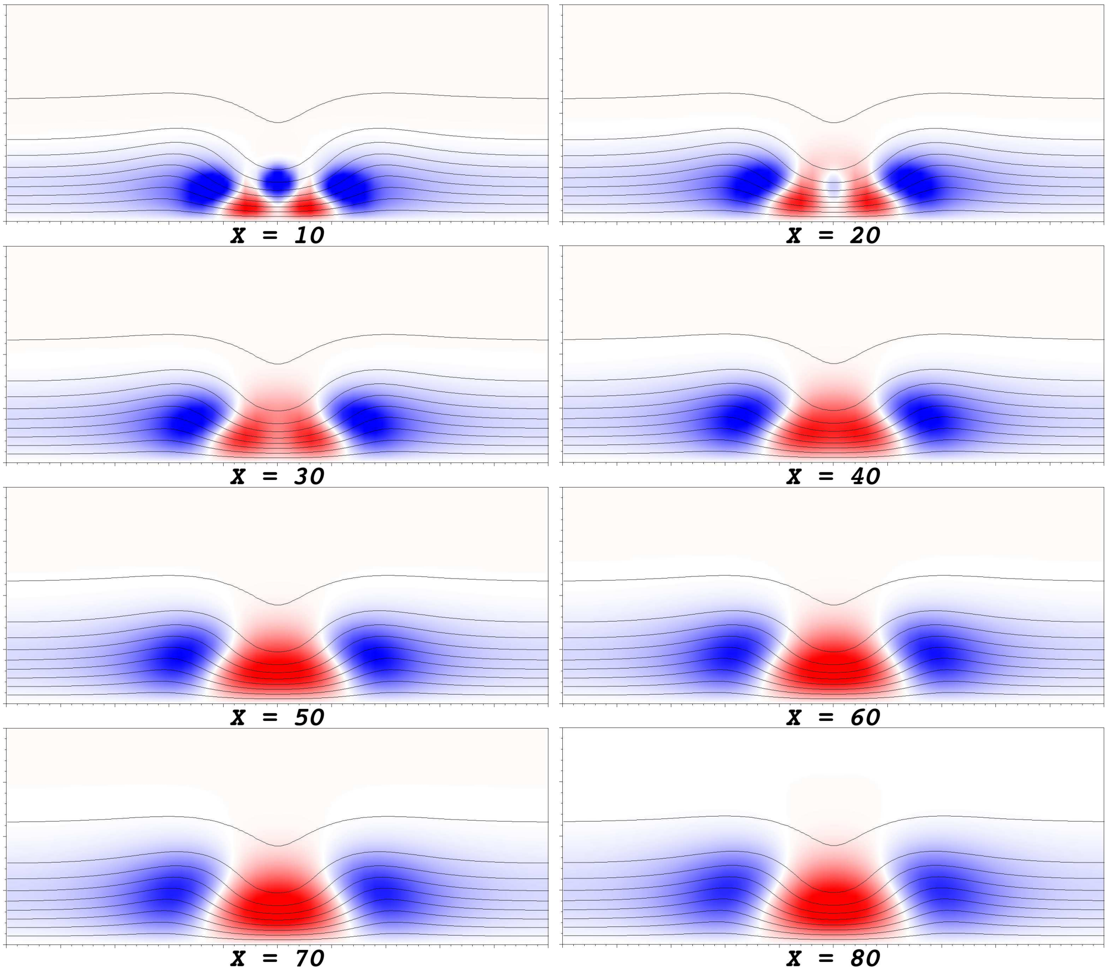

Figure IV.13: Streamwise evolution of the streaks in yz-plane. Red region represent high speed streaks, blue region low speed streaks highlight looking at $\bar{u} = U - U_{BL}$. Continuous lines depict isolevel of U form 0.1 to 0.99.

vortex that wraps the roughness (Baker, 1979). The second mechanism is the shear on the head of the cylinder that represents an obstacle for the incoming flow. The first mechanism produces the high and low speed streaks on both sides. On the contrary, the second mechanism produces the low speed streaks in the middle that extends up to $x \approx 20$. To better display the streamwise evolution of the streaks, the difference between the steady state and the analytical Blasius solution is displayed in the yz-plane for different streamwise positions in figure IV.13.

The presence of the low speed streaks at $z = 0$ just behind the roughness makes the base flow highly non parallel in the streamwise direction. Nevertheless, a quasi-parallel evolution is recovered from $x = 40$ when the two high speed streaks join together. Another way to quantify the streamwise evolution of the streaks is to define the streaks amplitude as explained by Shahinfar et al. (2013)

$$A_{ST}^{int}(x) = \frac{1}{U_\infty} \int_{-1/2}^{+1/2} \int_0^{\eta^*} |U(x,y,z) - U^z(x,y)| d\eta d\zeta \tag{IV.5}$$

where

$$\eta = \frac{y}{\delta} = \frac{y}{\sqrt{x\nu/U_\infty}} \text{ and } \zeta = \frac{z}{L_z}. \tag{IV.6}$$

$U^z(x,y)$ being the streamwise velocity averaged in the crossflow direction. The deviation of the streamwise velocity from its spanwise averaged value is then integrated on the whole spanwise direction and from $0 < \eta < \eta^*$ in the wall normal direction at each x position. η^* is the truncated wall-normal distance opportunely fixed equal to 9. The value of A_{ST} as reported in eq. (IV.5) is displayed in figure IV.14. Thanks to the definition (IV.5), it is straightforward to separate the contribution of each negative and positive streak. At each position the positive contribution (H_{ext}) of A_{ST} is always equilibrated by its negative counterpart ($L_{ext} + L_{mid}$). Just behind the roughness, the amplitude of the high speed and low speed streak in the middle is comparable. This is not the case far from the roughness. After $x = 4$ the external low speed streaks grow rapidly up to $x = 20$ where the lift-up can be considered completely triggered. It is also interesting to observe how the area associated to each positive and negative streak evolves with the streamwise direction. Figure IV.15 illustrates how despite the external low speed streaks increase their size proportionally with the boundary layer growth, the high speed streak keeps an almost constant area along x. The last observation suggests that the streamwise velocity of the high speed streak has to increase to achieve the same amplitude of the external low speed streaks as depicted in figure IV.14. As a result, moving downstream, $\partial U/\partial z$ increases in the region close to the inflectional points. If the position $x = 20$ corresponds

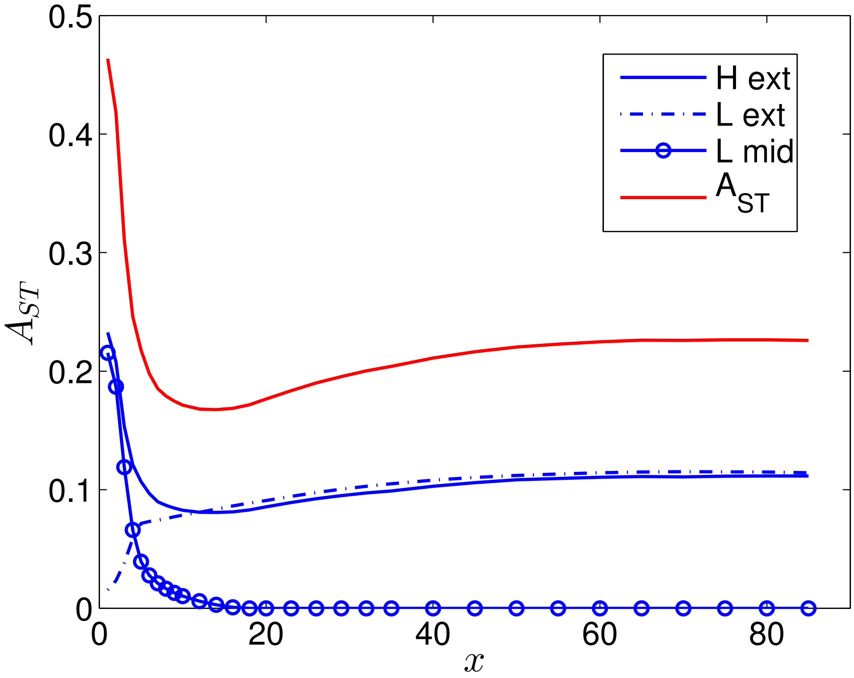

Figure IV.14: Evolution of the streaks amplitude in streamwise direction. In red the value of A_{ST} as reported in eq. (IV.5). In blue the contribution of the high speed streak (H_{ext}), external low speed streaks (L_{ext}) and low speed in the middle (L_{mid}).

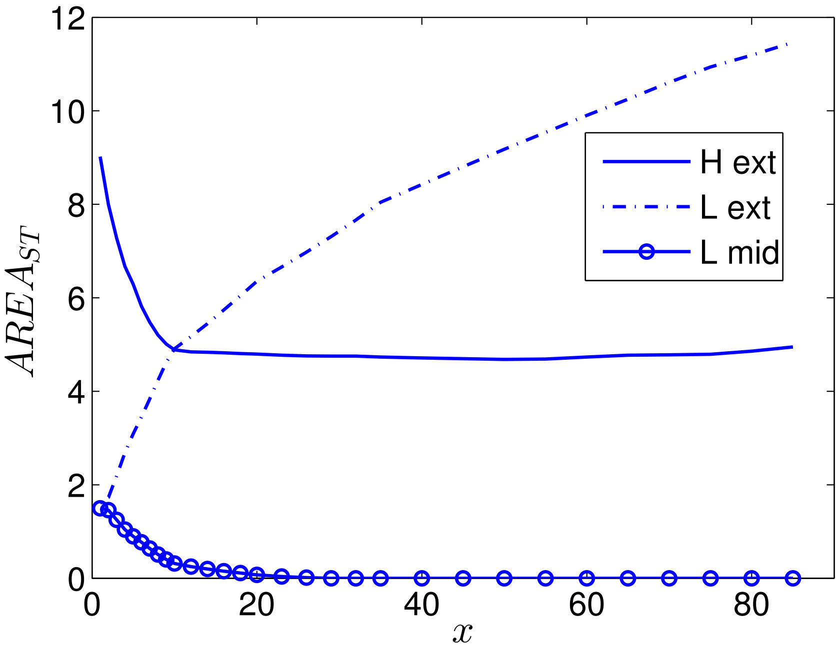

Figure IV.15: Evolution of the area associated to each positive and negative streaks in streamwise direction. In blue curves the area of the high speed streak (H ext), external low speed streaks (L ext) and low speed in the middle (L mid).

with the disappearance of the middle streak (see fig. IV.13), $x = 4$ coincides with the disappearance of the separation zone as shown in figure IV.16. As one can observe, there is another stagnation point in front of the cylinder due to the presence of the horseshoe vortex (Baker, 1979; Loiseau et al., 2014).

The base flow velocity has been compared with the experimental mean flow in figure IV.17. Despite the different behaviour experienced in the experiments and in the numerical simulation, a low distortion can be noted just on the low streak on the middle. On the both side of the middle streak a perfect superposition of the velocity profiles can be appreciated.

IV.3.3 Linear stability

IV.3.3.1 Local stability analysis

A further investigation is necessary to explain the mismatch between experiment and numerical simulation. The unsteadiness experienced in the experiment can be triggered by receptivity of a steady global mode or by transient growth of the energy. In both cases the local stability analysis is a mandatory step since the presence of local unstable modes can be linked to the presence of an absolutely unstable region (Huerre and Monkewitz, 1985) or to the non-normality of the NS operator which allows the energy growth of an initial perturbation that evolves in streamwise direction (Cossu and Chomaz, 1997).

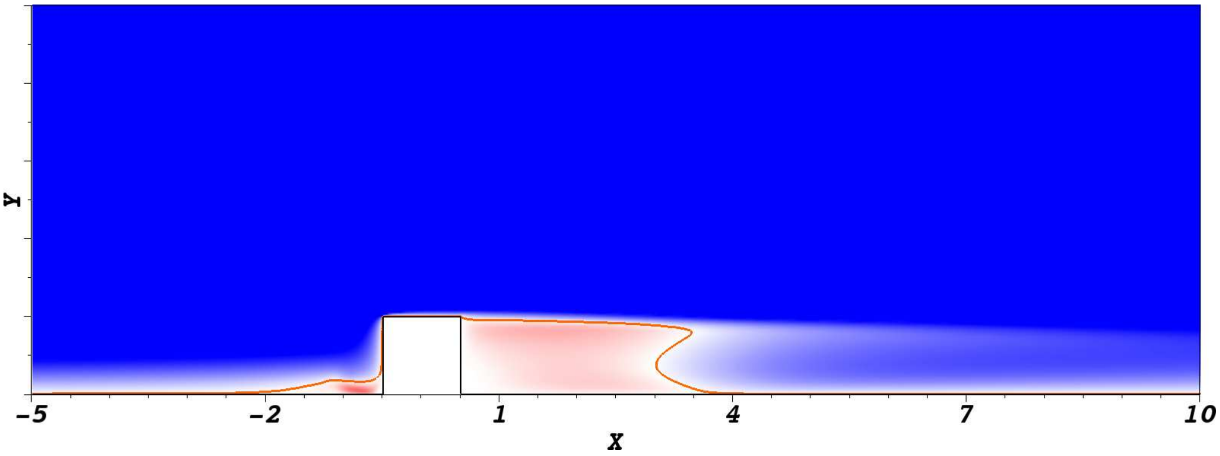

Figure IV.16: Recirculation bubble behind cylinder. The red colour highlight negative streamwise velocity. The orange continuous line depicts the zero streamwise velocity.

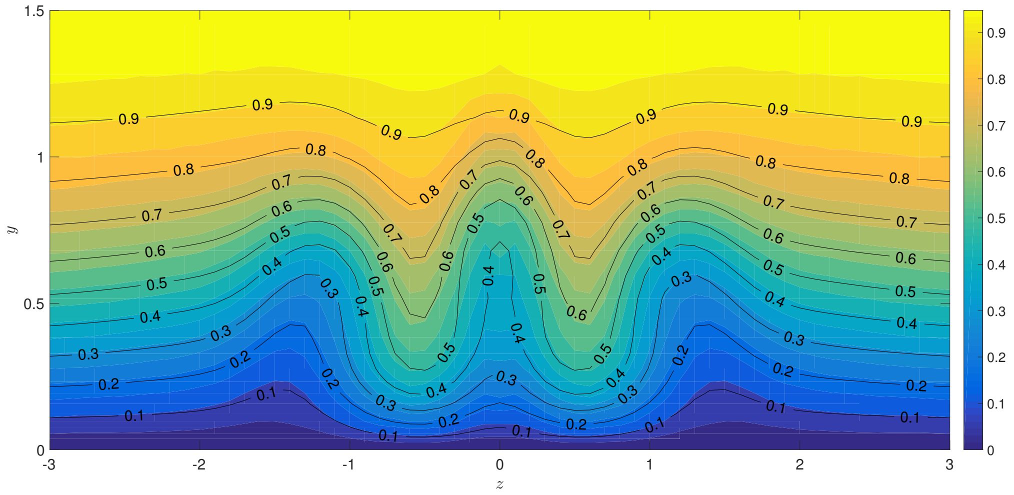

Figure IV.17: Comparison between experimental mean flow (pseudocolor) and numerical base flow (isolines) at $x = 10$.

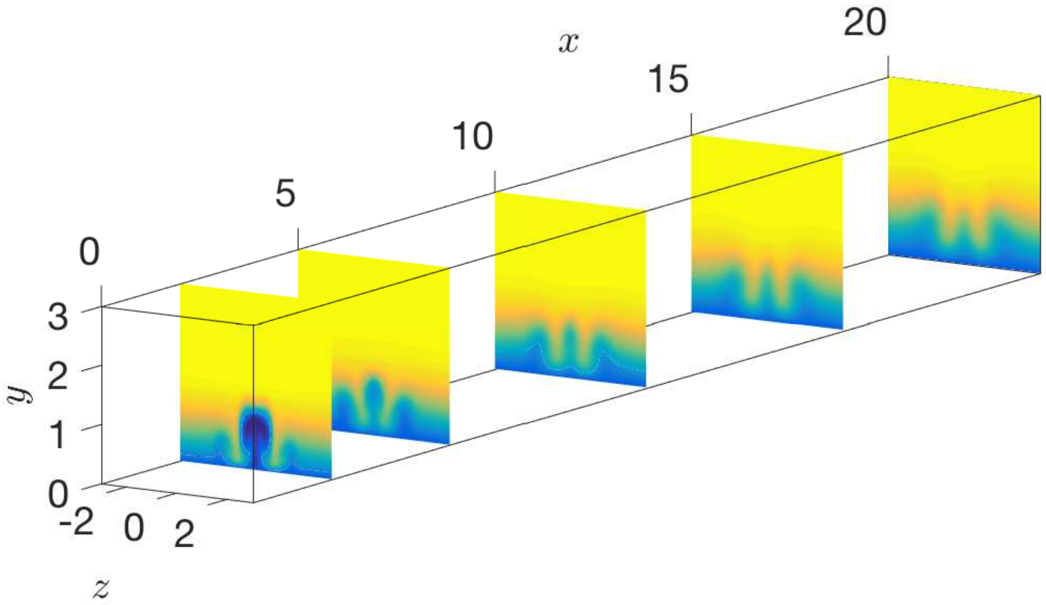

Figure IV.18: 2D slices of the base flow used to evaluate the local stability analysis. The pseudocolors highlight the streamwise velocity field in yz-sections. $z \in [-5;\ 5]$ and $y \in [0;\ 30]$

Imposing a modal decomposition in the streamwise direction (α) and in time (ω)

$$\mathbf{u}(x, y, z, t) = \hat{\mathbf{u}}(y, z)e^{(\alpha x + \omega t)} \tag{IV.7}$$

it is possible to study the local stability of the base flow at each streamwise position. A temporal stability analysis has been performed with $\alpha \in \mathbb{R}$ and $\omega \in \mathbb{C}$. Different yz planes have been extracted behind the roughness from the base flow velocity field IV.18.

The 2D velocity field goes from -5 to 5 in the spanwise direction and from 0 to 30 in the wall-normal direction. The z-direction is discretized with 100 Fourier collocation points and the y-direction with 120 Chebyshev collocation points with the first 60 points concentrated from $y = 0$ to $y = 5$. The local stability has been evaluated for different streamwise positions from $x = 2$ to $x = 80$. The LSA is performed for $0 \leq \alpha \leq 3$. From $x = 2$ to $x = 20$ four leading modes are present. Both sinuous and varicose symmetries are observed. Moreover, two modes are linked just to the streak in the middle and the other two are linked to the streaks on both sides of the cylinder. The sinuous and varicose modes localized on the middle and the external streaks are depicted in figure IV.19. In all the cases, the unstable modes are wrapped on the low speed streaks where inflectional points in the velocity profile are present. For $2 \leq x \leq 15$ the most unsteady mode is a

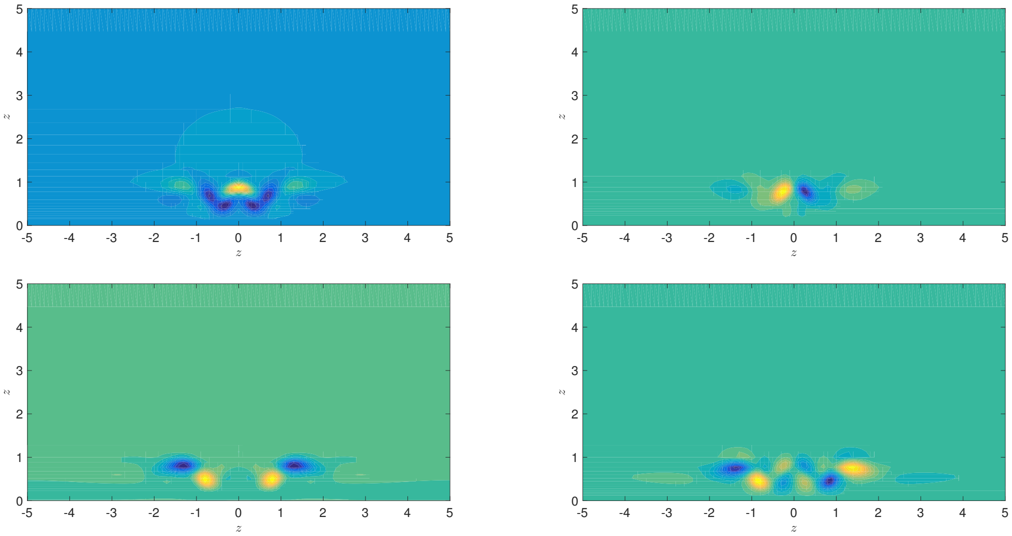

Figure IV.19: Local eigenmodes at $x = 10$ for $\alpha = 1.2$. Local eigenvalues that wrap the middle low streak (top) and the external low streaks (bottom). Both symmetries can be observed varicose (left) and sinuous (right).

sinuous perturbation on the low speed middle streak (see fig. IV.20). The modes localized on the two external low speed streaks have always a growth rate lower than that wrapped on the middle streak. This is true up to $x \approx 17$ where the perturbation on the middle streak becomes stable and only the perturbation on the lateral streaks remains unstable. If for the middle streak the sinuous perturbation is always more unstable than the varicose one, on the external streaks the varicose perturbation shows a growth rate greater than the sinuous one up to $x \approx 24$ where all modes become stable. The presence of sinuous and varicose unstable modes in the local spectrum makes both sinuous and varicose scenarios possible. In particular, the sinuous scenario might match that proposed by Loiseau et al. (2014), whereas varicose unsteadiness are currently observed in experiments, as previously discussed. Nevertheless, the local stability analysis is not capable to explain the reason why just the varicose perturbation is observed in the IAG experiment. The experimental dynamics could be projected onto the invariant subspace defined by the eigenvectors of the local stability spectrum to provide a weight to each eigenvector as done by Piot et al. (2008). Anyhow, this further study would not explain the source of the unsteadiness.

IV.3.3.2 Global stability analysis

To overcome the limitations of the local stability, the homogeneous hypothesis of the base flow in the streamwise direction is dropped, leading to a three-dimensional, global stability analysis. The dynamics of infinitesimal perturbations evolving onto the base flow $\mathbf{U}_b$ are governed by the linearized Navier-Stokes equations

$$\begin{gathered}\frac{\partial \mathbf{u}}{\partial t} + (\mathbf{u} \cdot \nabla)\,\mathbf{U}_b + (\mathbf{U}_b \cdot \nabla)\,\mathbf{u} = -\nabla p + \frac{1}{Re}\nabla^2 \mathbf{u} \\ \nabla \cdot \mathbf{u} = 0.\end{gathered} \tag{IV.8}$$

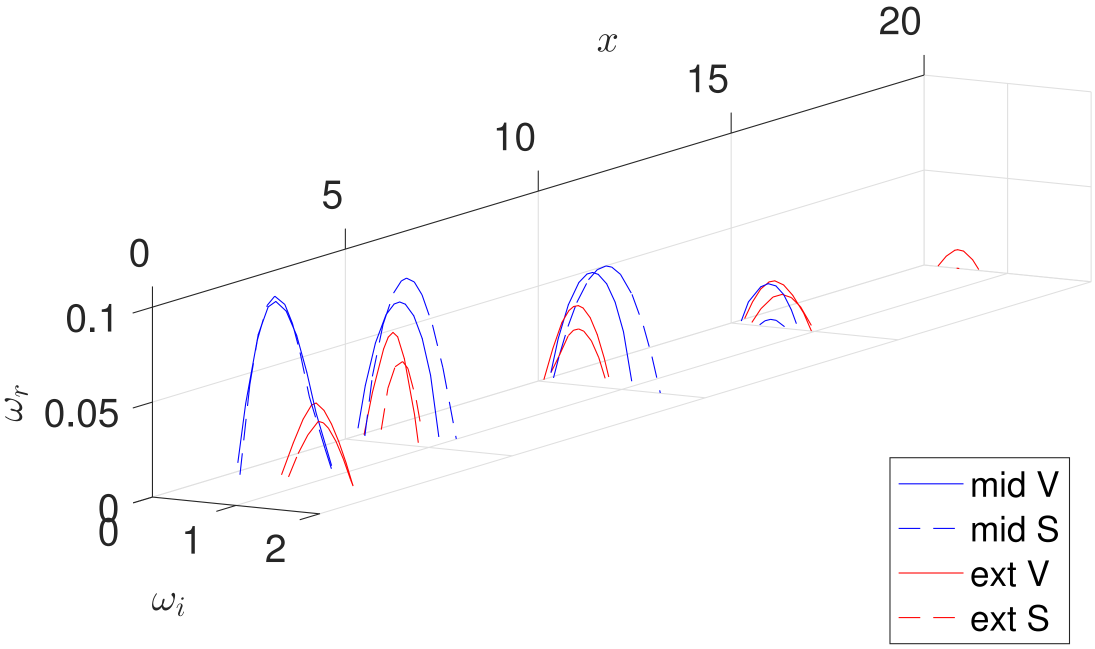

Figure IV.20: From $x = 2$ to $x = 20$ four leading modes are present in the local eigenspectrum. The evolution of the unstable modes is highlighted in $\omega_i - \omega_r$ plane at $x = 2$, 5, 10, 15 and 20. Continuous lines are linked to varicose mode, dashed lines to sinuous one. The red lines depict the modes evolution which live on the external low streaks for different alpha values. Blue lines depict the evolution of the modes which wrap the low streak in middle along $z = 0$.

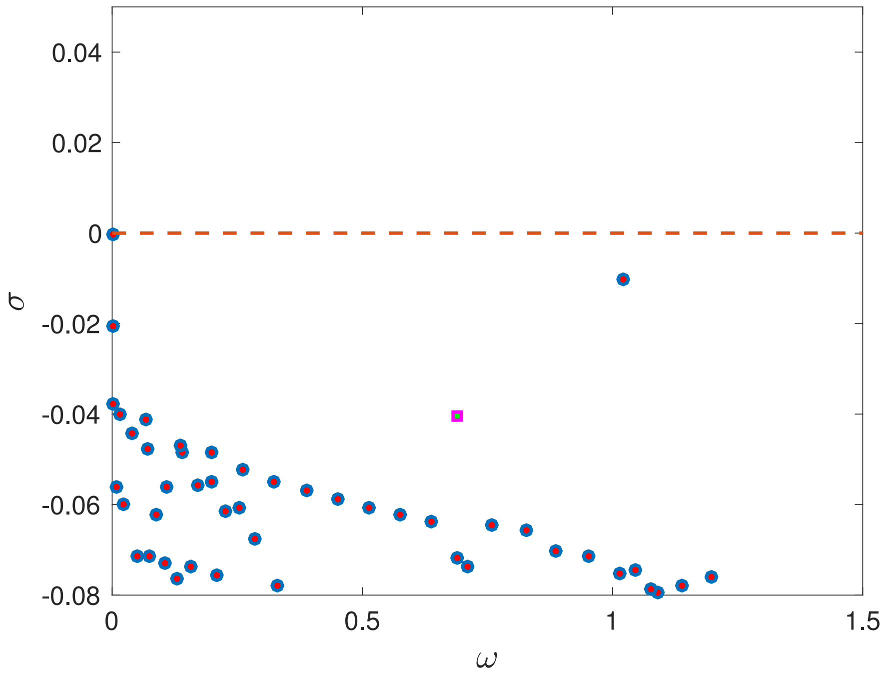

Figure IV.21: Global eigenspectrum for the experimental case $Re = 700$ and $\delta_1/h = 0.491$. The circle markers (◯) are linked to varicose perturbation and the square marker (□) to the sinuous one.

where $\mathbf{U}_b$ is the base flow velocity field, while $\mathbf{u}$ is the direct perturbation. Although one should traditionally use a Neumann condition at the outflow for the direct equations, a zero-velocity condition has been prescribed at both the inflow and outflow in all cases for the sake of computational simplicity and for coherence with the successive analysis. Additionally, fringe regions have been used as to kill the perturbation once it reaches the outflow. Note that the streamwise extent of the domain and the characteristics of the fringe regions have been chosen so that our results are not hardly influenced by the inflow-outflow boundary conditions. The linearised Navier Stokes equations are evolved forward in time to build the Hessenberg matrix that represent a reduced order model of the propagation matrix. A Krylov space dimension equal to $k = 400$ and a sampling period $\Delta t = 0.748$ is used. The eigenmodes have been considered converged if a residual level lower than $1e^{-6}$ is reached. The eigenspectrum is displayed in figure IV.21

Figure IV.21 provides the eigenspectrum which does not present any unstable mode. At the bottom of the spectrum, one can observe a branch of modes characterized by a varicose symmetry (circles). On top of them, two isolated modes, characterized by different symmetries, can be seen: a varicose mode with $\omega = 1.02$ lying close to the instability threshold (square), along with a more stable sinuous one (red plus) with $\omega = 0.68$. The varicose leading eigenvector, depicted in figure IV.22 (top), shows patches of spanwise-symmetric streamwise velocity perturbations, which are alternated in the streamwise direction. They are placed on top of the near-wake central low-speed streak of the base flow, as well as on the low-speed streaks placed at the sides of the central one further downstream (black isocontours). The sinuous one, shown in figure IV.22 (bottom)

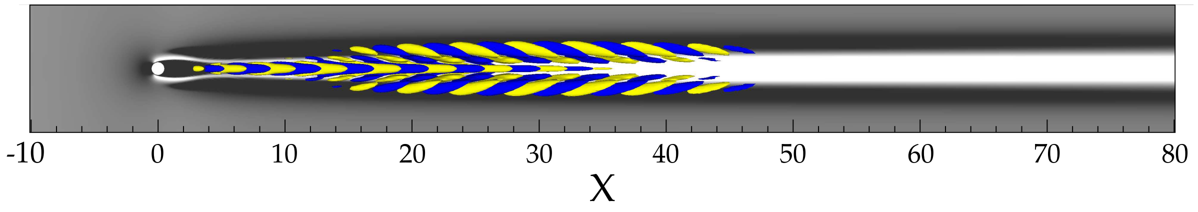

(a)

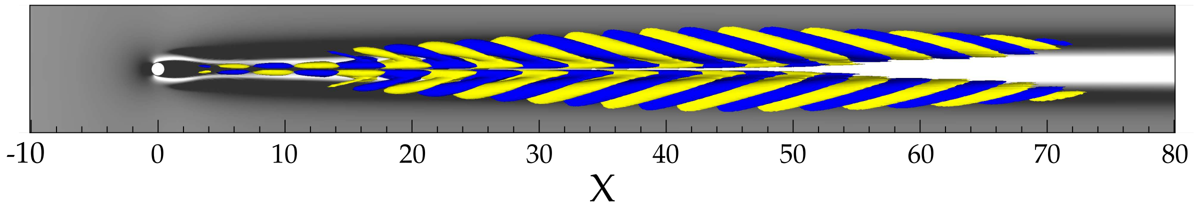

(b)

Figure IV.22: Eigenvector associated with (a) the isolated varicose and (b) sinuous mode for case $(\eta, Re) = (1, 700)$. Isosurfaces of streamwise velocity perturbation ($\pm 10\%$ of maximum amplitude, yellow for positive, blue for negative values). Greyscales are related to base flow streamwise velocity deviation from Blasius flow, extracted at $y = 0.8$ (black for negative, white for positive values).

exhibits a very similar shape, except for its opposite symmetry and its longer streamwise extent. In agreement with the local stability, in both cases sinuous and varicose global modes originate onto the middle streaks and move on the external low speed streaks downstream.

The main features of the experimental unsteadiness are compared with those of the isolated global mode in table IV.3.

	ω	λ_x	sym
Exp	1.05 ± 0.11	4.8 ± 0.5	V
Num$_v$	1.02	4.7	V
Num$_s$	0.68	3.3	S

Table IV.3: Comparison between experimental observation and numerical isolated eigenmodes.

As one can see, the main character of the varicose global mode matches perfectly the experimental observation. This new result open news perspectives that can be summarized in the following two questions:

- If the varicose global mode matches the experimental unsteady observation, why it is stable?
- If the varicose stable eigenmode is observed, why the sinuous stable mode is totally absent in the unsteady dynamics?

One possible explanation to these two questions is that these two modes might be characterized by a highly different receptivity, only one of these being trigged by external noisy perturbations.

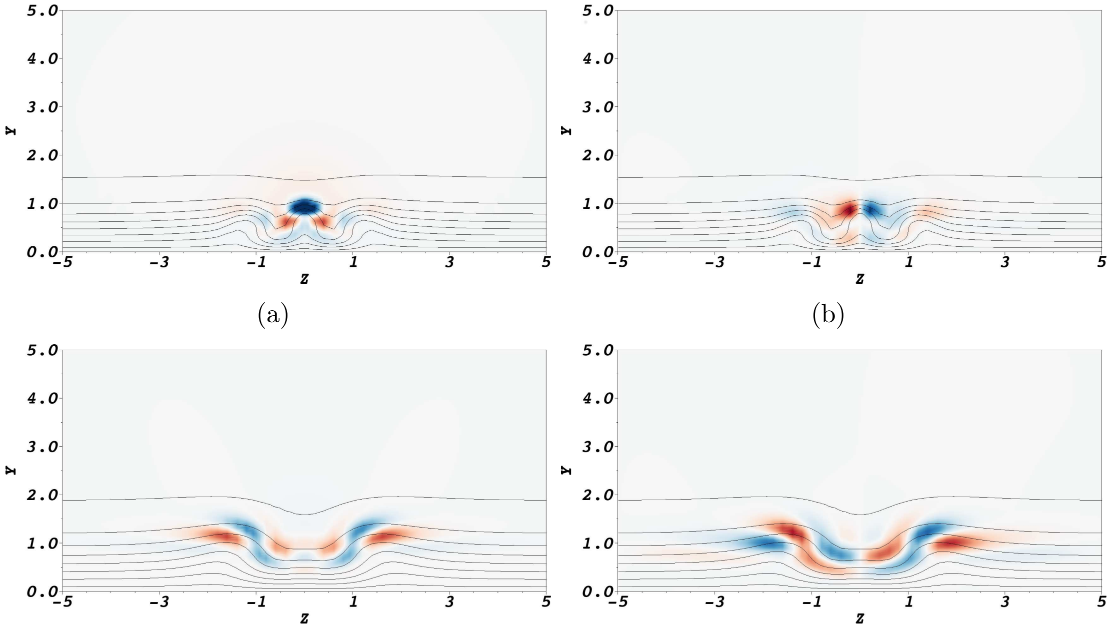

(a) (b)

(c) (d)

Figure IV.23: Superposition of the real part of sinuous (right) and varicose (left) global mode (pseudocolors) with the streamwise velocity of the base flow (isolevel) at $x = 10$ (top) and $x = 40$ (bottom).

IV.3.3.3 Pseudospectrum

For the experimental set-up, all the modes in the eigenspectrum are stable. Hence, the unsteadiness observed experimentally cannot be explained by a linear instability of the underlying base flow. It might however results from a large receptivity of the flow, which can be either linked to a strong transient growth of perturbations due to the non-orthogonality of the eigenvectors, or to a strong sensitivity of specific modes to external forcing. In the first case, the flow will act as an amplifier of a large range of frequencies, whereas in the latter case, it will 'resonate' at a precise frequency. To quantify the receptivity of the flow, the pseudospectrum of the linearized Navier-Stokes operator is evaluated using the Hessenberg matrix as done by Toh and Trefethen (1996)

$$\Lambda_\epsilon(\mathbf{A}) = \{z \in \mathbb{C} : \|(z\mathbf{I} - \mathbf{A})^{-1}\| > \epsilon^{-1}\} \approx \{z \in \mathbb{C} : \lambda_{\min}(z\mathbf{I} - \log(\mathbf{H})/\Delta t) < \epsilon\}. \quad \text{(IV.9)}$$

where the quantity $(z\mathbf{I} - \mathbf{A})^{-1}$ is known as the resolvent of $\mathbf{A}$ (Trefethen and Embree, 2005), measuring how sensitive the eigenvalues of $\mathbf{A}$ are to some perturbations of $\mathbf{A}$, and $\lambda_{\min}$ is the smallest singular value of a matrix, approximating its norm.

The pseudospectrum of $\mathbf{A}$ for $(\eta, Re) = (1, 700)$ is shown in figure IV.24. The solid lines depict the $\log_{10}(\epsilon^{-1})$ contours, representing the response of the system to a perturbation $z\mathbf{I}$. As can been seen, very high levels of $\log_{10}(\epsilon^{-1})$ are reached in the vicinity of the eigenvalue associated to the varicose isolated mode, hence indicating that this particular eigenpair is highly sensitive to disturbances: even a disturbance as small as $\epsilon \approx 10^{-5}$ is sufficient to destabilize the system.

The sinuous mode appear to be not receptive at all, this means that just a perturbation really close to the eigenmode can trigger a sinuous unsteadiness and besides the interaction

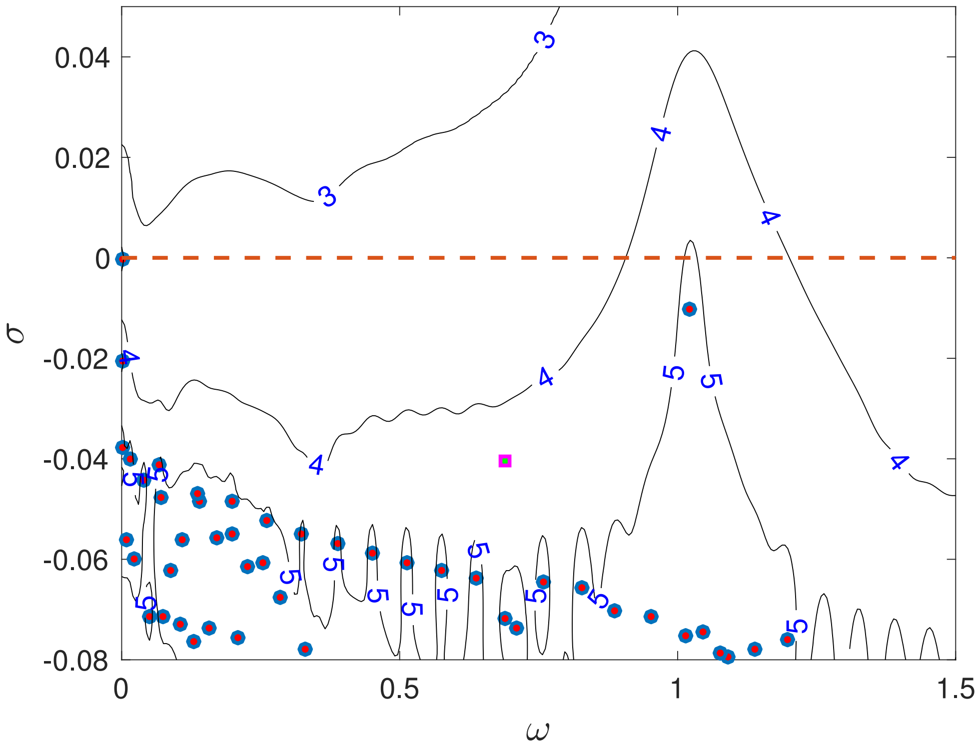

Figure IV.24: Eigenspectrum (colored symbols) and pseudospectrum (solid lines) of the linearised Navier-Stokes operator for $(\eta, Re) = (1, 700)$. Circles (squares) represent varicose (sinuous) modes. The iso-lines represent pseudospectrum given by $\log_{10} \epsilon^{-1}$ contours, with ϵ ranging from 10^{-6} to 10^{-3}.

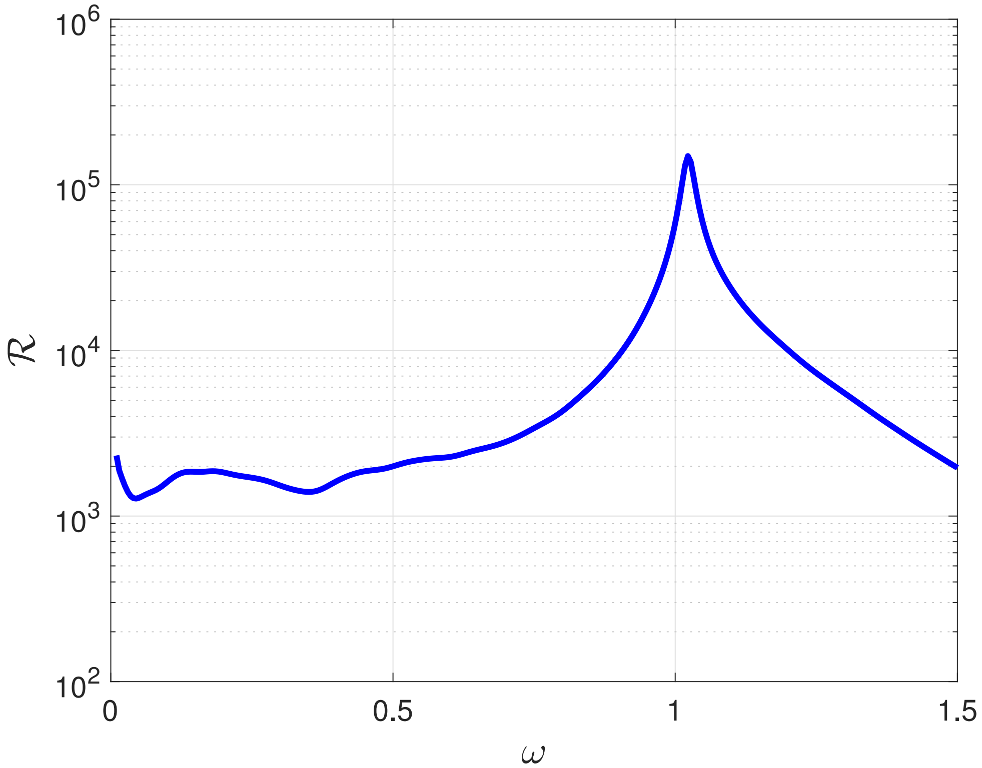

Figure IV.25: Approximation of the resolvent norm extracted from the pseudospectrum for $(\eta, Re) = (1, 700)$ on the $\sigma = 0$ line.

between a sinuous and varicose mode is null since they will be always orthogonal to each other. Looking at all points on the complex plane $(\omega - \sigma)$ at $\sigma = 0$ it is possible to get an approximation of the resolvent norm like in the optimal forcing framework. The resulting resolvent $(i\omega\mathbf{I} - \mathbf{A})^{-1}$ expresses the relation between an harmonic forcing and its response. The approximation of the resolvent norm is displayed in figure IV.25.

The curve in IV.25 confirms the high receptivity of the varicose global mode. By using an harmonic forcing with $\omega = 1.02$ to perturb the system an amplification factor of the forcing amplitude equal to $\mathcal{R} = \|\hat{\mathbf{u}}\|/\|\mathbf{f}\| = 104100$ is achieved on the final energy of the response. This result explains the varicose unsteadiness observed in the experiment despite the steady base flow. A low external perturbation is able to trigger the varicose global mode since it is the most receptive mode.

IV.3.3.3.a Numerical convergence At this point, a numerical convergence analysis is necessary in order to demonstrate the independence of the achieved results from numercial parameters. In the present work, the grid convergence analysis has been performed using a h-type refinement due to its simplicity. Figure IV.26(a) depicts the eigenspectrum of the linearized Naver-Stokes operator for the case $(\eta, Re) = (1, 700)$ for three different polynomial orders, namely $N = 6$, 8 and 10. For the present configuration, the spectral element mesh is kept constant (figure IV.27 depicts the coarse grid distribution of the spectral elements in a given horizontal plane). As shown, the eigenvalues of interest are hardly influenced by the mesh refinement. On the other hand, figure IV.26(b) depicts the approximation of the resolvent norm $\mathcal{R}(\omega)$ as obtained by the pseudospectrum analysis.

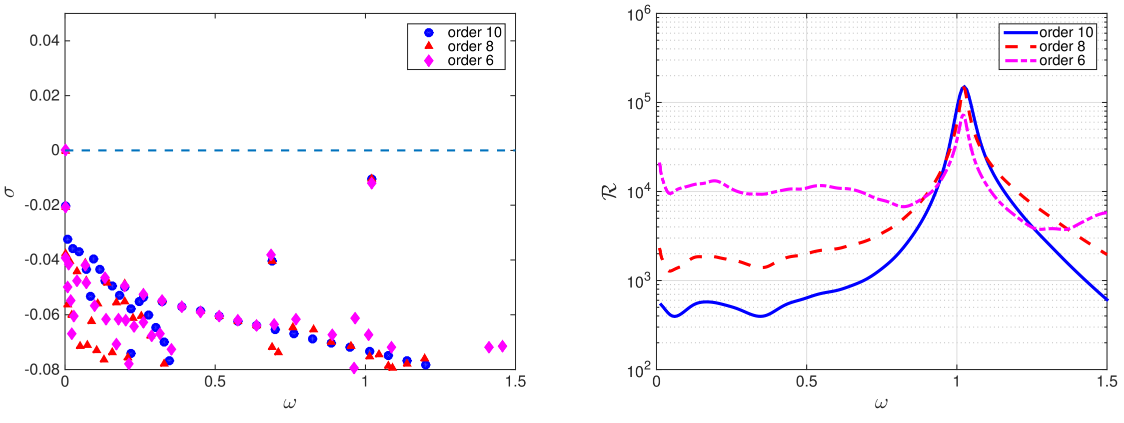

(a) (b)

Figure IV.26: Grid convergence analysis on the case $(\eta, Re) = (1, 700)$. (a) Evolution of the linearized Navier-Stokes operator as the degree of the Lagrange interpolants is increased from $N = 6$ up to $N = 10$. (b) Same as (a) for the approximation of the resolvent norm based on the pseudospectrum analysis.

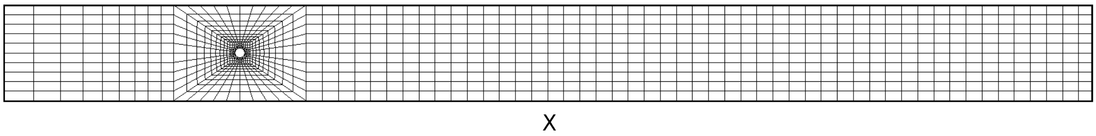

Figure IV.27: Coarse grid distribution of the spectral elements in a given horizontal plane for the aspect ratio $\eta = 1$ case. Note that in the simulation N Lagrange interpolants are used in the three directions of space within each of these elements

Although the peak frequency and resolvent gain do not seem to be largely influenced by the polynomial order of the Lagrange interpolants used, the low-frequency part of this resolvent (i.e. $\omega < 0.75$) appears to be significantly stabilized as the polynomial order is increased as the solution becomes less sensible to the numerical discretization.

IV.3.4 Varicose mode analysis

In the light of the last result, an in-depth analysis of the varicose mode is mandatory to understand how far the linear result can driver the unsteady non-linear dynamics. More precisely the kinetic energy budget of the global mode provides information onto the energy exchange between the base flow and the perturbation highlighting the stabilizing and destabilizing mechanisms involved in the global eigenvector under consideration. The same analysis was done by Brandt (2007) in the local framework to characterize varicose and sinuous instabilities. Brandt shows how the destabilizing effect for the varicose instability is provided by the work of the Reynolds stress tensor $\tau_{xy} = -uv$ on the wall normal-basic shear $\partial U_b/\partial y$. In the global stability framework and for flow over roughness Loiseau et al. (2014) showed that the production term $P_2 = -uv\frac{\partial U}{\partial y}$ is just one of the destabilising terms. A further contribution to the destabilization of the varicose mode is provided by the spanwise production term $P_3 = -uw\frac{\partial U_b}{\partial z}$. However, it should be considered that the varicose instability observed by Loiseau et al. (2014) appears only for aspect ratios higher than 1. The high aspect ratio of the cylindrical roughness induces a high distortion of the boundary layer flow in the spanwise direction. This could not be the case for $\eta = 1$. To localize the source of the varicose global mode a *wavemaker* (Giannetti and Luchini, 2007) analysis has also been carried out.

IV.3.4.1 Perturbation kinetic energy budget

The kinetic energy rate of exchange for a periodic or bounded flow is described by the Reynolds-Orr equation:

$$\frac{\partial E}{\partial t} = -\int_V \mathbf{u} \cdot (\mathbf{u} \cdot \nabla)\mathbf{U}_b dV - \frac{1}{Re}\int_V \nabla\mathbf{u} : \nabla\mathbf{u} dV \tag{IV.10}$$

where the energy is defined as

$$E = \frac{1}{2}\int_V \mathbf{u} \cdot \mathbf{u} dV. \tag{IV.11}$$

For the case of interest the flow is neither bounded nor periodic but the perturbation goes naturally to zero towards the end of numerical domain. On the right hand of equation (IV.10) the first term is the production term and the second is the dissipation one. The production term can be decomposed in nine contributions of the Reynolds stress tensor

$$\begin{aligned} P_1 &= -u^2\frac{\partial U_b}{\partial x},\ P_2 = -uv\frac{\partial U_b}{\partial y},\ P_3 = -uw\frac{\partial U_b}{\partial z} \\ P_4 &= -uv\frac{\partial V_b}{\partial x},\ P_5 = -v^2\frac{\partial V_b}{\partial y},\ P_6 = -vw\frac{\partial V_b}{\partial z} \\ P_7 &= -wu\frac{\partial W_b}{\partial x},\ P_8 = -wv\frac{\partial W_b}{\partial y},\ P_9 = -w^2\frac{\partial W_b}{\partial z} \end{aligned} \tag{IV.12}$$

For the complexity of the base flow the physical interpretation of each term is not intuitive. To better understand the mechanisms involved in the production energy rate we follow the Albensoeder et al. (2001) work. The perturbation is decomposed in two parts $\mathbf{u} = \mathbf{u}_\perp + \mathbf{u}_\parallel$ where $\mathbf{u}_\perp$ is the component of the perturbation perpendicular to the base flow field and $\mathbf{u}_\parallel$ is the parallel one:

$$\mathbf{u}_\parallel = \frac{(\mathbf{u} \cdot \mathbf{U}_b)}{\|\mathbf{U}_b\|^2}\mathbf{U}_b \quad ; \quad \mathbf{u}_\perp = \mathbf{u} - \mathbf{u}_\parallel \tag{IV.13}$$

The decomposition (IV.13) is injected in the production term of (IV.10). The production term is now composed by four terms, namely:
Bearing in mind that the base flow is streaked, the perturbation parallel to the base flow is a disturbance aligned with the streaks, whereas the perpendicular one are in plane with the counter rotating vortices. The most important production term in the configuration under consideration is I_2 that can be defined as the production of the lift-up mechanism and represents the exchange of energy from the counter-rotating vortices to the streaks. I_3 is the anti-lift-up production and I_1 and I_4 can be defined respectively as the self production of counter-rotating vortices and self production of streaks. The kinetic energy budget with the decomposition proposed by Albensoeder et al. (2001) is displayed in figure IV.28 normalized by the unitary dissipation rate.

$I_1 = \int_V \mathbf{u}_\perp \cdot (\mathbf{u}_\perp \cdot \nabla)\mathbf{U}_b dV$	The transport of energy from the perpendicular component to the perpendicular one by means of the gradient of the base flow
$I_2 = \int_V \mathbf{u}_\parallel \cdot (\mathbf{u}_\perp \cdot \nabla)\mathbf{U}_b dV$	The transport of energy from the perpendicular component to the parallel one by means of the gradient of the base flow
$I_3 = \int_V \mathbf{u}_\perp \cdot (\mathbf{u}_\parallel \cdot \nabla)\mathbf{U}_b dV$	The transport of energy from the parallel component to the perpendicular one by means of the gradient of the base flow
$I_4 = \int_V \mathbf{u}_\parallel \cdot (\mathbf{u}_\parallel \cdot \nabla)\mathbf{U}_b dV$	The transport of energy from the parallel component to the parallel one by means of the gradient of the base flow

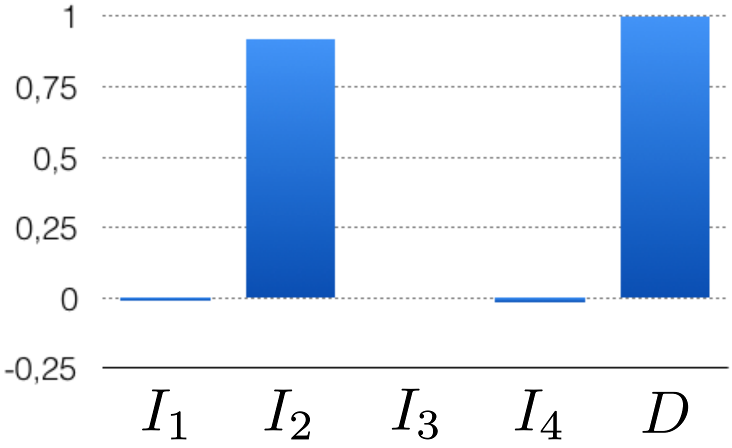

Figure IV.28: Energy budget of varicose global mode. Production term normalized with the dissipation.

As one can see, the only active term for the varicose global mode is the lift-up production term. Of course the sum of the production terms is lower than the dissipation as the case is globally stable. The spatial distribution of the lift-up production is depicted in figure IV.29. The lift up production is localized on the shear generated by the low streaks in the middle and the production peak is exactly in the $z = 0$ plane. As previously discussed, the middle low speed streak is not driven by the lift up mechanism, since the counter-rotating vortices generated by the horseshoe vortex wrapped around the roughness push down the flow momentum, which should generate a high speed streak in the $z = 0$ region. Indeed, a high speed streak in the $z = 0$ plane is recovered downstream at $x \approx 20$, but for $0.5 < x < 20$ the lift-up mechanism is overtaken by the deficit of velocity induced by the separation behind the roughness. The energy imbalance of these two mechanisms in the region $0.5 < x < 20$ provides the destabilising effect of the varicose mode. In figure IV.30 the experimental u_{rms} is depicted in function of the streamwise position at fixed (y, z) coordinates. The curve reveals a peak at $x = 8$ that is in agreement with the distribution of the I_2 in the streamwise direction (see fig. IV.30), indicating that this

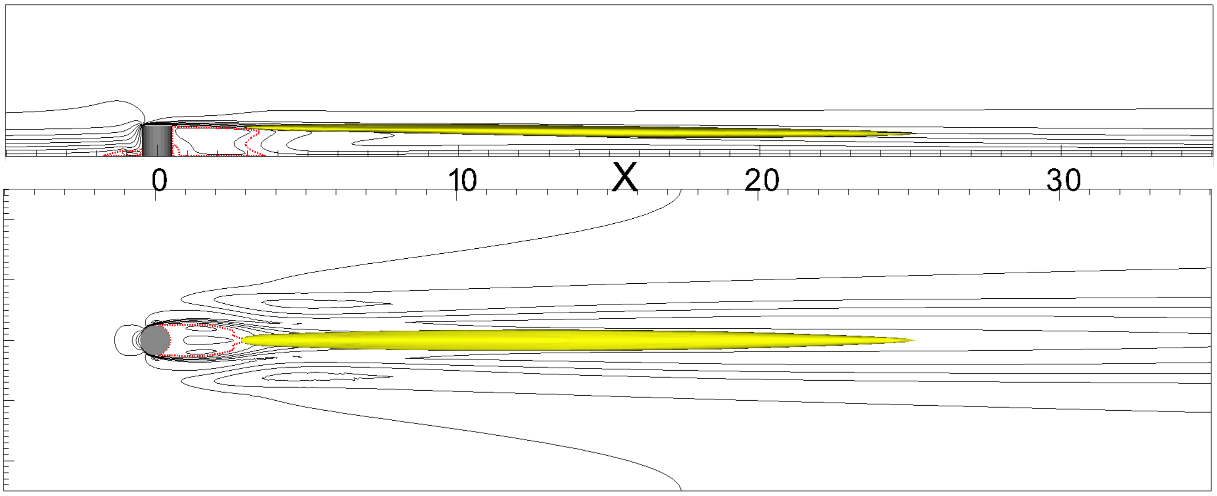

Figure IV.29: Spatial distribution of the lift-up production. The I_2 integrand (yellow isocontour) is localized on the shear related to the low middle streaks. The black line highlight isolevel of streamwise velocity in the palne at $z = 0$ (top) and $y = 0.5$ (bottom) plane. Red dashed lines depict the separation zone.

fluctuation peak is indeed linked to the onset of the varicose global mode. Once it is triggered by receptivity, the varicose global mode drives the main characteristics of the observed unsteadiness in terms of pulsation, wavelength and turbulent energy production. Moreover, looking at the spatial distribution of the I_2 term, once can observe that it is localized in the close neighbourhood of the $z = 0$ plane. In this plane, $\partial \bullet / \partial x \approx 0$ and $\partial V_b / \partial y$ is negligible compared to $\partial U_b / \partial y$. This means that only the work of the Reynolds stress tensor $\tau_{xy} = -uv$ on the wall normal basic shear $\partial U_b / \partial y$ provides the observed energy production. Hence, differently from the varicose mode found by Loiseau et al. (2014) for a higher aspect ratio ($\eta > 1$) the P_3 production term is close to zero and only P_2 provides energy extraction from the base flow as assessed by Brandt (2007) for a varicose instability of the streaks . The P_3 production works on both sides of the low velocity streaks (Loiseau et al., 2014) and it turns out to be triggered just for higher aspect ratios since the deformation of the boundary layer flow in the crossflow direction is remarkably higher for $\eta > 1$.

IV.3.4.2 Wavemaker

The energy budget analysis helps to understand the non-linear asymptotic behaviour but it cannot provide any indication on the spatial origin of the mode. The core of the global instability is known as wavemaker (Giannetti and Luchini, 2007; Marquet et al., 2008), which indicates the area where the self-sustained oscillator acts. Taking advantage of the continuous adjoint Navier-Stokes equations:

$$\begin{gathered}\frac{\partial \boldsymbol{u}^\dagger}{\partial t} + (\nabla \boldsymbol{U}_b)^T \boldsymbol{u}^\dagger + (\boldsymbol{U}_b \cdot \nabla)\, \boldsymbol{u}^\dagger = -\nabla p^\dagger + \frac{1}{Re} \nabla^2 \boldsymbol{u}^\dagger \\ \nabla \cdot \boldsymbol{u}^\dagger = 0,\end{gathered} \tag{IV.14}$$

it is possible to use the Krylov-Schur algorithm to get the adjoint eigenmode associated to the direct varicose eigenvector. As the adjoint equations are driven by the gradient of the

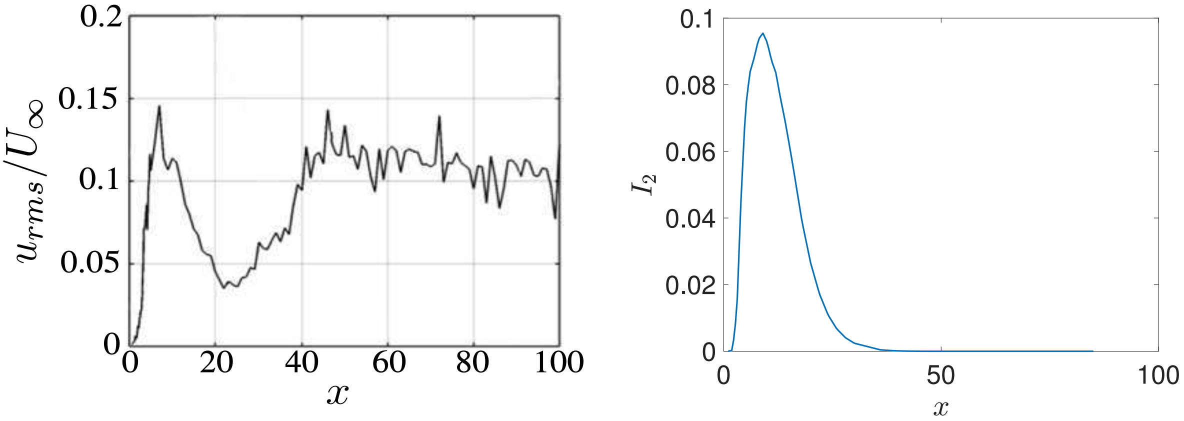

Figure IV.30: Comparison between experimental perturbation u_{rms} at $(y, z) = (1, 0)$ (left) and the integrand I_2 integrated over crossflow planes (right) for different streamwise position.

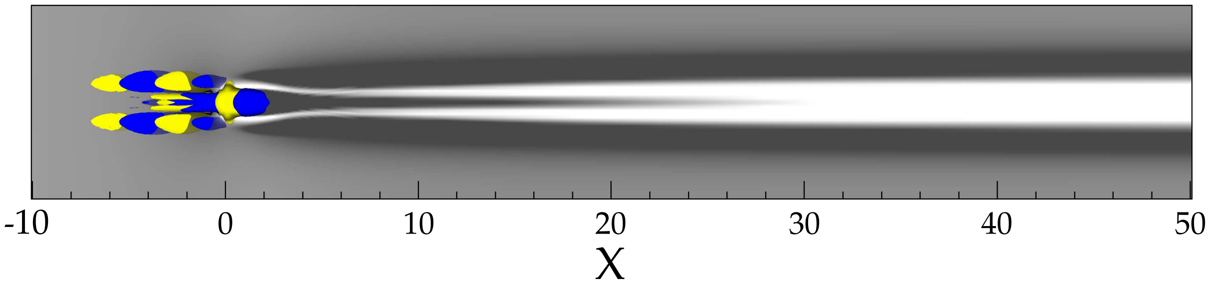

Figure IV.31: Real part of adjoint mode associated to the varicose global mode. ±5% isocontour of negative (blue) and positive (yellow) streamwise sensitivity. Grey scale highlight base flow streamwise velocity.

base flow, the adjoint variables express the sensitivity of the mode itself. More precisely the adjoint eigenvector is the most efficient forcing that has to be used to observe the associated direct eigenmode. The adjoint mode associated to the varicose global mode is depicted in figure IV.31. The adjoint mode is highly concentrated on the head of the roughness where strong gradients are present. The eigenvector extends itself in the upstream direction and rapidly goes to zero. Following the definition given by Giannetti and Luchini (2007), the wavemaker is given by the overlap of the direct $\mathbf{u}$ and adjoint global mode $\mathbf{u}^\dagger$:

$$\zeta(x, y, z) = \frac{\|\mathbf{u}(x, y, z)\| \|\mathbf{u}^+(x, y, z)\|}{\langle \mathbf{u}^+, \mathbf{u} \rangle} \tag{IV.15}$$

It represents the sensitivity of the mode to a base flow modification. Acting on the ζ field of the eigenvector of interest the growth rate and the pulsation of the eigenmode can be drastically changed (Marquet et al., 2008). For this reason, the most sensitive zone is also considered the core of the instability itself. The ζ field is reported in red in figure IV.32. For the varicose mode the wavemaker is a small zone that wraps the separation zone. The shear on the recirculation bubble is the cause of inflectional velocity profiles. The presence of the reverse flow in the separation bubble makes the separation zone a closed

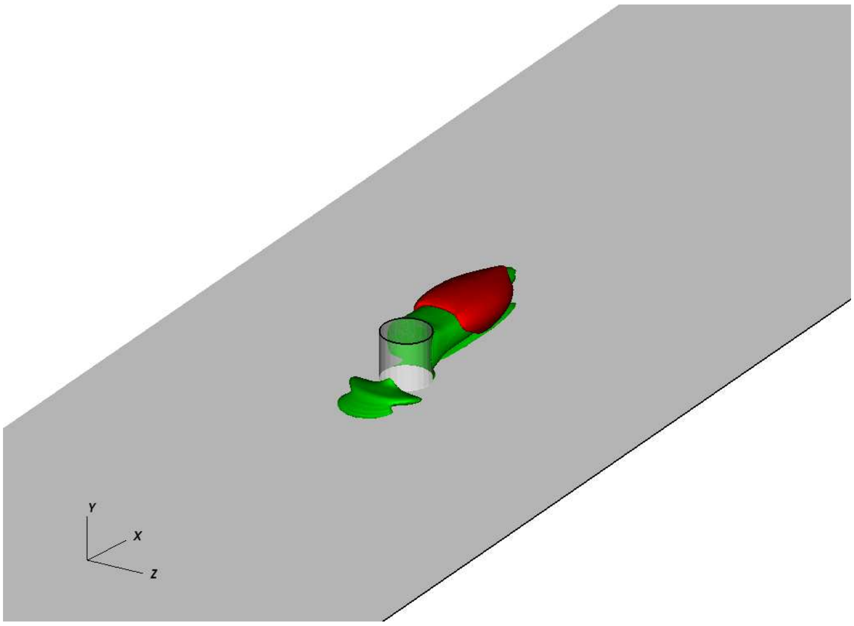

Figure IV.32: Red isocontour highlight the $\zeta(x, y, z)$ field that represent the wavemaker for the varicose global mode. Green isocontour indicate zero streamwise velocity field.

loop where the instability could be self sustained. A stronger shear behind the roughness can make the global mode unstable.

IV.3.5 Optimal forcing and response analysis

The resolvent curve in figure IV.25 shows that a harmonic forcing that pulses at $\omega = 1.02$ can induce a harmonic response with a kinetic energy 10^5 times higher than the amplitude of the forcing. Unfortunately, as far as well evaluated, the pseudospectrum cannot give any information about the spatial structure of the forcing that causes the energy amplification. To recover the forcing shape an optimal forcing analysis should be carried out. Toward this aim, the direct-adjoint optimization loop introduced by Monokrousos et al. (2010) is used to find the forcing $\hat{\mathbf{f}}$ that maximises the resolvent norm $\lambda = \|(i\omega\mathbf{I} - \mathbf{A})^{-1}\|_2$ at $\omega = 1.02$. The solution to this convex problem converges in few iterations to a residual level lower than 10^{-6}. The shapes of the optimal forcing and response are shown in figure IV.33 (top and bottom, respectively).

The optimal forcing is constituted by streamwise-alternated patches of velocity perturbations, placed upstream of the cylinder. Remarkably, it shows a varicose symmetry, similarly to the most sensitive isolated mode previously analysed. As it might be expected, the shape of the optimal response induced by such a forcing is very close to the shape of the isolated varicose mode, as one can observe by comparing figure IV.33 to figure IV.22. By using the bi-orthogonality condition it is possible to express the response of a steady system to a harmonic forcing as a linear combination of the direct eigenmodes (IV.16)

$$\mathbf{u} = \left(\hat{\mathbf{u}}_j^{\dagger}, \frac{\hat{\mathbf{f}}}{\omega - \lambda_j} \right) \frac{\hat{\mathbf{u}}_j}{\hat{\mathbf{u}}_j^{*}, \mathbf{A}\hat{\mathbf{u}}_j} \exp(i\omega t) \tag{IV.16}$$

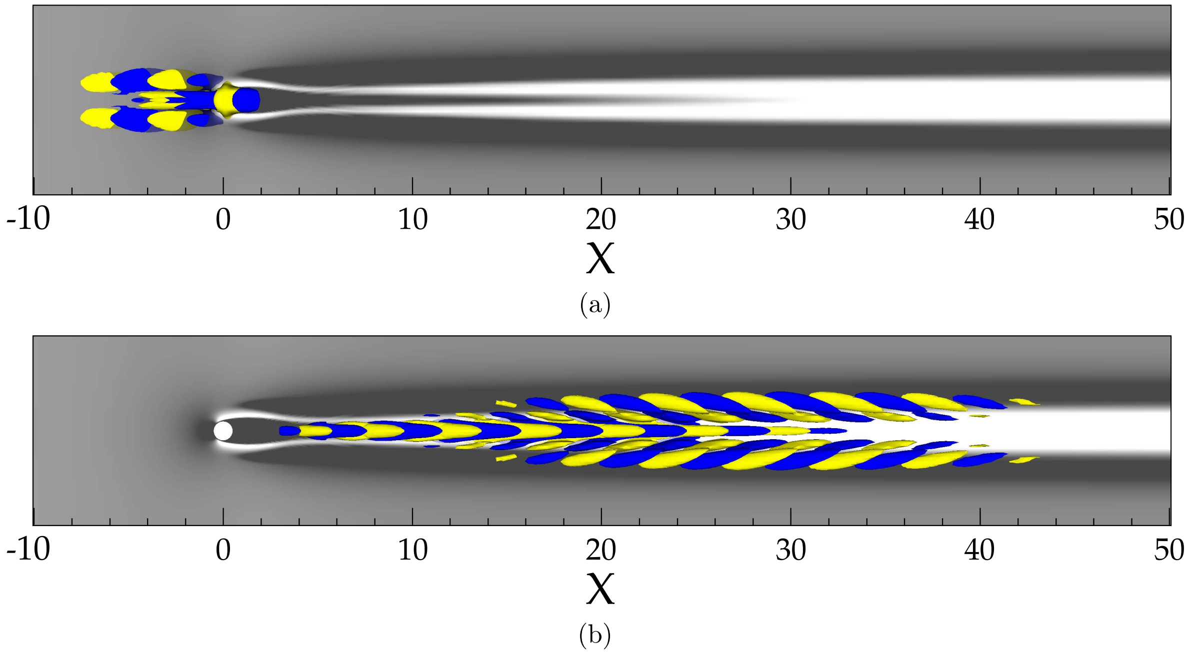

(a)

(b)

Figure IV.33: Shape of the optimal forcing (top) and the optimal response (bottom) for $\omega = 1.02$. Greyscales and isosurfaces are the same as in figure IV.22.

if $\mathbf{u}$ is equal to the varicose eigenmode $\hat{\mathbf{u}}_j$ then the scalar product $(\hat{\mathbf{u}}_j^\dagger, \hat{\mathbf{f}}) \neq 0$ just for the adjoint eigenvector $\hat{\mathbf{u}}_j^\dagger$ associated to the direct varicose mode. This behavior can be ascribed to the quasi-orthogonality of the varicose mode with respect to the other modes. The optimal gain associated to $\omega = 1.02$ is reported in table IV.4.

Pseudospectrum	Adjoint forcing	Optimal forcing
104100	143970	149 170

Table IV.4: Comparison between the gain estimation obtained by the pseudospectrum, the adjoint forcing and the optimal forcing.

A further demonstration of the orthogonality of the varicose mode is that forcing the system with the adjoint eigenvector the obtained gain is comparable with that of the optimal forcing. Moreover the Hessemberg matrix turns out to be able to predict the gain with the pseudospectrum evaluation.

IV.3.6 General receptivity of the varicose mode

In order to demonstrate the generality of the results achieved for $(\eta, Re) = (1, 700)$ other two cases have been studied both experimentally and numerically. The objective was to verify the high receptivity of the varicose perturbation also for an aspect ratio different from one. For instance, the case studied experimentally Fransson et al. (2005) and numerically by Loiseau et al. (2014) has been further investigated to highlight the main characteristics of the subcritical transition linked to the varicose global mode. The analysed cases are reported in table IV.5. Two Reynolds numbers close to each other have been

η	$h/(mm)$	Re	Re_h	h/δ_1	ω_{exp}	ω_{th}	$\lambda_{x,exp}$	$\lambda_{x,th}$
3	10	500	420	1.72	0.82 ± 0.08	0.77	5 ± 0.5	4.78
3	10	550	474	1.8	0.90 ± 0.09	0.8	5 ± 0.5	4.53

Table IV.5: Summary of the flow parameters, circular frequencies and wavelengths for cylindrical aspect ratio $\eta = 3$.

chosen to figure out how the receptivity changes when the global mode approaches the instability threshold ($Re_c = 564$ (Loiseau et al., 2014)). As for the case $(\eta, Re) = (1, 700)$ the time signal of the velocity field in the point located at $(x, y, z) = (10, 1.5, 0)$ is recorded and displayed in figure IV.34.

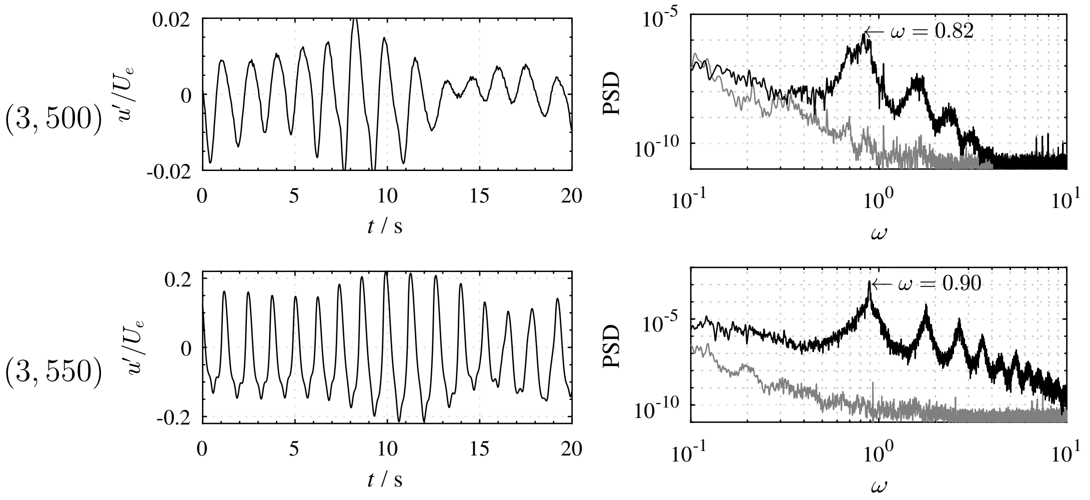

Figure IV.34: (Left) Time signals and (right) power spectral densities (PSD) of streamwise velocity fluctuations u'/U_e. Probe located at $(x, y, z) = (10, 1.5, 0)$. Grey lines in the spectra represent freestream turbulence spectrum at $(x, y, z) = (0, 6, 0)$.

Note that the ordinate of the configuration $(\eta, Re) = (3, 550)$ is not identical with the other two configurations. This case is close to the critical Reynolds number $Re_c = 564$ determined by Loiseau et al. (2014) and therefore fluctuates stronger and with more constant amplitudes. On the contrary, for $(\eta, Re) = (3, 500)$, the oscillations have a significantly smaller amplitude. They moreover sustain themselves only transiently, rapidly fading away before being regenerated again. The unsteadiness is even more spatially displayed by PIV snapshot in wall-normal plane at $y = 1$ (see figure IV.35). The instantaneous flow field displays the varicose perturbation that appears for $Re < Re_c$. As already assesed by Loiseau et al. (2014) at $Re < 564$ the baseflow is steady and then the DNS converge toward the steady state without any supplementary algorithm. The reader can refer to the Loiseau work (Loiseau et al., 2014) and its Ph.D thesis (Loiseau, 2014) for the base flow analysis of the $\eta = 3$ case. The global stability analysis reveals the presence of a varicose global mode with a pulsation close to that observed in the experiments. The numerical wavelength and pulsation are compared with the experimental one in table IV.5.

As one can see the resolvent curve estimated by the pseudospectrum displays a higher amplification factor around the global varicose mode. From $Re = 550$ to $Re = 500$ the

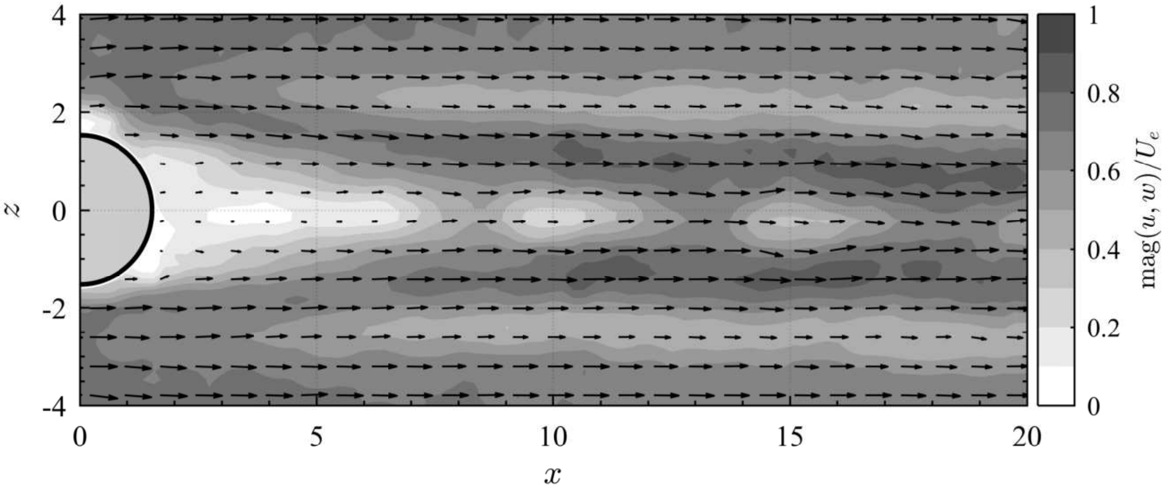

Figure IV.35: PIV snapshot at $y = 1$ for $(\eta, Re) = (3, 500)$. Greyscales indicate the in-plane velocity magnitude and black vectors indicate the vector sum of streamwise and spanwise velocities.

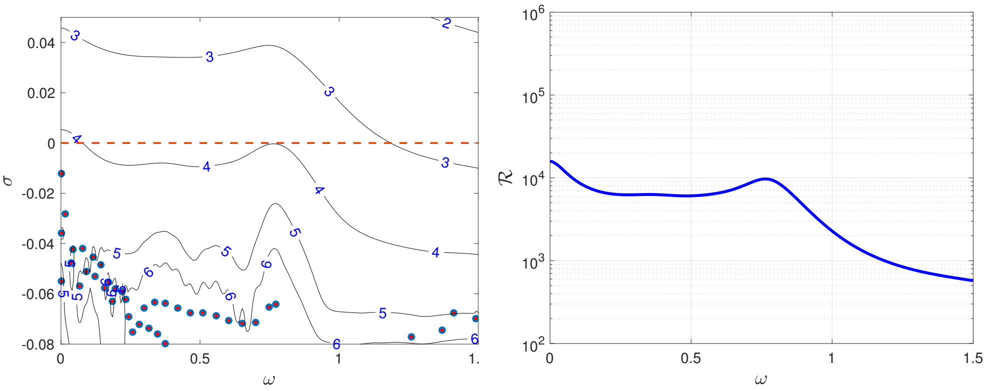

(a)

(b)

Figure IV.36: Same as in figure IV.24 and IV.25 for $(\eta, Re) = (3, 500)$.

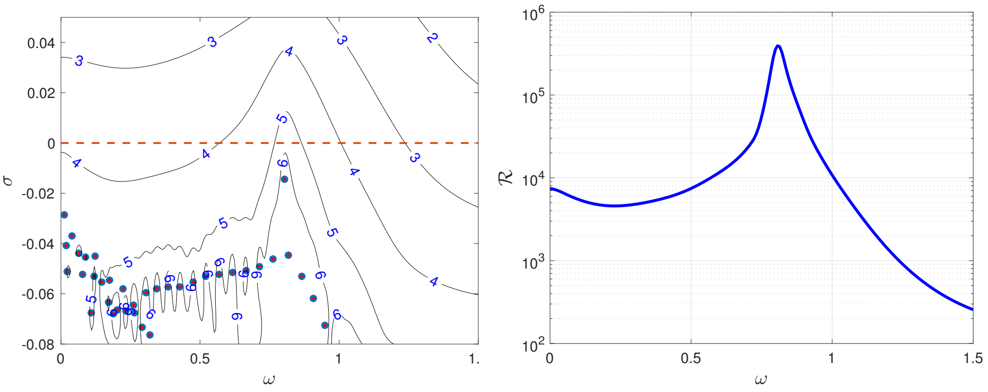

(a)

(b)

Figure IV.37: Same as in figure IV.24 and IV.25 for $(\eta, Re) = (3, 550)$.

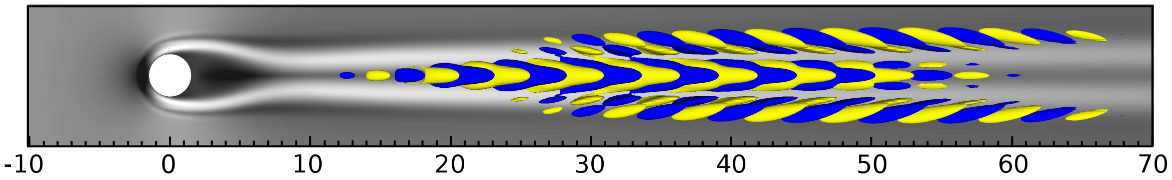

(a)

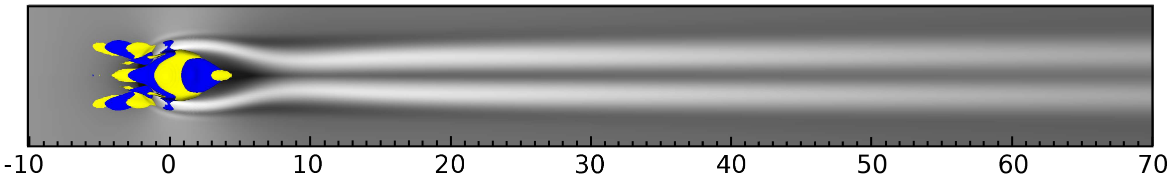

(b)

Figure IV.38: (a) Eigenvector associated with isolated varicose mode, and (b) its adjoint counterpart for case $(\eta, Re) = (3, 550)$. Greyscales and isosurfaces are the same as in figure IV.22.

peak is smoothed, explaining the transient behaviour observed in the experiments for $Re = 500$ as the amplitude of the external perturbation is not high enough to self sustain continuously the varicose mode. The direct and the adjoint eigenvector for $(\eta, Re) = (3, 550)$ are displayed in figure IV.38. As for the case $(\eta, Re) = (1, 700)$, close to the roughness element the varicose perturbation is located on the middle streaks; then, moving downstream, it moves onto the two external low speed streaks. It turns out to be more extended than the eigenvector at $(\eta, Re) = (1, 700)$ as the low middle streaks does not disappear far from the roughness. The associated adjoint eigenvector is always localized onto the head of the cylinder that turns out to be the most sensitive zone. The optimal forcing analysis at $\omega = 0.8$ for $(\eta, Re) = (3, 550)$ depicts the same scenario observed in the case $(\eta, Re) = (1, 700)$. The optimal response looks like the direct global mode and the optimal forcing looks like the adjoint global mode. Despite the linearly stable nature of the underlying base flows, these observations strongly suggest that the unsteadiness observed experimentally results from a quasi-resonance of the least stable varicose eigenmode due to the external forcing inherent to an experimental facility. Concerning the gain associated to $\omega = 0.8$, its values as estimated by the pseudospectrum, the adjoint forcing, and the optimal forcing are reported in table IV.6. The contribution of the other modes is taken into account by the optimal forcing since there is a slightly difference between the gain obtained by the adjoint forcing and that obtained by optimal forcing. For this reason the pseudospectrum obtained by the Hessenberg matrix has just a qualitative and not quantitative validity.

As a conclusion, one can say that a varicose unsteadiness is much more receptive than a sinuous one to external perturbations. The scalar product between a sinuous and varicose mode is equal to zero due to the different symmetries of these modes. Thus, the probability to observe a subcritical sinuous unsteadiness is low since a specific non-symmetric external perturbation is necessary to trigger it.

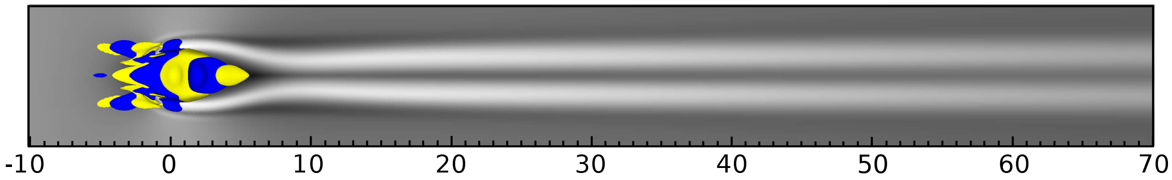

(a)

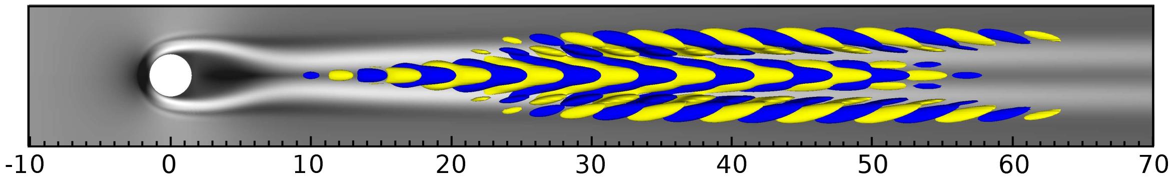

(b)

Figure IV.39: Shape of (a) the optimal forcing and (b) the optimal response for case $(\eta, Re) = (3, 550)$. Greyscales and isosurfaces are the same as in figure IV.22.

Pseudospectrum	Adjoint forcing	Optimal forcing
393'400	3'284'750	5'300'092

Table IV.6: Comparison between the gain estimation obtained by the pseudospectra, the adjoint forcing and the optimal forcing for $(\eta, Re) = (3, 550)$.

IV.3.7 Overall discussion about varicose dynamics

The performed linear studies provide a complete picture of the dynamics of the experimentally observed varicose unsteadiness. At this point; the receptivity process, the unsteady mechanism and the resulting transitional[1] behaviour are clear and they can be summarized step-by-step as follows:

1. The flow impacting the roughness element generates a horseshoe vortices that wraps the cylinder. The counter rotating vortices push down the momentum in the symmetry plane at $z = 0$ and move up the momentum on both sides of the roughness. The resulting lift-up mechanism should produce a high streaks in the middle (linked to negative wall normal velocity) flanked by two low speed streaks (linked to positive wall normal velocity). Close to the cylinder, the high speed streak is hampered by the presence of the separation zone, resulting into a low speed elongated region close to the roughness.

2. The presence of the recirculation bubble introduces in the system a zone with a back flow that makes possible the existence of a stable global mode well confined in the

---

[1] It would not be correct to call it turbulent as the unsteadiness is dominated by just one pulsation and the resulting spatial spectrum is "coloured" by the wavelengths related to the global varicose eigenvector. In the experiments the turbulence appears far from the roughness for the case $Re = 700$.

numerical domain. The wavemaker analysis illustrates how the structural sensitivity of the base flow to the varicose global mode is localized into the separation zone.

3. An external perturbation that acts on the wavemaker zone triggers the varicose global mode that arises in the separation zone and successively is convected downstream, first on the low speed streak along $z = 0$, then on the two lateral low speed streaks as suggested by the shape of the global mode and by the bi-local stability analysis.
4. Once triggered, the perturbation works to restore the high speed streak on the middle by the lift-up production. This explains why the low distortion between the experimental mean flow and the numerical base flow in figure IV.17 is localized on the low velocity middle streak.

In the unsteady scenario just depicted the physical origin of the instability has been made clear. However, a quantitative evaluation of the external perturbation needed to trigger this mode has not been made, and the connection between the shape of the varicose perturbation and the observed hairpin structures is yet to be explained. To conclude this linear study and open the road to a successive nonlinear investigation, two questions should be asked:

1. What is the minimum amplitude of the external perturbation needed to trigger by receptivity the global mode?
2. How the eigenvector shape is linked to the non-linear structures observed in the experiments?

Chapter V

Non-linear analysis of flow over cylindrical roughness

Contents

V.1 Non-linear analysis

The different analyses presented in §IV have demonstrated the high receptivity of the considered flow, despite its linearly stable nature. More specifically, the pseudospectrum and optimal forcing analyses have strongly underlined the receptivity of the flow at the frequency corresponding to the least stable varicose eigenmode and its quasi-resonant response. Despite their success, these analyses rely on the linearized Navier-Stokes equations and, as such, do not provide any insight into the nonlinear evolution of the perturbation. In order to properly quantify this response, one would need to perform a nonlinear resolvent analysis. Such an analysis is however beyond the scope of our current work. One can nonetheless gain some insights into the nonlinear evolution of the perturbation by means of direct numerical simulations. For that purpose, two different types of direct numerical simulations are considered hereafter:

- An impulse-response direct numerical simulation
- Direct numerical simulations forced by the optimal forcing obtained from the resolvent analysis with three different amplitudes.

Regarding the boundary conditions, a Blasius velocity profile is now prescribed at the inflow boundary while a classical outflow condition is used at the other end of the domain. Note furthermore that the fringe regions included in the linear analyses are no longer used.

V.1.1 Impulsively forced DNS

The pseudospectrum and optimal forcing analyses provided in the previous sections suggest that the flow can be highly receptive at the frequency of the isolated global mode. Thus, even a direct numerical simulation initialized by a generic perturbation can be expected to give rise to a response dominated by the frequency of that mode, as observed in the experiments presented in section IV.2. To ascertain this hypothesis, we focus our attention on the case $(\eta, Re) = (1, 700)$ and perform a DNS initialized by a superposition of an impulsive wavepacket of the form $v(x, 0) = \sin(\pi x/5)\sin(\pi x/20)$ onto the linearly stable base flow, shown in the upper right box of figure V.1. The wavepacket, placed right downstream of the cylinder in the region $0 < x < 20$, has an initial amplitude $A = 5 \times 10^{-5}$, which is sufficiently low to allow a (mostly) linear evolution of the flow response. The main frame of figure V.1 provides a space-time diagram showing the evolution of the wavepacket, that is initially amplified and stretched in the streamwise direction up to $x \approx 40$. After its initial transient growth, the wavepacket begins to decrease in amplitude and streamwise extent, slowly fading away as time increases, as it might have been anticipated by the initial low amplitude of the wavepacket and linearly stable nature of the flow. Figure V.2 provides the time trace of the vertical perturbation velocity component monitored by a probe located at $(x, y, z) = (10, 1.2, 0)$. After a relatively short transient, the signal oscillates at a preferential frequency, followed by an exponential decay. This decay is well approximated by an exponential function characterized by a decay rate of -0.01, that is in close agreement with the decay rate of the isolated varicose mode (see the figure IV.24). Moreover, a Fourier transform of that signal highlights the existence of a dominant peak at $\omega = 1.02$, demonstrating that the most unstable mode of the spectrum can indeed be triggered by a generic perturbation injected impulsively into the flow.

V.1.2 Optimally-forced DNS

Once ascertained that the dominant frequencies observed within the flow are likely to result from a quasi-resonance of the isolated varicose mode, it is interesting to shed some light on the transition scenario induced by this phenomenon, with the final aim of comparing the generated coherent structures with those observed experimentally. We thus focus once again on the case $(\eta, Re) = (1, 700)$, using the optimal forcing at $\omega = 1.02$ to force a DNS. The optimal forcing is scaled with three different initial amplitudes ($A = 10^{-5}$, 10^{-4}, and 10^{-3}) in order to investigate the effect of the nonlinearity on the time evolution of the flow. The resulting wall-normal velocity fluctuations, given by the instantaneous velocity minus its temporal mean value, are monitored by a probe located at $(x, y, z) = (10, 1.5, 0)$. The time traces (left) obtained for the three amplitudes considered and their frequency spectra (right) are provided in figure V.3.

For the lowest amplitude (top frame), a time-periodic behavior appears to settle after a short initial phase characterized by a transient growth of the perturbation. After this initial phase, a periodic signal with associated circular frequency equal to that of the

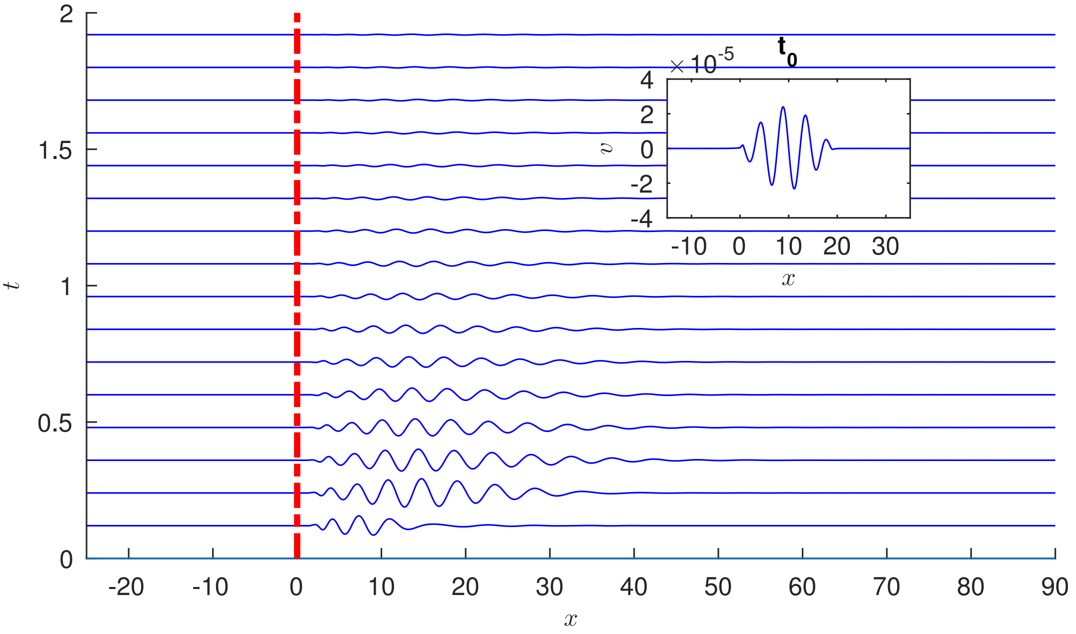

Figure V.1: Time evolution of the wall-normal velocity perturbation v measured at $(y, z) = (1.2, 0)$ for the impulsively perturbed DNS. In the upper-right box is provided the shape of the wall-normal perturbation added to the base flow at $t = 0$. The red dashed line indicates the cylinder position. The case considered is $(\eta, Re) = (1, 700)$.

varicose mode is observed. An increase of the forcing amplitude causes the non-linearities to be triggered, hence resulting in the emergence of smaller-amplitude harmonics which rapidly fade away leading, again, to the establishment of a quasi-periodic signal (middle frame of figure V.3). For the largest amplitude considered herein, an even larger number of harmonics are generated by the nonlinearities, inducing a saturation of the signal amplitude as shown in the bottom frame of figure V.3.

In order to obtain a quantitative criterion defining whether transition to turbulence has occurred or not, the skin friction coefficient $C_f(x)$ is computed. Figure V.4 depicts the streamwise evolution of $C_f(x)$ for the optimally forced DNS at the three amplitudes considered. Note that the evolution of $C_f(x)$ for the unperturbed steady base flow is also reported for the sake of reference. For the lowest value of the forcing's amplitude, the flow remains laminar behind the roughness, as indicated by the C_f curve which is superimposed to that of the base flow (compare the dashed and the solid lines). For $A = 10^{-4}$, the skin friction begins to deviate from the reference state, while for $A = 10^{-3}$, it strongly increases. Such an increase of the skin friction typically indicates the onset of transition towards a turbulent flow, although the values of C_f typical of high Reynolds number turbulent boundary-layer flows have not been reached yet in the computational domain considered.

Figure V.5 provides a snapshot of the instantaneous flow where the vortical structures are highlighted using the λ_2 criterion (Jeong and Hussain, 1995). One can observe the generation of hairpin vortices right downstream of the roughness element, the first one being placed at $x \approx 2$. Up to $x \approx 30$, a train of hairpin vortices can be observed, whose

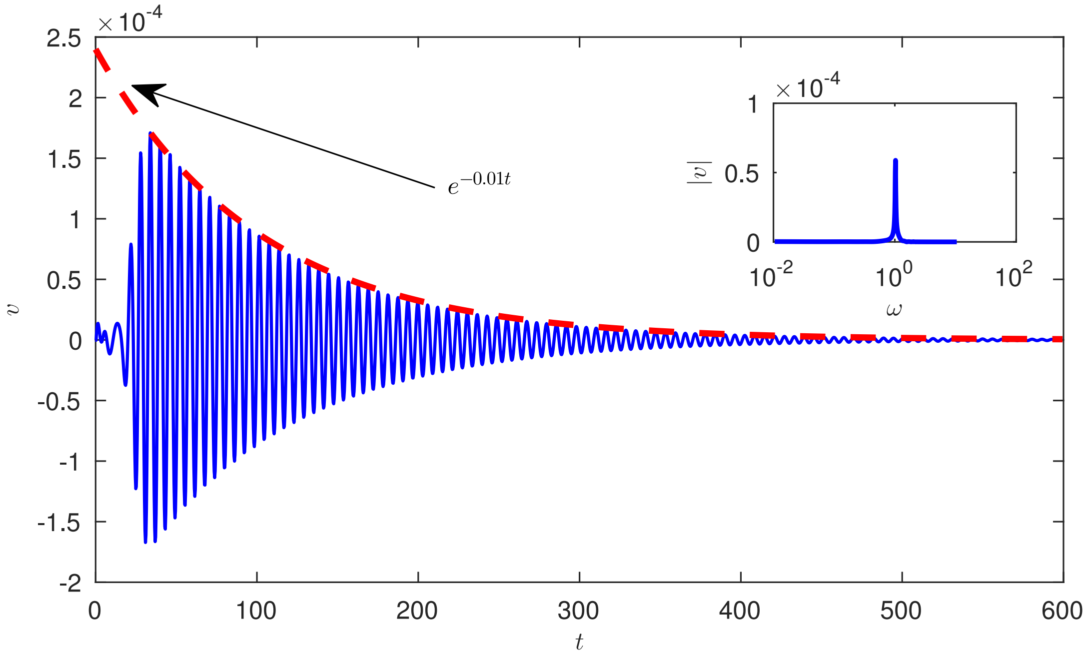

Figure V.2: Time evolution of the wall-normal velocity perturbation v extracted at $(x, y, z) = (10, 1.2, 0)$. The upper-right box shows the Fourier transform of that time signal, showing that the response of the flow to a generic perturbation is indeed dominated by the most receptive global mode $(\sigma, \omega) =$ (-0.01,1.02). The case considered is $(\eta, Re) = (1, 700)$.

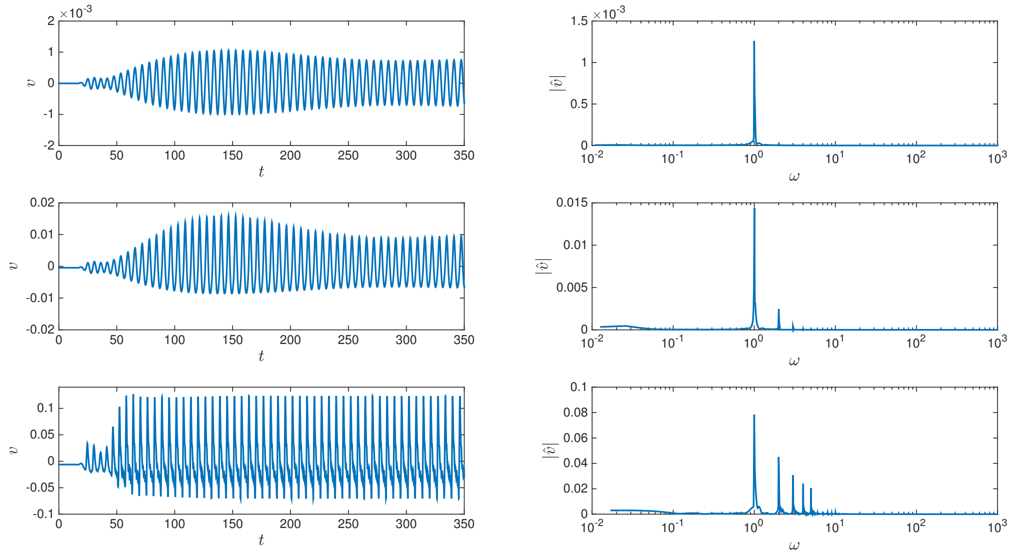

Figure V.3: (Left) Time evolution of the wall-normal velocity fluctuation for initial amplitudes $A = 1 \times 10^{-5}$ (top), $A = 1 \times 10^{-4}$ (middle) and $A = 1 \times 10^{-3}$ (bottom), and related Fourier transform (right). The case considered is $(\eta, Re) = (1, 700)$.

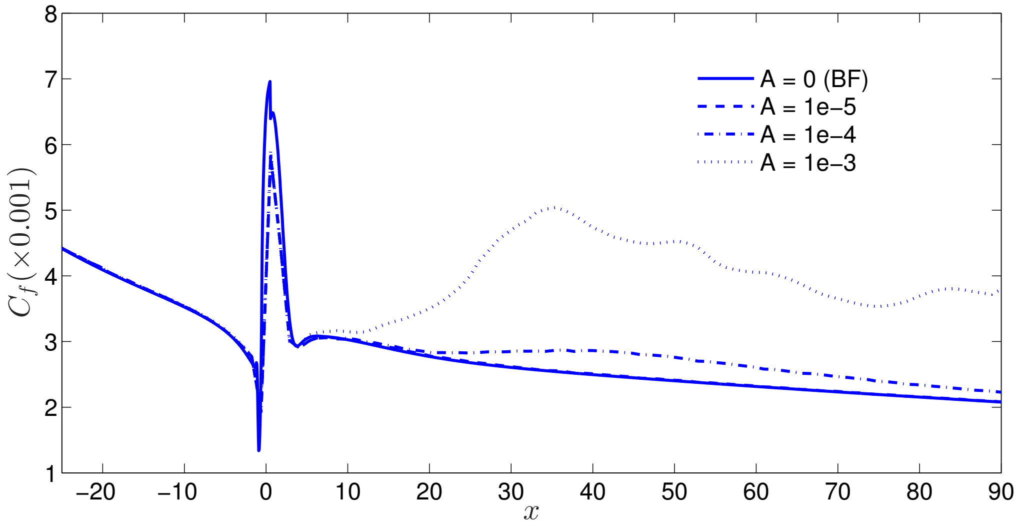

Figure V.4: Streamwise evolution of the skin friction factor $C_f(x)$ for four different amplitudes of the optimal forcing. The case considered is $(\eta, Re) = (1, 700)$.

heads appear to have a streamwise spacing of $\Delta x \approx 4.7$. The vortical structures also spread in the spanwise direction generating Λ vortices at their spanwise sides. These primary hairpin vortices then start to break down at $x \approx 30$, corresponding to the streamwise position at which the skin friction C_f reaches its highest value. This transition scenario closely resembles the one observed experimentally, showing the shedding of hairpin vortices having a varicose symmetry with streamwise wavelength ≈ 5. However, due to the nature of the optimal forcing, the flow remains symmetric up to the end of the domain (see fig. V.5) and the associated spatial and temporal Fourier spectra remain characterized by a limited number of different wavelengths.

Finally, to further characterize the spatial spreading of the fluctuation, a spanwise Fourier transform of the u_{rms} field for different selected y and x positions has been performed. The wall-normal position of the dominant Fourier mode in the y-direction for a fixed x position (circles) and the associated spanwise wavenumber (colors of the circles as specified by the colorbar) are shown in figure V.6. The first peak ($x = 9$) is associated to the generation of the train of hairpin vortices behind the cylinder, the corresponding spanwise wavelength, $\beta = 0.63$, being close to the spanwise dimension of the first hairpin. For $x \geq 10$, the first hairpin vortex starts to disappear, whereas a second one is generated downstream, inducing a second peak at $x = 23$ due to the growth of a second perturbation that wraps the two low streaks. For $x > 26$, the wall-normal position of the dominant Fourier mode of u_{rms} rapidly moves towards the wall, where the flow starts to become turbulent (see figure V.4). Further downstream, the maximum amplitude of the Fourier transform is characterized by $\beta = 0$, but, due to the spanwise symmetry of the flow field, a second peak at $\beta = 1.26$ is observed, which becomes predominant for $85 \leq x \leq 90$.

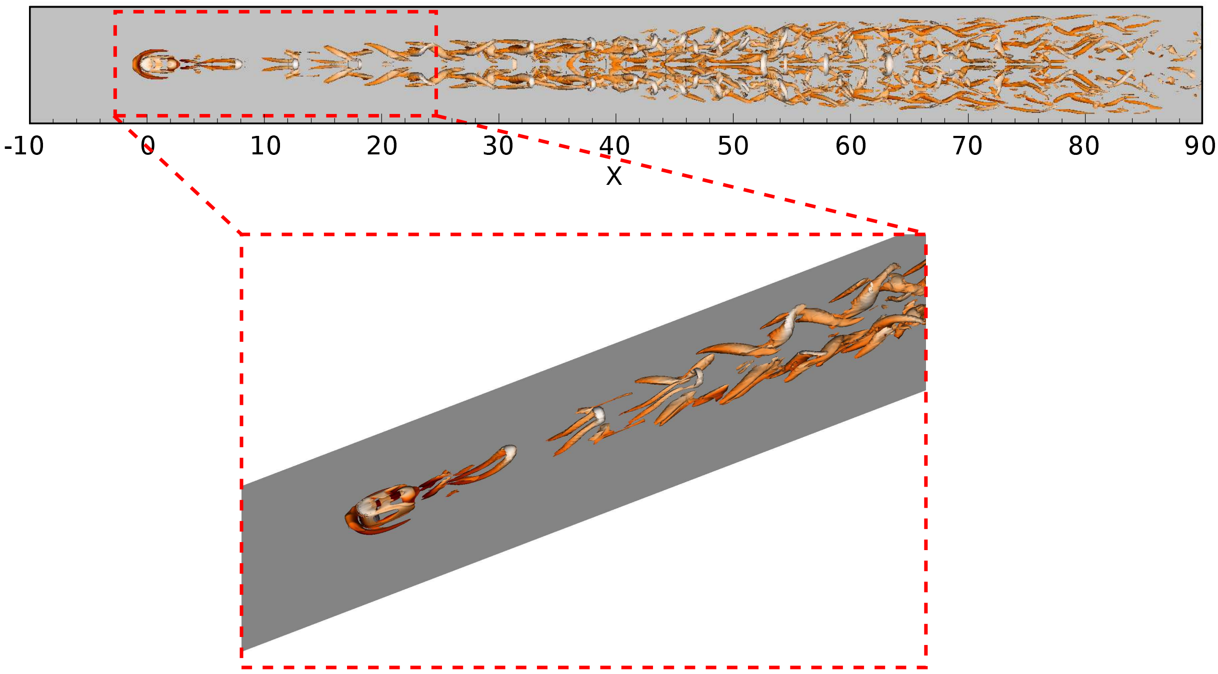

Figure V.5: Hairpin vortices highlighted by lambda-2 criterion ($\lambda_2 = -0.02$) and colored by streamwise velocity. The case considered is $(\eta, Re) = (1, 700)$.

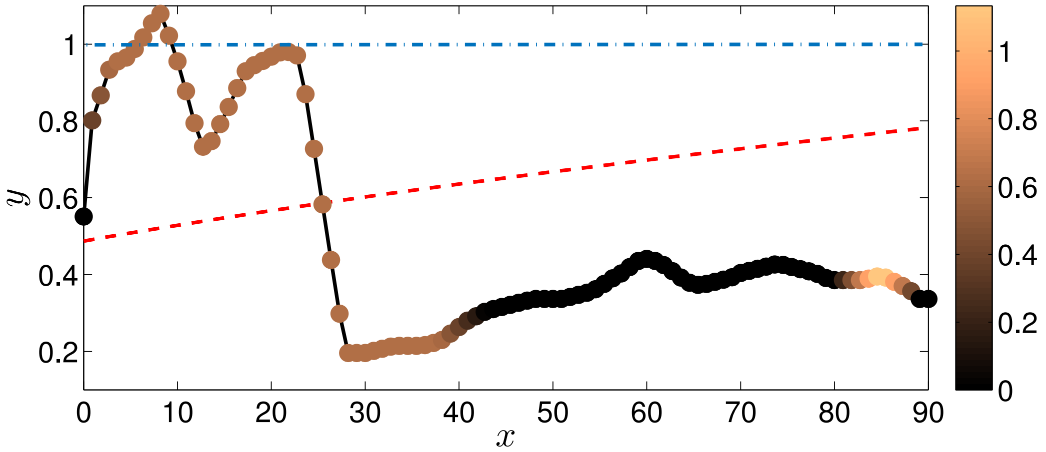

Figure V.6: Variation in the streamwise direction of the wall-normal position of the maximum amplitude mode of the spanwise Fourier transform of the u_{rms}. Colorbar indicates the spanwise wavenumber of the dominant Fourier mode. Red dashed line provides the analytical displacement thickness of the Blasius solution whereas the blue dashed-dotted line indicates the height of the cylinder. The case considered is $(\eta, Re) = (1, 700)$.

V.2 Receptivity to Free Stream Turbulence

In section §V.1.1 and §V.1.2 it has been demonstrated how a generic perturbation in the wavemaker zone is able to trigger the varicose global mode and how the optimal forcing associated to the pulsation observed in the experiment can reproduce the hairpin vortices when it is used in a non-linear numerical simulation. Nevertheless, the uncontrolled perturbation in the hydro-channel has not the structure of the optimal forcing and it does not act just on the wavemaker region of the varicose global mode. The spatial structure of the perturbations in figure V.5 is exclusively linked to the spatial structure of the optimal response structure. The good agreement between the numerical spatial wavelength (e.g. distance among two successive hairpins) and the experimental one could be interpreted as an obvious result.

1. Can a non localized and non structured perturbation trigger the receptivity mechanism of the varicose global mode?

The only information about the external perturbation in the hydro-channel is the Tu (turbulence intensity) that is much lower than 1. To reproduce the receptivity of the boundary layer to the external turbulence an artificial Free Stream Turbulence (FST) has been built in the Nek5000 code.

V.2.1 FST generation

The easiest and most common way to introduce grid turbulence is to use Fouries modes with a random amplitude and then rescale the total turbulent kinetic energy to the desired Tu level (Rogallo, 1981). Unfortunately, in the presence of one inhomogeneous direction (wall-normal) this is no longer possible as the Fourier modes are appropriate only in the periodic directions. The inflow turbulence needs to be damped within the boundary layer and it has to be unbounded at the upper boundary of the numerical domain. The natural choice is to use a sum of modes of the continuous branch of the Orr-Sommerfeld Squire operator as done by Brandt et al. (2004); Jacobs and Durbin (2001). These eigenvalues can be found analytically once defined the Reynolds number and the streamwise, wallnormal and spanwise wavenumbers (α, γ, β, respectively) . The 1-D eigenvector is equal to zero at the wall in order to respect the no-slip boundary condition and it is modulated with wavenumber γ outside the boundary layer in the y-direction with a constant maximum amplitude value. Invoking Taylor's hypothesis, the streamwise wave number α is replaced by a frequency $\omega = \alpha U_\infty$:

$$\mathbf{u}_i = A_i \hat{\mathbf{u}}_i(y) e^{(i\beta z - i\omega t)} \tag{V.1}$$

where A_i is the amplitude associated to the eigenvector $\hat{\mathbf{u}}_i(y)$. The velocity perturbation profile $\mathbf{u}_i$ added to the base flow velocity profile can be now used as inflow condition. The amplitude A_i must be conform to a common turbulent energy spectrum. For this purpose the Von-Karman spectrum has been chosen:

$$E(k) = \frac{2}{3}\frac{a(kL)^4}{(b + (kL)^2)^{17/6}} Lq \tag{V.2}$$

where $a = 1.606$ and $b = 1.350$, L is the integral length scale and q the turbulent kinetic energy. Fixing the minimum k_l and the maximum k_u depending on the chosen numerical resolution, the energy is distributed in 20 k-shell. These are homogeneously divided in 20 triads of (ω, γ, β) values defined by the vertices of a dodecahedron inscribed in the k-shell. A sketch of the discretized Von Karman spectrum and shell discretization is shown in figure V.7.

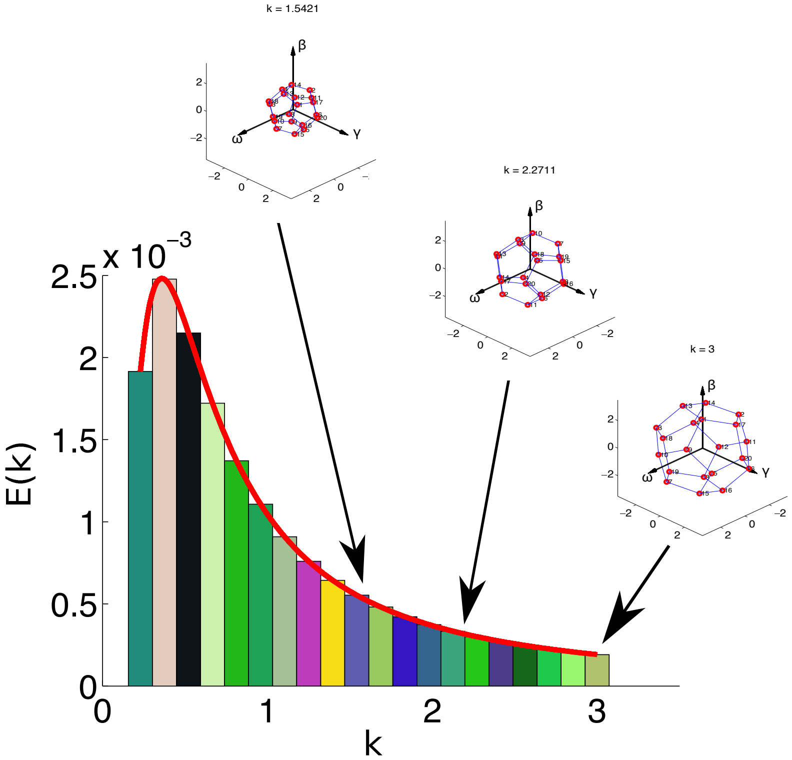

Figure V.7: Discretized Von Karman spectrum and k-shell discretization by a regular dodecahedron. The shape of the Von-Karman spectrum is discretized once k_u, k_l and L have been defined.

Defining $Tu = \sqrt{u_{rms}^2 + v_{rms}^2 + w_{rms}^2}$, the equation (V.2) can be recast as:

$$E(k) = \frac{a(kL)^4}{(b + (kL)^2)^{17/6}} L Tu^2 \tag{V.3}$$

To set the inflow turbulence it is necessary to define Tu, L, k_l and k_u. Unfortunately L is not accessible in the available experiments and a value from the bibliography is used $L = 1.64$[1]. The integral length scale is then linked to the wave number (k) with the maximum energy $E(k)$ by the relation

$$L = \frac{1.8}{k_{max}}. \tag{V.4}$$

---

[1] In Brandt et al. (2004) an integral length scale of $5\delta_1$ has been chosen for three numerical cases at $Re_{\delta_1} = 300$. In Jacobs and Durbin (2001) an integral length scale of $5.1\delta_1$ has been chosen for $Re_{\delta_1} = 274$. In our case the $Re_{\delta_1} = 300$ is achieved at $x_h = 43$ downstream of the leading edge with $\delta_1/h = 0.43$. If $L_{x=47} = 5\delta_1$ is adopted, at the inflow position $L_{x=32} = 1.64$ set knowing that the integral length scale is proportional to $L \propto x^{-0.29}$ (Jacobs and Durbin, 2001).

The maximum energy is injected at $k_{max} = 1.09$. L is also linked to the the length scale L_{11} defined by the longitudinal two-points correlation as:

$$L_{11} \approx 0.643L. \tag{V.5}$$

k_l is set equal to 0.63 and k_u to 4.08. Due to the stable nature of the modes on the continuous branch of the OSS spectrum, the turbulence in the free stream has to decay exponentially. For a $Tu = 0.18\%$ and at a distance from the wall equal to 30 an exponential decay of the turbulence can be observed (fig. V.8). The FST intensity follows the decays law $Tu \propto (x+x_0)^{-n}$ with $n \approx 0.71$ as also suggested by Jacobs and Durbin (2001). Further informations about the Orr-Sommerfeld and Squire modes and about the turbulent energy spectrum discretization are provided in Appendix .1 with a validation test case presented by Brandt et al. (2004).

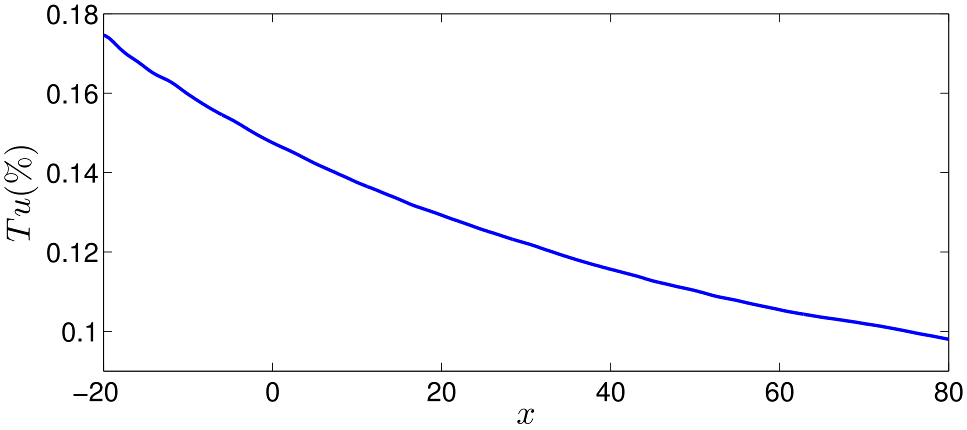

Figure V.8: Exponential turbulent decay in streamwise direction.

V.2.2 FST results

The experiment shows transition with a $Tu = 0.089\%$ of the free stream velocity. Nevertheless, one needs to consider that the turbulent spectrum in the water channel is characterized by wave numbers intrinsic to the experimental set-up (e.g. pump, presence of the leading edge, free water surface, ...). The implemented free stream turbulence does not take into account the hydro-channel features, however it is a guideline to understand the receptivity process. For the study of the flow over a roughness in the presence of free stream turbulence the numerical discretization has been changed in order to get the same spatial resolution in the whole computational domain and avoid numerical dissipation of the turbulence. The turbulent intensity is progressively increased until the appearance of hairpin vortices. Three different $Tu = 0.045\%$, 0.09% and 0.18% are here presented. The evaluation of the skin friction drag helps to highlight the Tu level and the streamwise position at which the global mode receptivity is triggered. The Cf versus the x position is reported in figure V.9 for the three cases. The turbulent intensity values used in the DNS are too low to trigger non-normal growth of the energy in the laminar boundary layer region. For $x < 0$ no influence on the skin friction is observed. For $x > 0$, already with

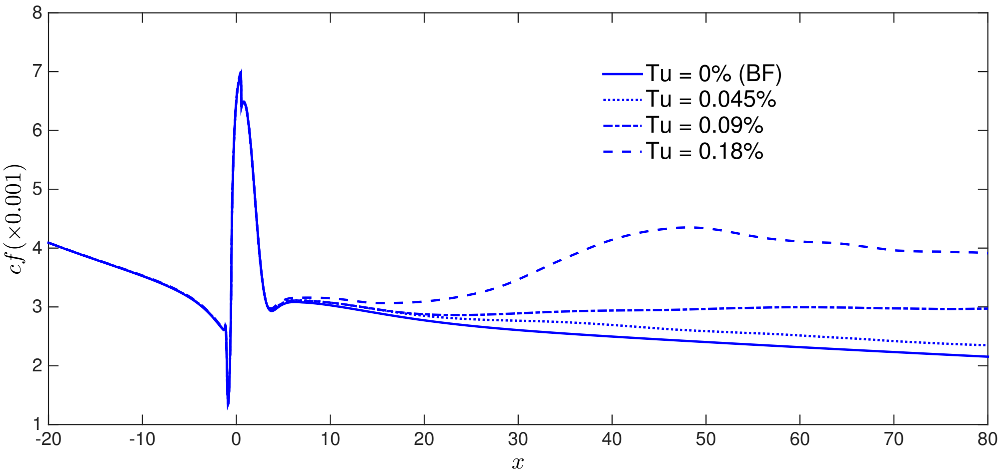

Figure V.9: $Cf(x)$ vs x for different turbulent intensity. The Cf for $Tu = 0\%$ is also reported as reference.

$Tu = 0.045\%$ the Cf curve slightly deviates from the laminar condition. Even though the structural turbulence is different between channel and numerical simulations, for an incoming turbulent intensity $Tu = 0.18\%$, only two times higher then the experimental one, a transitional flow is observed. The hairpin vortices noticed in the experiments and in the DNS forced by the optimal forcing are still present in this case as illustrated in figure V.10 by the isolevel of λ_2-criterion. The unsteady perturbation starts with the generation of the hairpin eddies from the cylinder head and develops on the low middle streak. After that, the hairpins are dissipated on the low middle streaks and new vortex structures start to grow spatially on the lateral low speed streaks as in the optimally forced case. If in the forced case the varicose symmetries are preserved also far from the roughness due to the symmetrical forcing structure, in this case non-symmetric structures are observed for $x > 55$. As for the optimal forcing transition, the behavior of the fluctuation in the y-direction has been investigated as reported in figure V.11. Qualitatively the same behavior can be observed by comparing fig. V.6 and fig. V.11. The first peak, that is linked to the growth of the perturbation on the middle streak, and the second peak, that is linked to the growth of the perturbation onto the lateral low speed streak, are now slightly damped with respect to the optimally forced case (see fig. V.6). Nevertheless, in this case once the flow is turbulent the Fourier transform has just one main peak at $\beta = 0$. This means that the maximum fluctuations are homogeneous in z also at the end of the domain. In figure V.6 the effect of the periodicity in the spanwise direction has to be taken into account. A symmetric perturbation that passes the boundary condition could induce an aliasing effect which annihilates or amplifies same spanwise wavenumbers. From a quantitative point of view a numerical probe in (10, 1.5, 0) is used to evaluate the temporal signal reported in figure V.12. In figure V.12 the instantaneous velocity field on the line at $y = 1.5$ and $z = 0$ is also reported. The Fourier transform of the two signals confirms again the dominance of the global varicose mode in the unsteady dynamics. The temporal spectrum shows a main pulsation at $\omega = 1.02$ and its subharmonics. In the temporal signal a low modulation also appears at $\omega = 0.1$. This modulation, also observed in

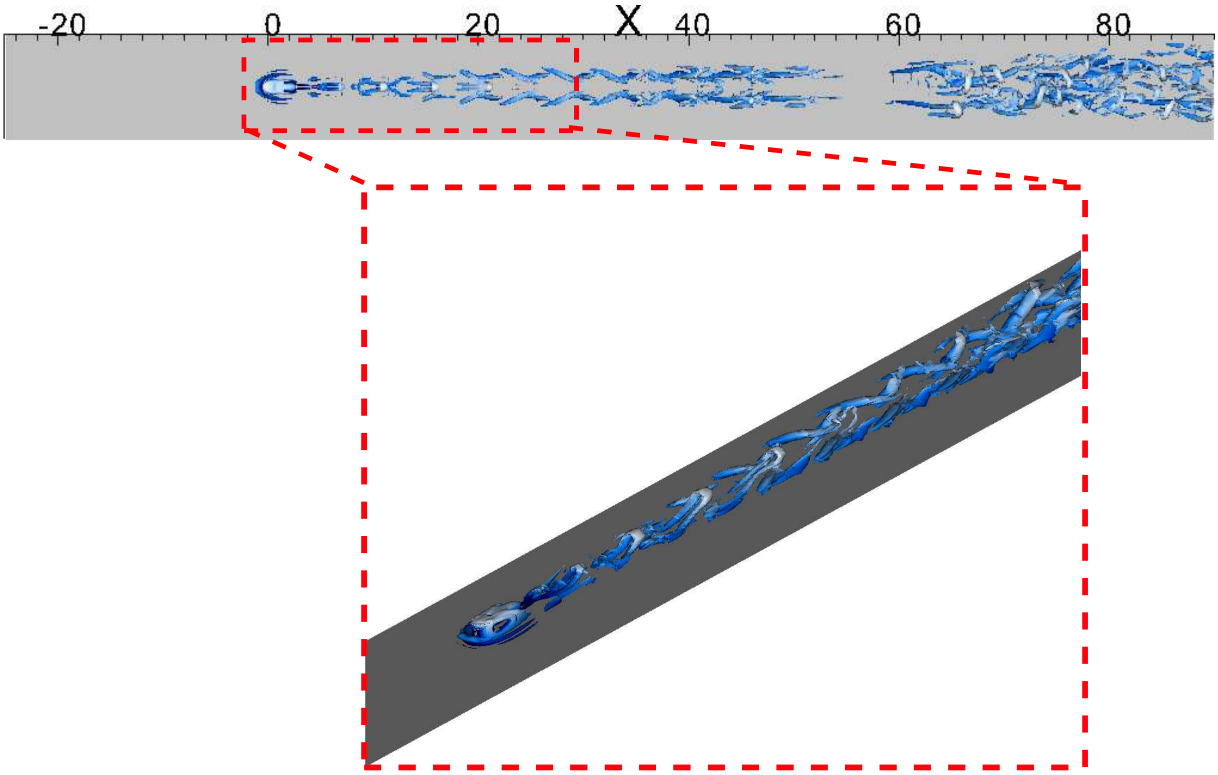

Figure V.10: Spatial evolution of the unsteady perturbation in the streamwise direction highlighted with isolevel of $\lambda_2 = -0.02$ for an incoming $Tu = 0.18\%$. The vortical structures are coloured by streamwise velocity field.

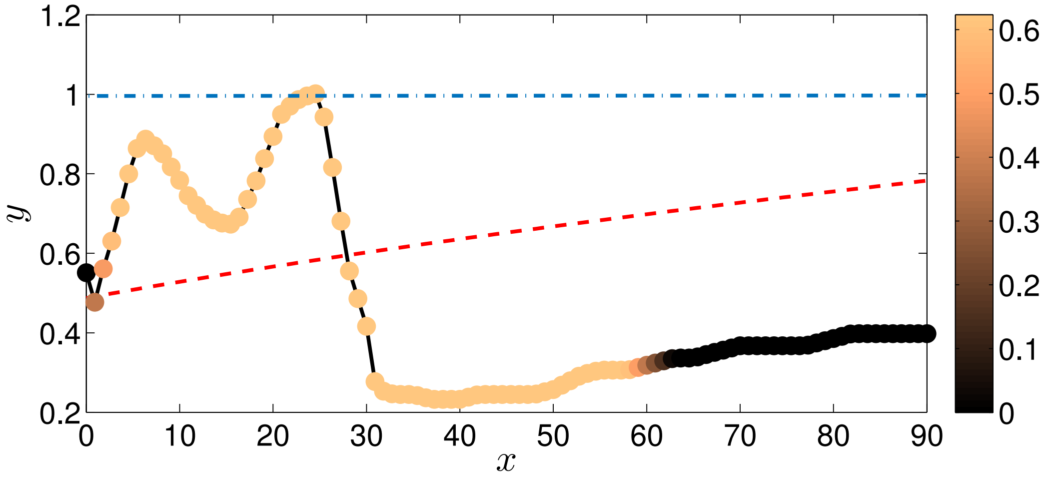

Figure V.11: Variation in the streamwise direction of the wall-normal position of the maximum amplitude mode of the spanwise Fourier transform of the u_{rms}. Colorbar indicates the spanwise wavenumber of the dominant Fourier mode. Red dashed line provides the analytical displacement thickness of the Blasius solution whereas the blue dashed-dotted line indicates the height of the cylinder. The case considered is $(\eta, Re) = (1, 700)$.

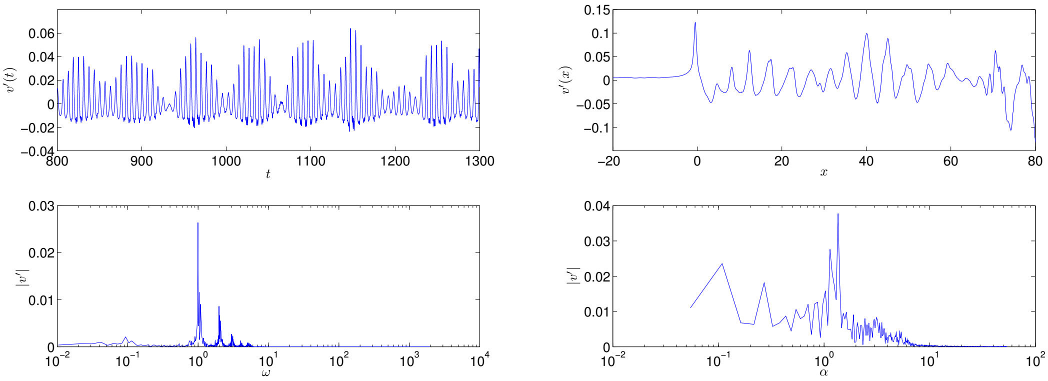

Figure V.12: A probe in (10,1.5,0) is used to catch the temporal signal and its spectrum with the main pulsation at $\omega = 1.02$ (left). Instantaneous wall-normal velocity on a line located at $y = 1.5$ and $z = 0$ shows a dominant spatial wavenumber $\alpha = 1.3$ (right). For both signals the Fourier spectrum is also reported. For the temporal signal the main harmonic is at $\omega = 1.02$ and for the spatial signal the main spatial wavelength is equal to 1.3.

the experiments IV.8, is linked to the receptivity of the streaky-TS waves. From a spatial point of view, despite the short length of the signal as limited by the size of the numerical domain a main spatial wavelength $\alpha \approx 1.3$ can be noticed.

V.2.2.1 DMD modes

Since the hairpin vortex shape observed experimentally and numerically behind the roughness is a non-linear structure[2], it could be interesting to decompose the evolution of the non-linear Navier-Stokes equations perturbed by the free stream turbulence to highlight the mechanisms involved in the hairpins generation with temporally uncorrelated structures. In accordance with Koopman theory it is possible to decompose the non-linear dynamics in an infinite-dimensional linear system. The DMD is an algorithm that approximates the Koopman operator as explained in chapter §III. Following the procedure explained in section §III.3.2.3 it is possible to decompose the non-linear dynamics with a linear combination of spatial structures temporally uncorrelated. To extract the DMD spectrum, 200 velocity snapshots have been used. The flow fields have been extracted from the DNS every $\Delta T = 0.78$. Only the first 21 SVD modes have been taken into account to ensure a Foebrenius norm higher than the 92% for the whole dynamics caught by the 200 snapshots. To facilitate the spectrum convergence, a spatial window from $x = -25$ to $x = 50$ has been applied to each snapshot in order to exclude the chaotic region and only keep the region having a "regular" motion. The DMD spectrum is illustrated in figure V.13. As one can observe the DMD modes are located on the line at $\sigma = 0$, confirming the periodicity of the used signal. In figure V.13 the weights associated to each mode

---

[2] It is not possible to observe the generation of hairpin vortices in a linear Navier Stokes numerical simulation. These non-linearities play an important role in the evolution of the initial perturbation that give rise to the Ω-shape structure (Zhou et al., 1999). The non-linearities are involved in the vortex tilting of the initial perturbation and in the vortex sustain once generated (Cherubini et al., 2011).

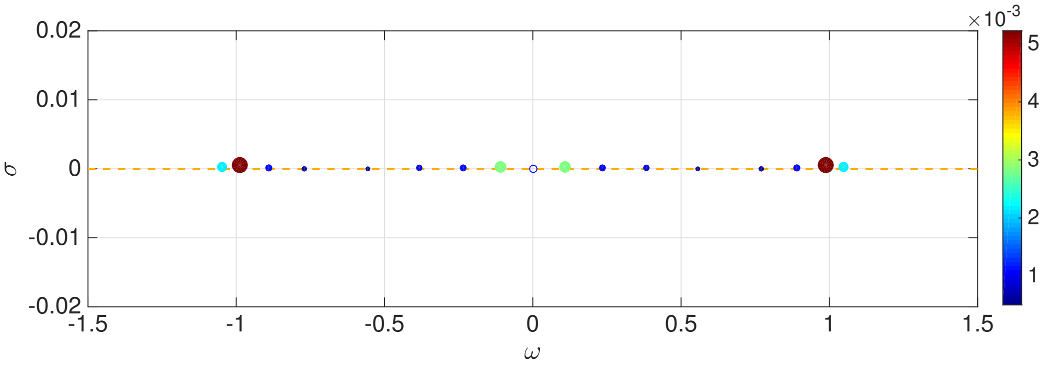

Figure V.13: DMD spectrum associated to the non-linear unsteady dynamics at $(Re, \eta, Tu) = (700, 1, 18\%)$. Evaluation with 200 velocity snapshots extracted each $\Delta T = 0.78$ from the non-linear DNS. 21 SVD modes have been used.

evaluated as explained in §III.3.2.3 are also reported. To better observe the contribution to the unsteady dynamics, the mode associated to $\omega = 0$ as been removed from the DMD spectrum as it has the highest contribution in the weights. Two main modes (and the relative complex conjugate) are present. The first one at $\omega = 1$ and the second one at $\omega = 0.11$, as predicted by the Fourier transform in V.12. The associated spatial DMD modes are reported in figure V.14. The structure of the mode at $\omega = 1$ approximates that of the global varicose mode. The perturbation firstly evolves onto the low middle streaks and then moves onto the two low lateral streaks. The DMD mode at $\omega = 0.11$ is composed by an oblique perturbation that alternates its sign onto the low velocity streaks and it is linked to the streaky-TS receptivity.

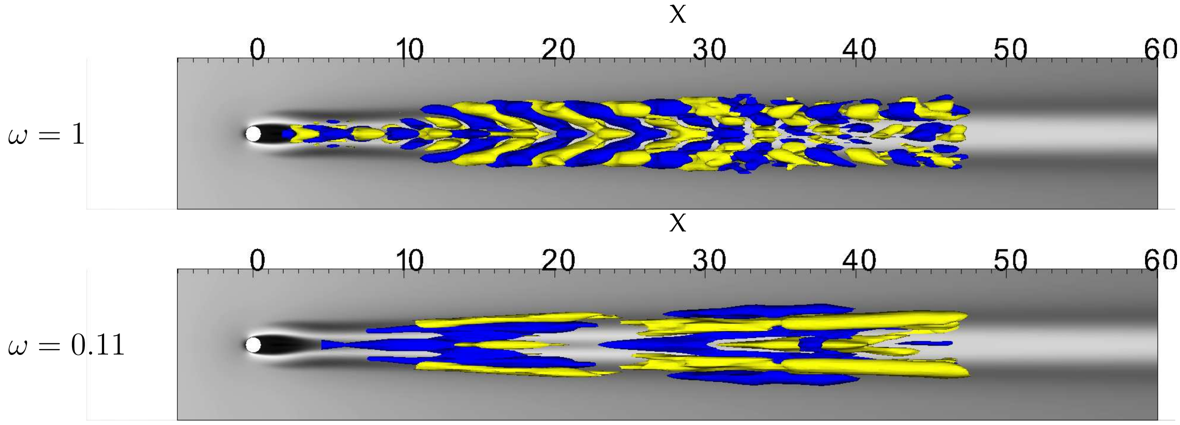

Figure V.14: ±10% of the maximum streamwise velocity of the real part of the DMD modes associated to $\omega = 1$ (top) and $\omega = 0.11$ (bottom) in spectrum V.13. Grey scale illustrate streamwise mean flow velocity at $y = 0.5$.

V.3 Generation of hairpin vortices

The contribution of the varicose global mode to the unsteady dynamics has been widely discussed. The link between the spatial distribution of the varicose mode and the observed structures needs further analysis. Information about the non-linear dynamics can be extracted by the distortion of the base flow towards the mean flow once the unsteadiness is triggered. A comparison between the base flow and the mean flow is then mandatory.

V.3.0.0.a Base flow Let us consider the base flow topology sketched in figure V.15. The flow hitting on the cylinder generates an horseshoe vortex (HP) that wraps the roughness. At the same time a secondary flow is induced by the fact that the flow has to turn around the cylinder. A particle that is located on **A** position moves to the position **B** due to centrifugal forces. Due to the presence of the HP vortex a particle on **B** moves toward **C** thanks to the momentum diffusion. Just behind the cylinder, a positive pressure gradient $\partial p/\partial z$ in the spanwise direction is generated by the presence of the separation zone. A particle is then pushed from **C** towards **D**. Finally, a particle located in the position **D** would have a low inertia; thus, for mass conservation, it would move from **D** to **A**.Due to the combination of these effects, a new pair of vortices, dubbed the *rear pair* (RP) vortices , is generated as shown in the sketch in figure V.15. The *rear pair* vortices have also been observed experimentally (Ye et al., 2016b). The presence of the HP and RP vortices has been highlighted by passive Lagrangian tracking of particles injected in the inflow and transported by the base flow field as shown in figure V.16. The particles are injected at $x = -15$, $z = 0.1$ and distributed along y from 0.1 to 0.7. A subset of particles is captured by the core of the horseshoe vortex, whereas the residual ones enter in the recirculation zone remaining locked in the core of the rear pair vortex. The presence of a RP vortex has no influence on the far field as they are dissipated when the low speed streak in $z = 0$ plane dies, as one can observe looking at the streamwise vorticity Ω_x in figure V.17. On the other hand, the RP vortices are a necessary ingredient for the hairpin vortices generation close to the cylinder. To understand the mechanisms involved in the hairpin creation we should refer to Cohen et al. (2014) work. In his work, Cohen *et al.* identify a minimal model for the generation of packets of hairpin vortices. The hairpin

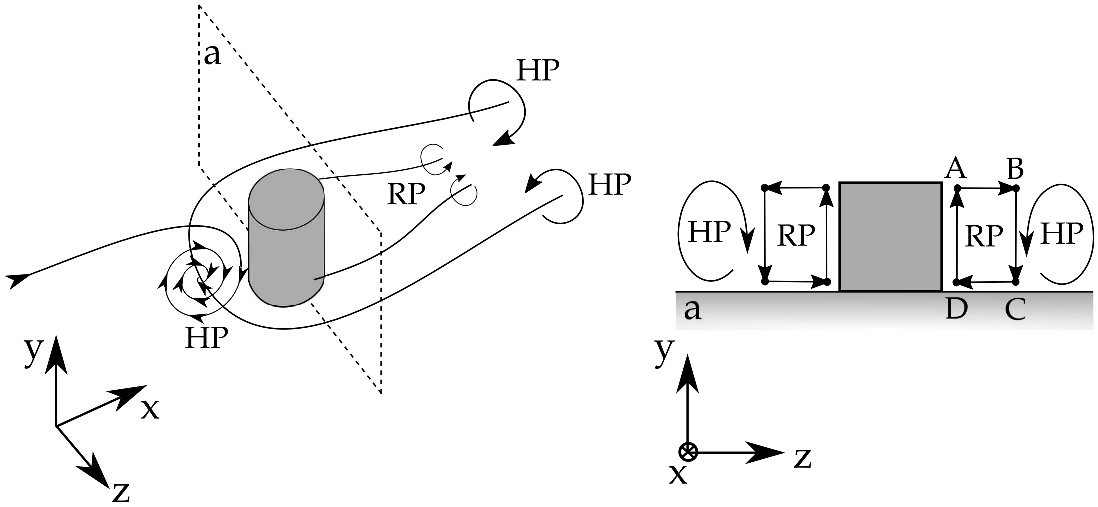

Figure V.15: Sketch of the generation of the streamwise vortices. Behind the cylinder the horseshoe vortices (HP) and the rearpair vortices (RP) are present. The rearpair vortices are generated by secondary flow.

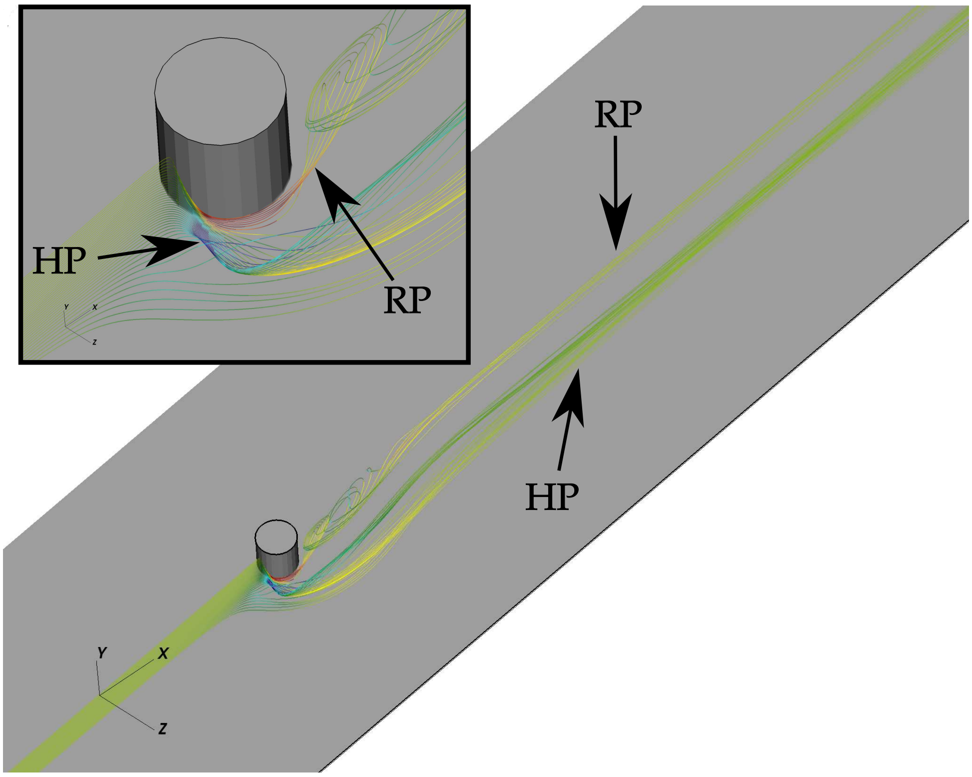

Figure V.16: Particle tracking transported by the base flow field. Tracking lines colored by vorticity module. Particles injected at $(x, y, z) = (-15, 0.1 : 0.7, 0.1)$.

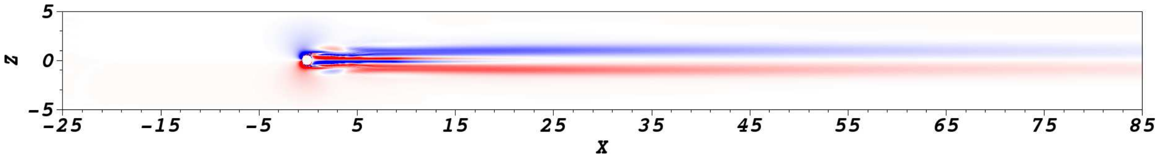

Figure V.17: $\Omega_x \pm 0.1$ of the base flow velocity field. The blue colour indicate negative stramwise vortices the red color the positive one. Slice at $y = 0.8$.

shape is generated by the non-linear interaction of three structural ingredients:

i) shear in the wallnormal direction

ii) counter-rotating vortex pairs (CVP)

iii) 2D wavy vortex sheet

The three ingredients are sketched in figure V.18 (picture from (Cohen et al., 2014)).

Looking at the velocity field just behind the cylinder at $x = 2$ (fig. V.19) we can recognize two of the structures predicted by the Cohen's model. The necessary counter-rotating vortices are represented by the RP vortices illustrated by the isolevel of the streamwise vorticity Ω_x and the shear is given by the reverse-flow in the recirculation bubble highlighted by the spanwise vorticity Ω_z in figure V.19. Finally, the 2D wavy vortex sheet is generated by the stationary oscillation provided by the wavemaker of the global mode,

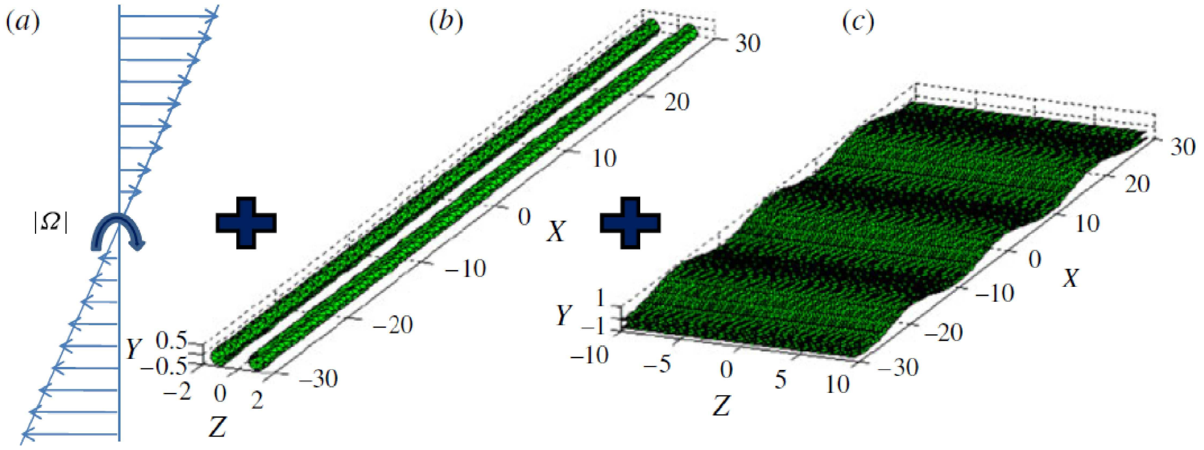

Figure V.18: Illustration of the three elements for the hairpin eddies generation: (a) simple shear; (b) CVP; (c) wavy vortex sheet. Picture from (Cohen et al., 2014) courtesy of Cohen.

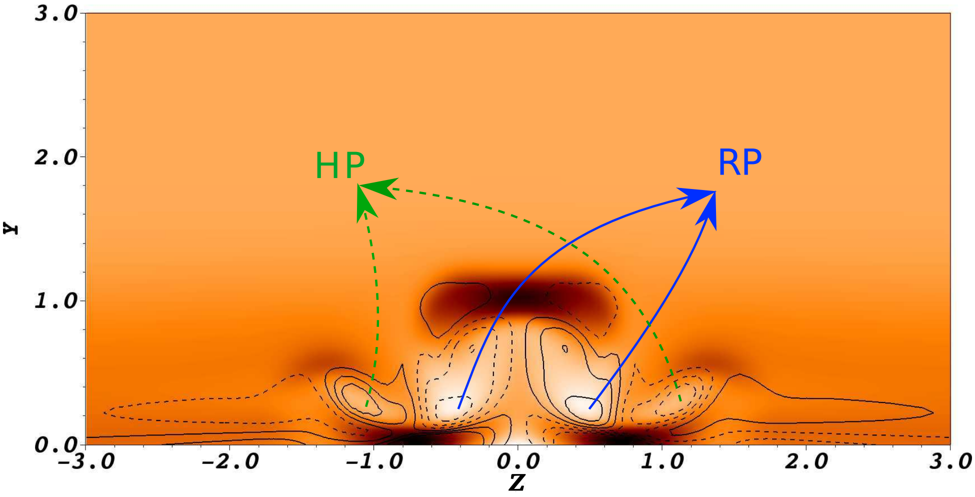

Figure V.19: Isolevel of negative (dashed line) and positive (solid line) streamwise vorticityΩ_x of the base flow field. Isocontour of spanwise vorticity Ω_z. Dark zones highlights negative vorticity.

that we remember to be on the separation zone, see fig. IV.32. This simple but effective model is able to explain the generation of hairpin vortices combining three linear mechanisms in a non-linear way.

Once generated, the hairpins are sustained in the streamwise direction by the gradients of the flow field (advection and tube stretching) and by the inflectional points. The variation of the flow in the x-direction is negligible with respect to the spanwise and wallnormal gradients and as first approximation the inflectional points are evaluated by looking at the zero value of the term in (V.6).

$$\frac{\partial^2 U}{\partial y^2} + \frac{\partial^2 U}{\partial z^2} = 0 \tag{V.6}$$

The location of the points in which the condition in (V.6) is verified are reported with red line in figure V.20 in the plane at $z = 0$. Close to $x = 9$ three inflectional points are present in the wall normal direction. This can explain the position of the maximum of the global mode energy production shown in figure IV.29. The disappearance of the two inflectional points can be also seen in figure V.21, where there is a change of sign of the crossflow vorticity Ω_z in $y \in [0.4;\ 0.6]$. After $x = 9$ just negative Ω_z is present. The peak associated to Ω_z at $y \sim 1$ slightly moves towards the wall in x-direction.

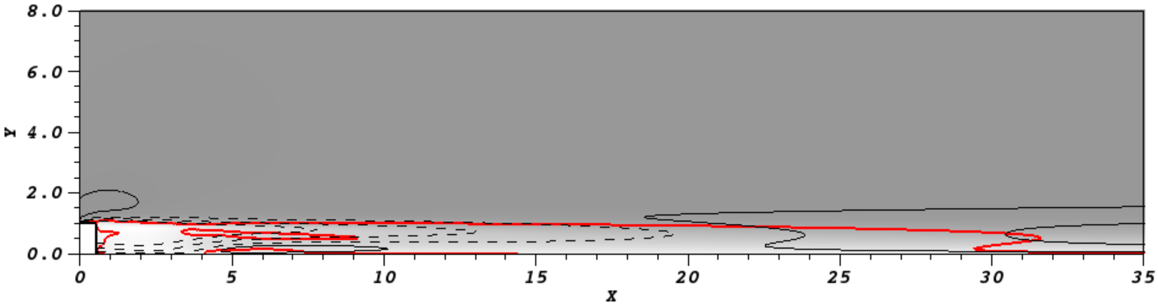

Figure V.20: Plane at $z = 0$. Tick red line indicate the line in which the term (V.6) is verified. Dash line refers to negative streak and continuous line to positive one. Gray scale colour depicts contour of streamwise velocity.

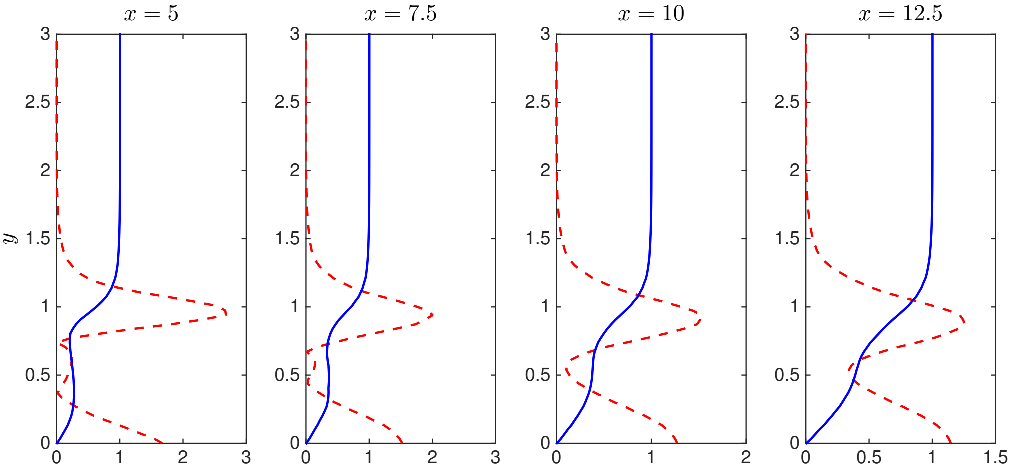

Figure V.21: Solid line represents the streamwise velocity in $z = 0$ plane. Dash line represents the absolute value of the vorticity in the crosflow direction $|\Omega_z|$. The vorticity at $y \sim 1$ is associated to negative spanwise Ω_z.

V.3.0.0.b Mean flow The unsteady fluctuation given by the triggered varicose mode modifies the baseflow. The distortion leads to differences between the baseflow and the mean flow not only in the field close to the cylinder, where the global mode works. Considering the unsteady case achieved with an incoming free stream turbulence at $Tu = 0.18\%$ of the U_∞, the resulting mean flow streamwise velocity profile is plotted in figure V.22 in plane at $z = 0$. The mean flow in V.22 can be compared to the base flow V.21. The first

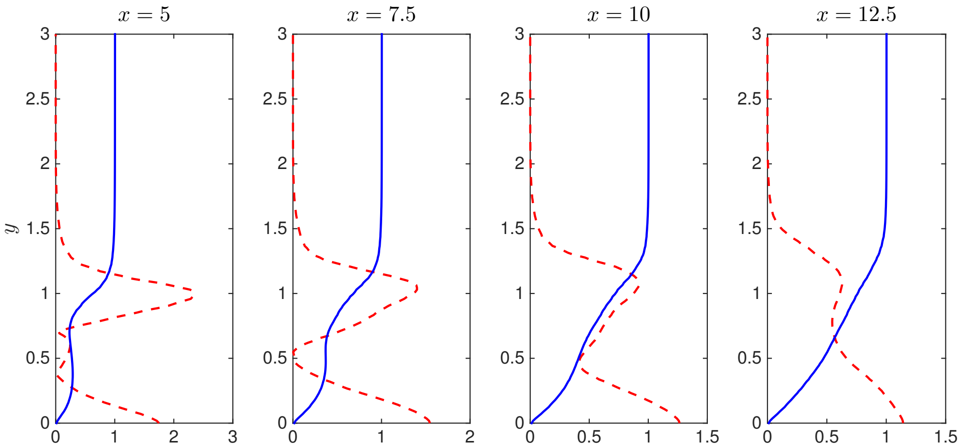

Figure V.22: Solid line represents the streamwise velocity at $z = 0$. Dash line represents the absolute value of the vorticity in the crossflow direction $|\Omega_z|$.

peak of the vorticity is diffused in the wallnormal direction and dissipated before that of the base flow. More importantly, the disappearance of the three inflectional points takes place already at $x = 7.5$. Once the positive peak of Ω_z vorticity is disappeared, the hairpin is no longer sustained. As explained by Farano et al. (2015), the hairpin generation is linked to sweeps and ejections events. Looking at the fluctuation field $\mathbf{u}'(t) = \mathbf{U}(t) - \bar{\mathbf{U}}$, the sweep event fails after the disappearance of the positive spanwise vorticity Ω_z (fig. V.23). When the sweep event is no longer active the hairpin moves far from the wall

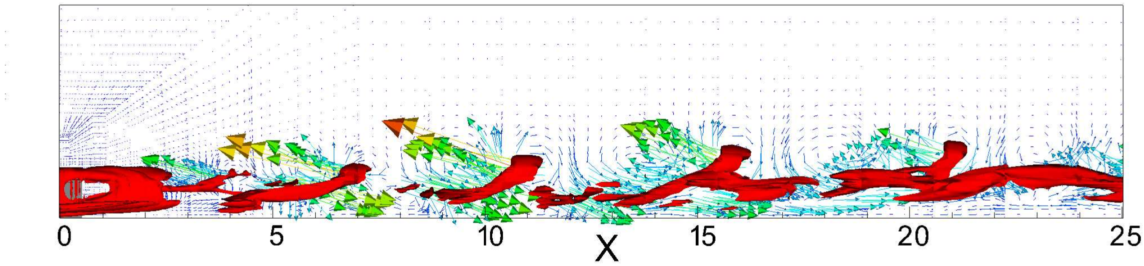

Figure V.23: Istantaneous fluctuation field $\mathbf{u}$ associated to the hairpin structure highlighted by the λ_2-criterion.

and is gradually dissipated. At the same time new vortical structures appear between the high speed streak and the low speed streaks due to the presence of a shear caused by an inflectional point on the streamwise velocity in the crossflow direction. This first vortical structure starts to wrap the two lateral low speed streak up to generate new hairpin vortices. With this mechanism the perturbation moves outwards in the z-direction, also promoted by the increasing inflectional velocity profile in the spanwise direction as observed in chapter §IV looking at the streaks evolution (fig IV.14 and IV.15). The increasing instability in the spanwise direction causes the generation of new streamwise vortices. The Ω_x field evaluated on the mean flow and illustrated in figure V.22 reveals how the vortices are multiplied in the crossflow direction moving downstream. The streamwise

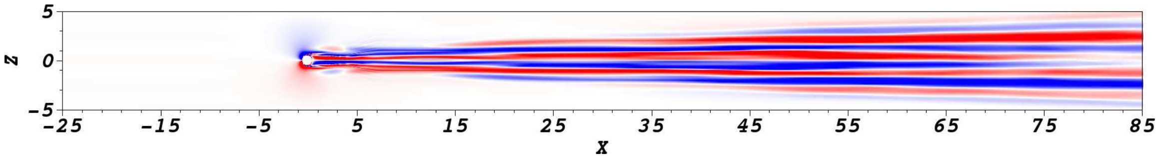

Figure V.24: $\Omega_x \pm 0.1$ on the mean flow. The blue colour indicate negative stramwise vortices the red color the positive one. Velocity field at $y = 0.8$.

vortices generation has been also observed experimentally by Ye et al. (2016b). Once the supercritical condition is reached, secondary and tertiary vortices are generated behind roughness elements of different shape. It seems that a secondary instability occurs when an unsteady perturbation rides the two lateral streaks. For a cylindrical case studied by Ye et al. (2016b), transition takes place on the horseshoe vortices when a secondary vortices is triggered. The same scenario is observed in the numerical case just shown.

V.4 Overall discussion about transition

The DNS calculations perturbed in three different ways always show the high receptivity of the varicose mode. Introducing an inflow turbulence it is possible to self sustain the varicose global mode. The route to transition can now be summarized as follows:

1. The external turbulence is able to penetrate the boundary layer that thickens up to the wavemaker zone of the varicose global mode. Low levels of turbulence are enough to observe the unsteady features of the global mode.

2. The shear in the wall normal direction of the streamwise velocity plus the rear pair vortices induced by a secondary flow plus the oscillating motion provided by the global mode constitute the sufficient ingredients for the hairpin vortices generation.

3. The hairpin vortices grow downstream on the low velocity middle streak up to $x \sim 8$. The hairpins are sustained by the presence of inflectional points in the wall normal direction of the streamwise velocity. The presence of positive spanwise vorticity ensures sweep and ejection events.

4. After $x \sim 8$ the hairpin vortices start to be dissipated (see figure V.6 and V.11) but a new perturbation is induced on the two lateral low speed streaks.

5. The perturbation on the horseshoe vortices grows up to $x \sim 25$ where a wall perturbation occurs as shown in figure V.6 and V.11.

6. This last perturbation, that goes towards transition, is accompanied by the generation of streamwise vortices in the spanwise direction.

The results achieved by global stability analysis, receptivity and perturbed DNS constitute a complete scenario to understand subcritical transition of flow over roughness elements. Usually, this subcritical transition is ascribed to the transient growth of perturbations induced by the non-orthogonality of convective modes in the discretized branch (see figure IV.21). As shown in figure V.3, a short transient growth is present for amplitude levels of the forcing lower then $A < 10^{-3}$. Of course, non-normality could have similar influences in cases different from $(\eta, Re, \delta_1/h) = (1, 700, 0.491)$, but when a varicose global mode is present, its strong receptivity will dominate other energy growth mechanisms such as non-normality.

Chapter VI

Parametrical analysis

Contents

VI.1 Re and δ_1/h variation effect

In the previous chapters the study of the case $(\eta, Re) = (1, 700)$ has been largely discussed. The varicose mode that was not present in Loiseau's work (Loiseau et al., 2014) (Loiseau, 2014) for $\eta = 1$ is found to be able to drive the unsteadiness by receptivity mechanisms. In the light of these results, some questions arise:

- What does it happen to the base flow topology when the Reynolds number and/or the shear ratio δ_1/h change?
- How do the global eigenvalues move in the complex eigenspectrum?

To answer at this questions, one of the unstable cases from Loiseau's work $(\eta, Re, \delta_1/h) = (1, 1200, 0.688)$ is chosen as a reference. By changing separately the Reynolds number and the aspect ratio, the reference case is reached from that studied in the last chapter, namely $(\eta, Re, \delta_1/h) = (1, 700, 0.491)$.

VI.1.1 Reynolds number effect

Three cases with the same shear ratio $\delta_1/h = 0.491$ and different Re number are selected. By increasing Re from 700 to 1200 the DNS shows a sinuous unsteadiness. By using the

BoosConv algorithm to reach the stationary solution at $Re = 900$ and 1200, the evolution of the streaks (as presented in chapter §IV) is reported in figure VI.1 for Re=700, 900 and 1200. The Reynolds number impacts on the amplitude of the higher and the two

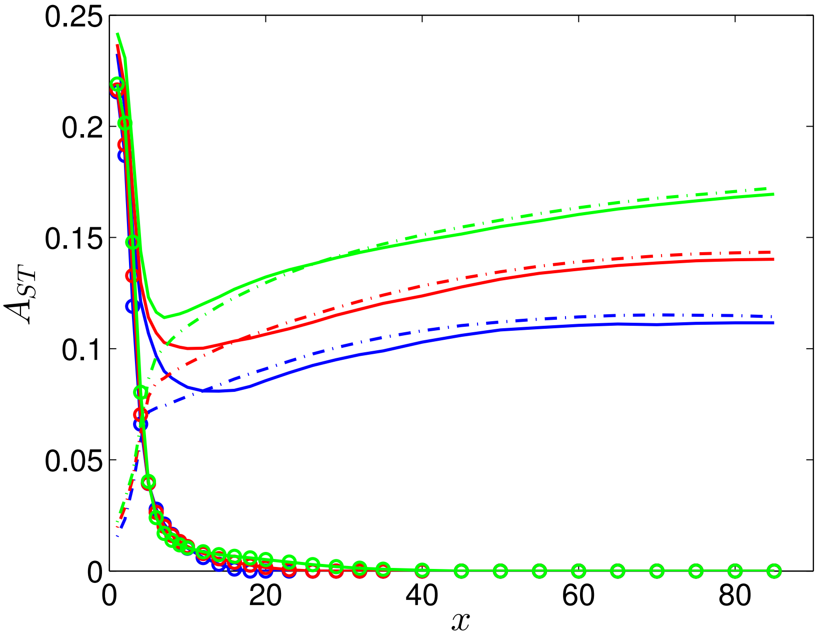

Figure VI.1: Streaks amplitude vs x-direction for Re =700 (blue), 900 (red) and 1200 (green). The curve with circle markers (○) depicts the low streak amplitude in the middle vs x. Continuous lines are related to the high speed streaks and dashed line to the lateral low speed streaks.

lateral low speed streaks. The low middle streak appears more elongated. By keeping constant the aspect ratio δ_1/h the theoretical Blasius profile at the cylinder position is always the same. Hence, the head of the cylinder is subject to the same dimensionless streamwise velocity. For this reason the curves are superimposed in the flow field close to the roughness. The areas associated to the streaks for the three cases are depicted in figure VI.2. The reduced viscosity effect induces a delay in the growth of the area of the three streaks proportionally to the boundary layer thickness growth. By increasing the Reynolds number the sinuous eigenvector becomes unsteady, as shown in figure VI.3. The increasing size of the low streak in the middle plane promotes the sinuous instability as assessed by the local stability analysis. The sinuous mode can become globally unstable if the local sinuous unstable mode becomes absolutely unstable. This could be possible since the wavemaker of the sinuous mode (Loiseau et al., 2014) is always located on the separation zone, precisely on both sides of the separation zone. If the absolute region is large enough, the absolute instability becomes self-sustained and then global (Pier and Huerre, 2001), (Siconolfi et al., 2017). The critical Reynold number is about $Re_c \approx 850$ for $\delta_1/h = 0.49$ that is lower than $Re_c = 1040$, as tracked by Loiseau *et al.* for $\delta_1/h = 0.688$.

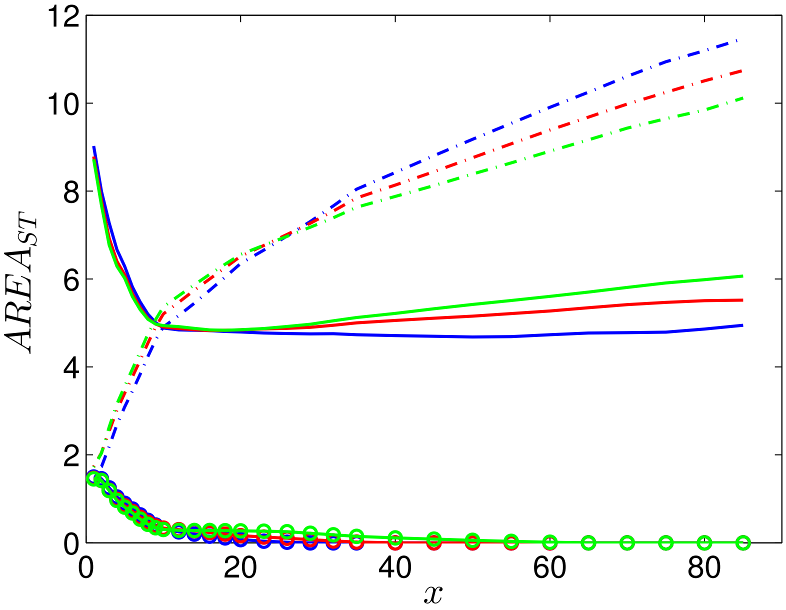

Figure VI.2: Streak areas vs x-direction for Re =700 (blue), 900 (red) and 1200 (green). Curves as in figure VI.1.

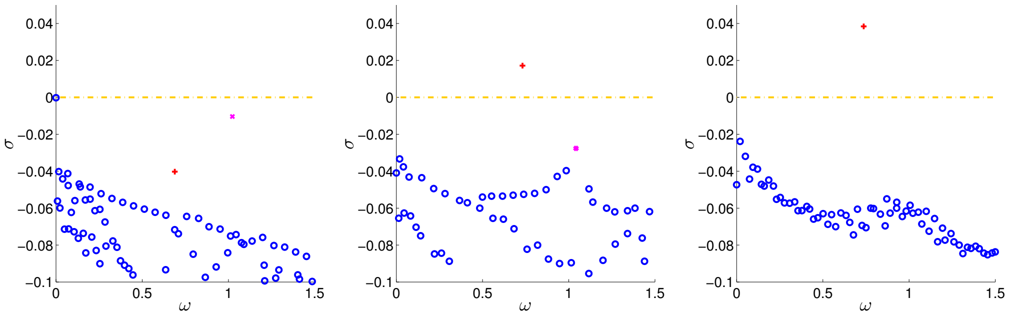

Figure VI.3: Eigenspectrum for Re =700, 900 and 1200. Red (+) marker represents the varicose mode, magenta (×) marker the sinuous one.

VI.1.2 Shear effect

Contrary to the previous analysis, the Reynolds number is now kept constant at 700 and the shear ratio ranges from $\delta_1/h = 0.491$ to 0.688, where the latter is the one fixed by Loiseau et al. (2014). Increasing the ratio δ_1/h the cylinder height becomes smaller with respect to the boundary layer thickness. It is known a priori that no unstable cases are present for this analysis since at $\delta_1/h = 0.688$ the critical Reynolds number is $Re_c = 1040$. The same analysis on the streaks amplitude is performed and displayed in figure VI.4 By increasing δ_1/h the amplitude of the streak decreases as the roughness is much more immersed in the boundary layer. For the same reason the velocity that hits the cylinder head is lower. This also explains the different amplitudes close to the roughness flow field. The areas at each streamwise section of the streaks are comparable between each other (see fig. VI.5). This implies that the velocity gradients in the spanwise direction

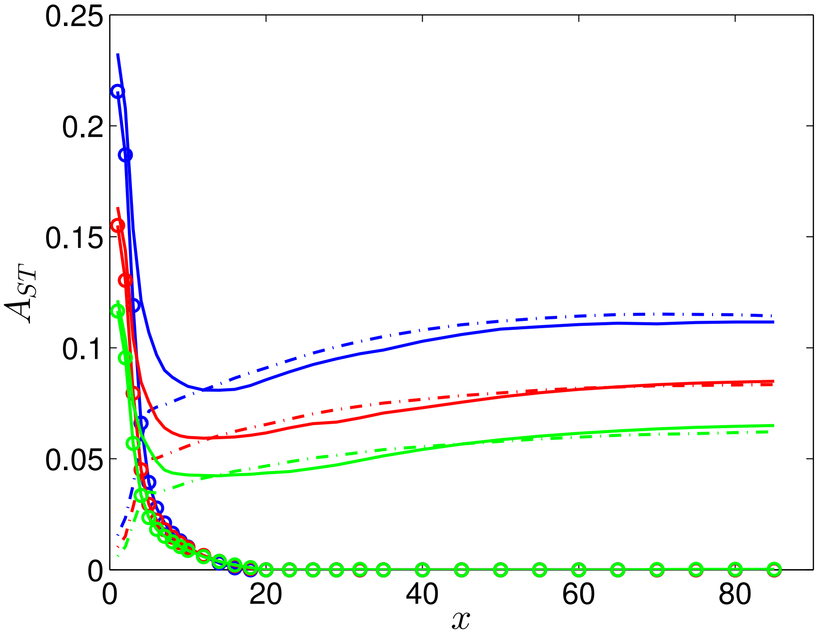

Figure VI.4: Streaks amplitude vs x-direction for δ_1/h =0.491 (blue), 0.59 (red) and 0.688 (green). The curve with circle marker ($\circ$) depicts the low streak amplitude in the middle. The continuous line is related to the hight speed streak and the dashed one to the lateral low speed streaks.

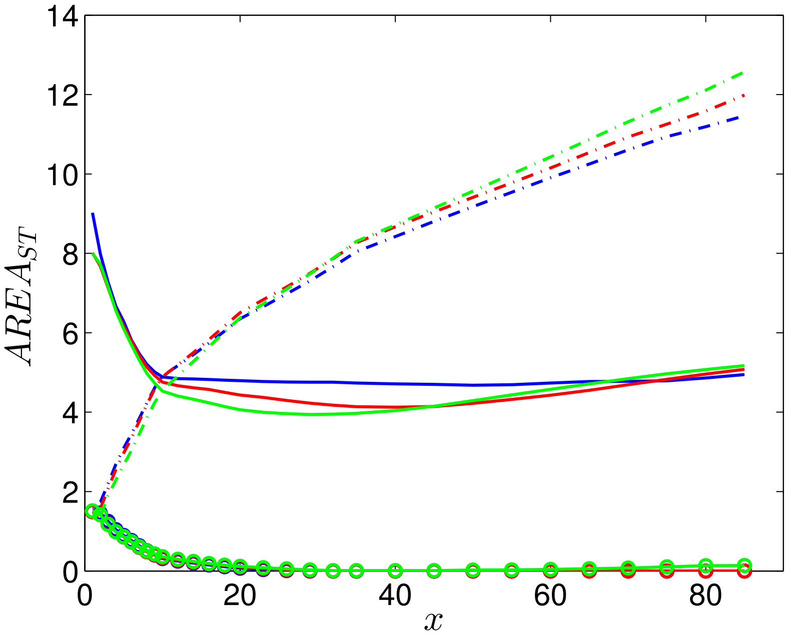

Figure VI.5: Streak areas vs x-direction for δ_1/h =0.491 (blue), 0.59 (red) and 0.688 (green). Curves as in figure VI.4.

are weaker for higher δ_1/h. Slow velocity variations in the spanwise direction and low amplitude level of the streaks make the case at $\delta_1/h = 0.59$ devoid of isolated global modes as illustrated in figure VI.6. Reducing the Reynolds number sinuous and varicose

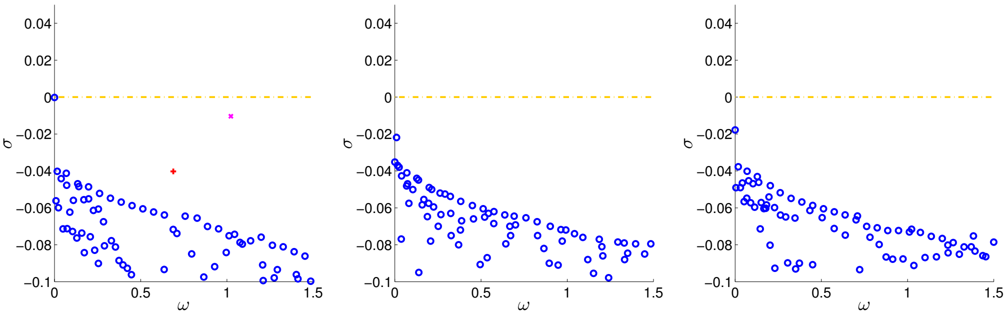

Figure VI.6: Eigenspectrum for δ_1/h =0.491, 0.59 and 0.688. Red (+) marker represents varicose mode, magenta (×) marker sinuous one.

mode become stable. Reducing even more the shear ratio up to δ_1/h =0.39 both sinuous and varicose mode are destabilized. Moreover the varicose global mode becomes unstable as illustrated in figure VI.7. It should be noted that in such flow condition the cylinder

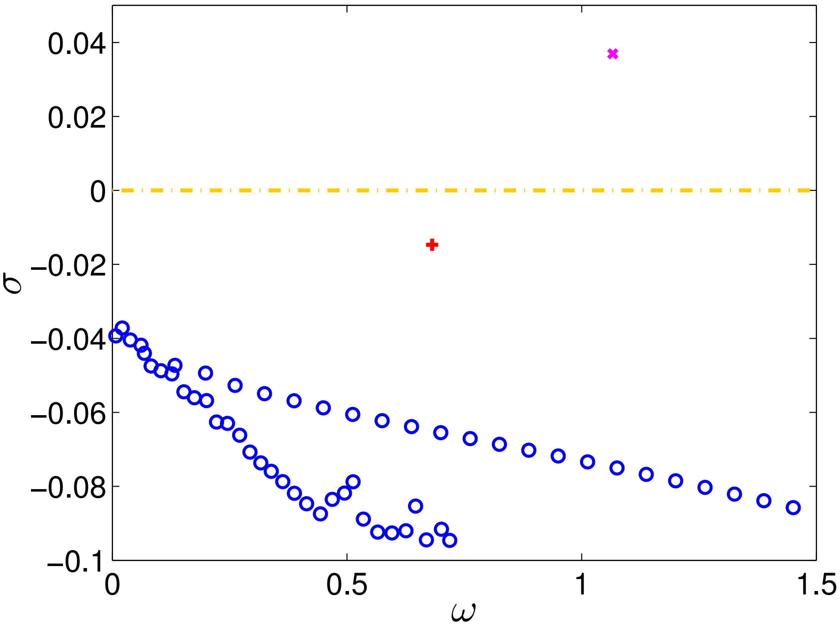

Figure VI.7: Eigenspectrum for δ_1/h =0.39. Red (+) marker represents varicose mode, magenta (×) marker sinuous one.

height is $h = 0.86\delta_{99}$. Hence, this case is on the limit of the roughness that can be defined as “miniaturized”. The shear ratio, and more precisely the velocity hitting the cylinder head, plays an important role on the critical *Re* number at which the system can become unsteady.

VI.2 Receptivity of the sinuous mode

In chapter §IV the pseudospectrum in figure IV.24 shows a low interaction between the sinuous mode and the others present in the eigenspectrum. This is possible because all the modes in the spectrum are varicose and the sinuous mode turns out to be always orthogonal to the others. As the isolated varicose mode approaches the instability threshold, it becomes highly susceptible to a harmonic forcing that works at the same pulsation. Thus, the following question arises:

- Is this the case also when the sinuous global mode approaches the instability threshold?

VI.2.1 Receptivity to harmonic forcing

To check the receptivity of the sinuous global mode the case $(\eta, Re, \delta_1/h) = (1, 1000, 0.688)$ has been studied. The chosen case corresponds to the same set-up selected by Loiseau et al. (2014), where no isolated varicose global modes are present. The reader can refer to Loiseau et al. (2014), Loiseau (2014) for the base flow analysis. The eigenspectrum and the related pseudospectrum estimation is reported in figure VI.8. No isolated global modes are present. The chosen case shows an isolated sinuous mode with a growth rate $\sigma = -0.01$ that is comparable to the growth rate of the varicose mode for the case

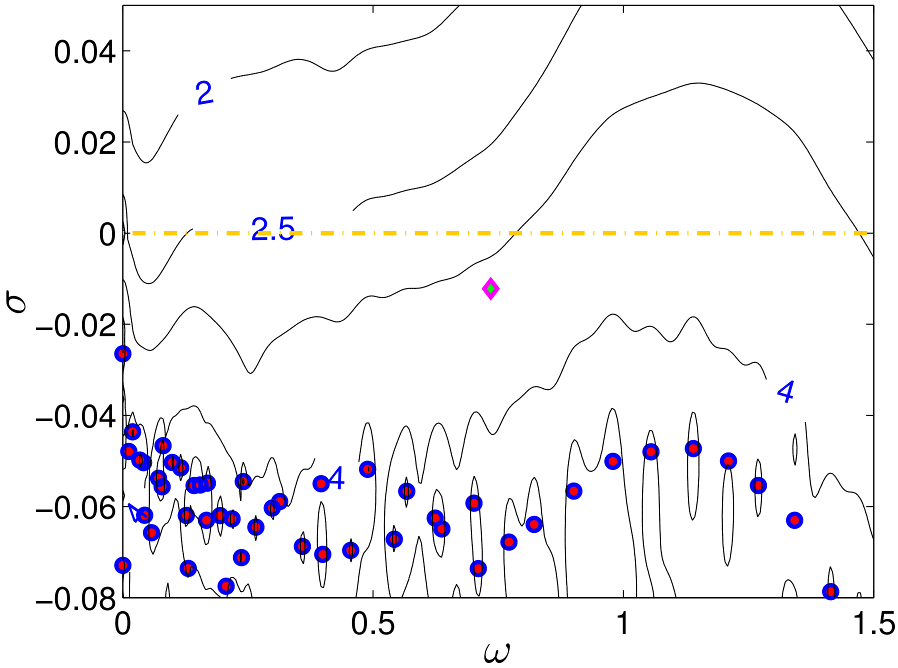

Figure VI.8: Eigenspectrum and pseudospectrum for $(\eta, Re, \delta_1/h) = (1, 1000, 0.688)$. Magenta square points highlight sinuous mode and blue circle points the varicose mode. The iso-lines represent the pseudospectrum given by $\log_{10} \epsilon$ contour.

$(\eta, Re, \delta_1/h) = (1, 700, 0.491)$. Despite the sinuous mode is close to the instability threshold, it seems that the receptivity of the sinuous mode is triggered just with a perturbation that acts in the complex plane close to $(\sigma, \omega) = (-0.01, 0.677)$. Due to the high interaction of the varicose modes between each other no convergence is reached in the pseudospectrum also with a spectral order equal to 12. For this reason the pseudospectrum provides just a qualitative interpretation of the resolvent. To achieve the true resolvent curve several optimal forcing computations have been performed. The resolvent curve VI.9 appears strongly linked to the distribution of the eigenvalues in the global spectrum in figure VI.8. The system appears to be highly receptive to a harmonic forcing that pulses at $\omega = 0.677$. The orthogonality of the sinuous mode is felt by the fact that the curve peaks with a gain of about 5.3×10^5. This is synonymous of the low interaction with the closest global mode. To verify the orthogonality of the sinuous mode, the optimal forcing shape is compared to the adjoint eigenmode in figure VI.10 and the optimal response to the direct eigenmode in figure VI.11. The adjoint mode is localized on the cylinder head non-symmetrically with respect to the streamwise velocity. The sinuous mode is tied to a Von-Karman instability (Loiseau et al., 2014), (Loiseau, 2014). Once again, when the global mode is orthogonal to the others the optimal forcing looks like the adjoint mode and the optimal response like the direct mode, following equation (IV.16) . This is not true for the resolvent modes at $0.8 < \omega < 1.3$, as illustrated in figure VI.12 and VI.13. For $\omega = 1.25$ the gain is equal to 3×10^5 and the resolvent mode shows a varicose distribution that does not look like the eigenvector associated at the same pulsation. The adjoint eigenmode in figure VI.12 is localized mostly on the cylinder sides. The optimal forcing, however, covers the whole cylinder surface and extends upstream in the symmetry plane at $z = 0$, while the adjoint mode does not. According to eq. (IV.16) the optimal response is for this case a

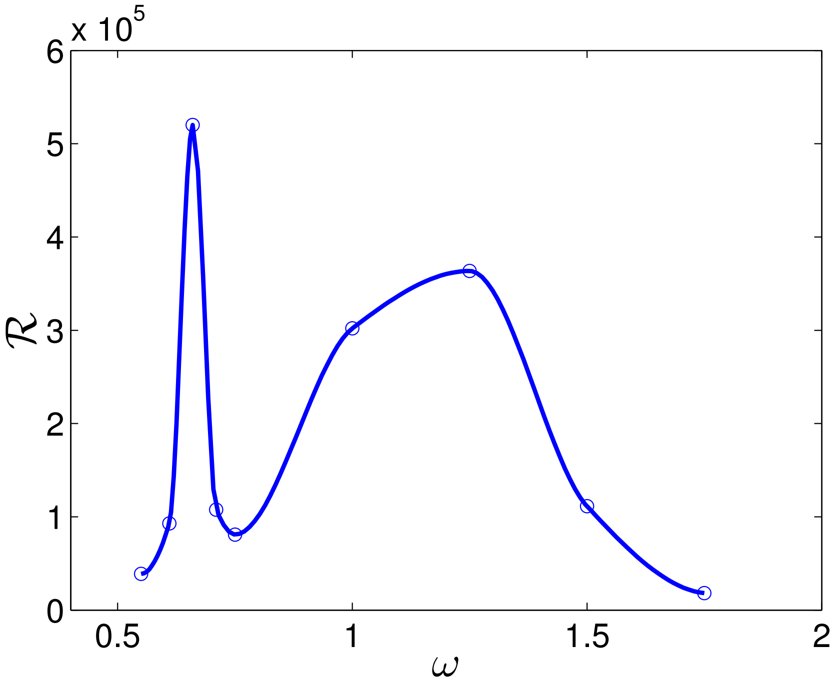

Figure VI.9: Amplification factor of the harmonic forcing for different ω for $(\eta, Re, \delta_1/h) = (1, 1000, 0.688)$.

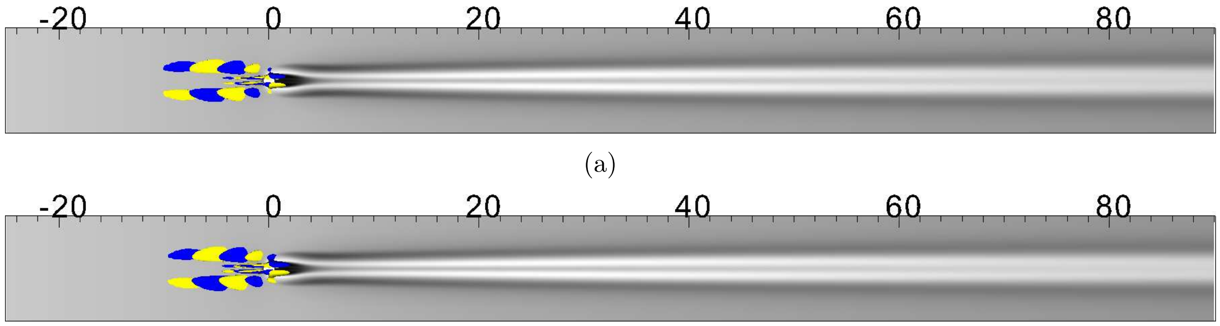

(a)

(b)

Figure VI.10: ±10% of streamwise component of sinuous adjoint eigenmode (top) and optimal forcing shape (bottom) at $\omega = 0.677$. Gray scales highlight streamwise velocity field at $y = 0.5$.

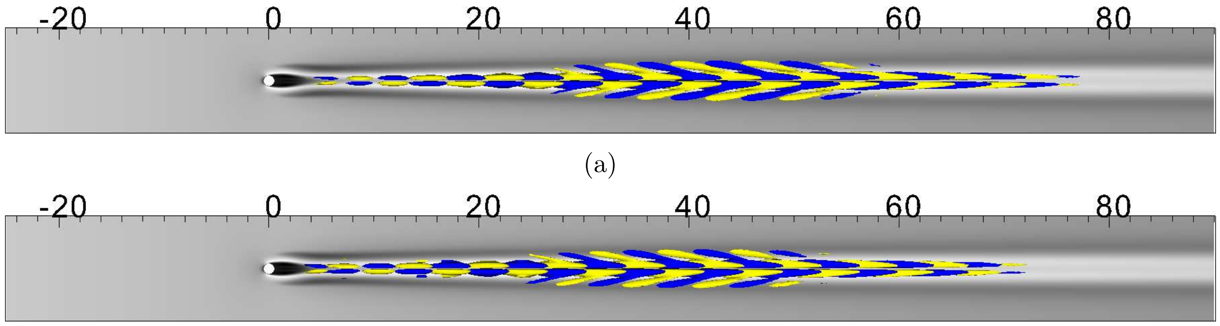

(a)

(b)

Figure VI.11: ±10% of streamwise component of sinuous direct eigenmode (top) and optimal response shape (bottom) at $\omega = 0.677$. Gray scales highlight streamwise velocity field at $y = 0.5$.

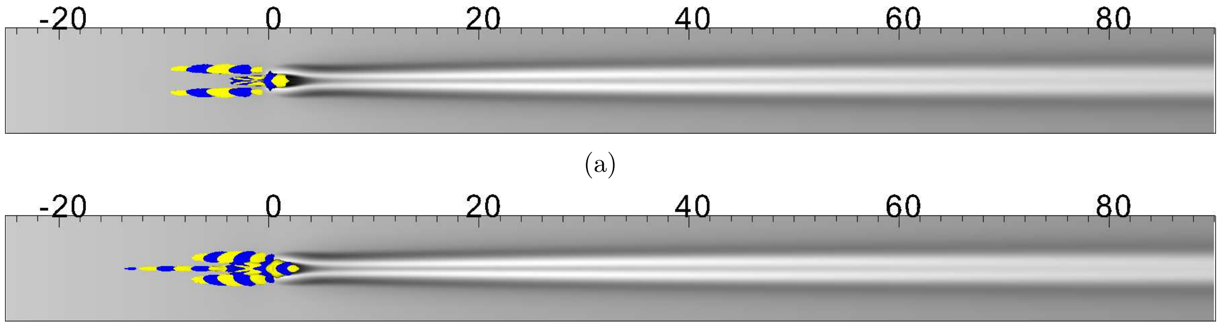

(a)

(b)

Figure VI.12: ±10% of streamwise component of varicose adjoint eigenmode (top) and optimal forcing shape (bottom) at $\omega = 1.25$. Gray scales highlight streamwise velocity field at $y = 0.5$.

linear combination of the direct global modes. Hence, it is not surprising that the spatial distribution of the optimal response does not match that of the eigenmode at $\omega = 1.25$.

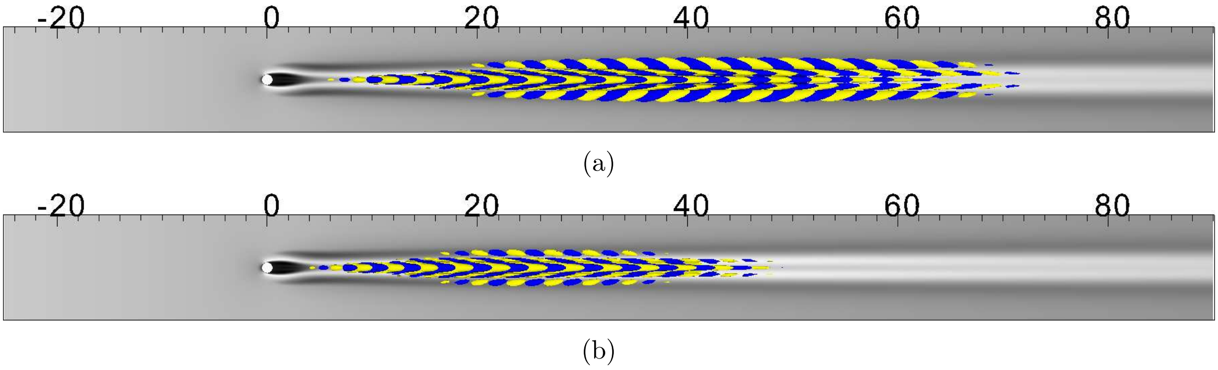

Figure VI.13: ±10% of streamwise component of direct varicose eigenmode (top) and optimal response shape (bottom) at $\omega = 1.25$. Gray scales highlight streamwise velocity field at $y = 0.5$.

VI.2.2 Receptivity to free stream turbulence

The gain curve in figure VI.9 suggests that the most amplified pulsation is $\omega = 0.667$ with a sinuous associated structure. Nevertheless, to verify how the system responds to a broadband perturbation a DNS with an incoming free stream turbulence has been performed. The set-up of the homogeneous turbulence is the same of the case presented in section §V.2.1. The turbulent intensity has been progressively increased up to the onset of unsteadiness in the flow. Differently from the case studied in the previous chapter §V, an incoming turbulent intensity $Tu = 0.06\%$ is sufficient for making the Cf curve diverge from the unperturbed case (see fig. VI.14). The perturbation associated to a turbulent intensity $Tu = 0.06\%$ is illustrated in figure VI.15 using iso-levels of the λ_2-criterion. Low values of λ_2 are used in this visualization to highlight how the free stream perturbation is able to penetrate the boundary layer and destabilize the rear pair vortices. The streamwise vortices behind the roughness show a varicose modulation that induces the merging of the two vortices providing wake hairpin eddies. The resulting perturbation is then decomposed in smallest scale structures moving downstream. Increasing the turbulent intensity up to $Tu = 0.26\%$ the rear pair vortices modulation increases its amplitude and the two lateral

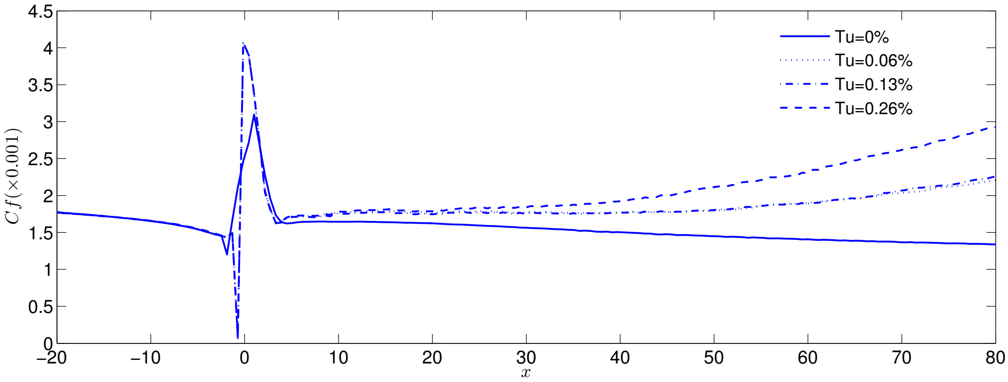

Figure VI.14: Skin friction drag vs the streamwise position at different turbulent intensities for the case $(\eta, Re, \delta_1/h) = (1, 1000, 0.688)$.

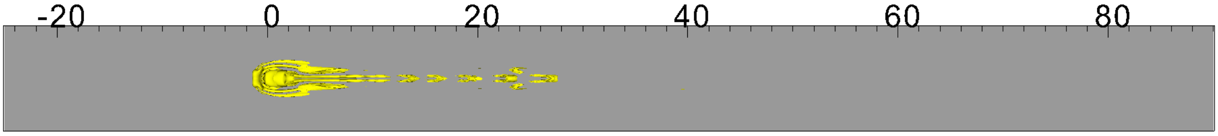

Figure VI.15: Instantaneous flow field with incoming turbulence at $Tu = 0.06\%$. Isocontours of $\lambda_2 = -0.005$.

low speed streaks are also destabilized. The transitional scenario is illustrated in figure VI.16. The resulting perturbation shows again a varicose symmetry. The receptivity of the varicose modes drives the transition although the gain is lower then the sinuous resolvent mode. This can also be appreciated by the fact that the Cf increases slowly along x confirming the convective character of the triggered modes. The time signal recorded by a probe in $(x, y, z) = (10, 1, 0)$ is reported in figure VI.17. The Fourier spectrum shows two main peaks at $\omega = 0.8$ and 1.05. These two peaks linked to the unsteadiness on the rear pair vortices and those on the low speed streaks live in the range of ω associated to varicose resolvent modes, as shown in fig VI.9. The reason why the sinuous instability is not triggered is because the probability to observe it, is rather low. The area under the resolvent curve associated to a sinuous perturbation is much smaller

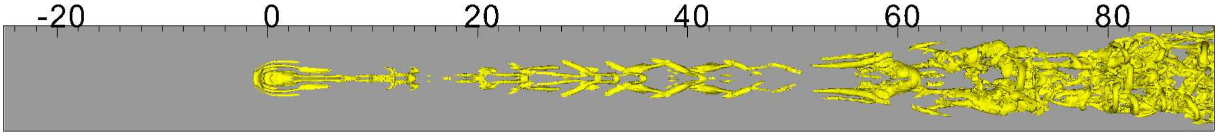

Figure VI.16: Instantaneous flow field with incoming turbulence at $Tu = 0.26\%$. Isocontours of $\lambda_2 = -0.005$.

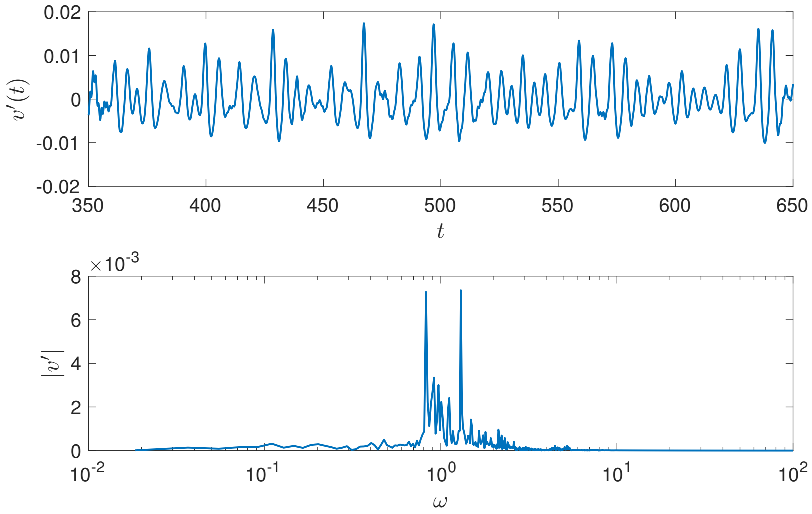

Figure VI.17: Time signal for incoming turbulence with $Tu = 0.26$ (top) and its FFT (bottom).

than the varicose one. Therefore, an external uncontrolled broadband perturbation that acts onto all the harmonics more effectively triggers a varicose response of the system. For several quantitative details and further mathematical explanations, the receptivity to a stochastic forcing has to be evaluated as done by Hœpffner and Brandt (2008).

VI.3 Overall discussion on the parametric analysis

The shear ratio δ_1/h is a critical parameter of the system since it takes into account the interaction of the boundary layer profile with the roughness element height. The symmetry of the unsteady global mode can be changed not only by varying the aspect ratio of the roughness element, but also changing the δ_1/h ratio. With low δ_1/h values, the growth of a varicose global mode is promoted. On the contrary, with a high δ_1/h just the sinuous global mode can become unstable. This means that with the same aspect ratio both symmetries (sinuous and varicose) can arise, depending on the shear ratio. When an almost unstable sinuous global mode is present in the eigenspectrum, the resolvent curve exhibits a high receptivity to the pulsation corresponding to the sinuous mode. The sinuous mode receptivity is highly picked, the receptivity to varicose ones is contrariwise lower in amplitude, but widely distributed onto a large range of ω. This makes varicose modes more likely to be observed. The receptivity of the streaky boundary layer to the free stream turbulence confirms the last conclusion.

Chapter VII

Flow over miniaturized vortex generators

Contents

VII.1 Streaks generation by MVGs

The use of small roughness elements to generate streaks is limited by the streaks amplitude level. Experimentally, this limit is set to 12% of the free stream amplitude (Fransson et al., 2004). Loiseau et al. (2014) have demonstrated how this limit is related to a supercritical bifurcation after which the system becomes globally unstable. In the previous chapters it has been shown how transition can be achieved also subcritically. This makes the cylindrical roughness a non-robust solution for the passive control. The receptivity to external perturbations can give rise to a varicose perturbation linked to the presence of one or more varicose global modes. For what has been seen, the supercritical and subcritical transition are always linked to the base flow structures behind the roughness, more precisely to the separation zone induced by the presence of the roughness.

VII.1.1 Experimental studies

Fransson and Talamelli (2012) proposed to install on the wall miniaturized vortex generators to produce stable steady streaks. The vortex generators shape is a known geometry already used in aeronautical application to delay or prevent separation by reducing pressure drag introducing large scale vortices. This kind of structure has been miniaturized up to $0.3 \div 0.5$ times the boundary layer thickness δ_{99}. In the boundary layer the MVGs generate wall vortices which modulate the boundary layer by the presence of high and low speed streaks. The streaks generation is provided by the lift-up mechanism triggered by controrotative vortices observed experimentally (Fransson and Talamelli, 2012) and numerically (Siconolfi et al., 2015b). The miniaturized vortex generators are sketched in figure VII.1. The geometry of the roughness is described by few parameters:

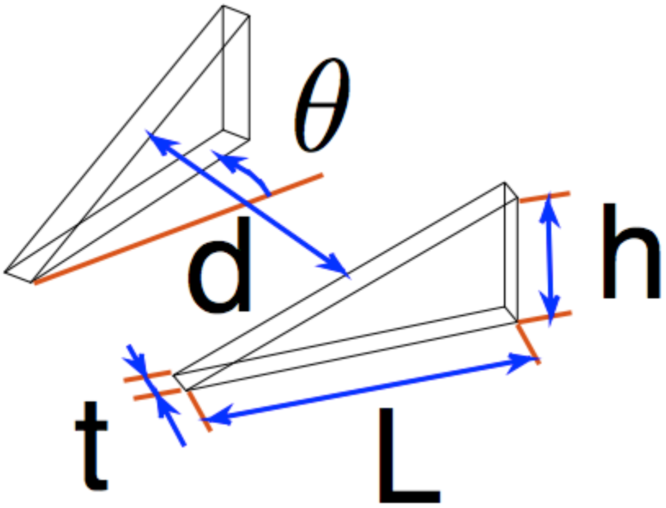

Figure VII.1: Sketch of miniaturized vortex generators.

- h the height of the roughness,
- d the distance between the MVG
- L the length of a single MVG
- t the MVG thickness
- θ the angle between the MVG and the streamwise direction

The main advantage of this roughness shape is that it does not produce a huge separation zone as for cylindrical (Loiseau et al., 2014) or hemispherical (Citro et al., 2015) roughness elements that can induce global instability. The resulting steady state can be considered quasi homogeneous already close to the roughness. A pattern of 15 equidistant MVG pairs is able to produce steady streaks up to an amplitude level equal to 32% of the free stream velocity. To use the words of the authors Shahinfar et al. (2012) this device is tremendously powerful in modulating the boundary layer in crossflow direction. The stabilizing energy production term in the spanwise direction $-uw\partial U/\partial z$ compensates the destabilizing one in the wallnormal direction $-uv\partial U/\partial y$ (Brandt, 2014). The stabilizing effect provided by the MVGs installation has been tested in several condition. Satisfactory results are achieved in presence of adverse pressure gradient (Fransson and Talamelli, 2012), for an incoming TS like perturbation at $\beta = 0$ (Shahinfar et al., 2013, 2014) and also oblique TS waves (Shahinfar et al., 2014). The MVGs can stabilize TS waves also when they work in the unstable region of the boundary layer velocity profile. Different parametric analysis have also been conducted. The amplitude of the streaks A_{ST} and its stabilization effect A_{ST}/A_{TS} were tracked in function of h, d and Λ that is the distance between two successive MVG pairs. A_{ST} is directly proportional to h, d and U_∞ and inversely proportional to Λ. Another important goal achieved with MVG roughness elements is the possibility to install successive arrays of vortex generators to restore or reinforce the wall streaks providing further transition delay Fransson and Talamelli (2012); Sattarzadeh et al. (2014).

VII.2 Numerical investigation

To understand the differences between the cylindrical case already studied and the MVGs one, the L1 experimental case in Shahinfar et al. (2014) has been studied numerically. The parameters for the experimental set-up are reported in table VII.1.

$U_\infty(m\ s^{-1})$	$h(mm)$	h/δ_1	Re	Re_h
7.6	1.3	1.17	659	421.71

Table VII.1: L1 case parameters in Shahinfar et al. (2014).

In table VII.1 Re is defined using the free stream velocity U_∞, the height of the MVGs h and the dynamic viscosity ν. On the contrary Re_h is known as roughness Reynolds number and is defined with the velocity that a theoretical Blasius profile should have at the MVG height. In the numerical simulation the first definition of Reynolds number is chosen. The dimensionless numerical domain is shown in figure VII.2. The geometrical sizes have been fixed by the experiments, $\theta = 15°$, $L = 3.25mm$, $t = 0.3mm$ and $d = 3.25mm$ and then made dimensioneless by $h = 1.3mm$. The spanwise dimension of the numerical domain is also set to respect the experimental MVGs periodicity $\Lambda/h = 10$ (Shahinfar et al., 2013, 2014). The other dimensions of the numerical domain are $L_0 = 40$, $L_1 = 100$ and $H = 40$. The analytical Blasius velocity profile is used as inflow boundary condition and it is set to match the required δ_1/h at the MVGs position. This choice is in agreement with the experimental configuration. Outflow boundary condition is used at the end of the domain and periodicity condition is imposed in spanwise direction. No-slip and slip condition are imposed at the wall and on the top of the numerical domain, respectively. The MVGs are located at $(x, y, z) = (0, 0, 0)$.

VII.2.0.0.a Set-up validation Unfortunately, a quantitative validation of the numerical set-up is not straightforward since quantitative values are provided for streamwise positions out of the chosen numerical domain. However, a qualitative but satisfactory validation can be performed. A perturbed experimental case is considered in Shahinfar et al.

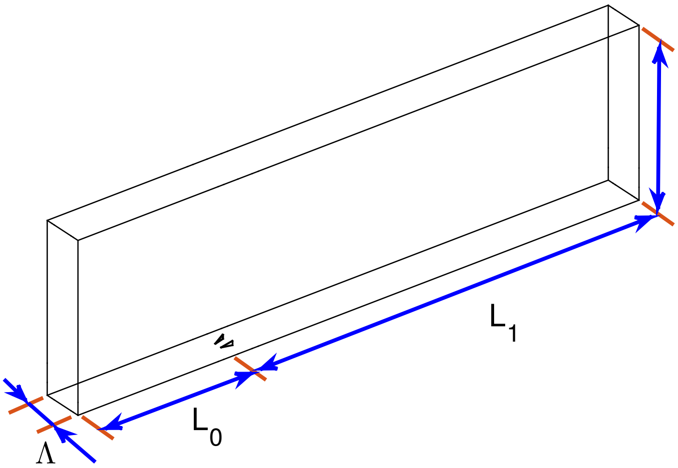

Figure VII.2: Sketch of numerical domain used for the MVG roughness.

(2014) as validation test case. In the T1 case (Shahinfar et al., 2014) a wall normal harmonic perturbation is produced by six loud speakers . The perturbation induces TS waves at $\beta = 0$. The T1 case set-up is resumed in table VII.2. In table VII.2 f_0 is the

$U_\infty (m\ s^{-1})$	$h(mm)$	h/δ_1	$f_0(Hz)$	Re_h	F
7.4	1.3	1.15	48	409	82.2

Table VII.2: T1 case parameters in (Shahinfar et al., 2014).

dimensional frequency used to yield the harmonic perturbation. F is the dimensionless frequency defined as

$$F = \frac{(2\pi f_0 \nu)}{U_\infty^2} \times 10^6 \tag{VII.1}$$

The same case without passive control shows transition around 1500 mm due to linear TS-wave growth (Shahinfar et al., 2014). Introducing MVGs, the TS-wave is stabilized and turbulent transition is delayed. The evolving perturbation in time and in space is divided in two contributions. The first one is the unsteady perturbation:

$$u_u = U(x,z,t) - U^t(x,z) \tag{VII.2}$$

and the second is the steady one

$$u_s = U^t(x,z) - U^{tz}(x) \tag{VII.3}$$

where $U(z,x,t)$ is the instantaneous stramwise velocity on the fictitious plane in which u_{rms} is maximum. U^t is the streamwise velocity averaged in time and U^{tz} averaged in time and in the crossflow direction. The total perturbation turns out to be:

$$u_{tot} = u_u + u_s = U(x,z,t) - U^{tz}(x). \tag{VII.4}$$

Just for the validation case the numerical domain extends up to $L_1 = 200$. The domain has been discretized with 62902 spectral elements which, in turn, are discretized with a

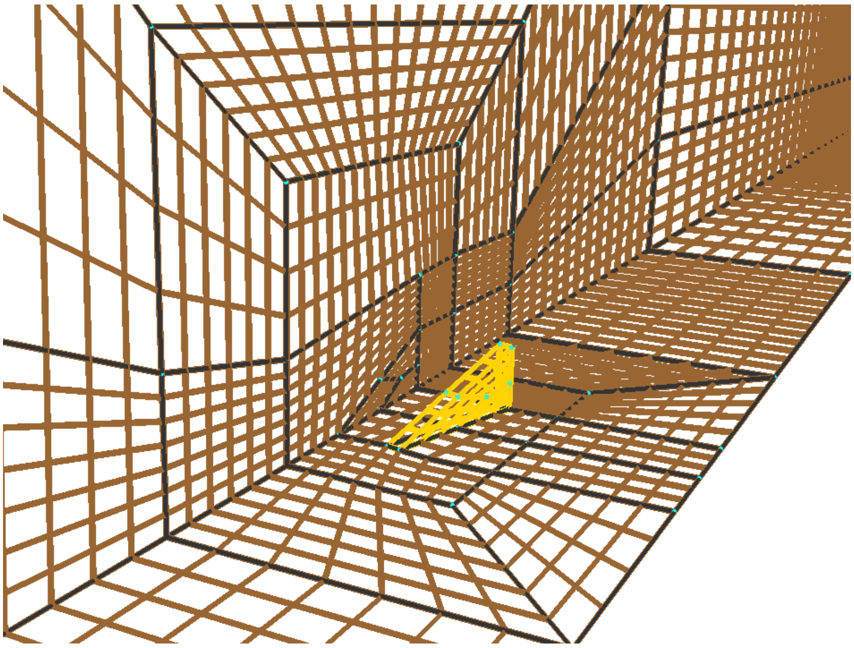

Figure VII.3: Spectral elements discretization of MVGs roughness.

spectral order equal to 8. The spectral elements grid, organized by blocks, is reported in figure VII.3. The wall perturbation produced by the loudspeakers is reproduced by a harmonic wall normal perturbation that has a maximum amplitude level equal to 10^{-4}. The comparison between experimental and numerical u_u, u_s and u_{tot} is reported in figure VII.4. The unsteady perturbation u_u (figure VII.4(b)) is represented by TS-waves modulated by the presence of the streaks induced by MVGs. The steady perturbation (figure VII.4(c)) highlights the presence of a high speed streak in the middle and two low speed streaks on both sides. The superposition of u_u and u_s gives rise to the streak modulation in streamwise direction as depicted in VII.4(a). Behind the MVG position the streaks

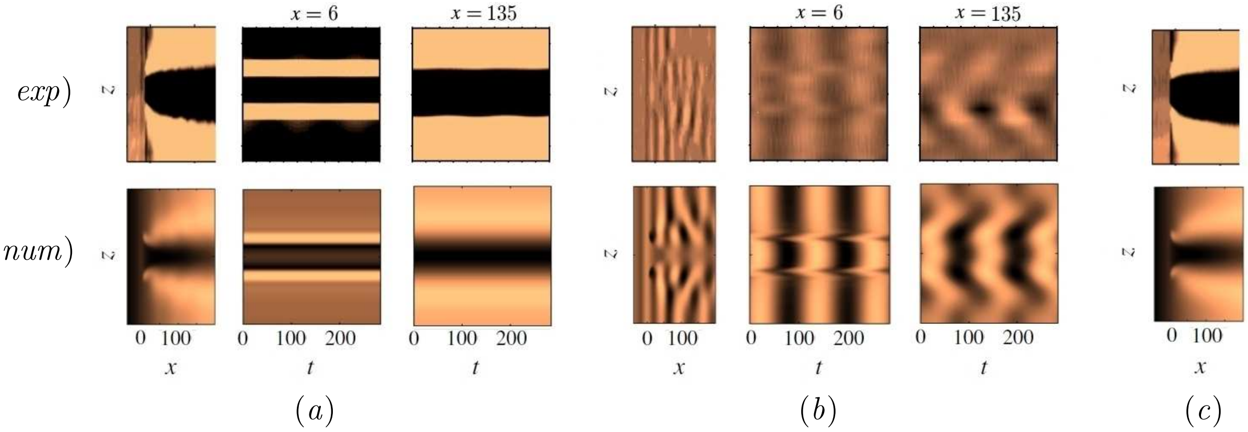

Figure VII.4: u_{tot}, u_u and u_s for T1 case in Shahinfar et al. (2014). First row experimental results, second row numerical one. (a) spatial and spatio-temporal distribution of u_{tot}, (b) spatial and spatio-temporal distribution of u_u and (c) spatial distribution of u_s. Dark colour refers to positive values, bright to positive one.

spread in the spanwise direction up to reach the periodic boundary condition.

VII.2.1 Motivation

The local stability analysis was performed by Siconolfi et al. (2015b) for the C01 and C09 cases in (Shahinfar et al., 2013). In the C01 case four unstable local modes are found. They show how the unstable region of the Blasius velocity profile is drastically reduced. But still, a new unstable region appears behind the MVGs. The numerical and experimental results have raised some question:

1. The presence of the miniaturized vortex generators represents a local geometrical perturbation that can not be taken into account using a local stability ansatz. The local approach extends the velocity profile extracted at one x position indefinitely downstream and upstream discarding the high gradients in the streamwise direction close to the roughness. Is there some global mode originated by the non-parallelism of the flow introduced by the MVGs?

2. All the experiments are carried out in the minimum turbulence level (MTL) wind tunnel at the Royal Institute of Technology (KTH) in Stockholm. In this wind tunnel the background turbulence level is about 0.025% of the free stream velocity at 25 ms^{-1} (Lindgren and Johansson, 2002). With such a low free stream turbulence level the non-normality mechanisms possibly present in the system cannot be expressed. Following the results achieved in the previous chapters, this is a key point in the usability of the roughness as passive control. How much influence on the flow dynamics does the eigenvectors non-orthogonality have? In other words, how much an initial perturbation can be amplified in a finite time?

To answer to these two questions, global stability and optimal perturbation analyses have been performed. The two studies are accompanied by a parametric analysis that helps to understand the critical and subcritical limits of the use of the MVGs as passive control device.

VII.3 Linear analysis

VII.3.1 Modal stability

The case L1 is studied by means of DNS and global stability analysis. The numerical simulation set with the parameters listed in table VII.1 with the geometrical sizes fixed in (Shahinfar et al., 2014) converges towards a steady solution without the use of supplementary tools (e.g. SFD, BoostConv, etc). The absence of self-sustained unsteady mechanisms underlines the absence of global unstable modes. The streaky base flow is illustrated in figure VII.5. Up to $x = 20$ there are two separated low and high speed streaks. After $x = 20$ the two high speed streaks merge together giving rise to a quasi parallel base flow that diffuses in wall-normal direction proportionally to the boundary layer growth. Contrary to the cylinder case, no low speed streaks are induced due to the blocking effect of the roughness. Further details about the flow field onto the MVG roughness are provided by Siconolfi et al. (2015b). The global stability analysis has been

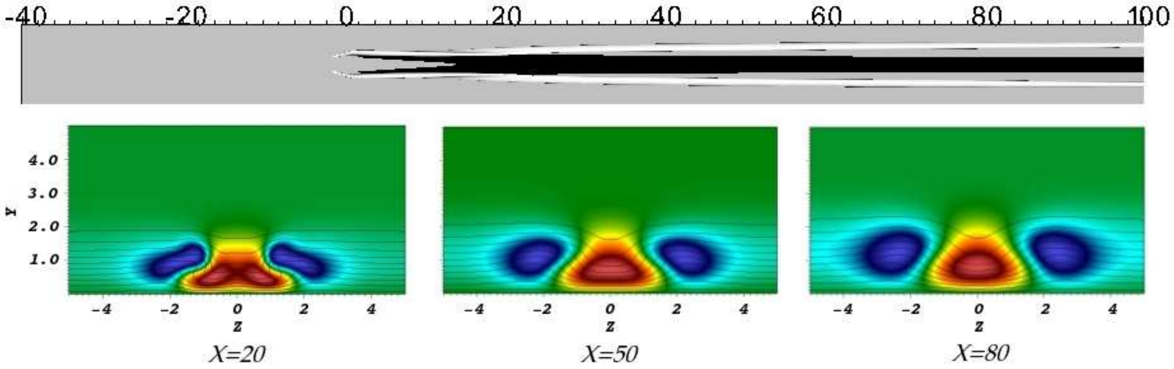

Figure VII.5: Streaked base flow behind MVGs for L1 case in Shahinfar et al. (2014). Isolevels (top) of $U - U_{BL}$ to highlight high speed streak (black) and low speed streaks (white). Isocontours (bottom) of $U - U_{BL}$ in three streamwise position $x = 20$, 50 and 80. Black lines (bottom) refers to streamwise velocity field from 0 to 0.95.

performed with a Krylov subspace equal to 750. The time sampling between two successive velocity vectors is 1 time unit. The eigenvalues computation stops when at least 100 modes reach a residual level lower than 10^{-6}. The global eigenspectrum is reported in figure VII.6. In figure VII.6 the eigenspectrum is superposed to the eigenspectrum related

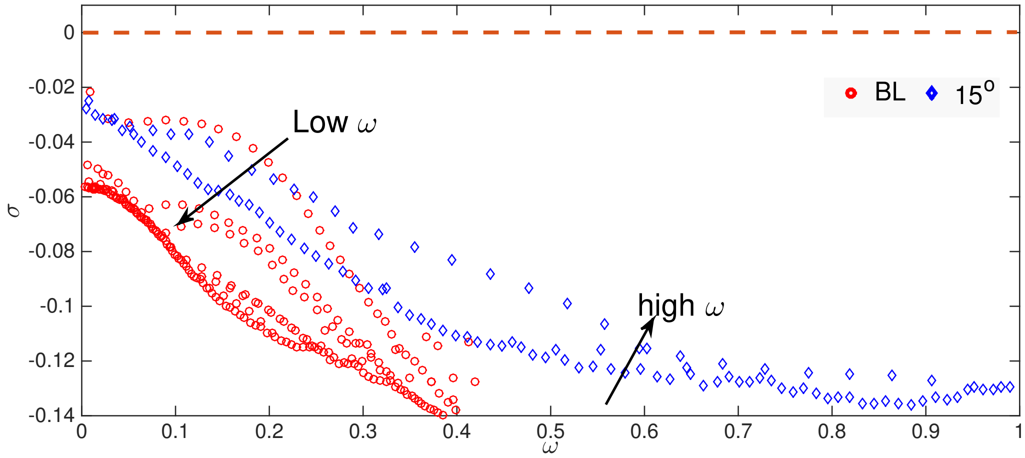

Figure VII.6: Blue diamond markers global eigenspectrum for L1 case in Shahinfar et al. (2014). Red circle markers global eigenspectrum for boundary layer without MVGs.

to the boundary layer case without MVGs. The boundary layer eigenspectrum has been evaluated in a numerical domain that has the same dimension of the case with MVGs. The boundary layer spectrum presents different branches of convective modes. The one close to the instability threshold is associated to TS-waves with $\beta = 0$. The other convective branches show TS-waves with a β different to 0 and compatible with the imposed periodicity condition. The eigenspectrum associated to the L1 case also exhibits convective modes. The eigenmodes in the TS-wave region are slightly damped $0.05 < \omega < 0.3$, but new modes are destabilized at $\omega > 0.3$. The eigenvectors associated to the spectrum in figure VII.6 are the streaky-TS predicted by Cossu and Brandt (2004) as shown in figure VII.7. Moving on the convective branch from low to high ω the streamwise wavenumber α

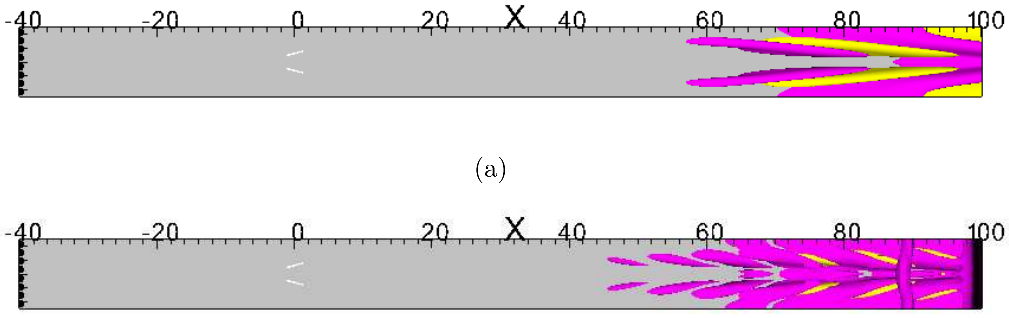

(a)

(b)

Figure VII.7: Streamwise velocity for eigenmodes associated to $\omega = 0.12$ (a) and $\omega = 0.48$ (b) for the eigenspectrum in figure VII.6.

also increases. All the modes on the discretized branch are varicose. This makes the eigenvectors non-orthogonal between each other. The pseudospectrum evaluation confirms the last observation (see fig. VII.8). A perturbation $z\mathbf{I}$ of the Hessenberg matrix gives rise to

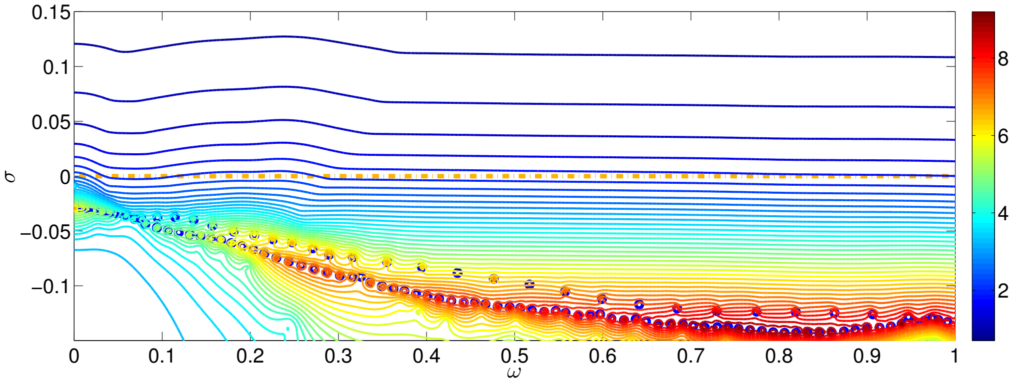

Figure VII.8: Pseudospectrum evaluation on the Hessenberg matrix. Iso-lines represent pseudospectrum given by $\log_{10} \epsilon$ contour.

a response ϵ that involves all the modes close to the z. Extracting the ϵ value on $\sigma = 0$ line, the resolvent curve approximation is depicted in figure VII.9. For a harmonic forcing that pulses at ω, the streaky-TS modes in between $0.1 < \omega < 0.3$ are highly amplified. In the eigenspecrum there are no eigenvectors associated to unstable mechanisms of the flow close to the MVGs. The MVGs are then able to produce streaks in the boundary layer without inducing subcritical transition. The receptivity is linked just to the streaky-TS modes.

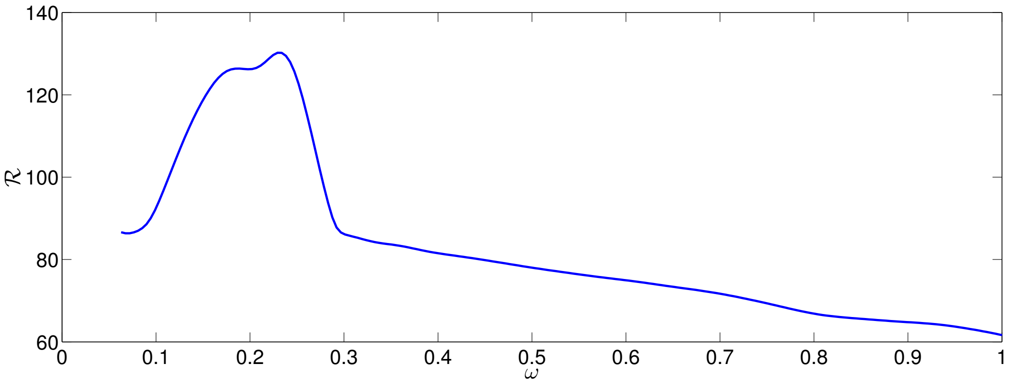

Figure VII.9: Resolvent curve extracted from pseudospectrum in VII.8 for a harmonic perturbation $\sigma = 0$.

VII.3.2 Non-modal stability

The receptivity analysis shows how the MVGs operate just on the TS stabilization without introducing further unsteadiness linked to the shear behind the roughness. Nevertheless, the resolvent modes basis is not representative of the dynamics of the flow in a finite time as it is based on the initial guess for which, when $t \to \infty$, only the particular solution of the forced system exists. It is then important to prove that for short time an initial solution is not highly amplified up to triggering non-linear effects that could make the linear stability non predictive. To verify the short time behaviour the linear optimal perturbation analysis has been performed. Taking advantage of the implemented Krylov-Schur decomposition, the SVD-Arnoldi decomposition is used to find optimal and sub-optimal perturbations. The used Krylov space was equal to 25 and the iterative procedure is stopped when the first 4 SVD modes are converged. The SVD is performed for different target times from 0 to 180. The energy gain associated to each optimization time T_{opt} is reported in figure VII.10. The gain curve reveals a maximum energy amplification equal to 1.4×10^4 at target time 27 with an antisymmetric initial condition. However, the optimal perturbation symmetry changes with the time optimization. The evolution of the optimal perturbation is constrained by the base flow topology. Close to the MVGs there are two separated high speed streaks (VII.5). The latter merge together at $x \approx 50$. For a short optimization time the optimal perturbation is symmetrically distributed and is confined on the small separation zone behind the MVGs (fig. VII.11(a)). For $7.5 < T_{opt} < 40$ the optimal perturbation is antisymmetric (VII.11(b)) and at the target time the perturbation are two wave packets localized in between the two high and low speed streaks (VII.12(b)). Increasing T_{opt} the wave packets move downstream up to the merger of the two high speed streaks (fig. VII.5). At this point, for $T_{opt} > 40$, the optimal perturbation becomes symmetric (VII.12(c)). With just one high speed streak the previous antisymmetric perturbation seems to be “rephased”. For this reason after $T_{opt} = 50$ there is not converged antisymmetric suboptimal. A further slightly peak at $T_{opt} = 125$ can be noticed in the gain curve VII.10. This can be associated with the interaction of the evolving wave packet with the periodic boundary condition as shown in figure VII.12(d). At $T_{opt} = 125$ the optimal perturbation at the target time looks like

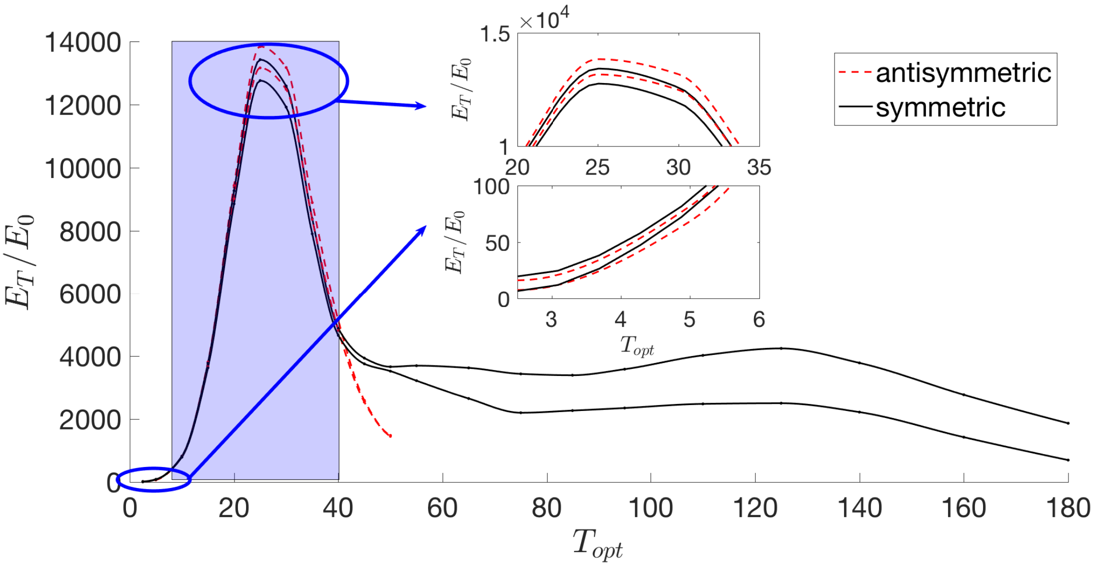

Figure VII.10: Energy gain curve for L1 case (Shahinfar et al., 2014). Dashed red line refers to antisymmetric perturbation, continuous black line to symmetric perturbation. Blue region highlight region where antisymmetric perturbation is optimal.

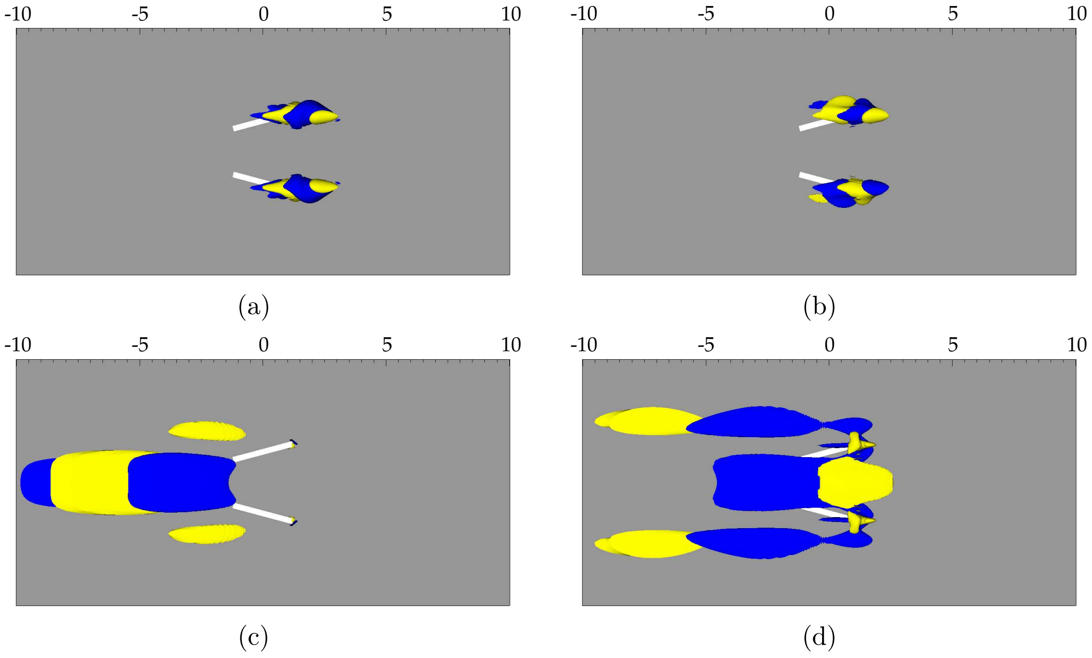

(a) (b) (c) (d)

Figure VII.11: Optimal initial perturbation for $T_{opt} = 5$(a), 27(b), 57(c) and 125(d). In all cases ±5% of maximum streamwise velocity.

the streaky-TS observed in the eigenvectors VII.7(a). After $T_{opt} > 125$ the energy gain decreases (fig. VII.10) since the wave packet is convected outside the numerical domain.

If the transient behaviour is driven by non-orthogonal eigenfunctions, it could seem strange that no antiymmetric converged eigenfunctions are present in the global spectrum

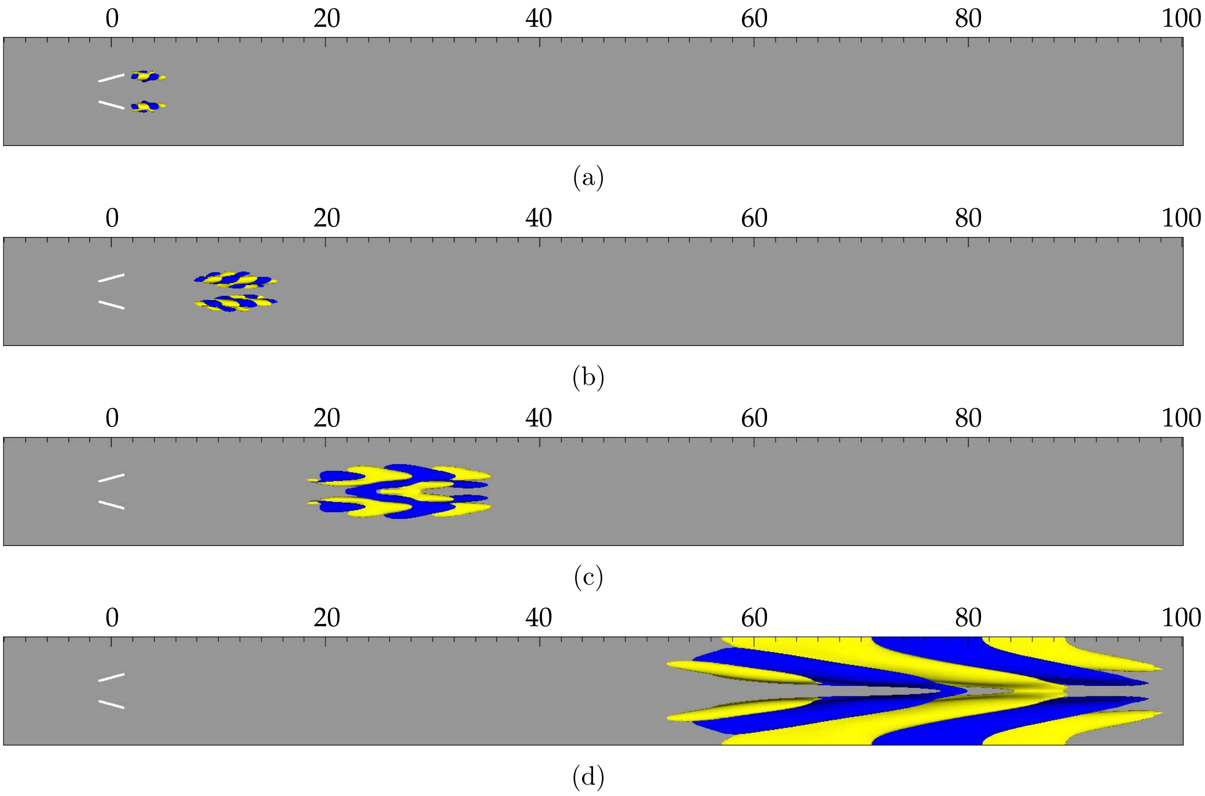

(a) (b) (c) (d)

Figure VII.12: Optimal perturbation at $T_{opt} = 5$(a), 27(b), 57(c) and 125(d). In all cases ±10% of maximum streamwise velocity.

in figure VII.6. Moreover, the SVD decomposition does not find a main singular value mode with an amplitude level much larger then the suboptimal one. On the contrary, up to $T_{opt} = 50$, three suboptimal perturbations have an amplitude level pretty close to the optimal one. Referring to Cossu and Chomaz (1997) work, the transient behaviour is linked to the presence of a locally unstable flow. Moreover, they claim that the energy gain quantifies exactly the energy growth of the locally unstable convective modes. For this reason a further analysis on the local stability is mandatory. In figure VII.13 the local eigenspectrum for a base flow extracted at $x = 10$ is shown. In figure VII.13, the α value is also varied from 0.1 to 3. In the example just shown, four unstable convective modes are present in agreement with Siconolfi et al. (2015b). The four eigenfunctions and their unstable region are reported in figure VII.14. Both symmetric and antisymmetric eigenfunctions are present. Hence, the local stability analysis justifies the presence of four main singular values together with their observed symmetries.

VII.3.3 Out-of-design control

The streaks control to delay transition works well if the amplitude of the external perturbation is low enough to not triggering a non-linear energy growth. This is true for instance on plane wings where the free stream turbulence level is lower than 1% of the free stream velocity. Far from the design setup (L1 case in Shahinfar et al. (2014)) the roughness element can trigger supercritical or subcritical bifurcations which accelerate

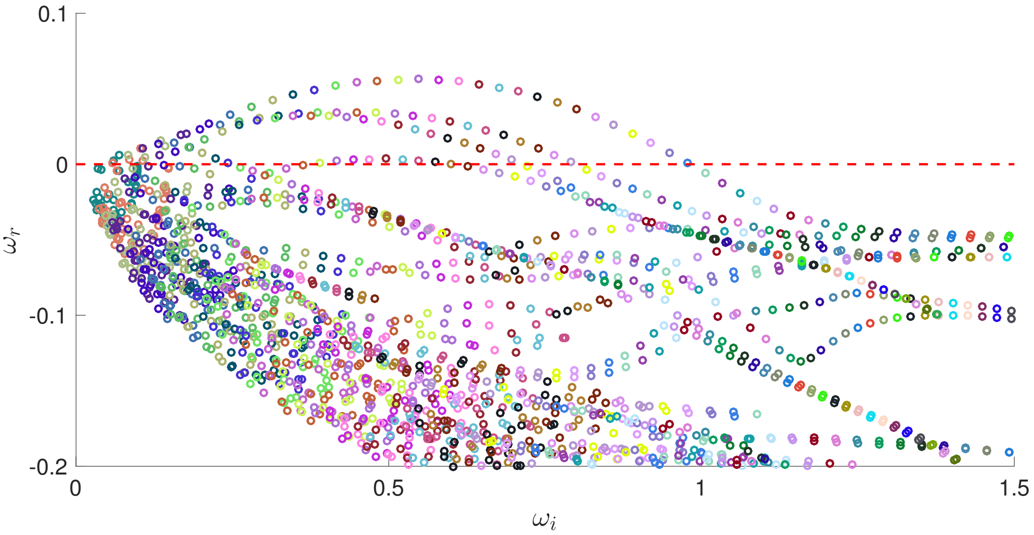

Figure VII.13: Local eigenspectrum for a baseflow extracted at $x = 10$. Different colours correspond to different streamwise wavenumber α. α is varied from 0.1 to 3 with a step equal to 0.05.

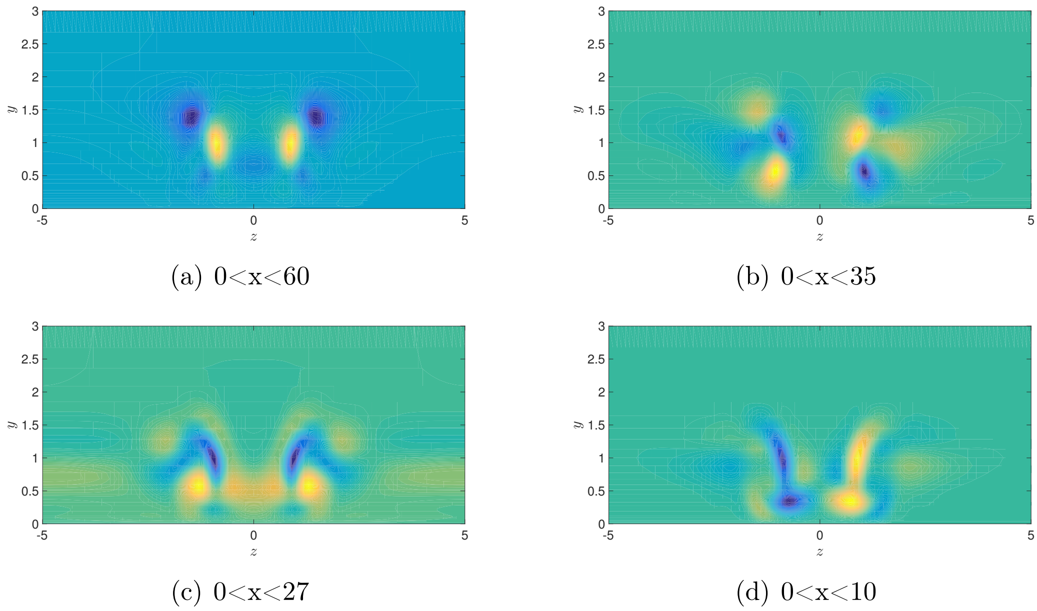

(a) 0<x<60

(b) 0<x<35

(c) 0<x<27

(d) 0<x<10

Figure VII.14: Real part of the four locally unstable eigenfunctions and its unstable region.

transition. To estimate the flow behaviour when the flow parameters change it is possible to refer to the Von Doenhoff-Braslow diagram IV.3. In such diagram the appearance of unsteadiness is strictly linked to the aspect ratio of the roughness d/h (d being the size of the roughness in the crossflow direction) and the roughness Reynolds number based on the Blasius velocity on the roughness head. In the Von Doenhoff-Braslow diagram IV.3 three zones exist. The first one is the lower one where the flow is laminar despite the presence of the roughness. The second one is the grey region in figure IV.3 and it identifies the flow conditions in which unsteadiness can be triggered. The last one is the upper one and it indicates the flow parameters for which turbulent flow is observed behind the roughness. Paying attention to this diagram the values of θ, δ_1/h and Re are changed and the global stability is then evaluated.

VII.3.3.1 θ effect

Let us assume as MVG's height the maximum height of the roughness h and as d the projection of the MVG's length L onto the crossflow plane. Starting from the experimental L1 case Shahinfar et al. (2014) the value of θ is changed. Increasing θ the considered flow case moves at iso-Re_h in figure VII.15. The four studied cases are listed in table VII.3. For $\theta = 60°$ the flow case enters the transitional zone and two isolated global modes appear in the eigenspectrum VII.16. The isolated global modes have a comparable pulsation and growth rate but different symmetry. The two eigenvectors are depicted in figure VII.17. The two global eigenvectors act on the flow field close to the roughness. Their appearance is linked to the recirculation bubble size. Increasing the MVG's impact angle θ the separation zone as well as the extension of the shear flow increase. Thus, global eigenmodes are recovered as for the cylindrical roughness case. Increasing the angle a new stagnation zone appears in front of the roughness. It has to be said that the $\theta = 60°$ case

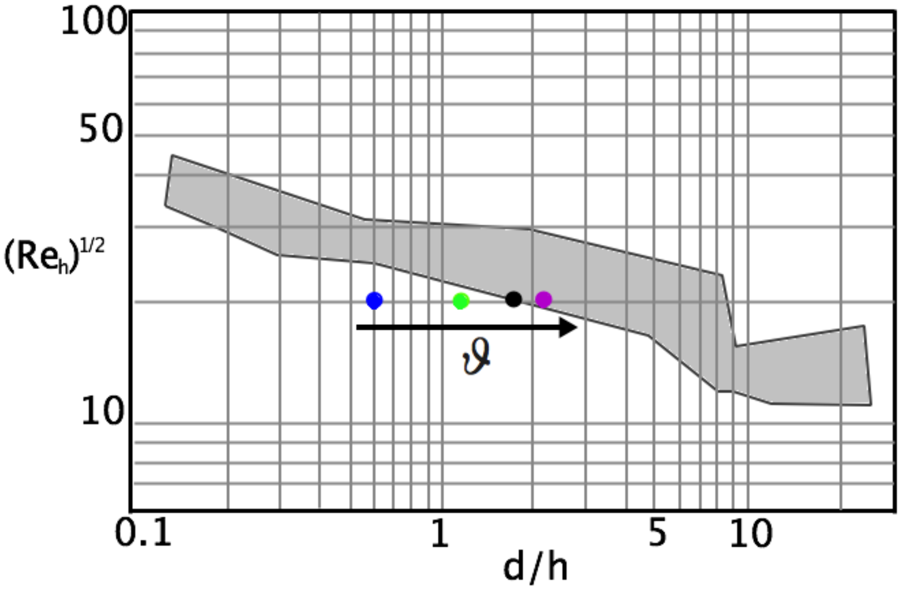

Figure VII.15: Von Doenhoff-Braslow diagram increasing θ. Blue marker refers to experimental L1 case (Shahinfar et al., 2014). θ values 15°, 30°, 45° and 60°

θ	**15°**	**30°**	**45°**	**60°**
d/h	0.64	1.25	1.77	2.2
$\sqrt{Re_h}$	20.5	20.5	20.5	20.5

Table VII.3: Studied cases for θ effect.

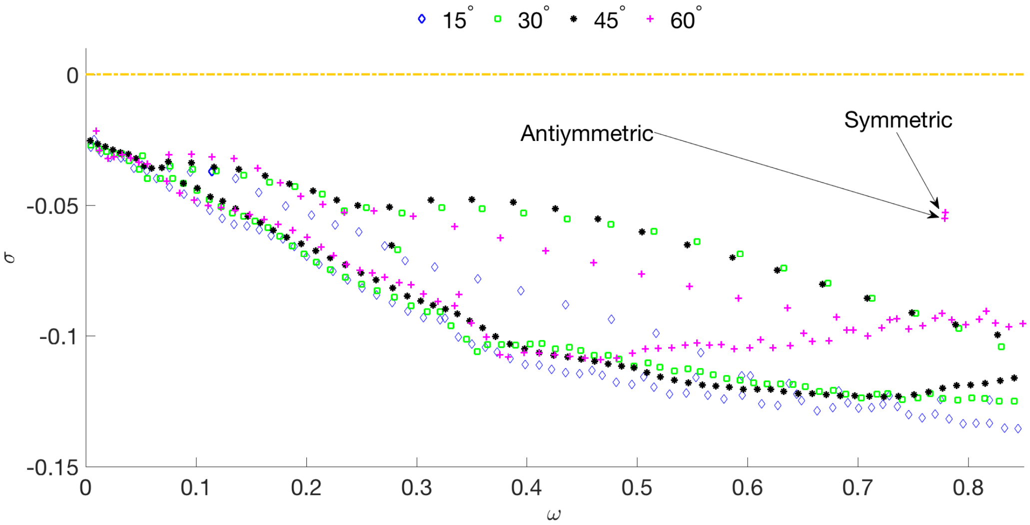

Figure VII.16: Global eigenspectrum increasing θ.

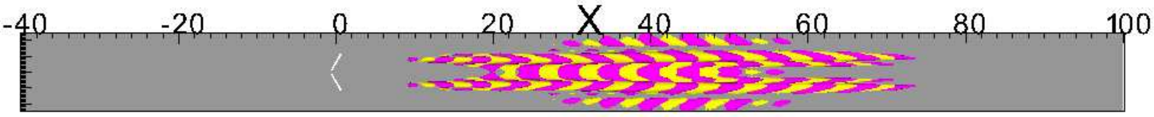

(a)

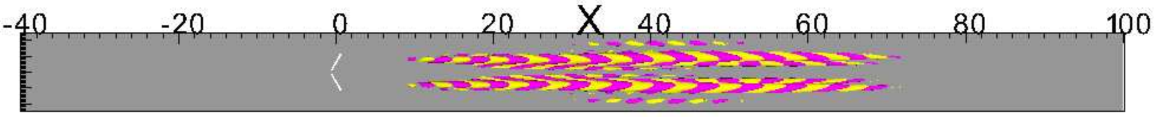

(b)

Figure VII.17: ±10% of real part of streamwise velocity perturbation for symmetric (a) and antisymmetric (b) global mode at $\theta = 60°$.

is just a numerical experiment that will never be used for control purposes. Nevertheless, it is a powerful example to emphasise the link between the separation zone size and the global character of the eigenmodes.

VII.3.3.2 *Re* effect

Now, we maintain the geometry unchanged, keeping constant $\theta = 15°$, and we change the Reynold number to observe unsteadiness in the direct numerical simulation. The flow case moves at iso-aspect ratio in the Von Doenhoff-Braslow diagram VII.19. The flow cases studied to evaluate the Re effect are summarized in table VII.4. At $Re = 1500$ the flow case moves into the unsteady region and also the DNS shows unsteady behaviour. The streaks start to oscillate in a varicose fashion far from the MVGs as illustrated in figure VII.21. The velocity signal measured by a probe placed at $(x, y, z) = (60, 1, 3)$

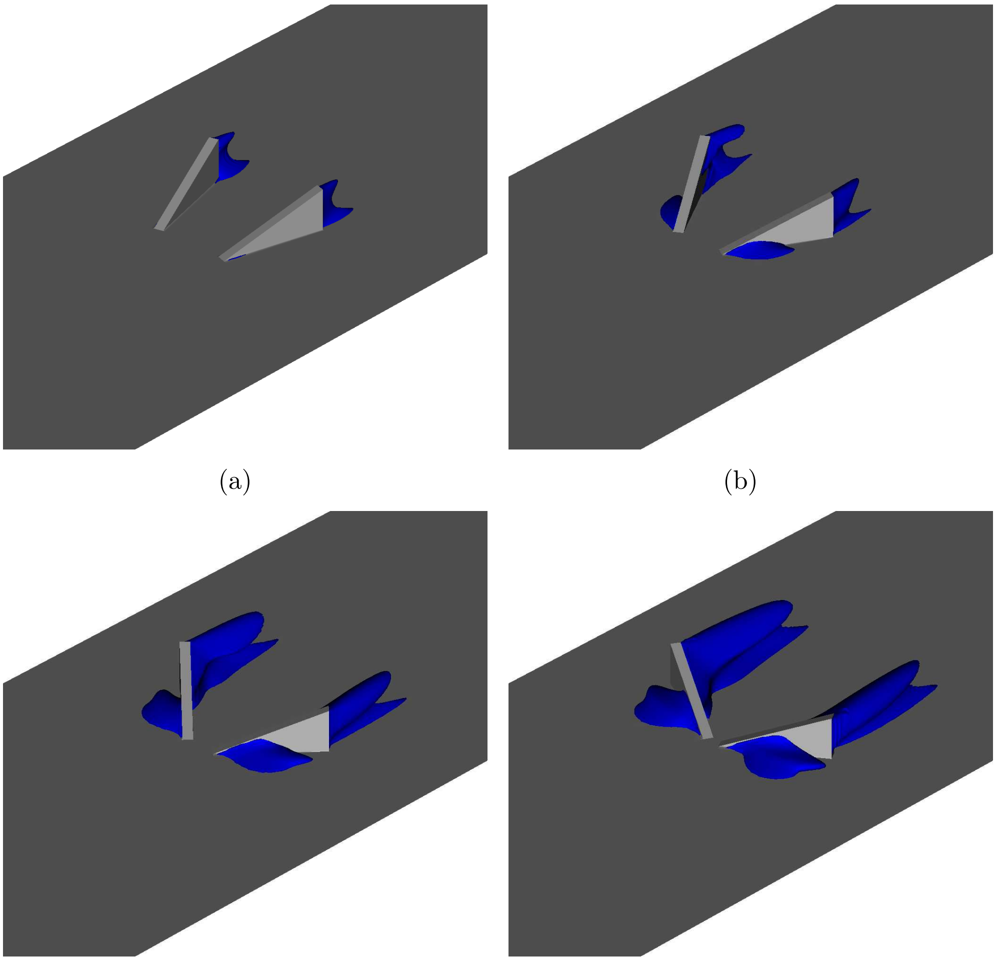

(a) (b)

(c) (d)

Figure VII.18: Separation zone for $\theta = 15°$(a), $30°$(b), $45°$(c) and $60°$(d).

Re	**657**	**1000**	**1350**	**1500**
d/h	0.64	0.64	0.64	0.64
$\sqrt{Re_h}$	20.5	25.3	29.2	30.9

Table VII.4: Studied cases for Re effect.

shows how the modal behaviour is characterized by just one pulsation at $\omega = 0.763$. The SFD has been used to recover steady solution and evaluate the global stability analysis. The superposition of the eigenspectrum at different Reynolds numbers shows (fig. VII.22) how increasing Re a collection of global modes become unsteady. In agreement with the DNS, the unsteady modes are around $\omega = 0.8$. Concerning the numerical dependence of the obtained eigenspectrum, further investigations are necessary. The unstable modes resemble convective modes pushed downstreams toward the outflow boundary condition (see figure VII.23). The presence of a collection of unstable global modes instead of just one isolated global mode could be due to a short numerical domain. As experienced by Loiseau in its Ph.D thesis (Loiseau, 2014), if the numerical domain is not longer

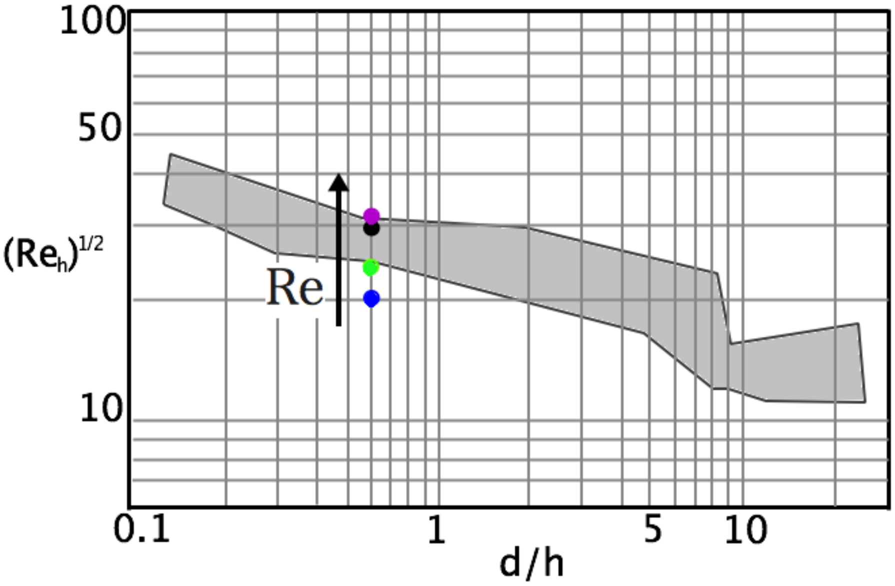

Figure VII.19: Von Doenhoff-Braslow diagram increasing Re. Blue marker refers to experimental L1 case (Shahinfar et al., 2014). Re values 659, 1000, 1350 and 1500.

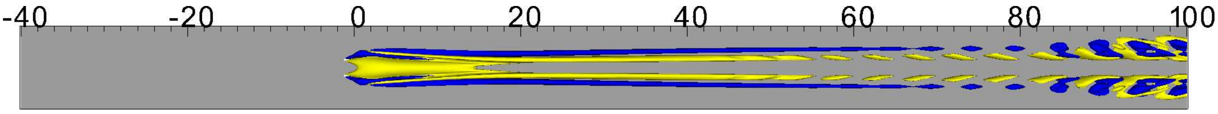

Figure VII.20: Positive and negative wall normal velocity for unsteady DNS at $Re = 1500$.

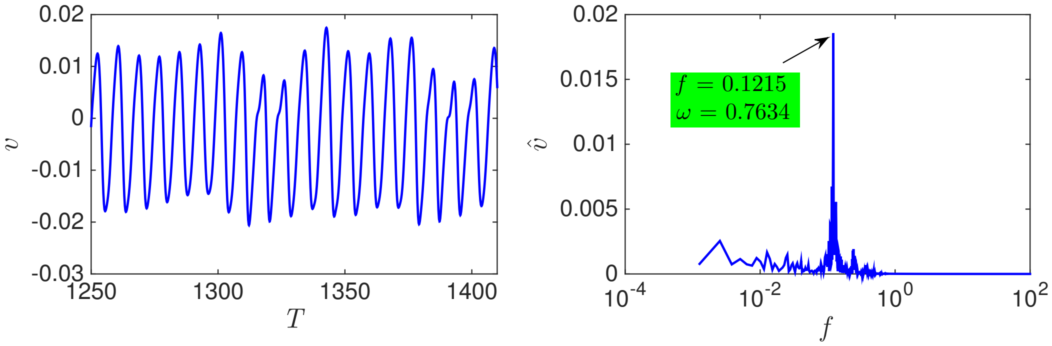

Figure VII.21: Time signal and its Fourier transform at $Re = 1500$.

enough to embed the whole eigenvector, the eigenspectrum shows a collection of unstable eigenmodes aligned with the pseudospectrum curves (Lesshafft, 2017) instead of just one isolated global mode recovered with a longer domain. In the present case also increasing the numerical domain up to $x = 180$, the isolated global mode is not achieved. Increasing the Reynolds number the viscosity effects are reduced and if the instability is provided by an inflectional velocity profile the global mode may need a huge numerical domain to be properly discretized. However, despite the numerical weakness of the achieved result, the critical Reynolds number could slightly change if the wavemaker is not embedded in the

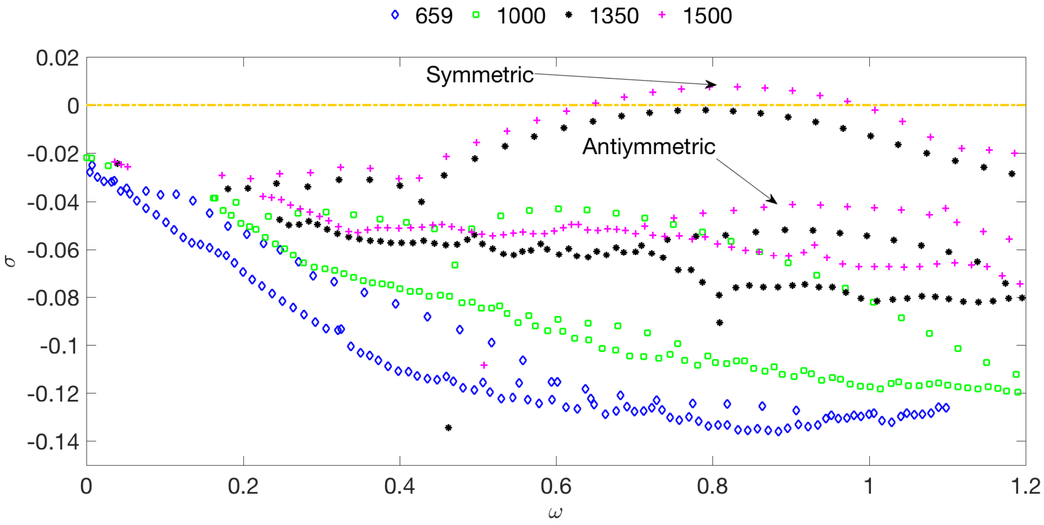

Figure VII.22: Global eigenspectrum increasing Re.

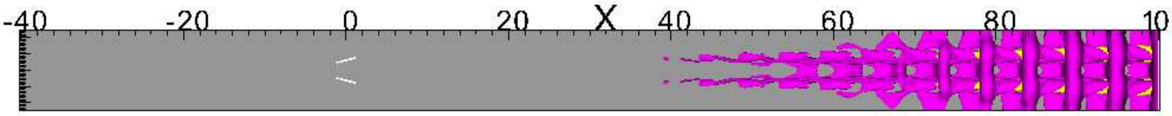

Figure VII.23: ±10% of streamwise velocity of unstable eigenvector at $\omega = 0.8$ for $Re = 1500$.

numerical domain but the supercritical nature of the bifurcation does not change. Finally, increasing Re leads to the arise of steady antisymmetric modes.

VII.3.3.3 h/δ_1 effect

To conclude the parametric analysis also the effect of the shear ratio h/δ_1 has been investigated. Increasing h/δ_1 the dimension of the roughness related to the boundary layer thickness increases. A sketch is reported in figure VII.24. The shear growth is achieved moving the MVGs toward the leading edge. Increasing h/δ_1 the streamwise velocity on

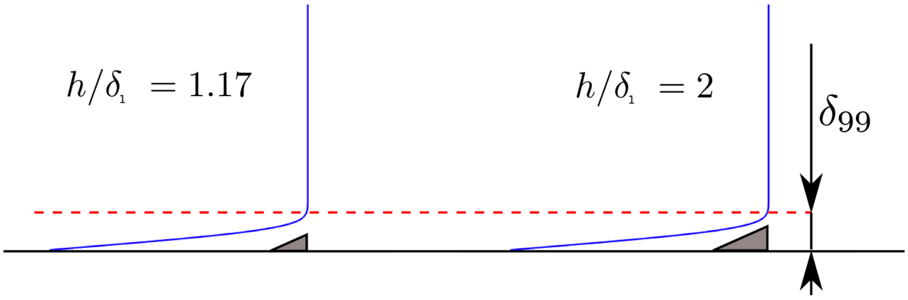

Figure VII.24: Sketch of the MVG dimension related to boundary layer thickness δ_{99}.

the roughness head increases. The flow case in the Von Doenhoff-Braslow diagram VII.19 moves at iso-shear ratio towards the transitional region. The four studied cases are listed in table VII.5. Even if the flow case enters in the transitional region, no unstable eigenmodes are observed in figure VII.27 for $h/\delta_1 = 2.3$. Also in this case symmetric and antisymmetric eigenmodes are present in the eigenspectrum. The shear value does not affect drastically the asymptotic behaviour but observing the initial optimal perturbation in figure VII.11 the MVG head is the most sensible zone. The optimal perturbation for the case with $h/\delta_1 = 2$ shows a dangerous energy transient growth. The gain curve at $h/\delta_1 = 1.17$ moves to higher gain level up to $E_t/E_0 \sim 10^7$. This last result reduces the applicability of the MVGs devices to control transition.

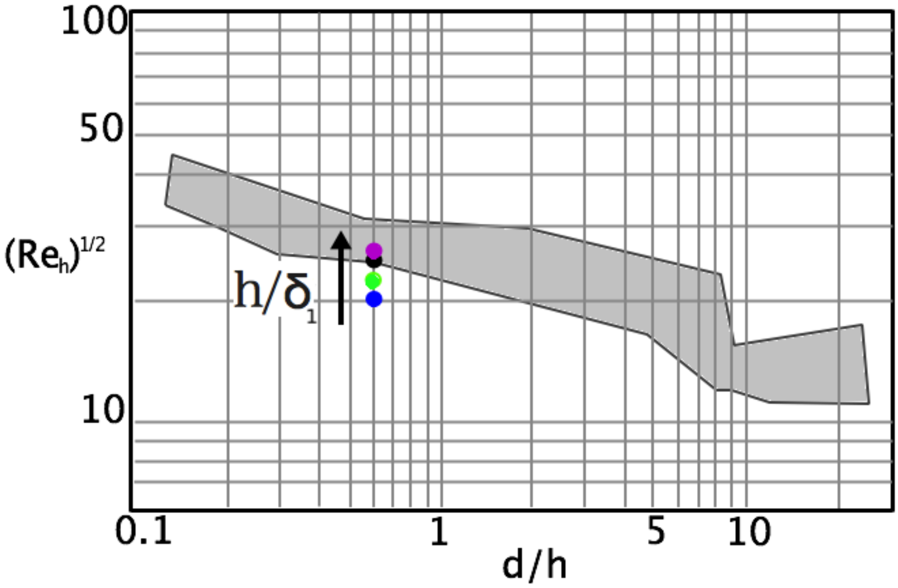

Figure VII.25: Von Doenhoff-Braslow diagram increasing h/δ_1. Blue marker refers to experimental L1 case (Shahinfar et al., 2014). h/δ_1 values 1.17, 1.5, 2 and 2.3.

h/δ_1	**1.17**	**1.5**	**2**	**2.3**
d/h	0.64	0.64	0.64	0.64
$\sqrt{Re_h}$	20.5	22.5	24.4	25

Table VII.5: Studied cases for h/δ_1 effect.

VII.4 Overall discussion about MVGs roughness

The global spectrum and pseudospectrum confirm the experimental results about MVGs. When they are used in the design set-up, the flow is globally stable and it is receptive to the streaky-TS mode. Unfortunately, if the asymptotic features promote the use of the MVGs, the short time behaviour is affected by the non-normalities of the system.

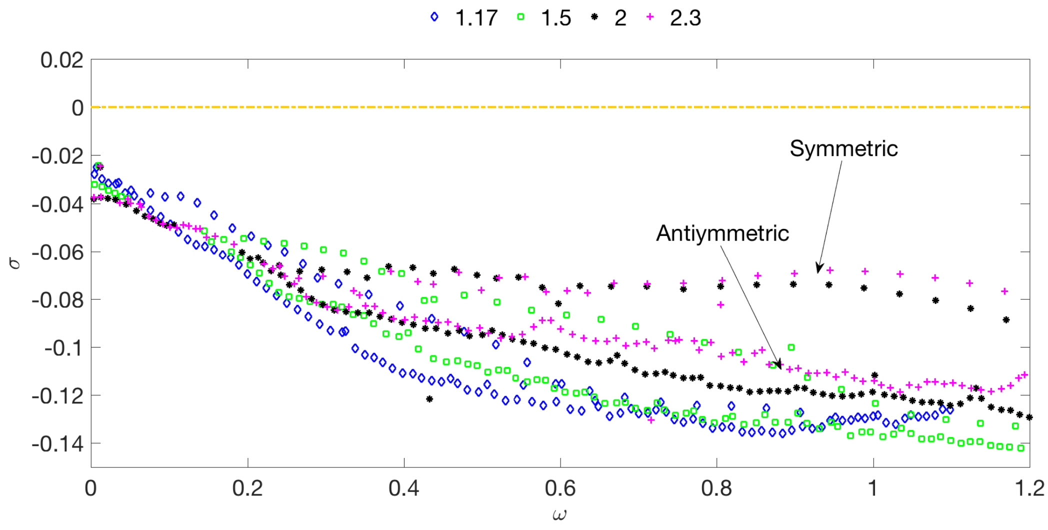

Figure VII.26: Global eigenspectrum increasing h/δ_1.

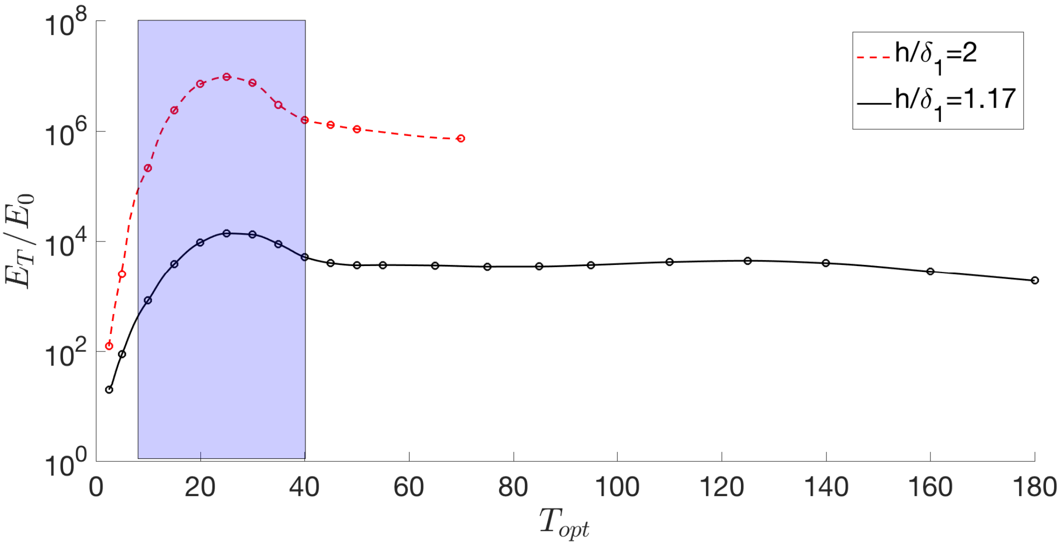

Figure VII.27: Transient energy growth comparison between $h/\delta_1 = 1.17$ (black continuous line) and $\delta_1 = 2$ (red dashed line). Blue region highlight T_{opt} range for which the optimal perturbation is antisymmetric.

The presence of the MVGs induces the presence of unstable convective local modes that allow transient energy growth. Depending on the target time, the optimal perturbation exhibits symmetric and antisymmetric optimal perturbations coherent with the presence of symmetric and antisymmetric local unstable modes. Increasing the impact angle θ or the Reynolds number Re it is possible to achieve supercritical bifurcation. The size of the separation zone is representative of the global features of the eigenvector. The experiments performed with low external perturbation are not representative of the non-normality introduced by the MVG roughness. The non-normality drastically increases as the MVG head approaches the height of the boundary layer thickness. Further analysis are necessary to quantify the amplitude of the external perturbation necessary to trigger non-modal unsteadiness.

Chapter VIII

Overall conclusion

VIII.1 Conclusion

In this thesis the flow over roughness elements has been studied. The recent studies on the use of wall roughness to delay transition justify the strong interest in the understanding of the operational limitations of this passive control. Roughness elements are able to generate counter-rotating vortices which trigger the lift-up effect. The induced high and low speed streaks modulate the boundary layer inducing a stabilizing energy production term that works in the spanwise direction against the destabilizing wall-normal one. If in the field far from the roughness a pattern of high and low speed streaks is recovered, close to the used roughness element the induced shear can introduce dangerous unsteadiness. The latter are propagated downstream inducing secondary instability of the streaks. The nature of the induced unsteadiness has been studied in detail in this thesis.

The flow field around a cylindrical roughness has been studied by means of:

1. comparison between DNS and experiments,
2. local stability analysis,
3. global stability analysis,
4. receptivity analysis,
5. perturbed DNS.

The possibility of a supercritical bifurcation induced by a global unsteady mode has been amply demonstrated for different roughness shapes. However, it was not clear how a globally stable case might induce unsteadiness in an experiment. Despite the stability of the global spectrum, the distribution of the eigenvalues in the complex plane provides many information. Such information are extracted by the evaluation of the pseudospectrum and the resolvent curve. These two tools show how the receptivity of a stable eigenvalue can so high that it can be easily triggered by an external perturbation with a really low amplitude. By using the optimal forcing procedure it was revealed how the spatial distribution of the forcing associated to the receptive mode looks like the spatial distribution of the adjoint mode associated to the same forcing pulsation. This is possible because the global mode has a spatial support that is close to the roughness, whereas the other modes are convective and then pushed towards the outflow boundary. The eigenvectors being orthogonal to each other, they do not interact when forced. Different symmetries also cause orthogonality between eigenvectors. When just the isolated sinuous global mode is present in the eigenspectrum, the perturbed DNS exhibits varicose response due to receptivity of varicose convective modes. This is in disagreement with the resolvent curve that reveals a high receptivity of the sinuous mode. This is possible because the non-interaction between sinuous and varicose modes makes improbable the emergence of a sinuous response when most of the frequencies are linked to a varicose feature of the associated optimal response.

When the global mode is triggered (by receptivity mechanisms or by supercritical bifurcation) the induced unsteadiness are very much shaped by the global mode. A dynamical mode decomposition (DMD) reveals how the shape of the leading DMD mode is similar to the global mode. Concerning the fluid structures observed in the unsteady behaviour, the global eigenvector appears to be involved in the hairpin vortices generation. Behind the cylinder, the hairpin eddies are generated by a non-linear interaction of linear ingredients and then sustained by the base flow topology. Once the first bifurcation is triggered, a second bifurcation arises giving rise to transition to turbulence. The topology of the base flow and more precisely the evolution of the streaks in streamwise direction, shows an increasing inflectional profile in the spanwise direction moving downstream. This allows the perturbation placed onto the low speed streaks to spread in the spanwise direction promoting the generation of new streamwise vortices also observed experimentally.

Spanning different Reynolds numbers and different values of the shear ratio, both sinuous and varicose global modes have been found. Increasing the Reynolds number the varicose mode is stabilized and the sinuous one is promoted. On the contrary, reducing the difference between the cylinder height and the boundary layer thickness both varicose and sinuous global modes are destabilized up to bring the varicose mode in the unstable region of eigenspectrum. With the same aspect ratio of the cylindrical roughness both sinuous and varicose supercritical bifurcations can be experienced. The first one is achieved with high value of δ_1/h and high value of Re. The second one can be observed with low δ_1/h value and low Re.

By replacing the cylindrical roughness with the miniaturized vortex generators the scenario completely changes. The miniaturized vortex generation shape induces a small separation zone that does not allow the presence of an isolated global mode. The pseudospectrum shows the high receptivity of the streaky-TS mode but no global modes linked to the shear induced by the geometrical disturbance are noticed. If the asymptotic behaviour is not affected by the MVG, the short-time dynamics reveals a high non-normality of the system. Different symmetries are recovered as optimal initial condition varying the optimization target time. The highest transient energy gain is linked to antisymmetric perturbation that at $t = 0$ is located on the MVG head and at $t = T_{opt}$ is located on the two separated high and low speed streaks. For a long optimization time the optimal perturbation is symmetric and the streaky-TS shape observed in the eigenfunctions is recovered. The presence of antisymmetric optimal and sub-optimal modes is due to the presence of antisymmetric convective unstable modes behind the MVGs. Increasing the angle between the MVG roughness and the streamwise direction, the separation zone increases and the appearance of isolated global modes is observed in the eigenspectrum. A supercritical bifurcation can be also obtained increasing the Re number. On the contrary increasing the ratio h/δ_1, thus reducing the difference between the boundary layer thickness and the MVG height the global stability does not exhibit significant variations but the optimal perturbation shows a drastic increase of the energy growth up to 10^7 times the initial energy. Low amplitude of the external perturbation can make the MVGs unusable to delay transition.

VIII.2 Perspectives

This thesis sheds light on the limits of the use of roughness elements to delay transition and contributes to give a mathematical and physical explanation to the transitional zone in the Von Doenhoff-Braslow diagram.

The perspectives for the continuation of this work arise from several discussion between the authors and the supervisors and more over from the innumerable DNS performed without a clear mathematical and physical explanation.

1. The work carried out in this thesis is a continuation of a part of the Jean-Christophe Loiseau's thesis. At the end of his thesis, he suggested to investigate onto the energy transient growth in presence of the cylindrical roughness. Unfortunately this was not possible in this work for lack of time. By the optimally forced DNS we know that a **transient energy growth** exists and maybe the role of the transient growth is important to select the perturbation symmetries when the flow over the roughness is randomly perturbed. For example, in the case of a globally unstable sinuous eigenmode initialized with a random flow field, a varicose perturbation is rapidly generated and only when the latter is out from the numerical domain the sinuous unsteadiness is experienced. Without a transient growth analysis we do not have any measure of the involved non-normalities in the transient behaviour.

2. As claimed in §V the transition behind the cylindrical roughness does not arise directly by the unsteady global mode. The unsteady global mode triggers a secondary perturbation that goes towards transition. For a case that shows an unstable sinuous global mode with a growth rate slightly above the stability threshold the DNS reveals a sinuous modulation of the low speed streak in the middle but no transition is observed. It would be interesting to show, by a **floquet analysis**, how the eigenmode associated to the secondary bifurcation extracts energy from the periodic base flow.

3. To complete the analysis of the flow over cylindrical roughness the spatial correlation of the stochastically perturbed case presented in section §VI needs to be computed by the numerical solution of a **Lyapunov equation** in order to check the possible presence of the sinuous mode. Further DNS with different turbulent design need to be carried out in order to check the sensitivity of the system to different integral scales of the turbulence. It would be interesting to check if the penetrability of the pure OS and pure Squire modes change if the boundary layer is modified by streaky structures.

4. Concerning the flow over MVG roughness elements, the study of the experimental case provides an exhaustive explanation on the limits of MVGs use as passive control to delay transition. If the steady asymptotic dynamics is preserved, the short time dynamics can induce dangerous transient energy growth. **Further DNS** need to be performed to shed light on the amplitude value that the optimal perturbation need to satisfy to trigger non-normalities.

5. An **optimal forcing** on a numerical domain extended on x-direction 1000 times the height of the roughness also need to be performed. If in the boundary layer the optimal forcing is located onto the lower branch of the neutral curve and the optimal response onto the upper branch, what happens when two unsteady zones exist in the numerical domain? In the MVG case the first neutral curve is located close the roughness and the second one is related to the streaky-TS wave. It is not clear if the optimal forcing takes place just onto the lower branch of the first unsteady zone or it should show a structure with two spatial supports, one for each lower branch.

6. The parametric analysis shows how asymptotic and short time dynamics can be highly modified varying Reynolds number, MVG angle and shear. In all cases the Von Doenhoff-Braslow is predictive of the unsteady dynamics. The Von Doenhoff-Braslow diagram is based just on the aspect ratio and on the roughness Reynolds Re_h. Is this enough to be predictive on the appearance of the unsteadiness? One can think to change simultaneously the shear ratio (and then the velocity on the roughness head) and the viscosity in order to keep constant Re_h. We tried to perform this numerical experiment and the answer to the previous question is negative. In figure VIII.1 there is one of the results achieved keeping the Re_h and d/h values equal to the experimental case. The case in figure VIII.1 is unsteady with a non-symmetric perturbation. The hairpin vortices are strong behind one streak and weak behind the other. A sort of intermittent behaviour is also observed. The strong hairpin generation moves between the two streaks. No stability analysis has been done yet but different scenarios are possible. In particular, this behaviour might be due to: 1) a superposition of symmetric and antisymmetric convective modes; 2) an energy transient growth of the first two singular modes; 3) a secondary instability of the wake behind two roughness elements like the Flip-Flop instability. At the end of this Ph.D the answer has not been found yet. In any case, a third axis that takes into account the parameter δ_1/h needs to be considered in an equivalent of the Von Doenhoff-Braslow diagram.

Roughness topic must be followed up to give an answer to all this question.

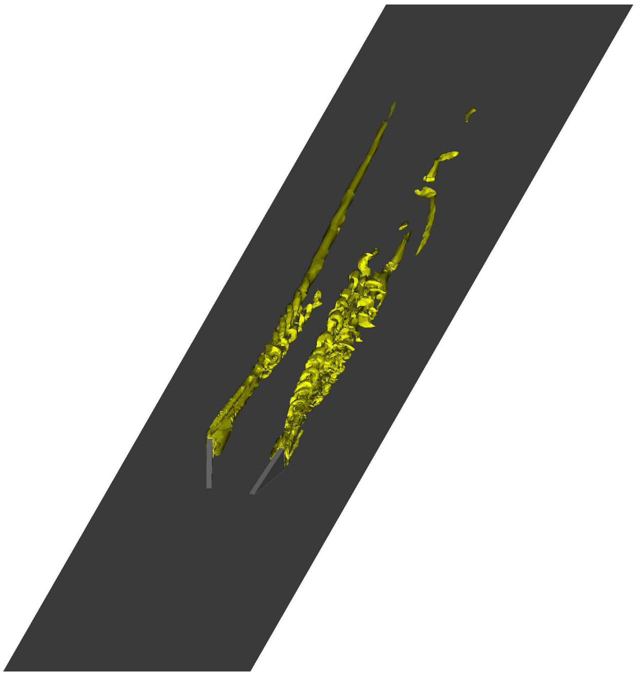

Figure VIII.1: Unsteady case despite $(Re_h)^{0.5} = 20.5$ and $d/h = 0.63$ as in the experiments.

Appendices

.1 Continuous adjoint equations

The *augmented functional* is defined as

$$
\begin{aligned}
\mathcal{L}\left(u_i, p, u_i^\dagger, p^\dagger, \lambda\right) = E(T)+ \\
-\int_0^T \int_V u_i^\dagger \left(\frac{\partial u_i}{\partial t} + \frac{\partial (u_i U_j)}{\partial x_j} + \frac{\partial (U_i u_j)}{\partial x_j} + \frac{\partial p}{\partial x_i} - \frac{1}{Re}\frac{\partial^2 u_i}{\partial x_j^2} + \frac{\partial (u_i u_j)}{\partial x_j} \right) dV dt + \\
-\int_0^T \int_V p^\dagger \frac{\partial u_i}{\partial x_i} dV dt - \lambda \left(E_0 - E(0)\right)
\end{aligned}
\tag{1}
$$

where

$$
E(T) = \frac{1}{2}\int_V u_i(T) u_i(T) dV; \qquad E(0) = \frac{1}{2}\int_V u_i(0) u_i(0) dV
$$

Seeking for the extrema of $\mathcal{L}$, one has to impose that its derivatives with respect to every independent variable are equal to zero, giving the equations that close the optimization problem

$$
\frac{\partial \mathcal{L}}{\partial \lambda} = 0 \Longrightarrow E_0 - E(0) = 0 \Longrightarrow E_0 = E(0) \tag{2}
$$

$$
\frac{\partial \mathcal{L}}{\partial u_k^\dagger} = 0 \Longrightarrow \frac{\partial u_k}{\partial t} + \frac{\partial (u_k U_j)}{\partial x_j} + \frac{\partial (U_k u_j)}{\partial x_j} + \frac{\partial p}{\partial x_k} - \frac{1}{Re}\frac{\partial^2 u_k}{\partial x_j^2} + \frac{\partial (u_k u_j)}{\partial x_j} = 0 \tag{3}
$$

$$
\frac{\partial \mathcal{L}}{\partial p^\dagger} = 0 \Longrightarrow \frac{\partial u_i}{\partial x_i} = 0 \tag{4}
$$

$$
\frac{\partial \mathcal{L}}{\partial p} = 0 \Longrightarrow \frac{\partial u_i^\dagger}{\partial x_i} = 0 \tag{5}
$$

$$
\frac{\partial \mathcal{L}}{\partial u_k} = 0 \Longrightarrow \frac{\partial u_k^\dagger}{\partial t} + \frac{\partial (u_k^\dagger U_j)}{\partial x_j} - u_i^\dagger \frac{\partial U_i}{\partial x_k} + \frac{\partial p^\dagger}{\partial x_k} + \frac{1}{Re}\frac{\partial^2 u_k^\dagger}{\partial x_j^2} + \frac{\partial (u_k^\dagger u_j)}{\partial x_j} - u_i^\dagger \frac{\partial u_i}{\partial x_k} = 0 \tag{6}
$$

$$
\frac{\partial \mathcal{L}}{\partial u_k(T)} = 0 \Longrightarrow u_k(T) - u_k^\dagger(T) = 0 \tag{7}
$$

$$
\frac{\partial \mathcal{L}}{\partial u_k(0)} = 0 \Longrightarrow u_k^\dagger(0) - \lambda u_k(0) = 0 \tag{8}
$$

Here follows the demonstration of eq. (1)-(8).

Demonstration of eq. (2) is immediate.

For eq. (3)

$$\frac{\partial \mathcal{L}}{\partial u_k^\dagger} = 0 \Longrightarrow$$

$$\Longrightarrow -\frac{\partial}{\partial u_k^\dagger}\int_0^T \int_V u_i^\dagger \left(\frac{\partial u_i}{\partial t} + \frac{\partial (u_i U_j)}{\partial x_j} + \frac{\partial (U_i u_j)}{\partial x_j} + \frac{\partial p}{\partial x_i} - \frac{1}{Re}\frac{\partial^2 u_i}{\partial x_j^2} + \frac{\partial (u_i u_j)}{\partial x_j}\right) dVdt = 0$$

$$\int_0^T \int_V \frac{\partial u_i^\dagger}{\partial u_k^\dagger} \left(\frac{\partial u_i}{\partial t} + \frac{\partial (u_i U_j)}{\partial x_j} + \frac{\partial (U_i u_j)}{\partial x_j} + \frac{\partial p}{\partial x_i} - \frac{1}{Re}\frac{\partial^2 u_i}{\partial x_j^2} + \frac{\partial (u_i u_j)}{\partial x_j}\right) dVdt = 0$$

$$\int_0^T \int_V \delta_{ik} \left(\frac{\partial u_i}{\partial t} + \frac{\partial (u_i U_j)}{\partial x_j} + \frac{\partial (U_i u_j)}{\partial x_j} + \frac{\partial p}{\partial x_i} - \frac{1}{Re}\frac{\partial^2 u_i}{\partial x_j^2} + \frac{\partial (u_i u_j)}{\partial x_j}\right) dVdt = 0$$

in fact it should be remembered that there is not dependence between *direct* variables and *adjoint* variables, that is $\frac{\partial q_i}{\partial q_k^\dagger} = 0$, and $\frac{\partial q_i^\dagger}{\partial q_k} = 0$, too. Bringing the *Knoneker delta* into the derivative operator and remembering its propriety that $q_i \delta_{ik} = q_k$, one has

$$\int_0^T \int_V \left(\frac{\partial (u_i \delta_{ik})}{\partial t} + \frac{\partial (u_i \delta_{ik} U_j)}{\partial x_j} + \frac{\partial (U_i \delta_{ik} u_j)}{\partial x_j} + \frac{\partial p}{\partial x_i}\delta_{ik} - \frac{1}{Re}\frac{\partial^2 (u_i \delta_{ik})}{\partial x_j^2} + \frac{\partial (u_i \delta_{ik} u_j)}{\partial x_j}\right) dVdt = 0$$

$$\int_0^T \int_V \left(\frac{\partial u_k}{\partial t} + \frac{\partial (u_k U_j)}{\partial x_j} + \frac{\partial (U_k u_j)}{\partial x_j} + \frac{\partial p}{\partial x_k} - \frac{1}{Re}\frac{\partial^2 u_k}{\partial x_j^2} + \frac{\partial (u_k u_j)}{\partial x_j}\right) dVdt = 0$$

Imposing that the last integral has to be null, it means that the integrand function has to be equal to zero in every point of the domain and for every moment of time. Finally, this brings to:

$$\frac{\partial u_k}{\partial t} + \frac{\partial (u_k U_j)}{\partial x_j} + \frac{\partial (U_k u_j)}{\partial x_j} + \frac{\partial p}{\partial x_k} - \frac{1}{Re}\frac{\partial^2 u_k}{\partial x_j^2} + \frac{\partial (u_k u_j)}{\partial x_j} = 0$$

For eq. (4), for the same reason as above

$$\frac{\partial \mathcal{L}}{\partial p^\dagger} = 0 \Longrightarrow -\int_0^T \int_V \frac{\partial u_i}{\partial x_i} dVdt = 0 \Longrightarrow \frac{\partial u_i}{\partial x_i} = 0$$

For eq. (5), it is necessary to do an integration by parts of the term $u_i^\dagger \frac{\partial p}{\partial x_i}$

$$\int_0^T \int_V u_i^\dagger \frac{\partial p}{\partial x_i} dVdt = \cancel{\int_0^T \left[u_i^\dagger p\right]_{\partial V}} dt - \int_0^T \int_V p \frac{\partial u_i^\dagger}{\partial x_i} dVdt = -\int_0^T \int_V p \frac{\partial u_i^\dagger}{\partial x_i} dVdt$$

where the first integral on the RHS is null because of the $u_i^\dagger = 0$ boundary condition used (*adjoint* perturbations equal to zero on the domain boundaries). In this way, eq. (1)

becomes

$$\begin{aligned}\mathcal{L} = E(T) - \int_0^T \int_V u_i^\dagger \left(\frac{\partial u_i}{\partial t} + \frac{\partial (u_i U_j)}{\partial x_j} + \frac{\partial (U_i u_j)}{\partial x_j} - \frac{1}{Re}\frac{\partial^2 u_i}{\partial x_j^2} + \frac{\partial (u_i u_j)}{\partial x_j} \right) dV dt + \\ + \int_0^T \int_V p \frac{\partial u_i^\dagger}{\partial x_i} dV dt - \int_0^T \int_V p^\dagger \frac{\partial u_i}{\partial x_i} dV dt - \lambda \left(E_0 - E(0) \right)\end{aligned}$$

which derivation provides

$$\frac{\partial \mathcal{L}}{\partial p} = 0 \Longrightarrow \int_0^T \int_V \frac{\partial u_i^\dagger}{\partial x_i} dV dt = 0 \Longrightarrow \frac{\partial u_i^\dagger}{\partial x_i} = 0$$

In order to obtain eq. 6, integration by parts of many terms of $\mathcal{L}$ is needed.

$$\begin{aligned}&\mathcal{L} = E(T) + \\ &- \int_0^T \int_V \left(\underbrace{u_i^\dagger \frac{\partial u_i}{\partial t}}_{1} + \underbrace{u_i^\dagger \frac{\partial (u_i U_j)}{\partial x_j}}_{2} + \underbrace{u_i^\dagger \frac{\partial (U_i u_j)}{\partial x_j}}_{3} + u_i^\dagger \frac{\partial p}{\partial x_i} - \underbrace{\frac{1}{Re} u_i^\dagger \frac{\partial^2 u_i}{\partial x_j^2}}_{4} + \underbrace{u_i^\dagger \frac{\partial (u_i u_j)}{\partial x_j}}_{5} \right) dV dt + \\ &- \int_0^T \int_V \underbrace{p^\dagger \frac{\partial u_i}{\partial x_i}}_{6} dV dt - \lambda \left(E_0 - E(0) \right)\end{aligned}$$

Integration by parts of terms 1, 2, 4, 6 and development of terms 3, 5 give

$$1 : \int_0^T \int_V u_i^\dagger \frac{\partial u_i}{\partial t} dV dt = \cancel{\int_0^T \left[u_i^\dagger u_i \right]_{\partial V} dt} - \int_0^T \int_V u_i \frac{\partial u_i^\dagger}{\partial t} dV dt = - \int_0^T \int_V u_i \frac{\partial u_i^\dagger}{\partial t} dV dt$$

$$2 : \int_0^T \int_V u_i^\dagger \frac{\partial (u_i U_j)}{\partial x_j} dV dt = \cancel{\int_0^T \left[u_i^\dagger u_i U_j \right]_{\partial V} dt} - \int_0^T \int_V u_i U_j \frac{\partial u_i^\dagger}{\partial x_j} dV dt = - \int_0^T \int_V u_i U_j \frac{\partial u_i^\dagger}{\partial x_j} dV dt$$

$$3 : \int_0^T \int_V u_i^\dagger \frac{\partial (U_i u_j)}{\partial x_j} dV dt = \int_0^T \int_V u_i^\dagger \left(u_j \frac{\partial U_i}{\partial x_j} + \cancel{U_i \frac{\partial u_j}{\partial x_j}} \right) dV dt = \int_0^T \int_V u_i^\dagger u_j \frac{\partial U_i}{\partial x_j} dV dt$$

$$\begin{aligned}4 : &\int_0^T \int_V \frac{1}{Re} u_i^\dagger \frac{\partial^2 u_i}{\partial x_j^2} dV dt = \cancel{\int_0^T \left[\frac{1}{Re} u_i^\dagger \frac{\partial u_i}{\partial x_j} \right]_{\partial V} dt} - \int_0^T \int_V \frac{1}{Re} \frac{\partial u_i^\dagger}{\partial x_j} \frac{\partial u_i}{\partial x_j} dV dt = \\ &= - \int_0^T \int_V \frac{1}{Re} \frac{\partial u_i^\dagger}{\partial x_j} \frac{\partial u_i}{\partial x_j} dV dt = - \cancel{\int_0^T \left[\frac{1}{Re} \frac{\partial u_i^\dagger}{\partial x_j} u_i \right]_{\partial V} dt} + \int_0^T \int_V \frac{1}{Re} u_i \frac{\partial^2 u_i^\dagger}{\partial x_j^2} dV dt = \\ &= \int_0^T \int_V \frac{1}{Re} u_i \frac{\partial^2 u_i^\dagger}{\partial x_j^2} dV dt\end{aligned}$$

$$5 : \int_0^T \int_V u_i^\dagger \frac{\partial (u_i u_j)}{\partial x_j} dV dt = \int_0^T \int_V u_i^\dagger \left(u_j \frac{\partial u_i}{\partial x_j} + \cancel{u_i \frac{\partial u_j}{\partial x_j}} \right) dV dt = \int_0^T \int_V u_i^\dagger u_j \frac{\partial u_i}{\partial x_j} dV dt$$

$$6 : \int_0^T \int_V p^\dagger \frac{\partial u_i}{\partial x_i} dV dt = \cancel{\int_0^T \left[p^\dagger u_i \right]_{\partial V} dt} - \int_0^T \int_V u_i \frac{\partial p^\dagger}{\partial x_i} dV dt = - \int_0^T \int_V u_i \frac{\partial p^\dagger}{\partial x_i} dV dt$$

with $\frac{\partial u_j}{\partial x_j} = 0$ in term 3 and 5 coming from the mass conservation, and $u_i = u_i^\dagger = 0$ imposed at the domain boundaries. After this, eq. (1) becomes:

$$
\begin{aligned}
&\mathcal{L} = E(T) + \\
&+ \int_0^T \int_V \left(\underbrace{u_i \frac{\partial u_i^\dagger}{\partial t}}_{1} + \underbrace{u_i U_j \frac{\partial u_i^\dagger}{\partial x_j}}_{2} - \underbrace{u_i^\dagger u_j \frac{\partial U_i}{\partial x_j}}_{3} - u_i^\dagger \frac{\partial p}{\partial x_i} + \underbrace{\frac{1}{Re} u_i \frac{\partial^2 u_i^\dagger}{\partial x_j^2}}_{4} - \underbrace{u_i^\dagger u_j \frac{\partial u_i}{\partial x_j}}_{5} \right) dV dt + \\
&+ \int_0^T \int_V \underbrace{u_i \frac{\partial p^\dagger}{\partial x_i}}_{6} dV dt - \lambda \left(E_0 - E(0) \right)
\end{aligned}
$$

Deriving the last expression with respect to the variable u_k, one has

$$
\begin{aligned}
&\frac{\partial \mathcal{L}}{\partial u_k} = 0 \Longrightarrow \\
&\Longrightarrow \frac{\partial}{\partial u_k} \int_0^T \int_V \left(\underbrace{u_i \frac{\partial u_i^\dagger}{\partial t}}_{1} + \underbrace{u_i U_j \frac{\partial u_i^\dagger}{\partial x_j}}_{2} - \underbrace{u_i^\dagger u_j \frac{\partial U_i}{\partial x_j}}_{3} + \underbrace{\frac{1}{Re} u_i \frac{\partial^2 u_i^\dagger}{\partial x_j^2}}_{4} - \underbrace{u_i^\dagger u_j \frac{\partial u_i}{\partial x_j}}_{5} + \underbrace{u_i \frac{\partial p^\dagger}{\partial x_i}}_{6} \right) dV dt = 0
\end{aligned}
$$

$$
\begin{aligned}
&\int_0^T \int_V \left(\underbrace{\frac{\partial u_i}{\partial u_k} \frac{\partial u_i^\dagger}{\partial t}}_{1} + \underbrace{U_j \frac{\partial u_i}{\partial u_k} \frac{\partial u_i^\dagger}{\partial x_j}}_{2} - \underbrace{u_i^\dagger \frac{\partial u_j}{\partial u_k} \frac{\partial U_i}{\partial x_j}}_{3} + \underbrace{\frac{1}{Re} \frac{\partial u_i}{\partial u_k} \frac{\partial^2 u_i^\dagger}{\partial x_j^2}}_{4} - \underbrace{u_i^\dagger \frac{\partial u_j}{\partial u_k} \frac{\partial u_i}{\partial x_j}}_{5.1} - \underbrace{u_i^\dagger u_j \frac{\partial}{\partial u_k} \left(\frac{\partial u_i}{\partial x_j} \right)}_{5.2} + \right. \\
&\qquad \left. + \underbrace{\frac{\partial u_i}{\partial u_k} \frac{\partial p^\dagger}{\partial x_i}}_{6} \right) dV dt = 0
\end{aligned}
$$

$$
\begin{aligned}
&\int_0^T \int_V \left(\underbrace{\delta_{ik} \frac{\partial u_i^\dagger}{\partial t}}_{1} + \underbrace{U_j \delta_{ik} \frac{\partial u_i^\dagger}{\partial x_j}}_{2} - \underbrace{u_i^\dagger \delta_{jk} \frac{\partial U_i}{\partial x_j}}_{3} + \underbrace{\frac{1}{Re} \delta_{ik} \frac{\partial^2 u_i^\dagger}{\partial x_j^2}}_{4} - \underbrace{u_i^\dagger \delta_{jk} \frac{\partial u_i}{\partial x_j}}_{5.1} - \underbrace{u_i^\dagger u_j \frac{\partial}{\partial u_k} \left(\frac{\partial u_i}{\partial x_j} \right)}_{5.2} + \right. \\
&\qquad \left. + \underbrace{\delta_{ik} \frac{\partial p^\dagger}{\partial x_i}}_{6} \right) dV dt = 0
\end{aligned}
$$

$$
\begin{aligned}
&\int_0^T \int_V \left(\underbrace{\frac{\partial (u_i^\dagger \delta_{ik})}{\partial t}}_{1} + \underbrace{U_j \frac{\partial (u_i^\dagger \delta_{ik})}{\partial x_j}}_{2} - \underbrace{u_i^\dagger \frac{\partial U_i}{\partial x_j} \delta_{jk}}_{3} + \underbrace{\frac{1}{Re} \frac{\partial^2 (u_i^\dagger \delta_{ik})}{\partial x_j^2}}_{4} - \underbrace{u_i^\dagger \frac{\partial u_i}{\partial x_j} \delta_{jk}}_{5.1} - \underbrace{u_i^\dagger u_j \frac{\partial}{\partial u_k} \left(\frac{\partial u_i}{\partial x_j} \right)}_{5.2} + \right. \\
&\qquad \left. + \underbrace{\frac{\partial p^\dagger}{\partial x_i} \delta_{ik}}_{6} \right) dV dt = 0
\end{aligned}
$$

$$
\int_0^T \int_V \left(\underbrace{\frac{\partial u_k^\dagger}{\partial t}}_{1} + \underbrace{U_j \frac{\partial u_k^\dagger}{\partial x_j}}_{2} - \underbrace{u_i^\dagger \frac{\partial U_i}{\partial x_k}}_{3} + \underbrace{\frac{1}{Re} \frac{\partial^2 u_k^\dagger}{\partial x_j^2}}_{4} - \underbrace{u_i^\dagger \frac{\partial u_i}{\partial x_k}}_{5.1} - \underbrace{u_i^\dagger u_j \frac{\partial}{\partial u_k} \left(\frac{\partial u_i}{\partial x_j} \right)}_{5.2} + \underbrace{\frac{\partial p^\dagger}{\partial x_k}}_{6} \right) dV dt = 0
$$

Terms 2 and 5.2 need further development.

$$2 : U_j \frac{\partial u_k^\dagger}{\partial x_j} = \frac{\partial (U_j u_k^\dagger)}{\partial x_j} - u_k^\dagger \cancel{\frac{\partial U_j}{\partial x_j}} = \frac{\partial (U_j u_k^\dagger)}{\partial x_j}$$

$$5.2 : \int_0^T \int_V u_i^\dagger u_j \frac{\partial}{\partial u_k} \left(\frac{\partial u_i}{\partial x_j} \right) dV dt = \cancel{\int_0^T \int_V \left[u_i^\dagger u_j \frac{\partial u_i}{\partial u_k} \right]_{\partial V}} dV dt - \int_0^T \int_V \frac{\partial u_i}{\partial u_k} \frac{\partial (u_i^\dagger u_j)}{\partial x_j} dV dt =$$

$$= - \int_0^T \int_V \delta_{ik} \frac{\partial (u_i^\dagger u_j)}{\partial x_j} dV dt = - \int_0^T \int_V \frac{\partial (u_i^\dagger \delta_{ik} u_j)}{\partial x_j} = - \int_0^T \int_V \frac{\partial (u_k^\dagger u_j)}{\partial x_j} dV dt$$

In this way, the last equation becomes

$$\int_0^T \int_V \left(\underbrace{\frac{\partial u_k^\dagger}{\partial t}}_{1} + \underbrace{\frac{\partial (U_j u_k^\dagger)}{\partial x_j}}_{2} - \underbrace{u_i^\dagger \frac{\partial U_i}{\partial x_k}}_{3} + \underbrace{\frac{1}{Re} \frac{\partial^2 u_k^\dagger}{\partial x_j^2}}_{4} - \underbrace{u_i^\dagger \frac{\partial u_i}{\partial x_k}}_{5.1} + \underbrace{\frac{\partial (u_k^\dagger u_j)}{\partial x_j}}_{5.2} + \underbrace{\frac{\partial p^\dagger}{\partial x_k}}_{6} \right) dV dt = 0$$

Imposing that the integral has to be null, finally one gets

$$\frac{\partial u_k^\dagger}{\partial t} + \frac{\partial (U_j u_k^\dagger)}{\partial x_j} - u_i^\dagger \frac{\partial U_i}{\partial x_k} + \frac{1}{Re} \frac{\partial^2 u_k^\dagger}{\partial x_j^2} - u_i^\dagger \frac{\partial u_i}{\partial x_k} + \frac{\partial (u_k^\dagger u_j)}{\partial x_j} + \frac{\partial p^\dagger}{\partial x_k} = 0$$

.2 Free Stream Turbulence implementation

.2.1 OSS modes

To generate a *synthetic* free stream turbulence we used the same method proposed by Brandt et al. (2004). A subset of 200 Orr-Sommerfeld Squire modes is used to generate the instantaneous inlet flow field in conjunction with the Blasius velocity profile

$$\mathbf{U}_{inflow} = \mathbf{U}_{Blas} + \sum_{i=1}^{200} A_i \hat{\mathbf{u}}_i(y) e^{(i\beta z - i\omega t)} \tag{9}$$

A_i being the weight associated to each mode. With the hypothesis that in the free stream the velocity field U is constant and equal to 1 and then $U' = U'' = 0$ being U' and U'' the first and the second derivative of the velocity profile in the wall-normal direction. Hence, the coupling therm in the Squire equation is then annihilate $-i\beta U' = 0$. In this scenario the Orr-Sommerfeld (10) and Squire (11) equation are decoupled to each other

$$\left[(-i\omega + i\alpha U)(D^2 - k^2) - \frac{1}{Re}(D^2 - k^2)^2\right] \hat{v} = 0 \tag{10}$$

$$\left[(-i\omega + i\alpha U) - \frac{1}{Re}(D^2 - k^2)\right] \hat{\eta} = 0 \tag{11}$$

and it is possible to get *pure Orr-Sommerfeld* and *pure Squire* modes. Introducing $U = 1$ the Orr-Sommerfeld equation can be recast as:

$$(D^2 - k^2)^2 \hat{v} - i\alpha Re\{(1 - c)(D^2 - k^2)\}\hat{v} = 0 \tag{12}$$

where c is the phase velocity, D^2 the second derivative operator, $k^2 = \alpha^2 + \beta^2$ and $\hat{v}(y)$ the wall normal perturbation. For $y \to \infty$ is

$$\hat{v} = Ae^{i\gamma y} + Be^{-}i\gamma y + Ce^{-ky} \tag{13}$$

and an analytical solution for the eigenvalue c can be extracted (Salwen and Grosch, 1981); (Grosch and Salwen, 1978)

$$c = 1 - i\left(1 + \frac{\gamma^2}{k^2}\right)\frac{k^2}{\alpha Re} \tag{14}$$

γ being the wavenumber in the wall-normal direction. Once α, β, γ and Re have been defined, the eigenvalue is fixed by (14) and it can be used in (12) to find the associated eigenvector. To solve the equation (10) four boundary condition have to be imposed. The firsts two are the no-slip at the wall $\hat{v}_0 = D\hat{v}_0 = 0$. The third is a dirichlet normalization boundary condition $\hat{v}_\infty = 1$. The last one is provided by Jacobs and Durbin (1998) and it is a numerical condition achieved once discretized the problem. The relation (13) is imposed onto two successive discretization points in the free-stream y_1, y_2

$$\frac{(D^2\hat{v} + \gamma^2\hat{v})_{y_1}}{(D^2\hat{v} + \gamma^2\hat{v})_{y_2}} = e^{k(y_2 - y_1)} \tag{15}$$

The boundary condition (15) is imposed on the last two point of the numerical domain. The imposition of the condition (15) is not straightforward as it can not be imposed directly in the OSS operator. A newton iteration is then implemented to restore iteratively the right boundary condition. The solution $\hat{v}_{y_2}$ is set equal to $\hat{v}_{y_1} = 1$ as first approximation. Of course this produces an error that can be evaluated as

$$\frac{(D^2\hat{v} + \gamma^2\hat{v})_{y_1}}{(D^2\hat{v} + \gamma^2\hat{v})_{y_2}} - e^{k(y_2-y_1)} = \xi_1. \tag{16}$$

Adding a small perturbation to $\hat{v}_{y_2} = 1 + \varepsilon$ a second error is achieved ξ_2. A first order sensibility can be now estimated as

$$\frac{d\xi}{d\varepsilon} = \frac{\xi_2 - \xi_1}{\varepsilon} \tag{17}$$

At this point a Newton iteration is used to find ε that annihilate ξ and then obtain the wanted solution. Usually with 500 Chebyshev collocation points to discretize the velocity profile 4 Newton iteration are enough to reach an error level $\xi < 10^{-10}$. In figure 2 the same OSS eigenmode of Brandt et al. (2002) is achieved. Since the Squire equation (11)

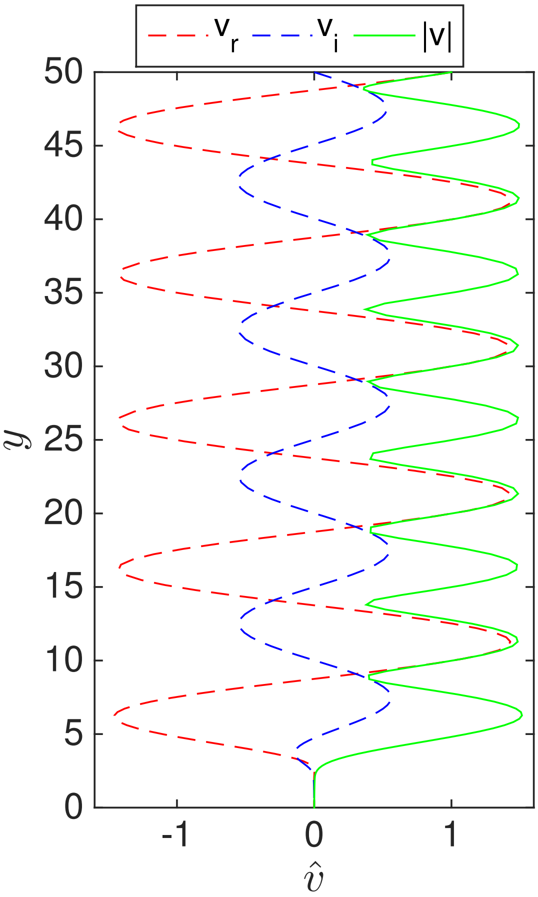

Figure 2: Orr-Sommerfeld eigenfunction vs y for $Re = 500$, $\alpha = 1$, $\beta = 0.2$ and $\gamma = 0.628$. The mode can is the same as in figure 6 of Brandt et al. (2002)

is decoupled from the OSS (10) one the normalization condition $\eta_\infty = 1$ is used at the top of the numerical domain and the no-slip condition $\eta_0 = 0$ at the wall.

The pure OSS mode $(\hat{u}_{oss}, \hat{v}_{oss}, \hat{w}_{oss})$ can now be obtained by

$$\hat{u}_{oss} = i\alpha D\hat{v}/k^2 \tag{18}$$
$$\hat{v}_{oss} = \hat{v} \tag{19}$$
$$\hat{w}_{oss} = i\beta D\hat{v}/k^2 \tag{20}$$

and the pure Squire mode $(\hat{u}_{sq}, \hat{v}_{sq}, \hat{w}_{sq})$ as

$$\hat{u}_{sq} = -i\beta\hat{\eta}/k^2 \tag{21}$$
$$\hat{v}_{sq} = 0 \tag{22}$$
$$\hat{w}_{sq} = i\alpha\hat{\eta}/k^2 \tag{23}$$

In order to increase the isotropy of the system a random phase $\phi_i \in [0, \pi[$ is added to OSS and Squire modes (Schlatter, 2001). The final perturbation is now

$$\hat{u} = \cos(\phi_1)e^{i\phi_2}\hat{u}_{oss} + \sin(\phi_1)e^{i\phi_3}\hat{u}_{sq} \tag{24}$$
$$\hat{v} = \cos(\phi_1)e^{i\phi_2}\hat{v}_{oss} \tag{25}$$
$$\hat{w} = \cos(\phi_1)e^{i\phi_2}\hat{w}_{oss} + \sin(\phi_1)e^{i\phi_3}\hat{w}_{sq} \tag{26}$$

The velocity vector $(\hat{u}, \hat{v}, \hat{w})$ is now normalized in order to have unitary energy density by taking in consideration just the numerical domain out from the boundary layer $y > 5\delta_1$. The resulting eigenfunction will not respect the boundary conditions imposed in the DNS at the top of the domain. As suggested by Brandt et al. (2004) a fringe zone as those explained in chapter §III can be used to damp to 0 the perturbation on the top of the domain. This will avoid small time step for the time marching of the DNS.

.2.2 Turbulent spectrum discretization.

As explained in §IV a turbulent energy spectrum has to be chosen to set the amplitude A_i at each eigenfunction of the turbulent basis. For this purpose the Von-Karman spectrum has been used

$$E(k) = \frac{2}{3}\frac{a(kL)^4}{(b + (kL)^2)^{17/6}}Lq. \tag{27}$$

Thanks to eq. 27 it is possible to associate at each k an energy. Following Brandt et al. (2004) the range of the available wavenumbers $[k_{min}, k_{max}]$ is divide in 20 shell and at each k_j is associate an $E(k_j)$. Since $k^2 = \alpha^2 + \beta^2 + \gamma^2$ then each k_i represents a sphere that can be discretized with a regular dodecahedron which is composed by 20 corners (see fig. 3). The dodecahedron is not symmetric, hence, each of the 20 (α, β, γ) triad is different. Using the dodecahedron for each k_j a total of 200 (α, β, γ) triads are generated. The amplitude of the eigenmode is equal to

$$A_i^2(k_j) = E(k_j)\frac{(k_{max} - k_{min})/19}{20}. \tag{28}$$

To increase the isotropy of the basis and to avoid concentric dodecahedron, a random rotation is added at each shell k_j.

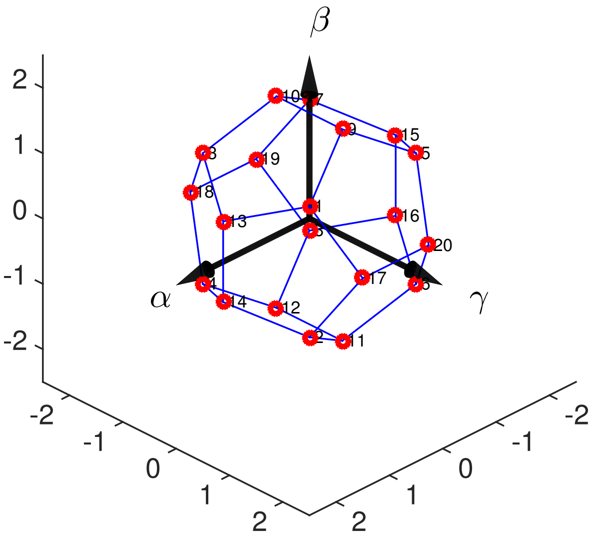

Figure 3: Example of the dodecahedron used to discretize k-shell. The dodecahedron is a regular non-symmetric polyhedron with 20 corners.

.2.3 Validation

Once generated, the eigenfunctions are read in Nek5000 and scaled to the good amplitude level. The streamwise wavenumber is converted in a pulsation invoking the Taylor hypothesis $\omega = U_\infty \alpha$. To validate the procedure the Case1 in (Brandt et al., 2004) is reproduced.

$x \times y \times z$	$nx \times ny \times nz$	Re_{δ_1}	$Tu\%$	L/δ_1
$1000 \times 100 \times 90$	$1152 \times 201 \times 192$	300	4.7	5

Table 1: Set-up of Case1 in Brandt et al. (2004).

A total of 133980 spectral elements with a spectral order equal to 12 are used in Nek5000 to achieve the same solution depicted in (Brandt et al., 2004). The exponential Tu decay with the streamwise direction is shown in figure 4. The figure 4 can be compared with the figure 2 in (Brandt et al., 2004). The turbulent intensity $Tu = \sqrt{(u_{rms}^2 + v_{rms}^2 + w_{rms}^2)/3}$ is evaluated at $y/\delta_1 = 60$ and averaged in z-direction. The homogeneous and isotropic turbulence decay obeys to a power low as observed experimentally and in agreement with the stable nature of the pure OSS modes used as basis to generate the inflow perturbation. A further comparison is provided by skin friction coefficient Cf vs Re_x in figure 5. The figure 5 can be compared with figure 3a in (Brandt et al., 2004). The Cf is used to highlight the transition position. In figure 5 the theoretical Blasius (laminar) Cf and the empirical turbulent one are also reported.

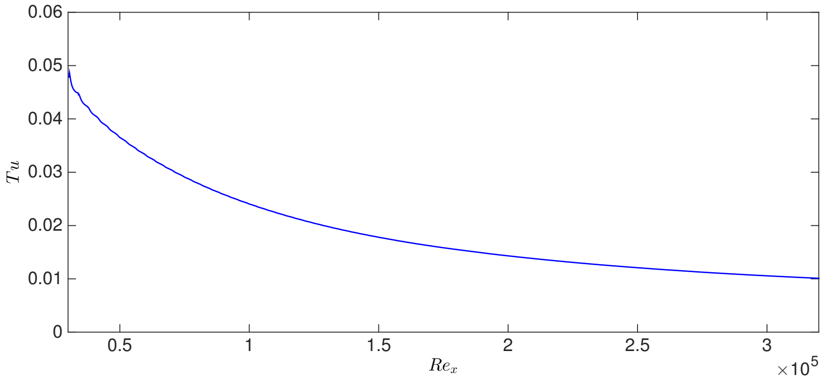

Figure 4: Exponential Tu decay for Case1 in (Brandt et al., 2004). The curve is extracted at $y/\delta_1 = 60$.

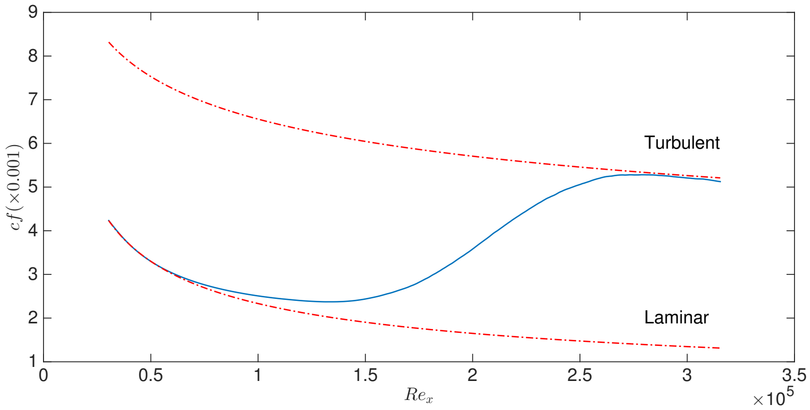

Figure 5: Skin friction coefficient Cf vs Re_x for Case1 in (Brandt et al., 2004).

Finally the instantaneous flow field is shown in figure 6. The figure 6 is extracted on the wall-normal plane at $y/\delta_1 = 2$. The streaks generation induced by the lift-up mechanism and the streaks instability with the generation of turbulent spots can be noticed in figure 6.

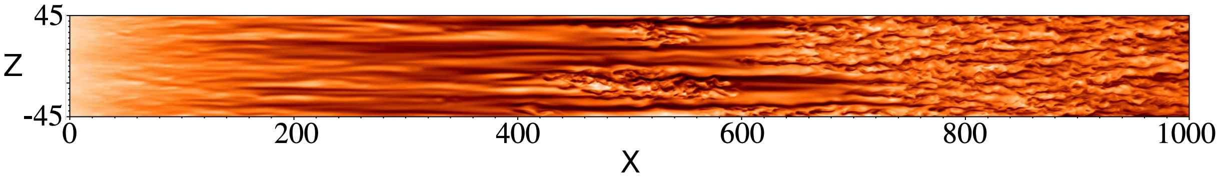

Figure 6: nstantaneous streamwise velocity field at $y/\delta_1 = 2$ for Case1 in (Brandt et al., 2004).

.2.3.0.a Acknowledgements I would like to thank Mr. Philip Schlatter who provided me his technical report Schlatter (2001) where useful numerical details are minutely discussed for the FST implementation. Moreover I would like to thank Mr. Luca Brandt for the private communication that helped me to achieve the good validation of the method just presented.

Scientific production

Scientific production

List of all conferences attended during this Ph.D thesis as well as al the paper accepted, submitted or currently in preparation

International conferences

- M. A. Bucci, S. Cherubini, J-C. Robinet
  Global stability analysis of the flow past micro vortex generators: the influence of the angle
  6th symposium, *Global Flow Instability and Control*, Crete, 2015

- M. A. Bucci, J-C. Robinet, S. Cherubini
  Global analysis of flow over MVG roughness
  11th *European Fluid Mechanics Conference*, Sevilla, 2016

- M. A. Bucci, S. Cherubini, J-C. Robinet, J-C. Loiseau
  Receptivity of roughness-induced streaky flow subject to free-stream turbulence
  ERCOFTAC, SIG 20, *European Drag Reduction and Flow Control Meeting*, Rome, 2017

- M. A. Bucci, D. K. Puckert, C. Andriano, J-C. Loiseau, S. Cherubini, J-C. Robinet, U. Rist
  Roughness-induced transition by quasi-resonance of a varicose global mode
  ERCOFTAC, SIG 33, *Progress in Flow Instability, Transition and Control*, Rome, 2017

- M. A. Bucci, J-C. Robinet, S. Cherubini
  Modal and non modal analysis of flow over MVG roughness
  16th *European Turbulence Conference*, Stockholm, 2017

- M. A. Bucci, D. K. Puckert, C. Andriano, J-C. Loiseau, S. Cherubini, J-C. Robinet, U. Rist
  Roughness-induced transition by quasi-resonance of a varicose global mode
  EUROMECH 591, *3-D Instability Mechanisms in Transitional and Turbulent flows*, Bari, 2017

Scientific papers

- M. A. Bucci, D. K. Puckert, C. Andriano, J-C. Loiseau, S. Cherubini, J-C. Robinet, U. Rist
  Roughness-induced transition by quasi-resonance of a varicose global mode
  Submitted to Jurnal of Fluid Mechanics

- M. A. Bucci, S. Cherubini, J-C. Loiseau, J-C. Robinet
  Receptivity of roughness-induced streaky flow subject to free-stream turbulence
  Under preparation

- M. A. Bucci, S. Cherubini, S. Cherubini, J-C. Robinet
  Subcritical and supercritical limitations in passive control with MVG roughness
  Under preparation

Projects out of thesis

The author also collaborated on the following paper and conferences out of the project of this thesis.

- M. A. Bucci, J-C. Robinet, S. Chibbaro
  Global stability analysis of 3D micro-combustion model
  6th International symposium on Bifurcation and Instabilities in Fluid Dynamics, Paris 2015

- M. A. Bucci, J-C. Robinet, S. Chibbaro
  Global stability analysis of 3D micro-combustion model
  Combustion and Flame, 2016

- M. A. Bucci, J-C. Robinet, S. Chibbaro
  Global stability analysis of 3D micro-combustion model
  19th Rencontre du non-lineaire, 2016

Bibliography

Acarlar, M. and Smith, C. (1987). A study of hairpin vortices in a laminar boundary layer. part 1. hairpin vortices generated by a hemisphere protuberance. *Journal of Fluid Mechanics*, 175:1–41.

Åkervik, E., Brandt, L., Henningson, D. S., Hœpffner, J., Marxen, O., and Schlatter, P. (2006). Steady solutions of the navier-stokes equations by selective frequency damping. *Physics of fluids*, 18(6):068102.

Albensoeder, S., Kuhlmann, H., and Rath, H. (2001). Three-dimensional centrifugal-flow instabilities in the lid-driven-cavity problem. *Physics of fluids*, 13(1):121–135.

Alizard, F., Cherubini, S., and Robinet, J.-C. (2009). Sensitivity and optimal forcing response in separated boundary layer flows. *Physics of Fluids*, 21(6):064108.

Alizard, F. and Robinet, J.-C. (2007). Spatially convective global modes in a boundary layer. *Physics of fluids*, 19(11):114105.

Alizard, F. and Robinet, J.-C. (2011). Modeling of optimal perturbations in flat plate boundary layer using global modes: benefits and limits. *Theoretical and Computational Fluid Dynamics*, 25(1):147–165.

Andersen, E., Bai, Z., Bischof, C., Demmel, J., Dongarra, J., Greenbaum, A., Hammarling, S., McKenney, A., Ostrouchev, S., and Sorensen, D. (1999). Lapack user's guide, 3rd. *Society for Industrial and Applied Math., Philadelphia.*

Anderson, G. F. and Wu, Y.-K. (1971). Drag reduction by use of mhd boundary-layer control. *J. Hydronaut.;(United States)*, 5(4).

Andersson, P., Brandt, L., Bottaro, A., and Henningson, D. S. (2001). On the breakdown of boundary layer streaks. *Journal of Fluid Mechanics*, 428:29–60.

Arnal, D., Houdeville, R., Séraudie, A., and Vermeersch, O. (2011). Overview of laminar-turbulent transition investigations at onera toulouse. In *41st AIAA Fluid Dynamics Conference and Exhibit*, number 2011-3074.

Babenko, V. and Kozlov, L. (1972). Experimental investigation of hydrodynamic stability on rigid and elastic damping surfaces. *Journal of Hydraulic Research*, 10(4):283–308.

Bagheri, S., Åkervik, E., Brandt, L., and Henningson, D. S. (2009). Matrix-free methods for the stability and control of boundary layers. *AIAA J*, 47(5):1057–1068.

Baines, P. G., Majumdar, S. J., and Mitsudera, H. (1996). The mechanics of the tollmien-schlichting wave. *Journal of fluid mechanics*, 312:107–124.

Baker, C. (1979). The laminar horseshoe vortex. *Journal of fluid mechanics*, 95(2):347–367.

Barkley, D., Blackburn, H., and Sherwin, S. J. (2008). Direct optimal growth analysis for timesteppers. *International journal for numerical methods in fluids*, 57(9):1435–1458.

Beaudoin, J.-F. (2004). *Contrôle actif d'écoulement en aérodynamique automobile*. PhD thesis, Paris, ENMP.

Berkooz, G., Holmes, P., and Lumley, J. L. (1993). The proper orthogonal decomposition in the analysis of turbulent flows. *Annual review of fluid mechanics*, 25(1):539–575.

Bernardini, M., Pirozzoli, S., and Orlandi, P. (2012). Compressibility effects on roughness-induced boundary layer transition. *International Journal of Heat and Fluid Flow*, 35:45–51.

Boiko, A., Westin, K., Klingmann, B., Kozlov, V., and Alfredsson, P. (1994). Experiments in a boundary layer subjected to free stream turbulence. part 2. the role of ts-waves in the transition process. *Journal of Fluid Mechanics*, 281:219–245.

Botella, O. (1997). On the solution of the navier-stokes equations using chebyshev projection schemes with third-order accuracy in time. *Computers & Fluids*, 26(2):107–116.

Boyd, J. P. (2001). *Chebyshev and Fourier spectral methods*. Courier Corporation.

Brandt, L. (2007). Numerical studies of the instability and breakdown of a boundary-layer low-speed streak. *European Journal of Mechanics-B/Fluids*, 26(1):64–82.

Brandt, L. (2014). The lift-up effect: The linear mechanism behind transition and turbulence in shear flows. *European Journal of Mechanics-B/Fluids*, 47:80–96.

Brandt, L., Henningson, D. S., and Ponziani, D. (2002). Weakly nonlinear analysis of boundary layer receptivity to free-stream disturbances. *Physics of fluids*, 14(4):1426–1441.

Brandt, L., Schlatter, P., and Henningson, D. S. (2004). Transition in boundary layers subject to free-stream turbulence. *Journal of Fluid Mechanics*, 517:167–198.

Brandt, L., Sipp, D., Pralits, J. O., and Marquet, O. (2011). Effect of base-flow variation in noise amplifiers: the flat-plate boundary layer. *Journal of Fluid Mechanics*, 687:503–528.

Braslow, A. L. (1960). Review of the effect of distributed surface roughness on boundary-layer transition. Technical report, ADVISORY GROUP FOR AERONAUTICAL RESEARCH AND DEVELOPMENT PARIS (FRANCE).

Brynjell-Rahkola, M., Shahriari, N., Schlatter, P., Hanifi, A., and Henningson, D. S. (2017). Stability and sensitivity of a cross-flow-dominated falkner–skan–cooke boundary layer with discrete surface roughness. *Journal of Fluid Mechanics*, 826:830–850.

Carini, M., Giannetti, F., and Auteri, F. (2014). On the origin of the flip–flop instability of two side-by-side cylinder wakes. *Journal of Fluid Mechanics*, 742:552–576.

Cary Jr, A., Bushnell, D., and Hefner, J. (1977). Slot injection for skin-friction drag reduction.

Cherubini, S., De Palma, P., Robinet, J.-C., and Bottaro, A. (2010a). Rapid path to transition via nonlinear localized optimal perturbations in a boundary-layer flow. *Physical Review E*, 82(6):066302.

Cherubini, S., De Palma, P., Robinet, J.-C., and Bottaro, A. (2011). The minimal seed of turbulent transition in the boundary layer. *Journal of Fluid Mechanics*, 689:221–253.

Cherubini, S., De Tullio, M., De Palma, P., and Pascazio, G. (2013). Transient growth in the flow past a three-dimensional smooth roughness element. *Journal of Fluid Mechanics*, 724:642–670.

Cherubini, S., Robinet, J.-C., Bottaro, A., and De Palma, P. (2010b). Optimal wave packets in a boundary layer and initial phases of a turbulent spot. *Journal of Fluid Mechanics*, 656:231–259.

Choudhari, M. (2004). Numerical simulation of roughness-induced transient growth in a laminar boundary layer.

Citro, V., Giannetti, F., Luchini, P., and Auteri, F. (2015). Global stability and sensitivity analysis of boundary-layer flows past a hemispherical roughness element. *Physics of Fluids*, 27(8):084110.

Citro, V., Luchini, P., Giannetti, F., and Auteri, F. (2017). Efficient stabilization and acceleration of numerical simulation of fluid flows by residual recombination. *Journal of Computational Physics*, 344:234–246.

Cohen, J., Karp, M., and Mehta, V. (2014). A minimal flow-elements model for the generation of packets of hairpin vortices in shear flows. *Journal of Fluid Mechanics*, 747:30–43.

Cossu, C. and Brandt, L. (2002). Stabilization of tollmien–schlichting waves by finite amplitude optimal streaks in the blasius boundary layer. *Physics of Fluids*, 14(8):L57–L60.

Cossu, C. and Brandt, L. (2004). On tollmien–schlichting-like waves in streaky boundary layers. *European Journal of Mechanics-B/Fluids*, 23(6):815–833.

Cossu, C. and Chomaz, J. (1997). Global measures of local convective instabilities. *Physical review letters*, 78(23):4387.

Daniello, R. J., Waterhouse, N. E., and Rothstein, J. P. (2009). Drag reduction in turbulent flows over superhydrophobic surfaces. *Physics of Fluids*, 21(8):085103.

De Tullio, N., Paredes, P., Sandham, N., and Theofilis, V. (2013). Laminar–turbulent transition induced by a discrete roughness element in a supersonic boundary layer. *Journal of Fluid Mechanics*, 735:613–646.

Denissen, N. and White, E. (2009). Continuous spectrum analysis of roughness-induced transient growth. *Physics of Fluids*, 21(11):114105.

Denissen, N. A. and White, E. B. (2008). Roughness-induced bypass transition, revisited. *AIAA journal*, 46(7):1874–1877.

Deville, M. O., Fischer, P. F., and Mund, E. H. (2002). *High-order methods for incompressible fluid flow*, volume 9. Cambridge university press.

Duriez, T. (2009). *Application des générateurs de vortex au contrôle d'Écoulements décollés*. PhD thesis, Université Paris-Diderot-Paris VII.

Edwards, W., Tuckerman, L. S., Friesner, R. A., and Sorensen, D. (1994). Krylov methods for the incompressible navier-stokes equations. *Journal of computational physics*, 110(1):82–102.

Ergin, F. G. and White, E. B. (2006). Unsteady and transitional flows behind roughness elements. *AIAA journal*, 44(11):2504.

Farano, M., Cherubini, S., Robinet, J.-C., and De Palma, P. (2015). Hairpin-like optimal perturbations in plane poiseuille flow. *Journal of Fluid Mechanics*, 775.

Farano, M., Cherubini, S., Robinet, J.-C., and De Palma, P. (2016). Subcritical transition scenarios via linear and nonlinear localized optimal perturbations in plane poiseuille flow. *Fluid Dynamics Research*, 48(6):061409.

Farano, M., Cherubini, S., Robinet, J.-C., and De Palma, P. (2017). Optimal bursts in turbulent channel flow. *Journal of Fluid Mechanics*, 817:35–60.

Farazmand, M. (2016). An adjoint-based approach for finding invariant solutions of navier–stokes equations. *Journal of Fluid Mechanics*, 795:278–312.

Fischer, P. F., Lottes, J. W., and Kerkemeier, S. G. (2008). nek5000 web page. *Web page: http://nek5000. mcs. anl. gov.*

Foures, D., Caulfield, C., and Schmid, P. (2013). Localization of flow structures using ∞-norm optimization. *Journal of Fluid Mechanics*, 729:672–701.

Foures, D., Caulfield, C., and Schmid, P. J. (2014). Optimal mixing in two-dimensional plane poiseuille flow at finite péclet number. *Journal of Fluid Mechanics*, 748:241–277.

Fraim, F. W. and Heiser, W. H. (1968). The effect of a strong longtitudinal magnetic field on the flow of mercury in a circular tube. *Journal of Fluid Mechanics*, 33(2):397–413.

Fransson, J. H., Brandt, L., Talamelli, A., and Cossu, C. (2004). Experimental and theoretical investigation of the nonmodal growth of steady streaks in a flat plate boundary layer. *Physics of Fluids*, 16(10):3627–3638.

Fransson, J. H., Brandt, L., Talamelli, A., and Cossu, C. (2005). Experimental study of the stabilization of tollmien–schlichting waves by finite amplitude streaks. *Physics of Fluids*, 17(5):054110.

Fransson, J. H. and Talamelli, A. (2012). On the generation of steady streamwise streaks in flat-plate boundary layers. *Journal of Fluid Mechanics*, 698:211–234.

Fransson, J. H., Talamelli, A., Brandt, L., and Cossu, C. (2006). Delaying transition to turbulence by a passive mechanism. *Physical review letters*, 96(6):064501.

Garnaud, X., Lesshafft, L., Schmid, P. J., and Chomaz, J.-M. (2012). A relaxation method for large eigenvalue problems, with an application to flow stability analysis. *Journal of Computational Physics*, 231(10):3912–3927.

Giannetti, F. and Luchini, P. (2007). Structural sensitivity of the first instability of the cylinder wake. *Journal of Fluid Mechanics*, 581:167–197.

Gottlieb, D. and Hirsh, R. S. (1989). Parallel pseudospectral domain decomposition techniques. *Journal of Scientific Computing*, 4(4):309–325.

Gregory, N. and Walker, W. (1956). *The effect on transition of isolated surface excrescences in the boundary layer*. HM Stationery Office.

Grosch, C. E. and Salwen, H. (1978). The continuous spectrum of the orr-sommerfeld equation. part 1. the spectrum and the eigenfunctions. *Journal of Fluid Mechanics*, 87(1):33–54.

Herbert, T. (1988). Secondary instability of boundary layers. *Annual Review of Fluid Mechanics*, 20(1):487–526.

Hœpffner, J. and Brandt, L. (2008). Stochastic approach to the receptivity problem applied to bypass transition in boundary layers. *Physics of fluids*, 20(2):024108.

Huerre, P., Batchelor, G., Moffatt, H., and Worster, M. (2000). Open shear flow instabilities. *Perspectives in fluid dynamics*, pages 159–229.

Huerre, P. and Monkewitz, P. A. (1985). Absolute and convective instabilities in free shear layers. *Journal of Fluid Mechanics*, 159:151–168.

Jacobs, R. and Durbin, P. (2001). Simulations of bypass transition. *Journal of Fluid Mechanics*, 428:185–212.

Jacobs, R. G. and Durbin, P. A. (1998). Shear sheltering and the continuous spectrum of the orr–sommerfeld equation. *Physics of Fluids*, 10(8):2006–2011.

Jeong, J. and Hussain, F. (1995). On the identification of a vortex. *J. Fluid Mech.*, 285:69–94.

Joslin, R. D. and Grosch, C. E. (1995). Growth characteristics downstream of a shallow bump: Computation and experiment. *Physics of Fluids*, 7(12):3042–3047.

Jovanović, M. R., Schmid, P. J., and Nichols, J. W. (2014). Sparsity-promoting dynamic mode decomposition. *Physics of Fluids*, 26(2):024103.

Juniper, M. P., Hanifi, A., and Theofilis, V. (2014). Modal stability theorylecture notes from the flow-nordita summer school on advanced instability methods for complex flows, stockholm, sweden, 2013. *Applied Mechanics Reviews*, 66(2):024804.

Kachanov, Y. S. (1994). Physical mechanisms of laminar-boundary-layer transition. *Annual review of fluid mechanics*, 26(1):411–482.

Karniadakis, G. and Sherwin, S. (2013). *Spectral/hp element methods for computational fluid dynamics*. Oxford University Press.

Kato, T. (2013). *Perturbation theory for linear operators*, volume 132. Springer Science & Business Media.

Klebanoff, P., Cleveland, W., and Tidstrom, K. (1992). On the evolution of a turbulent boundary layer induced by a three-dimensional roughness element. *Journal of Fluid Mechanics*, 237:101–187.

Klebanoff, P. and Tidstrom, K. (1972). Mechanism by which a two-dimensional roughness element induces boundary-layer transition. *The Physics of Fluids*, 15(7):1173–1188.

Kong, F. Y. and Schetz, J. A. (1982). Turbulent boundary layer over porous surfaces with different surface geometries. In *AIAA, Aerospace Sciences Meeting*.

Kong, F. Y., Schetz, J. A., and Collier, F. (1982). Turbulent boundary layer over solid and porous surfaces with small roughness.

Koopman, B. O. (1931). Hamiltonian systems and transformation in hilbert space. *Proceedings of the National Academy of Sciences*, 17(5):315–318.

Kurz, H. B. and Kloker, M. J. (2016). Mechanisms of flow tripping by discrete roughness elements in a swept-wing boundary layer. *Journal of Fluid Mechanics*, 796:158–194.

Landahl, M. (1980). A note on an algebraic instability of inviscid parallel shear flows. *Journal of Fluid Mechanics*, 98(2):243–251.

Landahl, M. T. (1975). Wave breakdown and turbulence. *SIAM Journal on Applied Mathematics*, 28(4):735–756.

Lesshafft, L. (2017). Artificial eigenmodes in truncated flow domains. *arXiv preprint arXiv:1704.08450*.

Lindgren, B. and Johansson, A. V. (2002). Design and evaluation of a low-speed wind-tunnel with expanding corners. *Department of Mechanics, KTH, Report No. TRITA-MEK*, 14.

Loiseau, J.-C. (2014). *Dynamics and global stability analysis of three-dimensional flows*. PhD thesis, Ecole nationale supérieure d'arts et métiers-ENSAM.

Loiseau, J.-C., Robinet, J.-C., Cherubini, S., and Leriche, E. (2014). Investigation of the roughness-induced transition: global stability analyses and direct numerical simulations. *Journal of Fluid Mechanics*, 760:175–211.

Luchini, P. and Bottaro, A. (2014). Adjoint equations in stability analysis. *Annual Review of fluid mechanics*, 46.

Lumley, J. L. (1969). Drag reduction by additives. *Annual review of fluid mechanics*, 1(1):367–384.

Lundbladh, A., Berlin, S., Skote, M., Hildings, C., Choi, J., Kim, J., and Henningson, D. S. (1999). An efficient spectral method for simulation of incompressible flow over a flat plate. *Trita-mek. Tech. Rep*, 11.

Lundbladh, A. and Johansson, A. V. (1991). Direct simulation of turbulent spots in plane couette flow. *Journal of Fluid Mechanics*, 229:499–516.

Marquet, O., Sipp, D., and Jacquin, L. (2008). Sensitivity analysis and passive control of cylinder flow. *Journal of Fluid Mechanics*, 615:221–252.

McCORMICK, M. E. and Bhattacharyya, R. (1973). Drag reduction of a submersible hull by electrolysis. *Naval Engineers Journal*, 85(2):11–16.

Michalke, A. (1964). On the inviscid instability of the hyperbolictangent velocity profile. *Journal of Fluid Mechanics*, 19(4):543–556.

Michalke, A. (1965). On spatially growing disturbances in an inviscid shear layer. *Journal of Fluid Mechanics*, 23(3):521–544.

Monokrousos, A., Åkervik, E., Brandt, L., and Henningson, D. S. (2010). Global three-dimensional optimal disturbances in the blasius boundary-layer flow using time-steppers. *Journal of Fluid Mechanics*, 650:181–214.

Morkovin, M., Reshotko, E., and Herbert, T. (1994). Transition in open flow systems-a reassessment. *Bull. Am. Phys. Soc*, 39(9):1882.

Orszag, S. A. (1971). Accurate solution of the orr–sommerfeld stability equation. *Journal of Fluid Mechanics*, 50(4):689–703.

Patel, V. and Head, M. (1969). Some observations on skin friction and velocity profiles in fully developed pipe and channel flows. *Journal of Fluid Mechanics*, 38(1):181–201.

Patera, A. T. (1984). A spectral element method for fluid dynamics: laminar flow in a channel expansion. *Journal of computational Physics*, 54(3):468–488.

Perraud, J., Arnal, D., Seraudie, A., and Tran, D. (2004). Laminar-turbulent transition on aerodynamic surfaces with imperfections. *ONERA: Tire a Part*, 13:2004.

Pier, B. and Huerre, P. (2001). Nonlinear self-sustained structures and fronts in spatially developing wake flows. *Journal of Fluid Mechanics*, 435:145–174.

Piot, E., Casalis, G., and Rist, U. (2008). Stability of the laminar boundary layer flow encountering a row of roughness elements: Biglobal stability approach and dns. *European Journal of Mechanics-B/Fluids*, 27(6):684–706.

Pringle, C. C. and Kerswell, R. R. (2010). Using nonlinear transient growth to construct the minimal seed for shear flow turbulence. *Physical review letters*, 105(15):154502.

Pringle, C. C., Willis, A. P., and Kerswell, R. R. (2012). Minimal seeds for shear flow turbulence: using nonlinear transient growth to touch the edge of chaos. *Journal of Fluid Mechanics*, 702:415–443.

Puckert, D., Subasi, A., Rist, U., and Gunes, H. (2015). Experimental investigations of critical roughness heights in a laminar boundary layer.

Puckert, D. K., Dieterle, M., and Rist, U. (2017). Reduction of freestream turbulence at low velocities. *Exp. Fluids*, 58(5):45.

Quadrio, M. and Ricco, P. (2004). Critical assessment of turbulent drag reduction through spanwise wall oscillations. *Journal of Fluid Mechanics*, 521:251–271.

Reddy, S. C. and Henningson, D. S. (1993). Energy growth in viscous channel flows. *Journal of Fluid Mechanics*, 252:209–238.

Reddy, S. C., Schmid, P. J., and Henningson, D. S. (1993). Pseudospectra of the orr–sommerfeld operator. *SIAM Journal on Applied Mathematics*, 53(1):15–47.

Robinet, J.-C., Gloerfelt, X., and Corre, C. (2005). Dynamics of two-dimensional square liddriven cavity at high reynolds number. In *3rd Global flow instability and control symposium, Hersonissos, Crete, GR.*

Rogallo, R. S. (1981). Numerical experiments in homogeneous turbulence.

Romanov, V. (1973). Stability of plane-parallel couette flow. *Functional analysis and its applications*, 7(2):137–146.

Rowley, C. W., Mezić, I., Bagheri, S., Schlatter, P., and Henningson, D. S. (2009). Spectral analysis of nonlinear flows. *Journal of fluid mechanics*, 641:115–127.

Salwen, H. and Grosch, C. E. (1981). The continuous spectrum of the orr-sommerfeld equation. part 2. eigenfunction expansions. *Journal of Fluid Mechanics*, 104:445–465.

Sattarzadeh, S. S., Fransson, J. H., Talamelli, A., and Fallenius, B. E. (2014). Consecutive turbulence transition delay with reinforced passive control. *Physical Review E*, 89(6):061001.

Schlatter, P. (2001). Direct numerical simulation of laminar-turbulent transition in boundary layer subject to free-stream turbulence. *Master's thesis, Royal Institute of Technology, Stockholm.*

Schlatter, P., Adams, N., and Kleiser, L. (2005). A windowing method for periodic inflow/outflow boundary treatment of non-periodic flows. *Journal of computational physics*, 206(2):505–535.

Schlatter, P., Brandt, L., De Lange, H., and Henningson, D. S. (2008). On streak breakdown in bypass transition. *Physics of fluids*, 20(10):101505.

Schlatter, P., de Lange, R., and Brandt, L. (2007). The effect of free-stream turbulence on growth and breakdown of tollmien-schlichting waves. In *Advances in Turbulence XI*, pages 179–181. Springer.

Schlatter, P., Deusebio, E., de Lange, R., and Brandt, L. (2010). Numerical study of the stabilisation of boundary-layer disturbances by finite amplitude streaks. *International Journal of Flow Control*, 2(4):259–288.

Schmid, P. J. (2010). Dynamic mode decomposition of numerical and experimental data. *Journal of fluid mechanics*, 656:5–28.

Schmid, P. J. and Brandt, L. (2014). Analysis of fluid systems: Stability, receptivity, sensitivitylecture notes from the flow-nordita summer school on advanced instability methods for complex flows, stockholm, sweden, 2013. *Applied Mechanics Reviews*, 66(2):024803.

Schmid, P. J. and Henningson, D. S. (2012). *Stability and transition in shear flows*, volume 142. Springer Science & Business Media.

Schmid, P. J. and Sesterhenn, J. (2008). Dynamic mode decomposition of numerical and experimental data. In *Sixty-First Annual Meeting of the APS Division of Fluid Dynamics*.

Sedney, R. (1973). A survey of the effects of small protuberances on boundary-layer flows. *AIAA J*, 11(6):782–792.

Shahinfar, S., Fransson, J. H., Sattarzadeh, S., and Talamelli, A. (2013). Scaling of streamwise boundary layer streaks and their ability to reduce skin-friction drag. *Journal of Fluid Mechanics*, 733:1–32.

Shahinfar, S., Sattarzadeh, S. S., and Fransson, J. H. (2014). Passive boundary layer control of oblique disturbances by finite-amplitude streaks. *Journal of Fluid Mechanics*, 749:1–36.

Shahinfar, S., Sattarzadeh, S. S., Fransson, J. H., and Talamelli, A. (2012). Revival of classical vortex generators now for transition delay. *Physical review letters*, 109(7):074501.

Shin, Y.-s., Rist, U., and Krämer, E. (2015). Stability of the laminar boundary-layer flow behind a roughness element. *Experiments in Fluids*, 56(1):11.

Siconolfi, L., Camarri, S., and Fransson, J. H. (2015a). Boundary layer stabilization using free-stream vortices. *Journal of Fluid Mechanics*, 764.

Siconolfi, L., Camarri, S., and Fransson, J. H. (2015b). Stability analysis of boundary layers controlled by miniature vortex generators. *Journal of Fluid Mechanics*, 784:596–618.

Siconolfi, L., Citro, V., Giannetti, F., Camarri, S., and Luchini, P. (2017). Towards a quantitative comparison between global and local stability analysis. *Journal of Fluid Mechanics*, 819:147–164.

Sipp, D. and Marquet, O. (2013). Characterization of noise amplifiers with global singular modes: the case of the leading-edge flat-plate boundary layer. *Theoretical and Computational Fluid Dynamics*, 27(5):617.

Sipp, D., Marquet, O., Meliga, P., and Barbagallo, A. (2010). Dynamics and control of global instabilities in open-flows: a linearized approach. *Applied Mechanics Reviews*, 63(3):030801.

Sorensen, D. C. (1992). Implicit application of polynomial filters in ak-step arnoldi method. *Siam journal on matrix analysis and applications*, 13(1):357–385.

Spangenberg, W., Rowland, W., and Mease, N. (1967). *Measurements in a turbulent boundary layer maintained in a nearly separating condition.* Elsevier, Netherlands.

Squire, H. B. (1933). On the stability for three-dimensional disturbances of viscous fluid flow between parallel walls. *Proceedings of the Royal Society of London. Series A, Containing Papers of a Mathematical and Physical Character*, 142(847):621–628.

Stewart, G. W. (2002). A krylov–schur algorithm for large eigenproblems. *SIAM Journal on Matrix Analysis and Applications*, 23(3):601–614.

Stratford, B. (1959). The prediction of separation of the turbulent boundary layer. *Journal of fluid mechanics*, 5(1):1–16.

Subasi, A., Puckert, D., Gunes, H., and Rist, U. (2015). Calibration of constant temperature anemometry with hot-film probes for low speed laminar water channel flows. *The 13th international symposium on fluid control, measurement and visualization. Doha, Qatar. Flucome 2015.*

Tatsumi, T. and Yoshimura, T. (1990). Stability of the laminar flow in a rectangular duct. *Journal of Fluid Mechanics*, 212:437–449.

Theofilis, V. (2003). Advances in global linear instability analysis of nonparallel and three-dimensional flows. *Progress in aerospace sciences*, 39(4):249–315.

Theofilis, V. (2011). Global linear instability. *Annual Review of Fluid Mechanics*, 43:319–352.

Toh, K.-C. and Trefethen, L. N. (1996). Calculation of pseudospectra by the arnoldi iteration. *SIAM Journal on Scientific Computing*, 17(1):1–15.

TREFETHEN, L., Trefethen, A., Reddy, S., Driscoll, T., et al. (1993). Hydrodynamic stability without eigenvalues. *Science*, 261(5121):578–584.

Trefethen, L. N. (2000). *Spectral methods in MATLAB.* SIAM.

Trefethen, L. N. and Embree, M. (2005). *Spectra and pseudospectra: the behavior of nonnormal matrices and operators*. Princeton University Press.

Viotti, C., Quadrio, M., and Luchini, P. (2009). Streamwise oscillation of spanwise velocity at the wall of a channel for turbulent drag reduction. *Physics of fluids*, 21(11):115109.

Waleffe, F. (1995). Hydrodynamic stability and turbulence: Beyond transients to a self-sustaining process. *Studies in Applied Mathematics*, 95(3):319–343.

Walsh, M. J. (1982). Turbulent boundary layer drag reduction using riblets. In *AIAA, Aerospace sciences meeting*.

Westin, K., Boiko, A., Klingmann, B., Kozlov, V., and Alfredsson, P. (1994). Experiments in a boundary layer subjected to free stream turbulence. part 1. boundary layer structure and receptivity. *Journal of Fluid Mechanics*, 281:193–218.

Wiegand, T. (1996). Experimentelle untersuchungen zum laminar-turbulenten transitionsprozess eines wellenzuges in einer plattengrenzschicht.

Ye, Q., Schrijer, F. F., and Scarano, F. (2016a). Boundary layer transition mechanisms behind a micro-ramp. *Journal of Fluid Mechanics*, 793:132–161.

Ye, Q., Schrijer, F. F., and Scarano, F. (2016b). Geometry effect of isolated roughness on boundary layer transition investigated by tomographic piv. *International Journal of Heat and Fluid Flow*, 61:31–44.

Ye, Q., Schrijer, F. F., and Scarano, F. (2017). Tomographic piv measurement of hypersonic boundary layer transition past a micro-ramp. In *47th AIAA Fluid Dynamics Conference*, page 4512.

Zhou, J., Adrian, R. J., Balachandar, S., and Kendall, T. (1999). Mechanisms for generating coherent packets of hairpin vortices in channel flow. *Journal of fluid mechanics*, 387:353–396.

Zuccher, S., Luchini, P., and Bottaro, A. (2004). Algebraic growth in a blasius boundary layer: optimal and robust control by mean suction in the nonlinear regime. *Journal of Fluid Mechanics*, 513:135–160.

Dynamique souscritique et supercritique d’un écoulement incompressible autour d’éléments de micro-rugosité

RÉSUMÉ : Cette thèse vise à mettre en évidence les limites du contrôle passif en utilisant des éléments de rugosité miniaturisés. La topologie des écoulements induite par la présence d’une rugosité cylindrique et des générateurs de tourbillons miniaturisés a été étudiée pour analyser la dynamique pour des temps court et long. Différentes bifurcations supercritiques ont été examinées au moyen d’une analyse de stabilité globale. La bifurcation souscritique est déclenchée par des mécanismes de croissance transitoire de l'énergie ou par la réceptivité de modes globaux stables. Des structures de forçage optimal 3D sont extraites pour comprendre la distribution spatiale liée à la fréquence de résonance du système. La simulation numérique directe perturbée révèle le rôle central du mode global le moins stable dans les instationnarités non-linéaires observées. Une analyse détaillée des structures tourbillonnaires montre qu’elles sont principalement liées aux mécanismes linéaires sous-jacents. La principale caractéristique globale du mode propre est liée à la présence d’une zone de séparation en aval de la rugosité cylindrique. En utilisant des générateurs de tourbillon miniaturisés, cette zone de séparation est fortement diminuée et aucun mode global isolé est alors présent. La dynamique de l’écoulement se révèle être conduit non seulement par le nombre de Reynolds de rugosité et par son rapport d'aspect géométrique, mais aussi par le rapport entre la hauteur de la rugosité et l’epaisseur de couche limite.

Mots clés : Ecoulements autour de rugosités, stabilité globale, forçage optimal 3D, réceptivité, transition vers la turbulence, croissance transitoire, contrôle passif.

Subcritical and supercritical dynamics of incompressible flow over miniaturized roughness elements

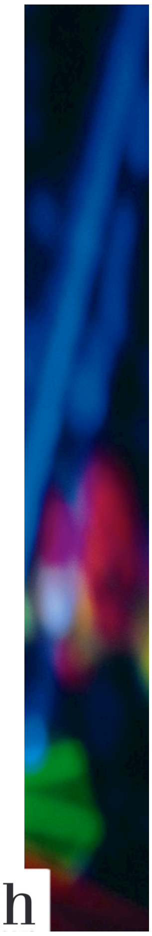

ABSTRACT : This thesis aims at highlighting the limits of passive control by using miniaturized roughness elements. The flow topology induced by the presence of cylindrical roughness and miniaturized vertex generators has been studied to uncover asymptotic and short time dynamics. Supercritical bifurcations has been investigated by means of global stability analysis. Subcritical bifurcation are induced by transient growth of the energy or receptivity of stable global modes. 3D optimal forcing structures are extracted to figure out the spatial distribution linked to the resonant pulsation. Perturbed direct numerical simulation reveals the pivotal role of the less steady global mode in the non-linear unsteadiness. A detailed analysis of the flow structures is provided and linked to the involved linear mechanisms. Global feature of the eigenmode are linked to the presence of the separation zone behind the cylindrical roughness. By using miniaturized vortex generators the separation zone is suppressed and no isolated global modes are present. The flow dynamics turns out to be driven not only by roughness Reynolds number and geometrical aspect ratio but also by the ratio between the roughness height and the boundary layer thickens.

Keywords : Flow over roughness, global stability, 3D optimal forcing, receptivity to turbulence, transient growth, passive control.